

TECHNISCHE  
UNIVERSITÄT  
WIEN

VIENNA  
UNIVERSITY OF  
TECHNOLOGY

DISSERTATION

High performance terahertz time-domain spectroscopy:  
Application, control and amplification of  
few cycle terahertz radiation

ausgeführt zum Zwecke der Erlangung des akademischen Grades eines  
Doktors der technischen Wissenschaften

unter der Leitung von

Univ.-Prof. Mag. rer. nat. Dr. rer. nat. Karl Unterrainer  
und Dipl.-Ing. Dr. tech. Juraj Darmo  
Institut für Photonik (E387)

eingereicht an der Technischen Universität Wien  
Fakultät für Elektrotechnik und Informationstechnik

von

**Dipl.-Ing. Josef Kröll**

Mat.-Nr.: 9527307

Seitenberggasse 67/7/7

A-1160 Wien

Wien, im März 2007









# Kurzfassung

Diese Dissertation ist der Weiterentwicklung von zeitaufgelöster Spektroskopie im Terahertz Frequenzbereich (THz-TDS) gewidmet. Dies wird speziell im Context von Anwendung, Kontrolle und Verstärkung von gepulster THz-Strahlung gezeigt.

Am Anfang werden die Grundprinzipien zur Erzeugung und Detektion von THz-Strahlung beschrieben und verglichen. Dies wird durch die Gegenüberstellung der Vor- und Nachteile von kohärenten bzw. nicht kohärenten Quellen und Detektoren erklärt. Ausgehend von einem leistungsschwachen THz-TDS System zu Beginn dieser Forschungsarbeit werden alle Fortschritte im Detail beschrieben. Speziell die verbesserten Messparameter des THz-TDS Systems, wie eine spektrale Bandbreite von über 7 THz und ein Rauschabstand von mehr als 60 dB trugen dazu bei, die hier gestellten Aufgaben zu erfüllen.

Zuerst werden die optischen Eigenschaften von ultra-dünnen Metallschichten an dielektrischen Grenzflächen untersucht. Durch eindimensionale Einengung des Elektronengases kann die elektrische Leitfähigkeit der Metallschicht gezielt vermindert werden. Dadurch kann der Reflexionskoeffizient an den Grenzflächen beeinflusst werden, was zusätzlich die Möglichkeit einer neuen Phasenanpassungsmethode eröffnet. Richtig dimensioniert sind solche Schichten in der Lage, jegliche Reflexion an einem optischen Übergang zu unterdrücken. Da die Phasenanpassungsbedingung nur durch die optischen Eigenschaften am Übergang bestimmt wird, wurde ein frequenzunabhängiger Anti-Reflexionseffekt erreicht, der annähernd bis zur Plasmafrequenz des jeweiligen Metalls reicht.

Im nächsten Teil werden die optischen Eigenschaften von Molekulkristallen anhand von Saccharose erklärt. Durch die schwachen Bindungskräfte von Wasserstoffbrücken können Absorbtionsmoden im THz-Frequenzbereich beobachtet werden. Zu diesem Zweck wurden Einkristalle gezüchtet und in dünne Plättchen geschnitten. Durch Kombination der orientierungsabhängigen Absorptionsspektren von zwei verschiedenen Orientierungen kann ein dreidimensionales Modell erstellt werden. Die Absorbtionsmoden werden dann der realen Kristallstruktur zugeordnet. Dies lässt weitere Rückschlüsse über die Molekülbereiche zu, die an diesen Absorbtionsmoden beteiligt sind.

Am Ende dieser Arbeit werden die optischen Eigenschaften von Quantenkaskadenlasern untersucht. Durch Einkoppeln von THz-Pulsen in die Laser, können deren Verstärkungsvermögen und Absorbtionsprofil vermessen werden. Dies wird anhand der Untersuchung von zwei verschiedenen Lasern dieses Typs gezeigt. Weiters werden Effekte wie spektrales oder örtliches Lochbrennen und ein neuer thermisch aktivierter Verlustmechanismus nachgewiesen. Letzterer Effekt zeigt klar, warum die hier untersuchten Laser keine Emission bei hohen Temperaturen aufweisen.



# Abstract

This thesis is dedicated to the further development of terahertz time-domain spectroscopy (THz-TDS) systems. This is shown in terms of application, control and amplification of few cycle terahertz radiation. The state-of-the-art principles in generation and detection of terahertz radiation are described and compared. This is mainly done by describing the pros and cons of incoherent and coherent radiation sources and detectors.

Starting with a low performance on-hand THz-TDS setup all improvements are described in detail which enabled the experiments and measurements shown later in this work. Especially, the massively improved measurement parameters of the developed THz-TDS system like a bandwidth of 7 THz and a signal quality better than 60 dB with high dynamic reserve helped to fulfill the here presented tasks. This is shown by manifold demonstrations and applications.

First the optical phase shift effect of ultra-thin metal layers deposited on dielectric optical interfaces is investigated. By confining the electron gas within the metal layer in one dimension its conductivity can be directly reduced down to zero. Equipped with such degree of freedom the complex reflection coefficient can be set. This results in a new technology of optical phase shift layers. Well dimensioned such layers are capable to suppress any type of reflections at an dielectric/air interface. Due to the phase shift effect those layers can be applied for broadband applications and work up to the plasma frequency of the used metal.

Second topic are the optical properties of molecular crystals. In this work represented by sucrose single crystals. Due to the soft forces caused by hydrogen bonds absorption at terahertz frequencies is observed. Large sucrose single crystals were grown and cut into slabs with given orientation in respect to the main crystal axes. By combining the absorption data from two individual planes a three dimensional absorption pattern is determined. Finally the orientation of the vibrational modes is mapped to the crystal structure. This gives new knowledge about the molecule constituents involved in these modes.

At the end of this work the dynamics and optical properties of THz quantum cascade lasers are measured. By coupling THz pulses into the laser's active zone the gain and absorption can be observed directly in time. By comparison of two different lasers, based on the same design, the quality of the heterostructure gain design is classified and verified. Further, many effects like spatial and spectral hole burning present in standard lasers are verified. Apart from the observed dynamic of the stimulated field emission thermally activated loss mechanisms in these devices are measured. The results show clearly a new effect in the lasers under investigation preventing lasing operation at high temperatures.



# Contents

<b>1. Introduction</b>	<b>1</b>
<b>2. Generation and detection of terahertz radiation</b>	<b>7</b>
2.1. Generation of incoherent THz radiation . . . . .	8
2.2. Generation of coherent THz radiation . . . . .	11
2.3. Generation of few cycle THz radiation . . . . .	13
2.4. Detection of incoherent THz radiation . . . . .	25
2.5. Detection of few cycle THz radiation . . . . .	29
<b>3. Advanced terahertz time-domain spectroscopy setup</b>	<b>39</b>
3.1. Principle of THz time-domain spectroscopy . . . . .	39
3.2. Performance parameters of time resolved experiments . . . . .	43
3.3. Data processing . . . . .	43
3.4. Development of a high performance THz-TDS setup . . . . .	45
<b>4. Metallic phase shift layers for broadband THz optical systems</b>	<b>59</b>
4.1. Motivation . . . . .	59
4.2. Theory of anti-reflection layers . . . . .	61
4.3. Electrical characterization of ultra-thin chromium layers on glass . . . . .	66
4.4. Optical characterization of ultra-thin chromium layers on silicon . . . . .	69
4.5. High performance electro-optic detector . . . . .	73
4.6. Conclusions . . . . .	73
<b>5. THz optical properties of sucrose single crystals</b>	<b>75</b>
5.1. Introduction . . . . .	75
5.2. Molecular crystals . . . . .	76
5.3. Sucrose single crystals . . . . .	77
5.4. Conclusions . . . . .	86
<b>6. Phase resolved transmission spectroscopy of terahertz quantum cascade lasers</b>	<b>87</b>
6.1. Motivation . . . . .	87
6.2. Introduction to Quantum cascade lasers . . . . .	89
6.3. THz quantum cascade laser samples and wave coupling . . . . .	97
6.4. Modulation spectroscopy technique . . . . .	102
6.5. Coherent probing of terahertz quantum cascade lasers . . . . .	103

*Contents*

6.6. Conclusions . . . . .	120
<b>7. Summary and outlook</b>	<b>123</b>
7.1. Summary . . . . .	123
7.2. Outlook . . . . .	125
<b>A. Pulse laser specifications</b>	<b>129</b>
<b>Bibliography</b>	<b>131</b>
<b>Publications</b>	<b>143</b>
<b>Acknowledgements</b>	<b>149</b>
<b>Cirriculum Vitae</b>	<b>151</b>

# List of Figures

1.1. Electromagnetic spectrum with embedded terahertz frequency band. . . . .	3
2.1. Spectral beam intensity of an ideal black body for different surface temperatures. . . . .	9
2.2. (a) Simplified bandstructure of GaAs (from [33]) and (b) drift velocity versus electric field of a typical Gunn diode. . . . .	10
2.3. Schematic diagram of backward wave oscillator: 1 - heater, 2 - cathode, 3 - electron beam, 4 - collector (anode), 5 - permanent magnet, 6 - slowing system, 7 - electromagnetic wave, 8 - waveguide, 9 - water cooling (from [37]).	11
2.4. Schematic comparison of pulses with different length in (a) time and (b) frequency domain. The pulses are normalized to the same energy for better comparison. . . . .	13
2.5. Sketch of a four-level system found in most laser gain media. . . . .	15
2.6. Elements of a typical laser resonator (from [52]). . . . .	15
2.7. Electric field of (a) the fundamental mode (10 Hz) and (b) 101 phase-locked modes with 10 mHz spacing. . . . .	17
2.8. Self-focusing caused by the Kerr effect for low and high beam intensities. Lines and arrows indicate beam waist and diameter (from [51]). . . . .	18
2.9. Pulse compression with a prisms pair. . . . .	18
2.10. Pulse compression with chirped mirrors. . . . .	19
2.11. Band profile of a plasmon emitter. . . . .	20
2.12. Standard THz-pulse generation from a photoconductive antenna pumped with a femtosecond optical pulse. Propagation of current pulses along the coplanar transmission line are in the top view (from [59]). . . . .	23
2.13. Calculated photocurrent in the emitter and amplitude of the radiated field versus time. The temporal shape of the laser pulse is drawn as a dotted line (from [60]). . . . .	24
2.14. Principle of difference frequency mixing for THz generation. . . . .	25
2.15. Working principle of a Golay cell infrared detector. . . . .	27
2.16. Scheme of a standard two beam FT-IR spectrometer (BS=beamsplitter, M=mirror, PM=parabolic mirror). . . . .	29
2.17. Illustration of the detection principle of dipole antennas (corrected drawing from [37]). . . . .	31
2.18. Phase matching function of (a) ZnTe and (b) GaP (from [88, 93]). . . . .	35

## List of Figures

2.19. Coordinate system of a (110)-oriented electro-optic crystal with probe and THz beam. . . . .	36
3.1. Scheme of a THz-TDS setup. (a) optional THz/optical pump part, (b) time-domain sampling scheme. . . . .	41
3.2. Standard electro-optic detection scheme (EOC=electro-optic crystal, QWP=quarterwave plate, WP=Wollaston prism, PD=photodiode). . . . .	41
3.3. THz-TDS signal trace of a 300 $\mu\text{m}$ thick GaP crystal including internal reflections. . . . .	45
3.4. Development level of the THz-TDS setup in the year 2003 (BS=beam splitter, BC=beam combiner, M=mirror, PM=parabolic mirror, SM=spherical mirror, L=lens, , LP=linear polarizer, QWP=quarter wave plate, WP=Wollaston prism, BPDD=balanced photodiode detector). . . . .	47
3.5. (a) Time-domain signal and (b) spectrum of the THz-TDS setup in the year 2003. . . . .	48
3.6. (a) Wrong and (b) optimal beam guiding (top: scheme with parabolic mirrors, bottom= resulting beam intensity distribution - from [98]). . . . .	50
3.7. Circuit for electrical modulation of the dipole emitter antenna in (a) 2003 and (b) 2006 (OPA=operational amplifier). . . . .	53
3.8. Detector circuit from (a) 2003 and (b) 2006 (OPA=operational amplifier, InstA=instrument amplifier). . . . .	53
3.9. Development level of the THz-TDS setup in 2006 (BS=beam splitter, BC=beam combiner, M=mirror, PM=parabolic mirror, L=lens, LP=linear polarizer, QWP=quarter wave plate, WP=Wollaston prism, BPDD=balanced photodiode detector). . . . .	56
3.10. THz-TDS signal in the year 2006. (a) Time-domain (inset:full time window) and (b) spectrum. . . . .	57
3.11. Photoconductive THz waveguide emitter. . . . .	57
4.1. Simplified THz optical system with silicon sample and electro-optic crystal (arrows indicate transmitted and reflected THz beams). . . . .	59
4.2. THz-TDS signal of 400 $\mu\text{m}$ thick silicon substrate measured with a 300 $\mu\text{m}$ GaP electro-optic sensor. (a) Time-domain and (b) spectrum. . . . .	60
4.3. General optical scheme of a thin layer (2) sandwiched between a substrate material (1) and air (3). . . . .	63
4.4. Scheme of two waveguides connected via a parallel shunt impedance. . . . .	65
4.5. AFM image (2x2 $\mu\text{m}$ ) of a 3 nm (left) and 8.3 nm (right) thick chromium film deposited by e-beam vaporization onto a glass plate at a pressure of $\sim 10^{-6}$ mbar. . . . .	68



4.6. (a) Resistivity and (b) sheet impedance of ultra-thin chromium films deposited on glass plates as a function of thickness measured by a 4-point probe. Data fit made by two exponential functions. . . . .	69
4.7. NIR transmission, reflection and absorption of ultra-thin chromium films on glass plates. . . . .	70
4.8. (a) Transmitted THz-TDS signal through a $400\mu\text{m}$ thick silicon plate and (b) zoomed time window of reflection caused by the silicon/air interfaces for two chromium film thicknesses. . . . .	70
4.9. Reflection and transmission amplitude as a function of chromium film thickness. Point data shows the optical results and the data plotted as lines is calculated from the sheet impedance fit from the electrical results. . . . .	71
4.10. THz signal comparison of a $300\mu\text{m}$ thick silicon plate with and without MARC. (a) Time-domain signals (data are offset for clarity) and (b) spectral ratio of the transmitted THz pulses [marked areas indicate low SNR regions]). . . . .	72
4.11. Transmission spectrum of $350\mu\text{m}$ thick GaAs substrate with and without MARC. (a) Full spectrum and (b) zoomed windows with marked $\text{CO}_2$ absorption line at $20.04\text{THz}$ . . . . .	72
4.12. THz signal from a $300\mu\text{m}$ thick GaP electro-optic sensor with and without MARC. Time-domain (left), spectrum (right). . . . .	73
5.1. Hydrogen bonds between benzoic acid molecules. . . . .	77
5.2. Molecular structure of sucrose. . . . .	78
5.3. Folded sucrose molecule with intra-molecular hydrogen bonds (marked by dotted lines). . . . .	78
5.4. Stereoscopic view of the sucrose molecule (from [114]) . . . . .	79
5.5. (a) Schematic of the typical shape of a sucrose single crystal with assigned main planes and (b) photo of typical sucrose single crystals. . . . .	80
5.6. Absorption spectra for three different orientations of polarization measured at 5 K. Polarization of THz radiation was parallel to a-, b-, and c'-axis of the sucrose crystal (5.5b). The curves are vertically offset for clarity and arrows indicate the identified vibrational modes. . . . .	81
5.7. Absorption spectra for different polarization orientations for A-cut (a) and C-cut (b) at 5 K (thin lines). Spectra were fitted with a sum of Lorentzian peaks (thick lines) whose parameters are listed in Tab. 5.1 and are off-set for clarity. . . . .	83
5.8. Angular dependence of the absorption peaks for A-cut (left) and C-cut (right). . . . .	84
5.9. Orientation of dipoles corresponding to the observed vibrational modes in the sucrose single crystal. . . . .	85
5.10. Single unit cell of sucrose with two molecules (dashed lines and arrows indicate hydrogen-oxygen bonds). . . . .	85

## List of Figures

6.1. Emission (top) and transmission spectroscopy (bottom) scheme of a laser. . . . .	88
6.2. Bandstructure scheme of a typical bandgap heterostructure semiconductor laser. . . . .	90
6.3. $E(k)$ -diagram of an interband (left) and an intraband (arrows indicate optical transition). . . . .	91
6.4. Quantized energy levels in a heterostructure quantum well (left) and simplified bandstructure diagram of a biased quantum cascade structure (right). . . . .	92
6.5. Simplified bandstructure $E(k)$ -diagram of a QCL with injector and active region states. . . . .	93
6.6. Typical realization a QCL fabricated on a semiconductor substrate. . . . .	94
6.7. (a) Mode intensity profile in the dielectric waveguide in the direction perpendicular to the layers. The numbers on top of the figure are their thicknesses in $\mu\text{m}$ . Material composition and the doping concentration in $\text{cm}^{-3}$ are also indicated. (b) Refractive index profile in the direction perpendicular to the layers (from [128]). . . . .	95
6.8. Mode intensities (solid lines) and the real part of the dielectric constant $\epsilon(\omega)$ (dashed lines) for the (a) SI-surface-plasmon waveguide and (b) double-sided metal waveguide. The dotted line represents the square of the modal effective index (from [134]). . . . .	97
6.9. Bandstructure diagram of the QCLs (from [136, 23]). (left) T1 and (right) T2. . . . .	99
6.10. Optical output spectrum of (a) T1 and (b) T2. The current values for T2 correspond to the laser measured in referred publication at 5 K and are scaled to lasers dimensions (from [137]). . . . .	99
6.11. Scheme of incouple optics into a QCL's waveguide (left). Photograph of a THz-QCL mounted on a cryostat finger (right). Arrows indicate the laser and the incouple optics with silicon lens. . . . .	100
6.12. Scheme of a THz waveguide emitter directly coupled with a QCL (left). Photograph of a THz-QCL mounted on a copper holder (right). . . . .	101
6.13. Typical transmission signal through T1 and T2 measured by THz-TDS. (a) Time-domain and (b) spectrum. . . . .	102
6.14. QCLs output power as a function of the driving current for the laser (a) T1 and (b) T2. . . . .	102
6.15. Modulation signal of two beating frequencies at 4 and 5 Hz in (a) Time-domain and (b) frequency. . . . .	104
6.16. Modulation signal of T1 (a) and T2 (b). Signal measured at QCLs maximum output power (insets show corresponding spectrum). . . . .	104
6.17. (a) Low-pass and (b) high-pass (right) filtered ( $f_G = 2.5 \text{ THz}$ ) modulation signal of T1 (Fig. 6.16) at full output power. . . . .	105

6.18. Time-resolved FFT analysis of the modulation signal of T1 operated of full power (Fig. 6.16). 2 ps time windows were shifted over the whole modulation signal. . . . .	106
6.19. Current dependency of single pass maximum gain of the QCLs T1 (a) and T2 (b) (shaded parts indicate the lasing region of the lasers) . . . . .	107
6.20. Spectrally resolved gain/reduced losses for T1 (a) and T2 (b) operated at full output power (dotted line indicate gain bandwidth fitted by a Gaussian line shape). . . . .	108
6.21. Phase diagram of the gain spectra of (a) T1 and (b) T2. . . . .	109
6.22. Gain spectra with observable spectral hole burning due to lasing operation in T1 (a) and T2 (a). (f.p.=full power, b.th=below threshold, a.th.=above threshold). . . . .	110
6.23. Gain/current dependency of the first round-trip signal within (a) T1 and (b) T2. . . . .	111
6.24. Scheme of the local power intensity distribution of a QCL waveguide below (a) and above threshold (b) current (SP=seed pulse, BW=backward wave, TW=transmitted wave). . . . .	112
6.25. Optical scheme of the THz signals transmitted through a QCL waveguide (MS: main signal, RTS: round trip signal, $\Delta T$ round trip time). . . . .	112
6.26. Round trip signals through T1. (a) 3 passes, (b) 5 passes and (c) 7 passes (signals are lowpass filtered $f_G = 3.5 THz$ ). . . . .	113
6.27. Round trip signals through T2 after (a) 3 passes and (b) 5 passes. . . . .	114
6.28. Spectral comparison of internal round-trip signal of (a) T1 and (b) T2 . . .	115
6.29. Arrhenius plot of the absorption feature at 3.1 THz. . . . .	117
6.30. Temperature dependent transmission absorption spectra for (a) QCL off, (b) QCL on and (c) change in the absorption transmission spectra (the figures are offset for clarity). . . . .	118
6.31. (a) Comparison of temperature depending absorption in QCL T1 switched on and off. (b) Internal temperature difference of operated QCL compared to heatsink temperature. . . . .	119
6.32. (a) Three stage model for thermally activated losses and (b) configuration coordinate diagram of silicon donors in a GaAs quantum well. (1 - phonon scattering of electrons on the energy level; 2 - capture of electron on the donor defect site; 3 - optical transition from the donor to the heterostructure energy level). The optical transition 1 widens towards the low energies with increasing temperature due to the phonon scattering. . . . .	119
A.1. Scheme of the Tsunami pulse laser (from [150]). . . . .	130
A.2. Emission spectrum of (a) Tsunami and (b) M1 pulse laser. . . . .	130
A.3. Scheme of the M1 pulse laser (from [151]). . . . .	130



# List of Tables

2.1. Structure of the Pockels coefficient matrix $r_{ij}$ of $LiTaO_3$ , $LiNbO_3$ , $ZnTe$ , and $GaP$ (from [91]). . . . .	34
2.2. Pockels coefficients of $ZnTe$ , and $GaP$ . . . . .	34
3.1. Efficiency of beam combiners (T = transparency, R = reflectivity). . . . .	51
3.2. Summary of the THz-TDS setup improvements implemented. . . . .	55
4.1. Parameters of gold and chromium (from [75, 106]). . . . .	67
4.2. Fitting parameters for chromium film resistivity. . . . .	69
5.1. THz optically active vibrational modes of sucrose crystals in the frequency range 0.5-3.5 THz observed at 5 K (error margins for the position and the linewidth are about 18 and 9 GHz, respectively). . . . .	81
5.2. Orientation of the unit dipoles ( $e_a, e_b, e_{c'}$ ) of THz optically active vibrational modes of a sucrose single crystal in the frequency range 0.5-3.5 THz given in the coordinate system of the sample (orthogonal a, b, and c') as well as in the crystal coordinates (a, b, and c) from Ref. [111, 122]. $\alpha$ means the angle from $a$ -axis in the $ab$ -plane, $\beta$ is the angle from $b$ -axis in the $bc'$ -plane, and $\gamma$ is the angle from the $c'$ -axis in the $ac'$ -plane. . . . .	86
6.1. Quantum cascade laser specification and dimensions. . . . .	98
A.1. Pulse laser specifications of Tsunami and M1 system. . . . .	129



# 1. Introduction

Since the last millennia mankind made big steps forward on the ladder of technological progress. All the time new tools were developed, improved and applied. For instance this started with sharpened stones and tools for inflaming lumber in the stone age [1]. But the more tools and inventions were developed men thought about the origin of effects he exploited. For instance, why is a flame hot and illuminates the surrounding area. Such questions represent the birth of applied science. In the particular case the development of furnaces and lighting. From this time on, light was an essential part of human everyday life. Soon people recognized the hotter a flame the brighter its color. Further, objects located close to a light source cast a shadow far away at a wall and by changing the object's distance or its shape the shadow changes as well. But these first primitive imaging systems found no real usage for a long time. It took many millennia until imaging and optics were used to monitor the position and movement of the moon, the sun and stars. First for astrology and horoscopes but later seriously for astronomy. Especially astronomy was the major driving motor for modern optics and photonics. Pioneers on this field were the Arabs [2]. Without restrictions from the catholic church like present in Europe in the middle age they built the first modern observatories and optical equipment including glasses and spyglasses. However, the wisdom and experiences spread to Europe due to the crusades where the next steps on the field of optics were made. For instance, here scientist like J. Kepler<sup>1</sup> and G. Galilei<sup>2</sup> postulated laws regarding the movement of planets and that they move around the sun which is the center of our solar system.

The next big step towards a better understanding of electromagnetic waves was done by J. C. Maxwell<sup>3</sup>. Although his work based on electrodynamics and its corresponding laws [3] he was the first showing the rules and conditions of wave propagation. In addition the results showed the close relationship between electrodynamics and optics. Further, it was found out that the wavelength of a wave determines its penetration capability for a given material. In general materials show a frequency depending complex refractive index resulting in the so called dispersion relation [4] and varying optical properties. But due to the lack proper tunable radiation sources till the end of the 19<sup>th</sup> century those material properties stayed hidden. Science mainly hooked on the properties accessible by visible light. Apart from this, there have been many efforts looking into and through objects which were mainly pushed forward by medicine. About this time, W.C. Röntgen<sup>4</sup> invented a new

---

<sup>1</sup>Johannes Kepler (1571-1630)

<sup>2</sup>Galileo Galilei (1564-1642)

<sup>3</sup>James Clerk Maxwell (1831-1879)

<sup>4</sup>Wilhelm Conrad Röntgen (1845-1923)

## 1. Introduction

method for the generation and measurement of high energetic radiation located beyond the visible light. For this purpose electrons were accelerated in a high voltage tube and hit a metal surface where they emitted short wavelength light due to bremsstrahlung [5]. The so called x-rays ( $\lambda < 30\text{ nm}$ ) can penetrate many materials such as flesh and bones. At this time such radiation could be sensed by simple photoplates used in photography. But soon was found out that this kind of radiation causes serious long term diseases due to its ionizing character. These problems and the resulting precautions for running x-ray devices motivated scientists to invent better and harmless methods.

In 1891 A. A. Michelson<sup>5</sup> invented the optical Interferometer. This device should proof the existence of an ether by exploiting the phase attribute of photons. At this time the ether was believed to be necessary for wave propagation in free space. But since the speed of light is a physical constant the experiment failed. Many years later, the idea surfaced to use this interferometer for measuring the frequency dependent complex refractive index of a material by using the Fourier transformation method. As radiation source a broadband light source like a globar was used. Since the radiation from such source is mainly located in the infrared this measurement method got the name FT-IR<sup>6</sup> spectroscopy. One of its problems at the beginning of the 20<sup>th</sup> century was the lack of computers to perform fast the necessary calculations to obtain the frequency depending optical parameters.

The efforts to observe and explore new regions in the electromagnetic spectrum triggered the development of new methods for the generation and detection of longer wavelengths starting from infrared light. One of the motives was the fact that many vibrational modes of various substances are located in the spectral region between the visible light and the microwaves [6, 7]. For instance, nearly all atmospheric constituents show fingerprint like absorption features here [8] and the larger the molecules are the red shifter are their modes. This results in very strong absorption characteristics of macromolecules like DNA<sup>7</sup> [9] and saccharides [10] at long wavelengths ( $\lambda > 30\text{ }\mu\text{m}$ ). Further, apart from measuring the optical properties of materials such waves have the capability penetrating many nonmetallic objects which enables its application for tomography [11]. Due to its low photon energy ( $E_{\text{Photon}} = 41.4\text{ meV}$  at  $10\text{ THz}$ ) it can be even used for biological and chemical analyses without harming the object under investigation.

For a long time the main problem was that for accessing the spectrum located around 1 THz no applicable sources or sensors existed, giving this region the name “THz-Gap”. Neither electronic nor photonic sources were available (Fig. 1.1). In the 1960s infrared laser diodes [12] were already developed but the THz gap between the microwaves and the infrared light was still not closed.

In the last 10 years several methods for the generation and sensing of electromagnetic radiation around 1 THz were invented. Once by increasing the emission frequency of electronic sources [13] and on the other side by decreasing the emission frequency of optical

---

<sup>5</sup>Albert Abraham Michelson (1852-1931)

<sup>6</sup>Fourier transform infrared

<sup>7</sup>deoxyribonucleic acid



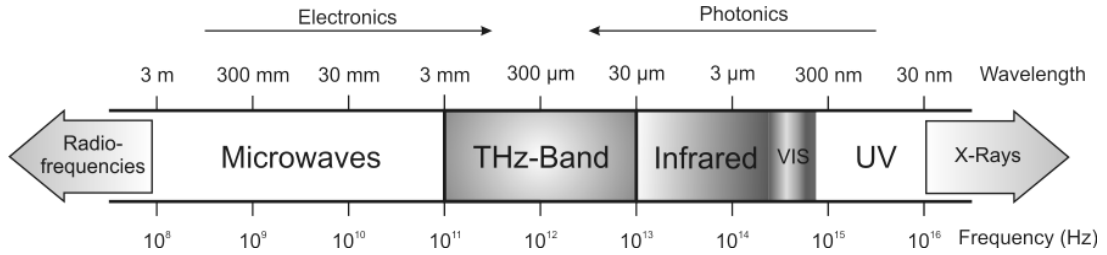


Figure 1.1.: Electromagnetic spectrum with embedded terahertz frequency band.

sources [14]. With increasing interest in this spectral region it also got its own name. A tight declaration does not exist but the spectral range of the so called T-rays or THz waves is usually between 0.1 and 10 THz (Fig. 1.1), this range varies within different publications.

In addition to generate THz radiation, there was big interest in the development of coherent light sources emitting ultra-short electric field transients. One of the first real sources of this kind was invented by D. H. Auston [15]. His photo-conductive antenna acts like a current switch and is able to emit THz radiation when excited by a short laser pulse. Many bulk semiconductors when excited with a short laser pulse are also able to emit THz radiation [16]. One of the main importance of THz waves is that the vibrational modes of many molecules are located in this region. So they can be used well for the characterization of materials without causing ionization effects compared to destructive x-rays. This makes it suitable for medical issues. Recently the possibility was demonstrated to study the vibrational modes of many organic materials [17, 18]. There are ongoing efforts to use THz waves to measure blood and skin [19]. For instance, the online measurement of sugar components in the blood stream is of great interest for diabetics. But as for many other tasks, the challenging problem of strong absorption by water molecules has to be handled first.

Recently the THz quantum cascade laser was introduced [20]. Currently, this very powerful light source is capable to emit more than 200 mW [21] at a footprint smaller than  $1\text{ mm}^2$ . Further, due to so called band gap engineering the emission wavelength can be set within the limits of the used materials. At the moment those devices cover nearly the complete frequency band from NIR<sup>8</sup> to THz frequencies and the development continuous as recent publications show [22, 23, 24]. However, although this device can be easily designed and made there are still many questions open. Especially room temperature operation is still not achieved but would be implicitly needed for commercial applications.

Another interesting advantage of THz waves in terms of basic research are their wavelengths from the viewpoint of fabrication technologies. As shown in Fig. 1.1 THz waves cover the wavelength range 0.33 - 3 mm, a region accessible by cheap patterning technologies. At this wavelengths fundamental optical properties and effects can be easily explored compared to visible light where much more precise optics at the nanometer scale would be needed.

<sup>8</sup>near infrared

## 1. Introduction

### The structure of this PhD thesis

In the chapter 2 the basic principles of generation and sensing of THz radiation is described in detail. Special attention is put there to the performance parameters and the type of radiation (incoherent, coherent, etc.) which is sensed or emitted. This chapter gives an overview of the state-of-the-art in THz technology at present.

Chapter 3 is dedicated to the applied ultra-fast measurement technique. One of the major tasks of this thesis was the development and fundamental improvement of the THz-TDS<sup>9</sup> setup available at the beginning of this work. The main improvements are described in detail and how they were integrated in the setup measurement scheme from the initial point. Further, for a better understanding of the achieved improvements, this chapter starts with an overview in basic principles in optics. Especially this includes the components of a time-domain measurement setup and the data processing of the obtained results.

One of the major breakthroughs during this thesis was the development of a new type of anti-reflection coating presented in chapter 4. Since this new type of technology has not only an impact on terahertz technology, due to its broadband application capability, a whole chapter is dedicated to this topic. In this section the properties of ultra-thin metallic layers in the terahertz frequency region are described. Since the thickness of these layers is in the range of the mean free path of the electrons therein the conductivity of the material can be adjusted by controlling the thickness. As representative metal the chromium is chosen due its outstanding adhesion properties and its stability. By choosing the optimal metal layer thickness every optical interface can be passed by an electromagnetic wave without generating an reflected wave there. Especially since the terahertz frequency band is the junction point of electronics and photonics the involved physic for this antireflection effect is described for both branches.

A direct demonstration of THz-TDS applied in material science is given in chapter 5 where there the absorption properties of molecular crystals are shown. Due to their weak bonding forces from hydrogen bonds they show material and crystal structure specific absorption characteristics in the THz frequency range. Especially the orientation dependence of absorption is of great interest since such materials find now application in commercial products. Since the THz-TDS technique is very sensitive to the polarization of the sensed radiation it is perfectly suited to measure the orientation dependence of fingerprints of this material type. For showing the capability of THz-TDS for this task the orientation and frequency depending absorption characteristic of sucrose single crystals are measured. Finally the resulting orientation of the vibrational modes is mapped to the crystal structure of sucrose.

The majority of this thesis is dedicated to the spectroscopic examination of THz active materials and the amplification of THz pulses presented in chapter 6. For combining both tasks at once a THz quantum cascade laser (THz-QCL) is used as sample. By coupling externally generated broadband THz pulses into the laser's waveguide the internal processes

---

<sup>9</sup>THz time-domain spectroscopy

during laser operation are accessed. By comparing the transmission through the active and inactive device the losses and the gain related to the device's band structure are measured. The results can be used as feedback for the improvement of the QCL design, but more important, the data show that QCLs have the capability for broadband pulse amplification. Latter could lead to the commercial breakthrough of QCLs in the future since there is a great need for powerful and cheap pulse laser sources.

In the last chapter I summarize all obtained results and reached goals. Since, the development of THz technology in the world has just started and so a lot of interesting work remains on this field, some of them are shortly introduced.



## 2. Generation and detection of terahertz radiation

This chapter is dedicated to the main techniques for generating and sensing of THz radiation. For a long time there was no urgent demand for powerful THz sources and sensors. Only space research paid attention to this, formerly called, THz gap located between 0.1 and 10 THz. However, the special interest of space research in THz radiation bases on the fact that specific information from objects in space can be best observed in certain frequency bands. For instance scientists presume that most of the radiation in space is located in the long wavelength regime including the THz frequency band [25] and is launching satellites which are equipped with special sensors to detect this type of radiation. Apart from those endeavors no interest was paid to this frequency band due to the lack of convenient sources and sensors. Furthermore, there was only poor demand to exploit this frequency band in commercial products and scientific analysis. This circumstance delayed the development of new sources and detectors working in this frequency range.

The first available sources in this frequency range were incoherent broadband sources like globars. Such radiation can be easily detected by simple power measurement techniques and in combination with a spectrometer even frequency resolved data can be obtained. But such systems suffered from a low SNR<sup>1</sup> due to low radiation intensities at THz frequencies. This problem shows very well the main task during the exploration of the THz frequency band. Sources and sensors had to be developed having a high sensitivity and a high SNR. Further, it was essential that a sensor's spectral responsivity should match as good as possible with the emission spectrum of the used radiation source.

One of the major breakthroughs was achieved by the development of pulse lasers operating on the femtosecond time scale. Such ultra short pulses in the NIR with high peak intensities can be easily converted to THz frequencies by proper media which opened new possibilities. First, intense THz pulses could be easily measured even with incoherent detection schemes. More important was, that with the help of short laser pulses also time resolved measurements are possible. For instance this gave a direct access to the dynamics in semiconductors and related structures but still THz radiation was generated in an indirect way. Either from a heated object or by NIR laser pulses. Latter had the drawback of very poor conversion efficiencies independent if down- (photonics) or upconversion (electronics) techniques were applied.

This situation changed completely with the development of new light sources like THz

---

<sup>1</sup>signal to noise ratio

## 2. Generation and detection of terahertz radiation

gas lasers and THz-QCLs<sup>2</sup>. They were the first direct sources for this frequency range. Especially THz-QCLs can be designed to nearly any frequency. Since such devices can be fabricated as single mode sources they can be used, in combination with a proper detector, as a chemical sensor by measuring certain spectral lines of the electromagnetic spectrum.

With all these inventions THz technology has become a fast emerging science and the amount of applications is still rising very fast. The following sections give an overview of the up-to-date commonly used sources and sensors.

### 2.1. Generation of incoherent THz radiation

In the first section a set of commonly used incoherent THz sources are described. Incoherent means, that the emitted photons from these sources have a random phase distribution and so, have no constant phase relation in time and space. The radiation from such sources is not able to produce a time independent stationary interference pattern. They can be compared best with a light bulb.

#### 2.1.1. Globars

One of the simplest and oldest methods to generate IR radiation reaching THz frequencies are globars. These are rods made of silicon carbide or other heat resistant materials which are heated up electrically to usually 1500 K. At such temperatures they emit thermal radiation covering a huge spectral range. According to Planck's law of black body radiation [26] the spectral beam intensity  $I(\lambda)$  from such heated objects can be described by

$$I(\lambda) = \frac{2 \cdot h \cdot c}{\lambda^5} \cdot \frac{1}{e^{\frac{h \cdot c}{\lambda \cdot k \cdot T}} - 1}, \quad (2.1)$$

where  $h$  is the Planck's constant<sup>3</sup>,  $c$  is the speed of light in vacuum<sup>4</sup>,  $k$  is the Boltzmann's constant<sup>5</sup>,  $T$  is the temperature of the black body, and  $\lambda$  is the wavelength of the emitted photons. At typical operation temperatures of 1000-1500 K the center wavelength of the emitted black body radiation is located between 2 and 3  $\mu\text{m}$  and the emission spectrum covers the whole NIR and parts of the MIR<sup>6</sup> as can be seen in Fig. 2.1. For THz frequencies (0.3-3 mm) the emitted beam intensity drops significantly. In numbers, for a globar at 1000 K the spectral intensity at 1 THz drops to  $2.4 \cdot 10^{-7}$  compared to its peak value. This example shows very well that a globar is not a convenient light source for THz applications. However, globars are cheap and simple light sources for NIR and MIR. Therefore they find application in FT-IR spectroscopy in these frequency ranges (see chapter 2.4.4).

---

<sup>2</sup>quantum cascade laser

<sup>3</sup> $h = 6.626 \cdot 10^{-34} \text{ J} \cdot \text{s}$

<sup>4</sup> $c = 2,998 \cdot 10^8 \text{ m} \cdot \text{s}^{-1}$

<sup>5</sup> $k = 1,38 \cdot 10^{-23} \text{ J} \cdot \text{K}^{-1}$

<sup>6</sup>mid-infrared

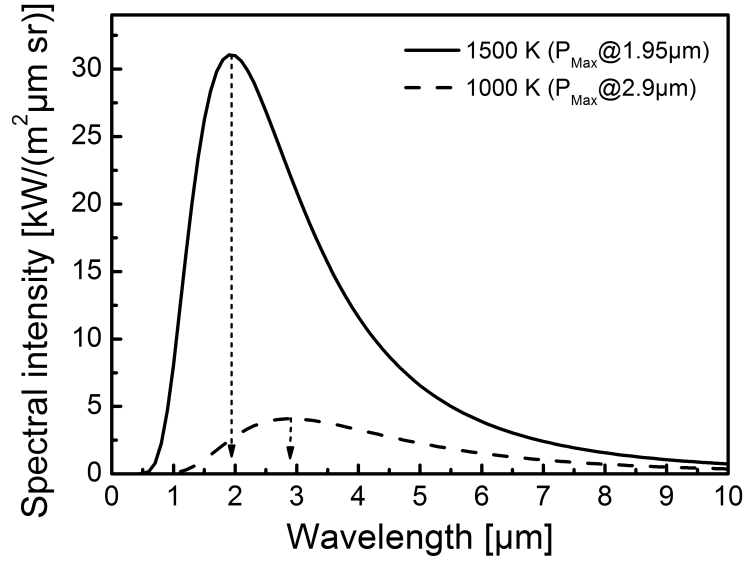


Figure 2.1.: Spectral beam intensity of an ideal black body for different surface temperatures.

### 2.1.2. Gunn diodes

Gunn diodes rely on an effect discovered by J. B. Gunn<sup>7</sup> in 1963 [13, 27]. He observed that in n-doped semiconductors at high electric fields a negative differential mobility (NDM) occurs. In this region with NDM he observed current pulses from the structure at frequencies in the microwave region. This so-called Gunn-effect is a high electric field effect and appears in semiconductor materials with valleys in the conduction band with relative close energetic distance to each other. For GaAs this energy is about 0.29 eV at 300 K (Figure 2.2a). If a steady electric field is applied to such material a current flow starts. Due to perturbations in the material like impurities the local electric field can exceed a threshold value (Figure 2.2b). In this electric field the electrons in the material can reach an energy corresponding to the energetic gap to the next valley. With the assistance of LO<sup>8</sup> phonons they can then be scattered to this neighbor valleys. There the electrons show a much higher effective mass so that locally the drift velocity in the semiconductor is decreased. Due to this reduced mobility the electrons start to pile up locally until the valley is filled up. Then the charge carriers are released in a kind of current shot and the process starts from the beginning.

This process was first exploited for local high frequency oscillators and for the generation of microwaves. By placing the diode in a resonator structure its center emission frequency can be tuned by adjusting the resonance frequency of the cavity [28]. At present Gunn diodes can operate up to THz frequencies by applying molecular beam epitaxy (MBE) techniques [29]. Previously reported high frequency operation of 400 GHz for InP [30] and

<sup>7</sup>John Battiscombe Gunn (born 1928)

<sup>8</sup>longitudinal optical

## 2. Generation and detection of terahertz radiation

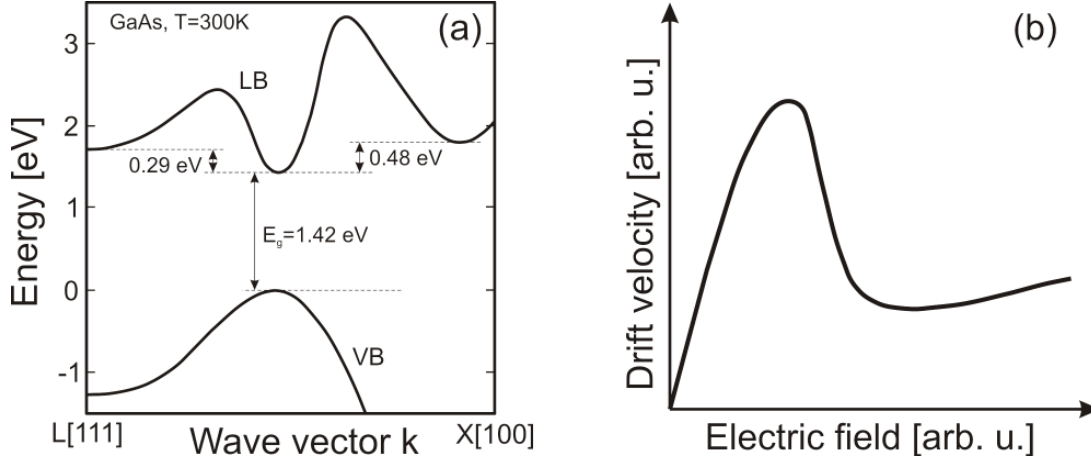


Figure 2.2.: (a) Simplified bandstructure of GaAs (from [33]) and (b) drift velocity versus electric field of a typical Gunn diode.

1.78 THz for GaN [31] shows that this kind of THz source has great potential for the future. In addition, first lasing operation with an output power of  $25.4 \mu W$  was reported [32].

### 2.1.3. Backward wave oscillators

Backward wave oscillators (BWOs), also called carcinotrons, are vacuum tube sources which were developed for the generation of strong microwave radiation. In such tubes an electron beam [34] is lead through a slow-wave structure (Fig. 2.3). As a result of the applied electric and magnetic field an electromagnetic wave is launched in the opposite direction of the electron beam. By adjusting the acceleration voltage the emission wavelength can be adjusted fast and easily. The capability of fast tuning the emission from one to the other end of the BWO's electromagnetic spectrum makes it a quasi broadband source.

At THz frequencies about 1 THz they offer output powers up to a few mW [35]. The low output power level at higher frequencies, which is mainly caused by metallic losses, the high supply voltage and the need of a magnetic field for operation are significant disadvantages of this type of THz source. In addition, as all vacuum tubes this radiation source has limited life time [36].

### 2.1.4. Schottky multiplier

Schottky multipliers are whisker contacted Schottky varactor diodes. In these devices nonlinearities of the varactor diode is exploited for the high harmonic generation of microwaves [38]. Usually the diode is driven by a strong microwave source at e.g. 100-200 GHz. Compared to BWO's they show less output power by one order of magnitude at the same emission frequency but they reach much higher frequencies up to 2.7 THz and can be cooled to increase the output power [36]. However, the multiplication efficiency falls significantly down with increasing frequency of about  $25 \text{ dB/THz}$ . Due to their scalability,



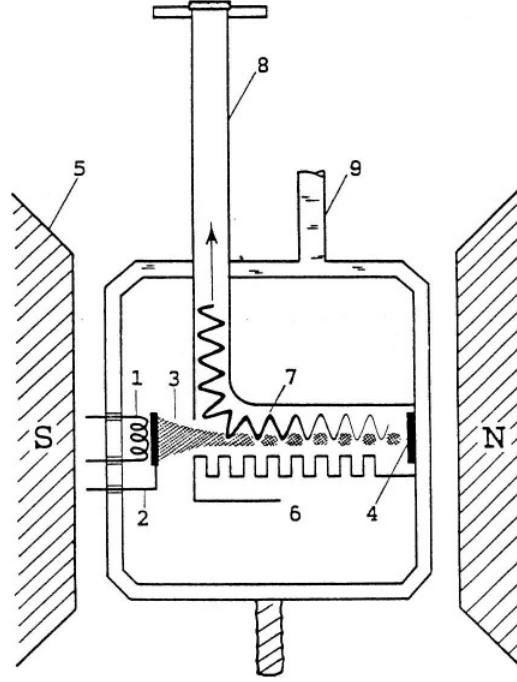


Figure 2.3.: Schematic diagram of backward wave oscillator: 1 - heater, 2 - cathode, 3 - electron beam, 4 - collector (anode), 5 - permanent magnet, 6 - slowing system, 7 - electromagnetic wave, 8 - waveguide, 9 - water cooling (from [37]).

in form of chains of multipliers, they find application in combination with e.g. Gunn diodes.

## 2.2. Generation of coherent THz radiation

In general, the photons of a coherent radiation source have a given phase relation between them. Due to this property they are capable to produce temporal and spatial interference effects [39]. Since the photons from a coherent light source have a fixed phase relation between them they can interfere constructively which can result in huge amplitudes. In addition, the knowledge of a light field's temporal phase can be exploited for measuring its electric field amplitude in time which is shown e.g. in section 2.5.2. Although this section is dedicated to coherent THz sources the basic laser principles and theory is described later in section 2.3 where pulsed laser system are explained in detail. Here only the specialties and main principles of coherent cw THz sources are described.

### 2.2.1. THz gas lasers

The first coherent light sources for the THz frequency range were optically pumped gas lasers (OPGLs). Many gases show strong vibrational/rotational absorption lines in the wavelength region of about  $10\text{ }\mu\text{m}$  and radiative rotational transitions in the THz frequency

## 2. Generation and detection of terahertz radiation

range [40, 41] caused by their permanent dipole moment. Due to a long relaxation of the excitation in some gases an inversion can be built up in the first excited state which makes lasing action possible. As gain media gases like vinyl chloride ( $\text{C}_2\text{H}_3\text{Cl}$ ), methyl alcohol ( $\text{CH}_3\text{OH}$ ), methyl fluoride ( $\text{CH}_3\text{F}$ ), ammonia gas ( $\text{NH}_3$ ) and many others are used [42, 43]. They are usually pumped by a nitrous oxide ( $\text{N}_2\text{O}$ ) or carbon dioxide ( $\text{CO}_2$ ) laser. These lasers have their typical lasing wavelength at about 9-11  $\mu\text{m}$  which is matching very well with the absorption lines of the involved gases. Since such pump sources provide a plenty of emission lines and the involved gain media has usually more than one lasing transition the pumping source has to be tunable. This is achieved by placing a dispersive element like a grating or etalon inside the cavity so that only one excited state can be filled. Since the lasing operation in OPGLs depends strongly on the gas pressure they are operated at low pressure levels of about  $40 - 170 \cdot 10^{-6}$  bar for keeping the collisional relaxation rate down [41, 44]. One drawback of this pressure level is that it reduces drastically the single pass pump beam efficiency. For achieving good pump conditions the pump beam is coupled to the THz oscillator and is then reflected several times in the cavity. Since it is difficult to find dichroic mirrors operating in the MIR and THz, and proper output couplers such lasers are equipped with a closed cavity. This means both beams (MIR and THz) are trapped between two high reflective metal mirrors. For pumping and outcoupling of THz radiation these metal mirrors have small holes in their middle which are filled with a transparent material. E.g. this can be potassium chloride (KCl) for the pump beam window and high-density polyethylene (HDPE) for the THz outcoupling window. So far more than a thousand emission lines from various gases in the frequency range 0.1-8 THz are reported [45]. The main disadvantage of these lasers is the life time limited pump source.

### 2.2.2. Quantum cascade lasers

Quantum cascade lasers (QCLs) are devices which base on an intersubband optical transition. This relatively new semiconductor device was introduced by J. Faist *et al.* [14] for MIR. Recently the emission of this laser type was extended to THz frequencies [46]. Compared to its size this unipolar device shows outstanding performance and power levels up to 248 mW [21]. Since chapter 6 is dedicated to THz-QCL measurements, including their working principle, they are not described in detail here.

### 2.2.3. Free electron lasers

All above described THz laser sources have their strict limitations during operation. Since they rely on an atomic or a molecular active medium their output power, emission wavelength, and tunability is limited. A coherent THz source which has not such limits is a free electron laser (FEL) which uses a relativistic electron beam as gain medium [47, 48]. The electron beam in a FEL travels through a periodic transverse magnetic field. Due to this periodic magnetic field the electrons travel on a sinusoidal path on which they

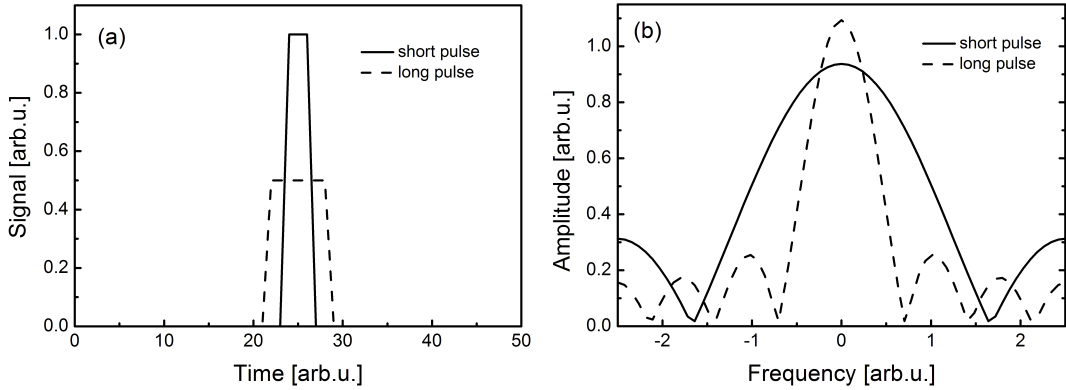


Figure 2.4.: Schematic comparison of pulses with different length in (a) time and (b) frequency domain. The pulses are normalized to the same energy for better comparison.

emit photons. These photons are collected by a mirror and sent back through the cavity. Here the electron motion in the beam path is in phase by active synchronization with the incoming light field which results in amplification. The output power of FELs can be adjusted by the intensity of the electron beam and its wavelength is tunable by the magnetic field strength. FELs can be used over a broad electromagnetic spectrum covering the THz frequency range up to ultra-violet (UV) and beyond [49]. The main application of FELs is basic research. As described they offer a large degree of freedom regarding emission wavelength and power. But due to their huge size (comparable to a large house), the high costs and the complicated maintenance of stable light emission they find application only in special cases. At the moment worldwide less than 50 FELs are in duty or planed respectively.

## 2.3. Generation of few cycle THz radiation

The light sources explained so far are either not coherent or their emission spectrum is not broadband enough showing just a few emission lines. An universal applicable light source would be a THz pulse laser emitting ultrashort electromagnetic transients covering the spectrum 0.1 - 10 THz. The imperative for this pulse property is illustrated in Fig. 2.4. The shorter a laser pulse of given energy is the broader is its spectrum and the higher is its peak intensity. Latter is the crucial parameter if nonlinear effects shall be targeted.

However, such broadband pulse lasers for the THz frequency range do not exist so far. This means no direct pulse light source is available but there do exist several methods for an indirect generation of few cycle THz radiation. Starting point is in general an ultrafast femtosecond Ti:sapphire pulse laser operating in the NIR [50]. The principles used for the THz pulse generation can be divided into three groups considering either optical or

## 2. Generation and detection of terahertz radiation

electrical effects:

1. Radiation from current transients (dipole antennas)
2. Radiation from polarization transients (plasmon emitters)
3. Radiation by nonlinear optical effects (difference frequency mixing)

The first two of them can be directly described by the Maxwell theorem [3], which states that every accelerated charge or changing polarization emits an electromagnetic field according to

$$E(t) \propto \frac{\partial J}{\partial t} \propto \frac{\partial^2 P}{\partial t^2}, \quad (2.2)$$

where  $J$  is the current density and  $P$  is the electric polarization. The third approach for the generation of few cycle THz radiation is difference frequency mixing. Two or more waves are mixed in a proper nonlinear medium so that the difference frequencies are located in the THz frequency band.

The detailed description of the generation processes and devices including the basics of ultrashort pulse laser generation are the topics of the following sections.

### 2.3.1. Generation of ultrashort laser pulses

The generation of ultrashort laser pulses is not a trivial task. For a cw laser only a material with a narrow amplification spectrum is needed. This situation changes if a pulse laser shall be built. Only a few materials are capable of broadband amplification which is the crucial parameter. A complete overview can be found in [51, 52].

#### Basic laser principles

The starting point of every femtosecond (fs) pulse laser is a normal cw-laser, usually a solid state laser. Most commonly materials with a four level energy system are used because they can be easily pumped compared to a three level system [53]. In Fig. 2.5 an illustration of a four level system is shown. Such system is needed to achieve a stable population inversion which is essential for the light amplification process. This means that the upper lasing energy level  $|3\rangle$  is more occupied than the lower level  $|2\rangle$ . A beam which comes e.g. from semiconductor laser diodes pumps electrons from the ground state  $|1\rangle$  to the excited state  $|4\rangle$ . Since the relaxation time back to the ground state is very long compared to the fast transition  $|4\rangle \rightarrow |3\rangle$ , nearly all electrons pumped to state  $|4\rangle$  relax to state  $|3\rangle$  where they produce an inversion due to the long relaxation from there to the state  $|2\rangle$ . If the charge carriers relax to state  $|2\rangle$  they emit a photon. After a fast energy transition  $|2\rangle \rightarrow |1\rangle$  the electrons can be pumped again to the upper state. For instance in a three-level system state  $|1\rangle$  and  $|2\rangle$  are the same. This results in problems if the pump power is not high enough causing an overpopulated ground state and a reduced population inversion.

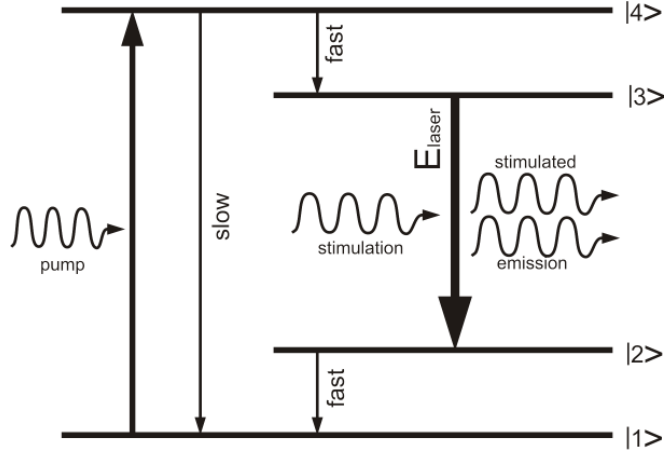


Figure 2.5.: Sketch of a four-level system found in most laser gain media.

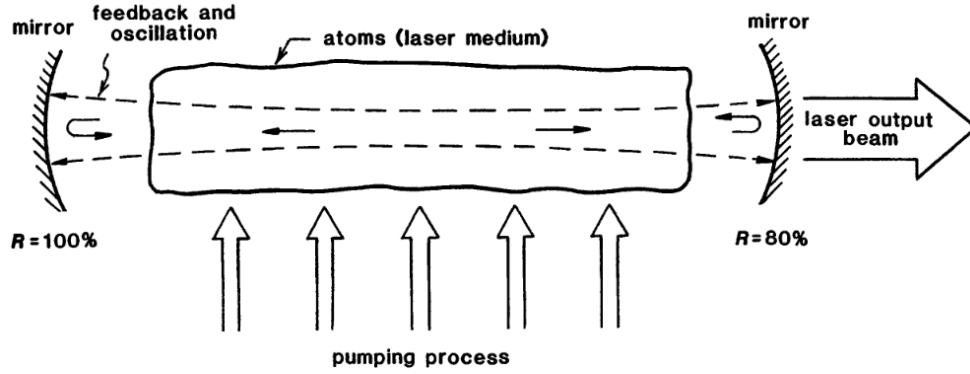


Figure 2.6.: Elements of a typical laser resonator (from [52]).

The energy  $E$  of the generated photons directly determines the frequency  $f$  of the emitted electromagnetic field given by the commonly known formula

$$E = h \cdot f, \quad (2.3)$$

where  $h$  is the energy quantum. But a population inversion does not result automatically in a coherent light field. Such a system would only emit photons of random phase by spontaneous emission.

To achieve stable lasing action or coherent light amplification, it is necessary to ensure that all emitted photons have the same phase. Therefore, the gain medium is placed in an optical resonator where the photons circulate (Fig. 2.6). Photons propagating through the gain medium interact with the electrons located in the excited state and stimulate the light emission process. Due to the standing wave condition the optical length of the resonator determines the possible frequencies where coherent light amplification can take

## 2. Generation and detection of terahertz radiation

place. These frequencies are given by

$$f_m = m \cdot \frac{c}{2 \cdot L}, \quad m \in \mathbb{N} \quad (2.4)$$

where  $m$  is a natural number,  $c$  is the speed of light in the gain medium and  $L$  is the resonator length. All emission lines are spaced by the ground frequency  $f_1$ . Further, the possible emission frequencies, also called modes, are limited by the gain/loss profile. This means only modes can built up for which the optical gain in the medium exceeds the sum of all losses within the optical resonator.

### Mode-locking

The modes of a multimode laser oscillate independently of each other, hence the phase relation between them is random. The resulting emitted electric field can be described by

$$E_{sum}(t) = \sum_i E_i \cdot \cos(\omega_i \cdot t + \phi_i(t)), \quad (2.5)$$

where  $E_i$  is the amplitude of the electric field strength,  $\omega_i$  is the angular frequency and  $\phi_i(t)$  is the time dependent phase of the individual modes. The random phase between the various modes results in random constructive and destructive interferences between them. Therefore, the emitted electromagnetic field of such a laser is strongly fluctuating. This is the reason why it is of great benefit to establish a constant phase between all modes. In this case the modes interfere completely constructive at a given time which is periodically repeated. This so called mode-locking of as many modes as possible means that the duration of the resulting pulse can be very short. How this theoretically looks like is shown in Fig. 2.7. By summing up the fundamental electric field oscillating at 10 Hz with 100 side modes which have a mode spacing of 10 mHz and no phase difference compared to the fundamental mode they periodically interfere constructively resulting a short pulse (Fig. 2.7b). Due to the mode spacing this interference pattern repeats every 100s. The more modes are locked to each other the shorter the resulting pulse and the higher its amplitude. In this particular case the amplitude rises by a factor of 101.

This gedanken experiment shows the importance of this effect. In a mode locked laser the energy is stored up and released in short energy rich bursts. The methods developed so far can be divided in passive and active mode-locking [51]. For instance, latter can be achieved by modulation of the cavity losses with a frequency given by the round trip time in the laser. One can imagine that this requires very fast and precise electronics which limits, of course, the pulse width. On the other hand passive methods are much more difficult to handle but offer shorter pulses. Thereby an additional element or in the ideal case the gain medium itself is responsible for the mode coupling. Apart from saturable absorbers one of the most often used methods in pulse lasers is Kerr lensing.

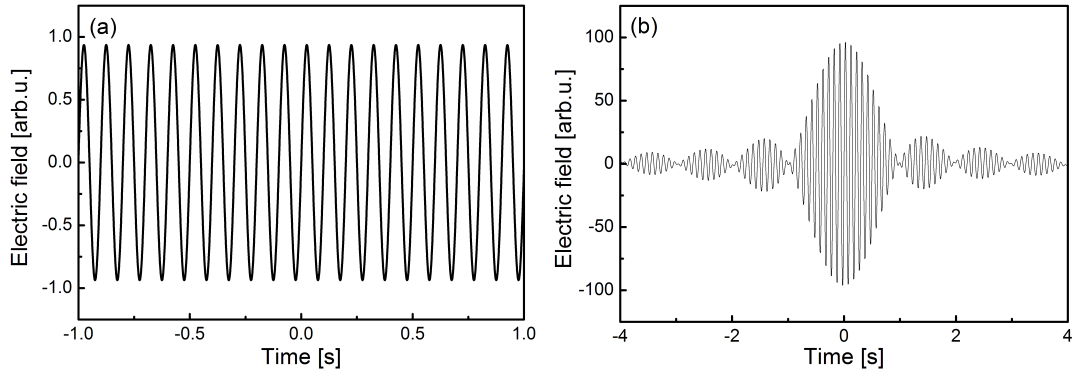


Figure 2.7.: Electric field of (a) the fundamental mode (10 Hz) and (b) 101 phase-locked modes with 10 mHz spacing.

### Kerr-Effect

The Kerr effect [39] is a second order, nonlinear electro-optic effect that describes the local change of a material's refractive index caused by the intensity of a light field. The influence on the refractive index is given by

$$n(I) = n_0 + n_2 \cdot I, \quad (2.6)$$

where  $n_0$  is the unaffected refractive index and the proportional factor  $n_2$  determines the influence of the power intensity. Since the power profile in a laser beam follows a Gaussian distribution [39] the highest intensity is located in the middle. As a result of this profile the refractive index profile changes in the same way according to Eq. 2.6. In this way the refractive index gradient forms a lens and leads to an effect which is often called beam self-focusing. Thereby the material behaves as a lens with an intensity depending curvature (Fig. 2.8). That influences the conditions within the laser cavity which can be used for passive mode-locking. If the optical system of the laser is built in a way that pulsed operation, with high temporal intensities, shows the lowest losses in the system this condition is preferred by the laser resonator itself. Due to this reason this effect is self-stabilizing. It means, that the self-focusing effect causes that the beam is more and more focused. In this way the mode of laser operation exceeds the optimal loss/gain condition and stabilizes at the upper edge of stable laser operation. The standard material for NIR pulse lasers showing a strong Kerr effect is Ti:sapphire. Such doped crystals have to be optically pumped by another cw laser. Ti:sapphire shows a very high optical damage threshold and a huge gain bandwidth of more than 300 nm [52]. Latter property makes it ideal for the generation of ultra-short laser pulses where the spectral bandwidth is the crucial parameter.

## 2. Generation and detection of terahertz radiation

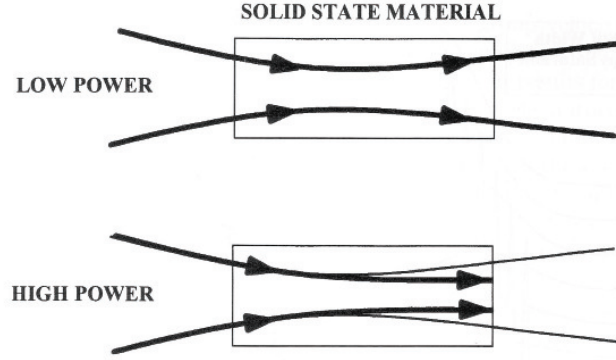


Figure 2.8.: Self-focusing caused by the Kerr effect for low and high beam intensities. Lines and arrows indicate beam waist and diameter (from [51]).

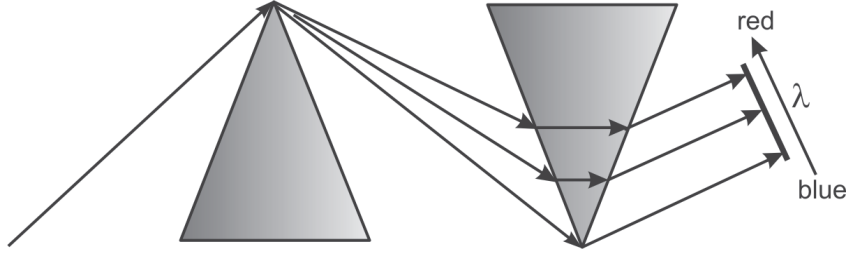


Figure 2.9.: Pulse compression with a prisms pair.

### Pulse compression

As mentioned at the beginning of this section, the laser pulses should be as short as possible to achieve a large bandwidth. Due to dispersive optical components inside and outside of the cavity the pulses are much longer than it could be in the optimal case. Most materials show a positive dispersion  $\frac{dn}{d\lambda} < 0$ . That means that they show a higher refractive index for shorter wavelengths. Even if the generated laser pulses were very short within the laser resonator the optical system outside can introduce a so-called chirp [53]. The main goal to maintain a short pulse duration is to introduce a additional opposite dispersion to compensate this pulse lengthening.

There are two main methods for introducing a negative dispersion for shortening laser pulses. First method consists of compressor made of two or more prisms [52] (Fig. 2.9). The key feature of this method is that light with a longer wavelength is propagating a longer distance through the second prism to the end mirror compared to waves with shorter wavelength. This produces a negative dispersion and shortens the laser pulse by compressing the wave packets. If the prisms are installed on a stage the dispersion can be adjusted and an additional pre-chirp can be set to compensate the dispersion of the optical system outside of the laser. In this way, at a certain position the laser pulse length is optimized. The main disadvantage of this method is its sensitivity to the position of the laser beam and the prisms. Any drift in time results in a changed pulse length.



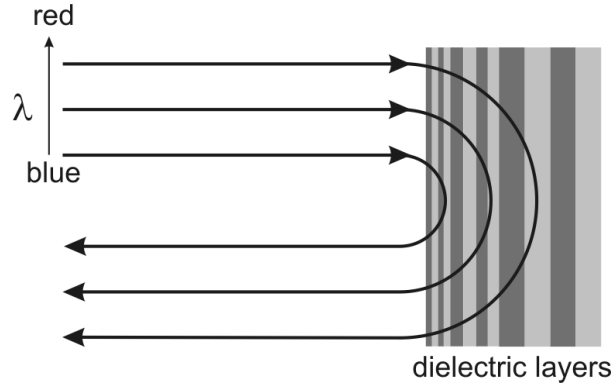


Figure 2.10.: Pulse compression with chirped mirrors.

The second method uses so-called chirped mirrors [54]. These mirrors have multiple dielectric layers of alternating materials of different thickness (Fig. 2.10). For introducing a negative chirp the mirrors have a stack of thin layers on the top whose thicknesses increase with depth. The thickness of the layers corresponds to the wavelength of the light which has to be reflected. Short wavelength light is reflected close to the surface while long wavelength light is reflected deeper in the mirror. Similar to the prism compression this introduces a longer propagation path to the red shifted light and so a negative dispersion. Since the dispersion introduced by these mirrors is independent of the hit position this method does not suffer from beam path changes. Further, such mirrors are highly adaptable. They can be designed for nearly every wavelength and dispersion, just by changing the thickness and the order of the deposited layers. In this way even dispersion of higher orders can be applied easily. The main disadvantage of this method is that a mirror's dispersion cannot be freely adjusted after its top surface was deposited. The dispersion can only be adjusted in steps by using multiple bounces between two of such mirrors. This explains why such mirrors are often installed outside of the cavity while prism compressors are mostly found within it.

### 2.3.2. Plasmon emitter

The principle of a coherent plasmon emitter [55] is shown in Fig. 2.11. An incoming laser pulse excites the surface of a doped semiconductor. In the ideal case a n-doped material with carriers of high mobility is used (e.g. n-GaAs or n-InAs). The generated charge carriers oscillate due to two different mechanisms. First, the generated charge carriers, mainly electrons, are accelerated by the surface field. This leads to a separation of electrons and holes. This, of course, causes Coulomb attraction between them which is moving the carriers back. Electrons moved in such way emit electromagnetic radiation

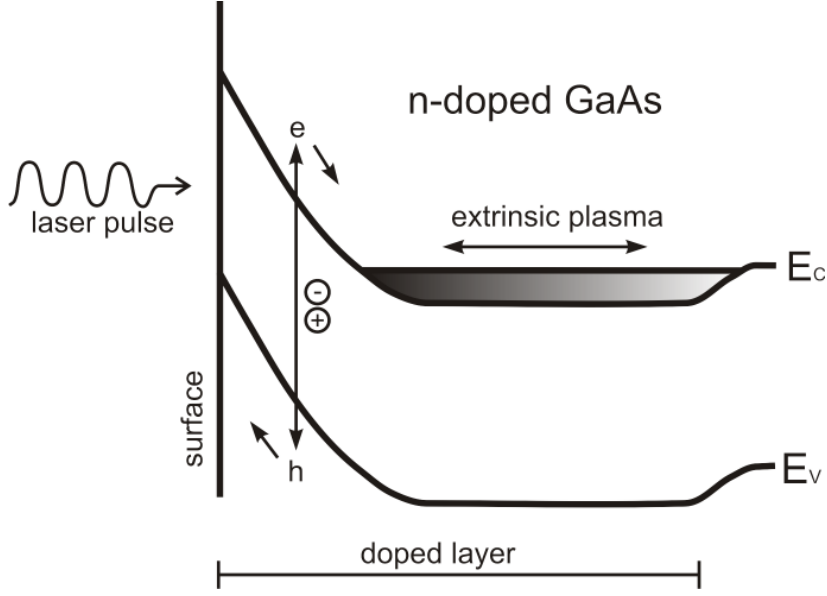


Figure 2.11.: Band profile of a plasmon emitter.

according to Hertzian dipole theory [3]. This process holds on until the carriers have recombined or dephased by electron/phonon scattering. The generated carriers are also responsible for the second process initiated because they screen the surface field partly. This causes that the surface space charge region shrinks resulting in a changed curvature of the band structure. The free electrons from the bulk material start to move towards the surface initiating a oscillation while the holes move vice versa. Due to this coherent movement the electron cloud is also called plasmon. The angular frequency of the carrier plasmon oscillation in both cases is given by

$$\omega = \sqrt{\omega_p^2 - \frac{\gamma^2}{4}}, \quad (2.7)$$

with

$$\omega_p = \sqrt{\frac{e^2 \cdot n}{\epsilon_0 \cdot m^*}}, \quad (2.8)$$

where  $\omega_p$  is the plasma frequency,  $\gamma$  is the damping factor of the oscillation,  $e$  is the elementary charge,  $n$  is the density of the photogenerated carriers,  $\epsilon_0$  is the permittivity of free space and  $m^*$  is the effective mass of the electrons. From the formulas is clear that the center emission frequency can be tuned directly by the doping concentration [55]. It is even possible to improve the emission efficiency by 40 % by using an LT<sup>9</sup>-GaAs layer at the surface [56].

This type of emitter is usually excited by the laser beam impinging under a certain angle. This has two reasons. First, to minimize the amount of reflected power, the emitter is hit

<sup>9</sup>low temperature

under the Brewster angle given by

$$\alpha_B = \arctan(n_{SC}), \quad (2.9)$$

where  $n_{SC}$  is the semiconductor's refractive index. In the case of GaAs with a refractive index of  $n \approx 3.66$  at IR wavelengths this angle is  $\sim 74.7^\circ$ . Further, since the oscillating dipoles are close to the semiconductor/air interface the emission profile can not be described by a Hertzian dipole [3] anymore. The resulting radiation pattern in this case can be calculated by [57]

$$P_e(\rho) = [(1 + n^2) \cdot \sin^2 \rho - 1]^{-1} \cdot \frac{3}{8 \cdot \pi} \cdot \frac{n^5}{n^2 - 1} \cdot \sin^2(2\rho), \quad (2.10)$$

where  $\rho$  is the angle measured from the dipole axis and  $n = \frac{n_2}{n_1}$  is the ratio of the refractive indexes of the materials building the interface. In principle the formula explains the circumstance that the radiation from a surface dipole has the tendency to concentrate in the material with higher refractive index. To optimize the THz generation process a trade off between both effects has to be found. Plasmon emitters are widely used although they need to be modulated optically. Their main advantage is the availability of cheap materials and that for such THz emitter no lithography patterning is needed.

### 2.3.3. Dipole antennas - photoconductive switches

The most often used devices for the emission of few cycle THz radiation are dipole antennas. The first application of this emitter type was the generation of optical induced ultrashort current pulses invented by D. H. Auston [15] who was the eponym of this device. In this case a light pulse illuminates an area on a semiconductor material between two biased metallic contacts. Due to the generated charge carriers in the gap the contacts are short-circuited leading to a short current transient until the carriers recombine or drift away. Apart from this original application Auston devices are also capable emitting THz radiation [58] due to those short current transients (see Eq. 2.2).

In the simplest case this emitter consists of coplanar metal stripes placed on a semiconductor material which should provide the following properties:

1. High carrier mobility
2. Short carrier life time
3. High breakdown voltage

A list of photoconductive materials including their parameters can be found in [59]. The emission process of photoconductive (PC) antennas is illustrated in Fig. 2.12 which behaves as Hertzian dipole.

When the gap between the metal stripes is illuminated by an femtosecond optical pulse with a photon energy larger than the bandgap (e.g.  $E_g = 1.43 \text{ eV}$  for GaAs at room

## 2. Generation and detection of terahertz radiation

temperature) electron/hole pairs are generated. Due to the applied electric field the carriers are accelerated in opposite directions and decay with a time constant given by the recombination rate of the corresponding material. Because the current density changes in the sub-picosecond regime the electrons within the illuminated area emit a sub-picosecond electromagnetic transient. Its spectrum depends strongly on the carrier mobility within the semiconductor material which should be as high as possible to obtain a broadband THz pulse. The electric far field  $E(r, t)$  can be described by a Hertzian dipole radiating into free space by [59]

$$E(r, t) = \frac{l_e}{4\pi\epsilon_0 c_0^2 r} \cdot \frac{\partial J(t)}{\partial t} \cdot \sin \Theta \propto \frac{\partial J(t)}{\partial t}, \quad (2.11)$$

where  $J(t)$  is the current density in the dipole,  $l_e$  is the dipole's length and  $\Theta$  is the angle measured from the main axis of the dipole. It clear that the amplitude of the radiated field is directly proportional to the derivative of the current density given by [60]

$$J(t) \propto I(t) \otimes [n(t) \cdot q \cdot v(t)], \quad (2.12)$$

where  $\otimes$  means the convolution product,  $I(t)$  is the optical intensity profile, and  $n(t)$ ,  $v(t)$  and  $q$  are, respectively, the density, the velocity and the charge of the optically generated carriers. The dynamic of the charge carriers is well described by the Drude model. According to this model the dynamics including the drift velocity  $v(t)$  of the photogenerated carriers can be described by a differential equation given by

$$\frac{\partial v(t)}{\partial t} = -\frac{v(t)}{\tau} + \frac{q}{m^*} E(t), \quad (2.13)$$

where  $\tau$  is collision rate and  $m^*$  is the effective mass of the electrons. Latter parameter explains why materials with low effective electron mass (e.g.  $m^* \approx 0.067 \cdot m_e$  for GaAs at room temperature) are best suited for such emitters. In general the pumping process can be approximated by a delta function. The resulting photo-current and radiated field amplitude is shown in Fig. 2.13.

The real shape of the antenna structure can vary depending on the application. Typical strip line distances range from  $10 \mu\text{m}$  up to  $1 \text{ cm}$ . Depending on the electrical break down voltage electric fields up to  $10 \frac{\text{kV}}{\text{cm}}$  are reached close to the semiconductor surface. In order to optimize the outcoupling efficiency and to avoid losses due to total internal reflection a hemispherical lens (see Fig. 2.12) is usually attached to the backside of the emitter made of the same or similar material.

A fact which is often underestimated and stands in close relation with this is the divergence of the generated beam. Especially this plays a major role if the illuminated area has a dimension comparable to the wavelength of the emitted radiation. The divergence angle

$\Theta$  of a Gaussian beam in respect to the optical axis of the beam is given by [53]

$$\Theta = \arctan \left( \frac{\lambda}{\pi \cdot \omega_0} \right), \quad (2.14)$$

where  $\lambda$  is the effective wavelength in the material and  $\omega_0$  the radius of the beam waist. This wavelength dependent effect results that the emitted beam profile is spectrally shaped. Long wavelengths are displaced to the edge of the beam while short wavelengths are concentrated in its center. Hence, owing to total internal reflection on the back side of the emitter long wavelength radiation can be lost. This and other practical considerations are topic of chapter 3 and are discussed there in detail.

However, dipole antennas are the primary used emitters for the generation of few cycle THz radiation. They are very powerful and scalable. Further, since the emitted radiation amplitude scales linearly, up to the breakdown voltage, with the applied electric field they can be used for the examination of nonlinear optical material parameters too.

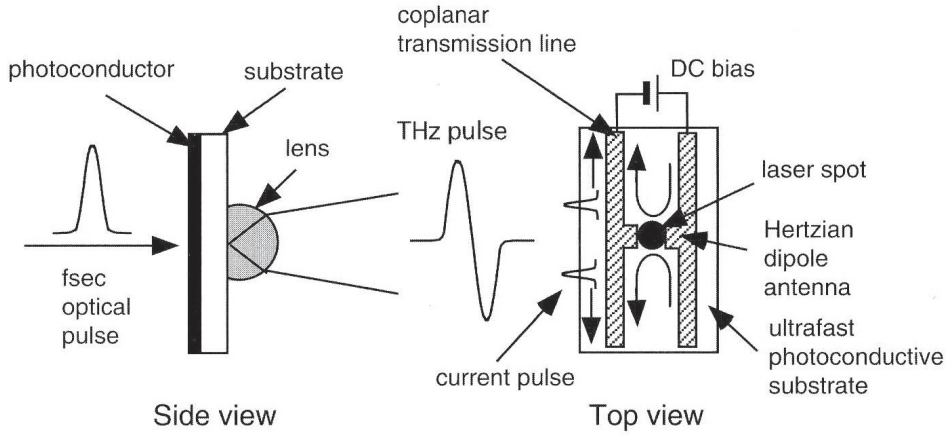


Figure 2.12.: Standard THz-pulse generation from a photoconductive antenna pumped with a femtosecond optical pulse. Propagation of current pulses along the coplanar transmission line are in the top view (from [59]).

#### 2.3.4. Difference frequency generation by optical non-linearities

The third approach for the generation of THz radiation is difference frequency generation [61]. Thereby a material's second order nonlinear optical effect is exploited. In general two waves of different frequency are mixed within a nonlinear medium. The resulting second order polarization  $P^{(2)}(\omega)$  in the material can be described by

$$\mathbf{P}^{(2)}(\omega_{THz}) = \epsilon_0 \cdot \chi^{(2)}(\omega_{THz} = \omega_1 - \omega_2) \cdot \mathbf{E}(\omega_1) \cdot \mathbf{E}^*(\omega_2), \quad (2.15)$$

where  $\chi^{(2)}$  is the second order susceptibility tensor and  $\omega_i$  are the angular frequencies of the involved fields. If two electric fields interact in a second order nonlinear crystal new fields

## 2. Generation and detection of terahertz radiation

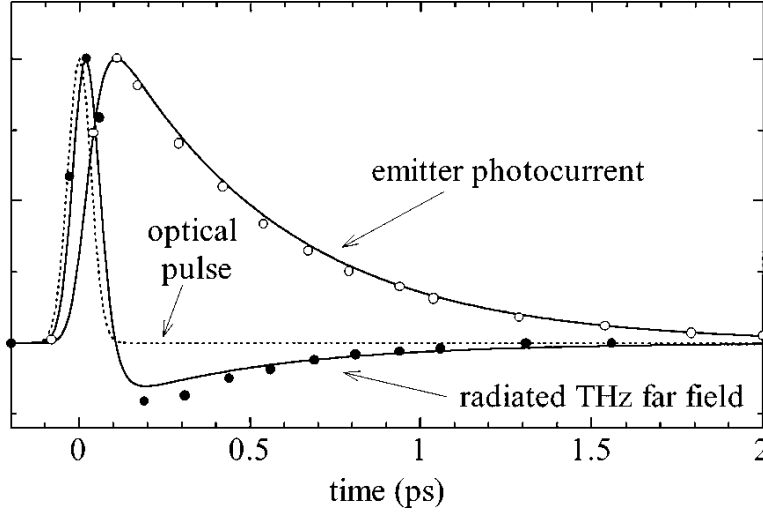


Figure 2.13.: Calculated photocurrent in the emitter and amplitude of the radiated field versus time. The temporal shape of the laser pulse is drawn as a dotted line (from [60]).

with the frequencies  $2 \cdot \omega_1$ ,  $2 \cdot \omega_2$ ,  $\omega_1 - \omega_2$ , and  $\omega_1 + \omega_2$  are generated. Even a zero frequency field component is generated giving this method also the name “optical rectification”.

For the generation of THz radiation the difference frequency generation ( $\omega_1 - \omega_2$ ) is exploited which is illustrated in Fig. 2.14. The spectral frequency components of a broad-band laser pulse are mixed in a way so that the difference frequency of certain parts of its spectrum are located in the THz frequency band. This happens for all frequencies where the phase matching condition

$$\mathbf{k}_3(\omega) = \mathbf{k}_1(\omega) - \mathbf{k}_2(\omega), \quad (2.16)$$

is fulfilled, where  $\mathbf{k}_i(\omega)$  are the frequency depending wave vectors of the involved waves in the corresponding material. Many materials are suited for this generation method. The most often used crystals for the generation of THz pulses illuminated by Ti:sapphire pulse lasers are GaSe, GaAs and ZnTe [62, 63].

Recently, a new method for the generation of intense THz pulses of more than  $400 \frac{kV}{cm}$  was developed [64]. Thereby the generation process takes place in an air plasma generated by the laser pulse itself which acts as a nonlinear medium. However, this method is complicated and needs pulses with high energy  $\sim 1 mJ$  and short length  $50 fs$ . Apart from this, difference frequency generation has in general lower output power than photoconductive switches. Their main advantages are their large bandwidth exceeding 10 THz and the slightly tunable emission profile. This can be done by changing the crystal’s optical axes in respect to the polarization of the incoming laser pulse which has a direct impact on the phase matching conditions (Eq. 2.16).

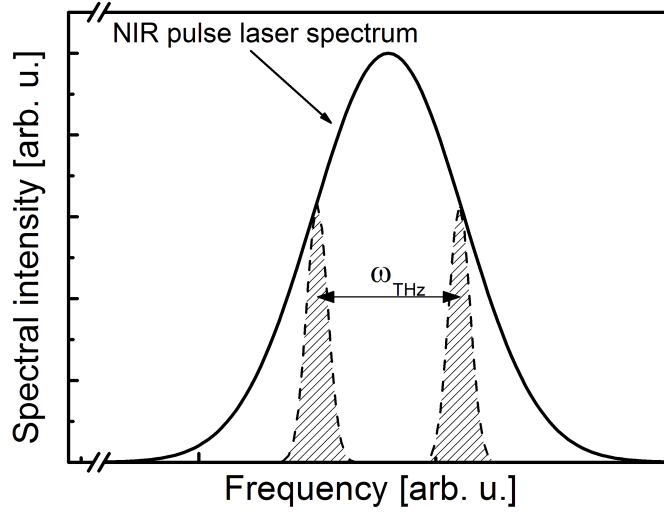


Figure 2.14.: Principle of difference frequency mixing for THz generation.

## 2.4. Detection of incoherent THz radiation

In the case of incoherent detection the phase information of the detected photons is neither obtained nor exploited for the measurement scheme like gated detection or interference effects shown later. Detectors based on this scheme measure the power absorbed by a material. The signal obtained by a sensor using this technique has an integral character and is given by

$$S = \int_0^\infty k(\omega) \cdot P(\omega) d\omega, \quad (2.17)$$

where  $P(\omega)$  is the frequency depending power density,  $k(\omega)$  is the sensor's responsivity for a given frequency and  $\omega$  is the angular frequency of the incoming radiation. Depending on the amount of absorbed power the parameters of the absorbing material or the whole heat sensitive object are changed. For instance, these can be a changed voltage drop, current, resistance or volume caused by thermal expansion. Latter can be measured by pressure sensors or markers whose position indicate the amount of absorbed power corresponding to the expanded volume.

Since such sensors are usually sensitive to the complete spectrum of thermal radiation the measured signal is not only related to the radiation source under investigation. Without any precautions the measured signal is a conglomeration of the real signal, other light sources operating in the sensor's sensitive spectral region and the thermal background. Even the application of narrow optical bandpass filters does not work. In this case the measured signal would still include the background radiation at the filters transmission range. To extract a clear signal from the thermal spectrum related with a certain radiation source it has to be marked by special measurement techniques. This is achieved by modulation of the light field of interest. Then the real signal can be obtained by mixing it with the modulation frequency. By using this scheme a signal from Eq. 2.17 modulated at  $\omega_{mod}$  can

## 2. Generation and detection of terahertz radiation

be extracted by demodulation with  $\omega_{demod}$  by

$$S_{Measured} = S \cdot \cos(\omega_{mod}) \cdot \cos(\omega_{demod}). \quad (2.18)$$

For the case that the modulation and demodulation frequencies match ( $\omega_{mod} = \omega_{demod}$ ) the above formula can be simplified and expressed by

$$S_{Measured} = S \cdot \left( \frac{1 + \cos(2 \cdot \omega_{mod})}{2} \right). \quad (2.19)$$

The measured signal consists of a constant component  $\frac{S}{2}$  and a signal part at the doubled original modulation frequency. Latter can be easily filtered out by low pass filters. This simple measurement technique can be applied to more or less any detection method to increase its sensitivity and masking interfering background signals. For this demodulation purpose lock-in amplifiers are used. This working principle and technique is explained in detail in [65]. Especially the techniques for the detection of incoherent THz radiation described in the following sections owe their universal application capability this measurement technique of marking a signal of interest.

### 2.4.1. Bolometers

One of the oldest measurement device for electro-magnetic radiation is the bolometer (gr. bole - “beam”). It was developed in 1878 by the astronomer S. P. Langley<sup>10</sup> for the detection of infrared radiation [66]. Mainly it consists of a radiation absorbing element, a heat sink and a temperature sensitive device. The measurement scheme is as simple as follows [67]. At first the incoming radiation increases the temperature at the absorbing element which is directly attached to a thermometer. Latter can be e.g. a silicon plate through which a steady current is flowing. Due to the temperature increase the resistivity and so the voltage drop across the sensor changes which is a direct measure for the amount of absorbed radiation. For achieving a high sensitivity the heat capacity of the whole system has to be kept as low as possible. This ensures that already small amounts of absorbed radiation result in a high and fast change in temperature corresponding to a high signal output. Further, the heatsink has to be kept cool, at a constant temperature to achieve a high sensitivity and speed of the device. Best performance and sensitivity is achieved with liquid Helium (lHe) cooled silicon bolometers [67] which can be operated up to a modulation frequency of a few kHz. The main disadvantages of standard bolometer are their bulky design, the need for a cryogenic coolant and the relative low speed.

Recently, the bolometer development made a big step forward which opened widely their application range. This was mainly achieved by miniaturization [68]. These so-called microbolometers have a very low heat capacity what improved the sensitivity by a factor more than 4 and increased the modulation frequency beyond 100 kHz. Another advantage of the sensitivity increase by reducing the sensor’s volume was room temperature

---

<sup>10</sup>Samuel Pierpont Langley (1834-1906)



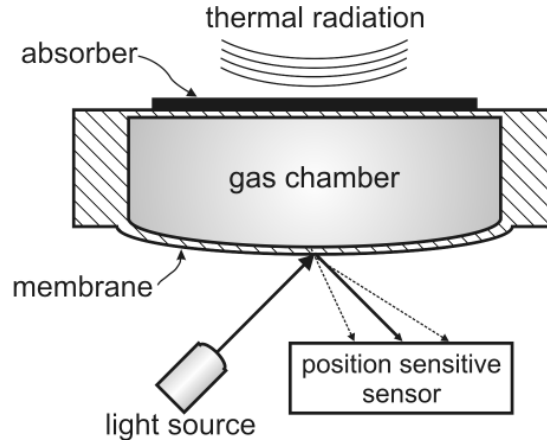


Figure 2.15.: Working principle of a Golay cell infrared detector.

operation [69] and the possibility of arranging many sensors in a two-dimensional array for imaging applications [70].

#### 2.4.2. Golay cell

The Golay cell is an opto-mechanical sensor for infrared radiation invented by M. Golay<sup>11</sup> and is based on a pneumatic principle [71]. A scheme of a usual Golay cell is shown in Figure 2.15. First, incoming thermal radiation is filtered by an appropriate window material. The transmitted radiation hits a highly absorbing material of low heat capacitance resulting in an temperature increase. This absorber is in close thermal contact to a chamber filled with a gas. Further, one side of the chamber is implemented as flexible membrane which acts as a highly reflective mirror. Light from a source is reflected under a certain angle from this membrane and is detected by a position sensitive optical sensor, e.g. a photodiode in the simplest case.

If now radiation is absorbed the temperature of the gas is changed leading to an increase of the gas pressure. Since only one side wall of the chamber is flexible the membrane there expands slightly. This change can be sensed by the deviation of a light beam reflected from this side wall by e.g. a position sensitive sensor. A Golay cell is a very sensitive sensor [71] but find mainly use in scientific applications. Its main limitations are their low speed and the vulnerability to vibrations [72] as a result of the opto-mechanical detection principle. However, since the invention of the Golay cell the available technology changed, and miniaturization improved the sensitivity and speed of these sensors [73].

#### 2.4.3. Pyroelectric sensor

The pyroelectric sensor is a thermal measurement device for the detection of infrared radiation. Such sensors do not need an external bias voltage and are operated at room temperature. Some crystalline materials exhibit a spontaneous electric polarization which

<sup>11</sup>Marcel Golay (1902-1989)

## 2. Generation and detection of terahertz radiation

means an alignment of dipoles within the domains in the crystal. Since the number of uniform aligned domains in these crystals depends strongly on the temperature they are called pyroelectric. Due to this effect a temperature depending charge is built up at the crystal's surfaces perpendicular to its ferroelectric axes [74]. The value of the spontaneous polarization across the crystal about room temperature can be approximated by

$$P_{py} = p \cdot \Delta T + P_0, \quad (2.20)$$

where  $p$  is the material depending pyroelectric constant,  $\Delta T$  is the temperature difference and  $P_0$  is the value of the spontaneous polarization at the reference temperature. Due to the ferroelectric nature of the pyroelectric effect it vanishes by approaching the material's corresponding Curie temperature [75] where the pyroelectric constant becomes strongly temperature depending. This effect can usually be neglected because such sensors are operated close to room temperature and the amount of absorbed radiation does not significantly change the sensor's properties.

As pyroelectric elements mostly ionic crystals or ferroelectric polymers are used [76]. The structure of pyroelectric sensors is similar to the other incoherent detectors described above. The pyroelectric element is sandwiched between two electrodes and attached to a radiation absorbing element. The direct measure for the sensor's temperature and so the absorbed incoming radiation is the voltage drop across the electrodes. In principle pyroelectric sensors are capacitors with a very high RC time constant making this detector rather slow. Since no mechanical components are used and no active cooling is needed they find wide application. Today modulation frequencies up to 30 Hz are achieved [77] and mostly materials like lithium tantalate ( $LiTaO_3$ ) are used [78].

### 2.4.4. Fourier transform infrared spectroscopy

As already mentioned in the introduction one of the main methods obtaining the spectrum of an incoming light field is Fourier transform infrared spectroscopy (FT-IR). Basically it consists of a Michelson interferometer invented by A. A. Michelson more than 100 years ago. Thereby a light field from a source is guided through the interferometric part and then sensed by a proper detector. A general overview of various types of interferometers and their field of application can be found in [53]. As indicated above, the interferometer is no light sensor per definition. It is a frequency sensitive component which is combined with a light source and detector to obtain a power density spectrum of the sensed radiation.

A typical layout of a FT-IR spectrometer system is shown in Fig. 2.16. The radiation from a light source is guided collinearly to the spectrometer part where the beam is split into two parts by a beam splitter. Within there, one beam is reflected by a movable and the other by a fixed mirror resulting in different propagation lengths. This time delay between the two beams leads to a phase difference between them. Depending on the delay the beams interfere either constructively or destructively, are led through a sample and are finally sensed by a detector. The result is an autocorrelation function given by

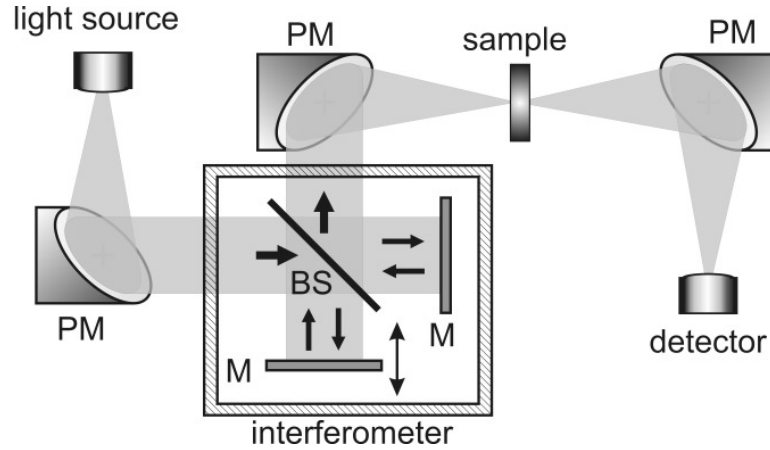


Figure 2.16.: Scheme of a standard two beam FT-IR spectrometer (BS=beamsplitter, M=mirror, PM=parabolic mirror).

$$S(\tau) = \int_{-\infty}^{\infty} [E_{sum}(t)]^2 dt = 2 \cdot \int_{-\infty}^{\infty} [E(t)]^2 dt + 2 \cdot \int_{-\infty}^{\infty} E(t) \cdot E(t + \tau) dt \quad (2.21)$$

where

$$E_{sum}(t) = E(t) + E(t + \tau) \quad (2.22)$$

is the instant electric field at the power detector and  $\tau$  is the time delay between the two beam parts. The first term in Eq. 2.21 corresponds to the power of the sensed radiation whereas the second term is the autocorrelation function which is of interest. The power density spectrum (PDS) of the beam is obtained by Fourier transformation. The applications of FT-IR systems are manifold. For instance, they are used for measuring the optical properties of materials. In this case e.g. a globar or a mercury lamp is used as light source for measuring the PDS with and without sample. Latter spectrum  $P(\omega)$  is used as reference which also illustrates the second application. If no sample is installed the FT-IR measures the PDS of the light source which is in this case the quasi sample. For this purpose the sensor's sensitivity spectrum has to be known exactly which acts in this case as reference. However, in this way incoherent, coherent and even the emission spectrum of pulsed sources can be measured. For latter purpose FT-IR is not the best choice. By measuring the PDS any kind of phase information is lost and time-domain measurements are usually performed for measuring the electric field strength including its phase.

## 2.5. Detection of few cycle THz radiation

The detection of few cycle THz radiation depends on the application. In principle any of the above mentioned detection methods can be used. But in this case the additional phase information carried by these pulses would be lost. Especially if few cycle THz pulses are sensed in time-domain including their phase information a lot of physical effects can

## 2. Generation and detection of terahertz radiation

be accessed. For instance a complete pulse trace including all reflections from the optical system offers much more information than the pure transmission data like the absorption coefficient. It includes the complete history of the wave propagation. This means reflections get clearly visible and can be exploited for e.g. the development of new anti-reflection coatings (see chapter 4) or the observation of the dynamics of various effects. In the pure power detection scheme these reflections are part of the sensed average signal and stay hidden. But furthermore, in time-domain the dynamic of processes in active materials can be observed which is the topic of chapter 6.

The sensing of THz pulses in time-domain is quite complicated. A typical THz pulse transient has a length of about 500 fs. The main problem is that there do not exist sensors which are fast and sensitive enough to operate at this time scale with high resolution [79]. A solution for this problem is gated detection explained in chapter 3 in detail. By overlapping a short IR probe pulse with the relative long THz transient in a properly gated sensor the shape of the THz transient is sensed point by point by varying the delay between them. The main techniques for the direct measurement of the electric field strength including the phase are explained in the following sections. Especially the electro-optic detection scheme is described in detail because it is the method of choice used in the experiments which are the main topic of this work.

### 2.5.1. Dipole antenna detection

The detection of few cycle THz radiation by a dipole antenna [80] is the inversed dipole antenna emitter scheme described in section 2.3.3. Like the dipole antenna emitter the sensor consists of two metal stripes placed on a semiconducting material (e.g. GaAs). The area between the two unbiased metallic stripe lines is excited by a short IR laser pulse which generates charge carriers there at the surface (Fig. 2.17). At the same time the area is hit by a THz electric field transient. Corresponding to the electric field strength of the THz transient overlapping with the optical probe pulse the carriers are accelerated. That is resulting in an induced current flow which is measured by an ammeter. The generated photocurrent  $I(t)$  as a function of time is described by [81]

$$I(t) = e \cdot \mu \cdot \int_{-\infty}^{\infty} E_{THz}(t') \cdot N(t' - t) dt', \quad (2.23)$$

where  $E_{THz}(t)$ ,  $N(t)$ ,  $e$  and  $\mu$  are the incident THz electric field strength, the number of photogenerated carriers, the elementary charge, and the electron mobility, respectively. The typical amplitude in the focus of the THz electric field is  $\sim 100 \frac{V}{cm}$  which is only 1 % of the electric field strength applied in the emitter configuration of this device. Hence, the stripe line distance is much narrower. Typical distances are a few  $10 \mu m$  [37]. Further, again a lens is used to focus the THz field directly onto the stripe line gap. In free space the wavelength of the sensed field would be much larger than the dimension of the sensor leading to a reduced sensitivity. At the moment they offer a sensing bandwidth up to

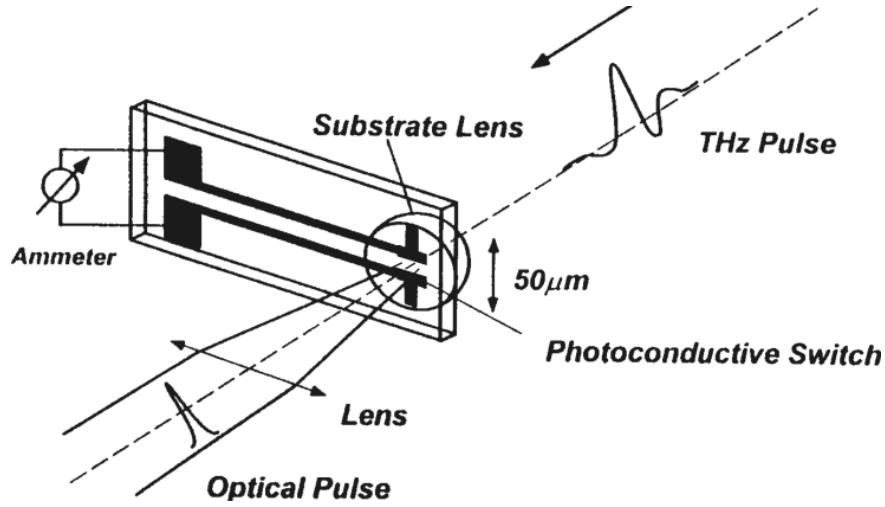


Figure 2.17.: Illustration of the detection principle of dipole antennas (corrected drawing from [37]).

20 THz [82]. Dipole antenna sensors are widely used but stand in direct competition with the electro-optic sampling technique which is explained later. The main disadvantages are the limited bandwidth given by the RC time constant of the device and the need for precise low noise current amplifiers because the typical generated photocurrents are usually in the range of  $pA - nA$ .

### 2.5.2. Electro-optic detection

Another type of sensors for the detection of few cycle THz pulses are electro-optic crystals. Sensing of pulsed THz radiation with electro-optic crystals (EOC) is a relatively new method. It was introduced by the group of X. C. Zhang [83, 84]. Compared to the dipole antenna detection scheme electro-optic sampling (EOS) offers some significant advantages [85, 86]. These are mainly the achievable bandwidth and the fact that EOS is by principle highly sensitive to the polarization of the incoming THz field. Recently a measured frequency spectrum up to 37 THz was reported [87]. Since EOS is a pure optical principle no additional micro fabrication is needed and EOCs are commercially available. Further, the detection principle is independent of the used position on the crystal making it an easy and robust detection scheme.

#### Principle

Usually the index ellipsoid of a material describing its orientation dependent optical properties can be in general written as

$$\left(\frac{x}{n_x}\right)^2 + \left(\frac{y}{n_y}\right)^2 + \left(\frac{z}{n_z}\right)^2 = 1, \quad (2.24)$$

## 2. Generation and detection of terahertz radiation

where  $n_i$  ( $i = x, y, z$ ) is the refractive index for a given direction in the Cartesian coordinate system. In the case of an isotropic material the formula can be simplified to

$$\frac{x^2 + y^2 + z^2}{n_0^2} = 1, \quad (2.25)$$

resulting in a spherical shape of the index ellipsoid. For instance EOCs like zinc telluride (ZnTe) and gallium phosphide (GaP) belong to this type of crystals [88, 89]. In general the refractive index of a material is given by its internal molecular structure. But this is not the case for EOCs. In this type of crystals the value of the refractive index depends on the material's electric polarization induced by an external static or quasi-static electric field. Such fields can be either applied by attached electrodes or in general by an incoming electromagnetic radiation, e.g. a THz electric field. This influence of the electric field on the refractive index in certain materials is called electro-optic (eo) effect. For EOCs the first order eo-effect, also called Pockels [39] effect, is exploited. The resulting first order nonlinear polarization in the material in this case is given by

$$P_i^{(2)}(\omega) = \varepsilon_0 \cdot \chi_{ijk}(\omega) \cdot E_j(\omega) \cdot E_k(0), \quad (2.26)$$

where  $\chi_{ijk}$  is the susceptibility tensor. The formula describes how the interaction of a high frequency and quasi-static electric field changes the local polarization in a material. Due to the presence of latter electric field the spherical shape of the index ellipsoid changes to an elliptical one with rotated main axes which are given by

$$\begin{aligned} & \left(\frac{1}{n_1^2}\right) \cdot x^2 + \left(\frac{1}{n_2^2}\right) \cdot y^2 + \left(\frac{1}{n_3^2}\right) \cdot z^2 + \\ & \left(\frac{1}{n_4^2}\right) \cdot x \cdot y + \left(\frac{1}{n_5^2}\right) \cdot y \cdot z + \left(\frac{1}{n_6^2}\right) \cdot z \cdot x = 1, \end{aligned} \quad (2.27)$$

where  $\frac{1}{n_i^2}$  are the optical constants for describing the index ellipsoid. A more convenient way describing the eo-effect is to use the impermeability tensor which is defined by

$$\boldsymbol{\eta} = \frac{1}{\varepsilon} = \frac{1}{n^2}. \quad (2.28)$$

With the impermeability tensor the index ellipsoid from Eq. 2.27 can be rewritten to

$$\eta_{11} \cdot x^2 + \eta_{22} \cdot y^2 + \eta_{33} \cdot z^2 + \eta_{44} \cdot x \cdot y + \eta_{55} \cdot y \cdot z + \eta_{66} \cdot z \cdot x = 1, \quad (2.29)$$

and the values of the impermeability tensor including the Pockels effect can be calculated by

$$\eta_{ij}(E_k) = \eta_{ij}^{(0)} + \sum_k r_{ijk} \cdot E_k. \quad (2.30)$$

The tensor  $r_{ijk}$  directly describes the influence of the first order eo-effect on a material's optical properties. Due to the effect the tensor is describing its elements are usually called

eo-coefficients. Since this tensor consists of real values and has a symmetric shape [39], it can be rewritten as a 2-dimensional matrix. In this form, it can be used to calculate the changes of the optical parameters of a material caused by an applied external field (Eq. 2.31).

$$\begin{bmatrix} \Delta\eta_{11} \\ \Delta\eta_{22} \\ \Delta\eta_{33} \\ \Delta\eta_{44} \\ \Delta\eta_{55} \\ \Delta\eta_{66} \end{bmatrix} = \begin{bmatrix} r_{11} & r_{12} & r_{13} \\ r_{21} & r_{22} & r_{23} \\ r_{31} & r_{32} & r_{33} \\ r_{41} & r_{42} & r_{43} \\ r_{51} & r_{52} & r_{54} \\ r_{61} & r_{62} & r_{63} \end{bmatrix} \cdot \begin{bmatrix} E_x \\ E_y \\ E_z \end{bmatrix} \quad (2.31)$$

In the case of eo-detection of THz radiation, the THz electric field changes the optical properties of the crystal. This leads to a change of polarization of the electro-magnetic NIR wave propagating through the EOC at the same time, later in this thesis called probe beam. This change depends strongly on the orientation of the main axes of the EOC with respect to the wave vector and polarization of the THz and probe beam. The calculation of the resulting index ellipsoid is quite complicated but generally the impermeability tensor is significantly reduced to several non-zero elements due to the crystal's symmetry.

### Electro-optic materials

Many materials are suitable for the electro-optic detection of THz radiation but only a few crystals are widely used. This depends strongly on how good they fulfill the optimal conditions and properties of an ideal EOC which are:

- High lattice symmetry (non-zero and equal coefficients only for  $r_{41}$ ,  $r_{52}$  and  $r_{63}$  )
- Weak frequency dependence of the optical properties
- No or only weak absorption
- High electro-optic coefficients

The materials used for eo-detection can be mainly divided into groups of isotropic and anisotropic materials. For instance  $LiTaO_3$  and  $LiNbO_3$  belong to latter group [90]. In their case the electro-optic coefficients are neither symmetric nor equal (Tab. 2.1). The calculation of the eo-effect is not trivial in this case. Since such materials were not used during this work they are not described in detail. The detailed description of these EOCs can be found in [91].

Another material with a huge potential is DAST<sup>12</sup> [92]. In contrast to the above described materials it is an anisotropic molecular crystal (see chapter 5) with a very high Pockels coefficient of  $75 \frac{pm}{V}$  at a wavelength of 820 nm which is more than one order larger compared to ZnTe (Tab. 2.2) but the aggravation that it is an anisotropic material showing

---

<sup>12</sup>4-dimethylamino-N-methylstilbazolium

## 2. Generation and detection of terahertz radiation

$$\begin{pmatrix} 0 & -r_{22} & r_{13} \\ 0 & r_{22} & r_{13} \\ 0 & 0 & r_{33} \\ 0 & r_{51} & 0 \\ r_{51} & 0 & 0 \\ -r_{22} & 0 & 0 \end{pmatrix} \quad \begin{pmatrix} 0 & 0 & 0 \\ 0 & 0 & 0 \\ 0 & 0 & 0 \\ r_{41} & 0 & 0 \\ 0 & r_{41} & 0 \\ 0 & 0 & r_{41} \end{pmatrix}$$

*LiTaO<sub>3</sub>* and *LiNbO<sub>3</sub>*      *ZnTe* and *GaP*

Table 2.1.: Structure of the Pockels coefficient matrix  $r_{ij}$  of *LiTaO<sub>3</sub>*, *LiNbO<sub>3</sub>*, *ZnTe*, and *GaP* (from [91]).

eo-crystal	$r_{41} \left[ \frac{pm}{V} \right]$	$n_0 \ (\lambda_0 = 840 \text{ nm})$
ZnTe	4.04	3.17
GaP	1	3.5

Table 2.2.: Pockels coefficients of *ZnTe*, and *GaP*.

very strong absorption for frequencies above 1 THz it has only limited importance in the field of sensing high frequency THz radiation.

The materials mainly used and which fulfill most of the requirements stated above are ZnTe and GaP. In the group of isotropic crystals ZnTe shows the largest eo-coefficient (Tab. 2.2). The main limitations of ZnTe are its low transverse optical (TO) phonon resonance frequency of 5.31 THz and a strong tendency of two photon absorption limiting the optical power of a NIR probe beam [89]. The other widely used material is GaP [88]. Its eo-coefficient is only one quarter compared to ZnTe but its TO phonon resonance frequency is located at 11 THz which makes it the EOC of choice for broadband applications. Which EOC is used depends finally on the application and the properties needed.

One of the main problems which have all EOCs in common is their dispersion. This means that NIR and THz waves are propagating through the crystal with different velocities. As a consequence this leads to a phase velocity mismatch resulting in a frequency dependence of the so-called response function of the crystal. The first step to calculate this function is to determine the delay of the NIR and THz waves passing the EOC by

$$\delta(f_{THz}) = \frac{n_g(\lambda_{NIR}) - n(f_{THz})}{c} \cdot d, \quad (2.32)$$

where  $n_g(\lambda_{NIR})$  is the NIR group index,  $n(f_{THz})$  is the THz phase index,  $c$  is the vacuum speed of light and  $d$  is the thickness of the crystal. The THz frequency depending response function is then given by [88]

$$G(f_{THz}) = \frac{t(f_{THz})}{\delta(f_{THz})} \int_0^{\delta(f_{THz})} e^{i \cdot 2 \cdot \pi \cdot f_{THz} \cdot t} dt = t(f_{THz}) \cdot \frac{e^{i \cdot 2 \cdot \pi \cdot f_{THz} \cdot \delta(f_{THz})} - 1}{i \cdot 2 \cdot \pi \cdot f_{THz} \cdot \delta(f_{THz})}, \quad (2.33)$$

where  $t(f_{THz})$  is the Fresnel transmission coefficient which determines the losses due to reflection. The absolute value of  $G(f_{THz})$  determines the frequency response function



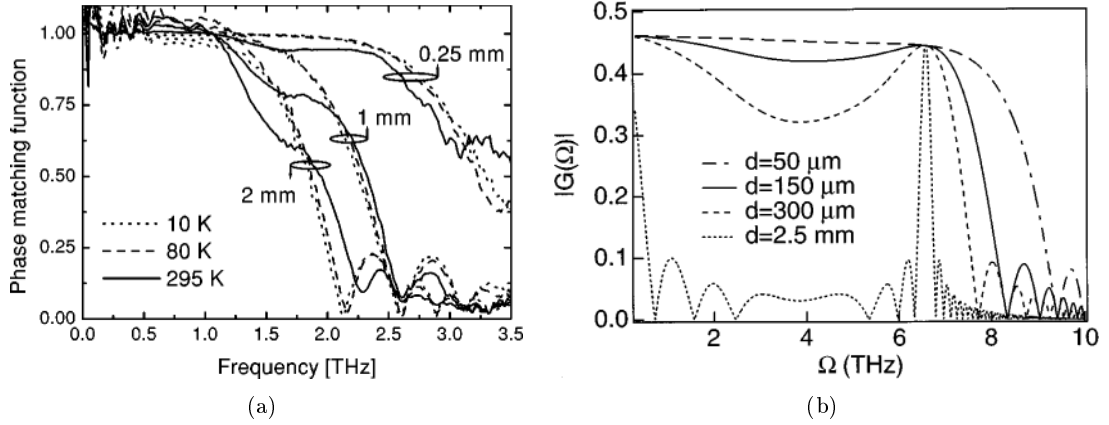


Figure 2.18.: Phase matching function of (a) ZnTe and (b) GaP (from [88, 93]).

of the electro-optic crystal. In Fig. 2.18 this function is shown for ZnTe and GaP of various thicknesses. It can be easily seen that the cut-off frequency depends strongly on the crystal's temperature and thickness. Generally, the thicker the crystal the lower the cut-off frequency and vice versa. But the thickness does not only affect the bandwidth of the sensor. In addition it determines the interaction length of the NIR probe beam and the quasi-static electric field corresponding to the induced polarization change which is proportional to the sensed THz electric field amplitude. However, depending on the application a trade-off has to be found between signal strength and bandwidth.

### Application principle of electro-optic detectors for THz radiation sensing

The electro-optic effect itself describes the physical changes of a crystal's properties due to the presence of a THz electric field. The effect on the passing optical beam depends, of course, on the orientation of the EOC with respect to the polarization of the co-propagating waves. For eo-detection of THz radiation (110)-oriented isotropic crystals are typically used. Only for this orientation the THz field amplitude can be sensed by the EOC as is described as follows.

The starting point of the calculation of the eo-effect is the scheme shown in Fig. 2.19. A NIR probe electric field  $E_P$  and a THz electric field  $E_{THz}$  passing the EOC with given wave vectors and polarization. The presence of the THz field induces a deformation of the index ellipsoid given by [94]

$$\frac{x^2 + y^2 + z^2}{n_0^2} + 2 \cdot E_{THz,1} \cdot r_{41} \cdot y \cdot z + 2 \cdot E_{THz,2} \cdot r_{41} \cdot x \cdot z + 2 \cdot E_{THz,3} \cdot r_{41} \cdot x \cdot y = 1, \quad (2.34)$$

where  $E_{THz,i}$  are the components of the applied THz electric field along the main axes (x-, y-, and z-direction) and  $n_0$  is the unaffected refractive index. The next step is to find a coordinate system which coincides with the main axes of the index ellipsoid, so that the mixed terms vanish. This results in a much easier and shorter calculation of the

## 2. Generation and detection of terahertz radiation

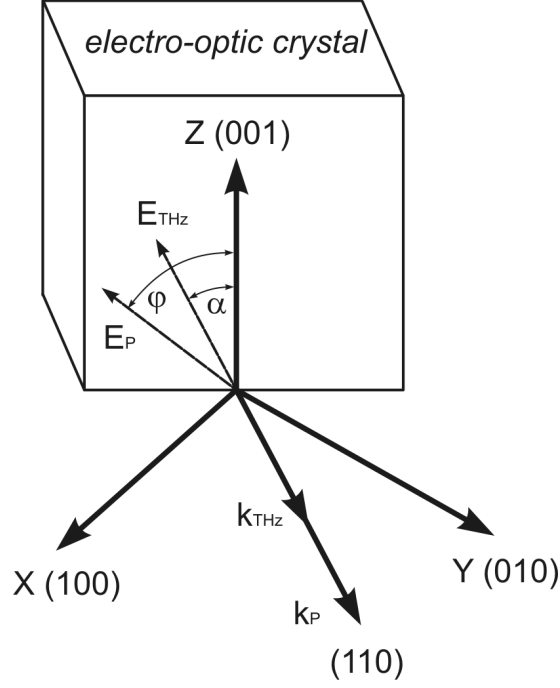


Figure 2.19.: Coordinate system of a (110)-oriented electro-optic crystal with probe and THz beam.

polarization change of the probe beam. This is achieved by two coordinate transformations.

First, the system is rotated by  $45^\circ$  around the z-axis. After this, two mixed terms vanish and an additional simplification  $E_{THz,1} = -E_{THz,2}$  can be done. Now the x-axis of the new system points in the same direction as the  $\mathbf{k}$  vectors of the co-propagating waves. In the next step the system is rotated around this new x-axis by the angle  $\Theta$ . In addition, the vector of the THz field can be projected at the new system:  $E_{THz,1} = E_{THz} \cdot \frac{1}{\sqrt{2}} \cdot \sin(\alpha)$ ,  $E_{THz,3} = E_{THz} \cdot \frac{1}{\sqrt{2}} \cdot \cos(\alpha)$  with  $E_{THz} = |\mathbf{E}_{THz}|$ . The resulting index ellipsoid is then given by

$$\begin{aligned}
 & x''^2 \cdot \left( \frac{1}{n_0^2} + E_{THz} \cdot r_{41} \cdot \cos \alpha \right) + \\
 & y''^2 \cdot \left( \frac{1}{n_0^2} + E_{THz} \cdot r_{41} \cdot (\cos \alpha \cdot \sin^2 \Theta + \cos(\alpha + 2 \cdot \Theta)) \right) + \\
 & z''^2 \cdot \left( \frac{1}{n_0^2} - E_{THz} \cdot r_{41} \cdot (\cos \alpha \cdot \sin^2 \Theta - \cos(\alpha + 2 \cdot \Theta)) \right) = 1,
 \end{aligned} \tag{2.35}$$

where

$$2 \cdot \Theta = -\arctan(2 \cdot \tan \alpha). \tag{2.36}$$

In the resulting coordinate system the THz field vector has no component in the  $x''$  direction so that this term can be neglected. This simplification leads to the resulting refractive

indexes including the electro-optic effect

$$\begin{aligned} n_y''(\alpha) &\approx n_0 + \frac{n_0^3}{2} \cdot E_{THz} \cdot r_{41} (\cos \alpha \cdot \sin^2 \Theta + \cos(\alpha + 2 \cdot \Theta)), \\ n_z''(\alpha) &\approx n_0 + \frac{n_0^3}{2} \cdot E_{THz} \cdot r_{41} (\cos \alpha \cdot \sin^2 \Theta - \cos(\alpha + 2 \cdot \Theta)). \end{aligned} \quad (2.37)$$

Since these refractive indexes are different, it is obvious that the optical probe beam will change its polarization. For instance from linear to elliptical polarization when passing the EOC in the presence of a THz electric field. How this principle is used in reality for sensing THz radiation is described in chapter 3 where the experimental setup is explained in detail.



## 3. Advanced terahertz time-domain spectroscopy setup

The initial point for the exploration of physical effects is a measurement tool capable to analyze it. In the simplest case an easy to use turn on key system. For standard applications like FT-IR spectroscopy those systems can be bought from various companies. The usage of such systems is reduced to a “press button to measure” scheme. As a result a lot of material parameters are calculated by the internal electronics and programs. But the situation changes if certain optical parameters of a light source or material shall be measured which are only accessible by an uncommon application specialized system. In this case the whole measurement system is built from the sketch which makes a fundamental knowledge in optics, electronics, programming and math necessary. In this chapter the basic principles of THz-TDS<sup>1</sup> are introduced and described in detail which includes:

- Time-domain spectroscopy measurements scheme
- Applied electro-optic sampling
- Data processing
- Initial THz-TDS setup in the year 2003
- Summary of all applied improvements and changes
- High performance THz-TDS system in the year 2006

Especially is shown there where this work started and what progress was achieved. The setup improvement was the key point of this work. Without it, most of the applied spectroscopy results in the following chapters would not be possible. Therefor an own chapter is dedicated to this very important topic not included in most theses.

### 3.1. Principle of THz time-domain spectroscopy

#### 3.1.1. Measurement scheme

As explained in the chapter before a direct single shot measurement of a THz electric field transient is not possible so far. No known detector is fast and sensitive enough to operate on the femtosecond time scale with a resolution better than 100 *fs* in the THz

---

<sup>1</sup>THz time-domain spectroscopy

### 3. Advanced terahertz time-domain spectroscopy setup

frequency band. Only by using electro-optic detection techniques the THz pulse can be measured indirectly by a NIR streak camera [95] in time-domain but only with a resolution of 200 fs [79].

The standard method used to detect few cycle THz electric field transients is THz-TDS. In contrast to FT-IR the signal is measured directly in time which includes the electric field strength AND the phase information. The method is similar to the sample & hold technique used in measurement engineering. The shape of the long THz pulse (FWHM  $\sim 500$  fs) is sampled point by point by a much shorter optical pulse (FWHM  $< 150$  fs), typically optical pulses from a femtosecond Ti:sapphire laser. For this purpose it is necessary to shift the pulses in respect to each other.

The scheme of an universal THz-TDS setup is shown in Fig. 3.1. The incoming NIR laser pulse is split in a so-called pump and probe beam. The pump pulses generate few cycle THz radiation with a suitable emitter e.g. a dipole antenna (see section 2.5). While propagating through the optical system including the sample object, certain frequency components of the THz pulse are absorbed and sustain a phase change. In addition, many setups are equipped with a second pump arm (Fig 3.1a). This can be either a THz or optical pump pulse which hits in addition the sample with a given time delay between these two pump pulses. For instance, in this way the relaxation time of very fast semiconductors can be measured. However, finally the THz pulse is measured by a detector gated by the probe pulses. An illustration of this sampling method is shown in Fig. 3.1b.

The main advantages of such systems are their huge dynamic range, the stability of the light source and a very low noise floor [96]. In addition, since the pulse trace is measured in time the optical interfaces penetrated on its way through the system can be partly deconvoluted. This means by measuring a long time delay reflections from those interfaces get visible in the time window. From them, the absorption coefficient and the refractive index of a penetrated object can be determined [97]. With FT-IR this would be not possible because the measured signal is simply the sum of all arrived signals and so the sum of all their power density spectra. For instance, since all phase information is lost the dynamics of an active media cannot be examined in detail. This phase sensitive property of THz-TDS is extensively used in chapter 6 later.

#### 3.1.2. Electro-optic sampling

Apart from the incoherent detection of THz radiation used for measuring the emission of an active media in the last chapter only electro-optic sampling was used to sense the THz pulses generated by a dipole antenna. All techniques were described in the previous chapters but at this point the real application of electro-optic sampling for sensing few cycle THz pulses shall be explained in detail. Especially this includes the involved optical components.

First element is the EOC, where the NIR probe and THz pulse co-propagate (Fig. 3.2). If there is no temporal overlap between them, the NIR pulse is passing it without any

### 3.1. Principle of THz time-domain spectroscopy

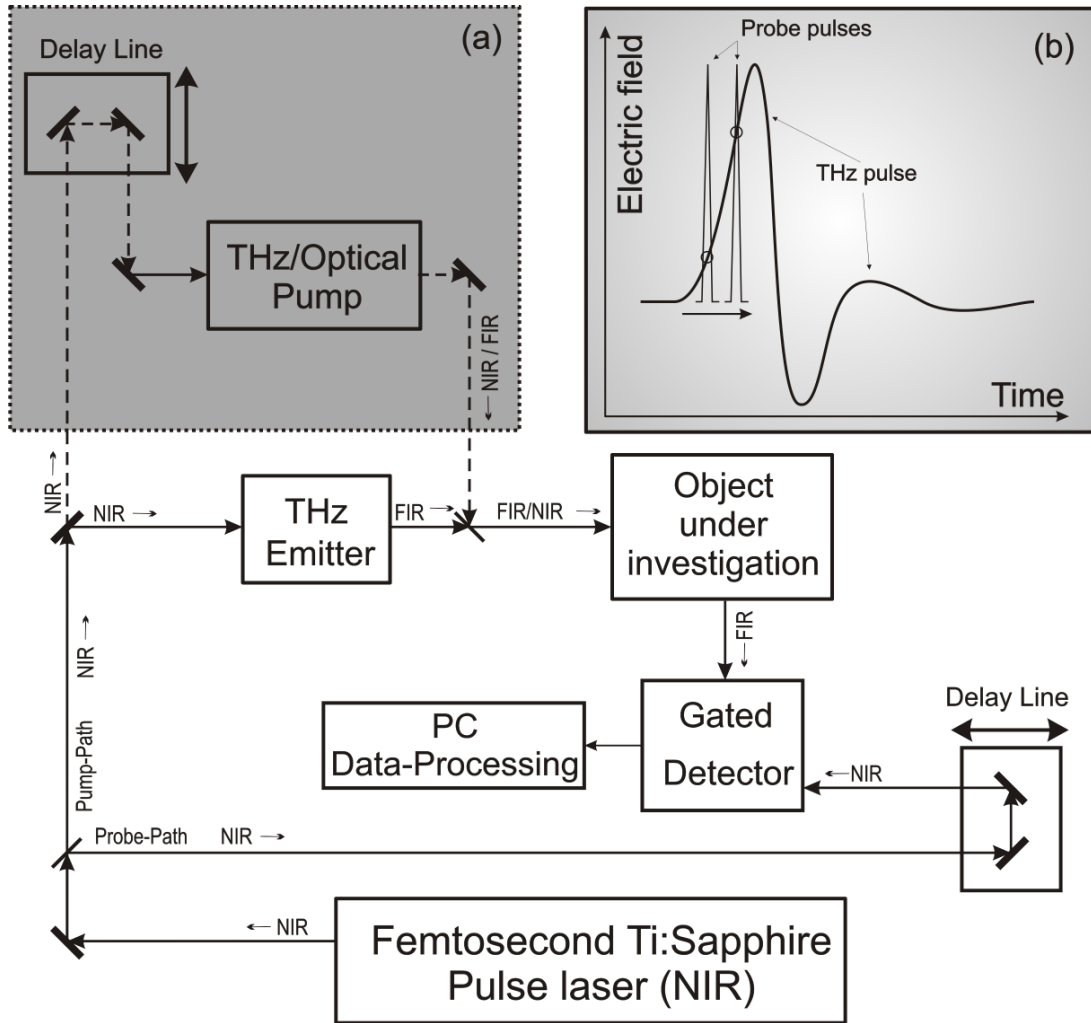


Figure 3.1.: Scheme of a THz-TDS setup. (a) optional THz/optical pump part, (b) time-domain sampling scheme.

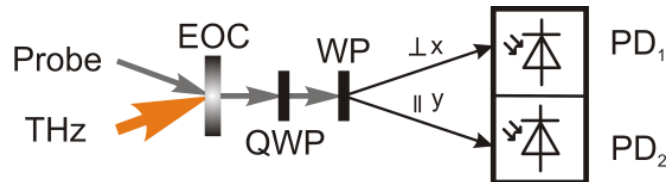


Figure 3.2.: Standard electro-optic detection scheme (EOC=electro-optic crystal, QWP=quarterwave plate, WP=Wollaston prism, PD=photodiode).

### 3. Advanced terahertz time-domain spectroscopy setup

change in polarization which is linear. Since in this work the probe beam was linearly polarized this is assumed for the rest of the text. After the EOC the probe beam passes a QWP<sup>2</sup> set to 45° to the NIR beam plane of polarization. This causes that the polarization changes from linear to circular. Finally it propagates through a WP<sup>3</sup>. Here the horizontal and vertical polarized light is split apart. The intensity of those beams is measured by photodiodes and compared by an electronic circuit or measurement device. In the case with no present THz electric field at the EOC while the probe pulse propagates through it the horizontal and vertical polarized beam intensities are equal and so the difference, which corresponds to the THz electric field, is zero.

This situation changes if the probe pulse passes the EOC with present THz electric field which induces a birefringency of the EOC. As a consequence the polarization of the probe beam changes from linear to elliptical. This causes, after passing the QWP and WP, that the horizontal and vertical polarized beam intensities are not equal and the difference is directly proportional to the present THz electric field amplitude.

Starting from a system shown in Fig. 2.19 the resulting signal can be expressed by using the Jones matrices formalism [53] and Eq. 2.37. The initial point is a completely horizontal polarized probe beam ( $\alpha = 90^\circ$ ). The electric field vector  $\mathbf{E}_{QWP}$  after passing the (110)-oriented EOC with the main axis  $\Theta = 45^\circ$  with respect to the other beam and the QWP can be described by

$$\mathbf{E}_{QWP} = \frac{E_{Probe}}{\sqrt{2}} \begin{bmatrix} 2 \cdot e^{-i \cdot n_0} (\cos \Delta n + \sin \Delta n) \\ 2i \cdot e^{-i \cdot n_0} (\cos \Delta n - \sin \Delta n) \end{bmatrix}, \quad (3.1)$$

with

$$\Delta n = \frac{n_0^3}{2} \cdot E_{THz} \cdot r_{41}, \quad (3.2)$$

where  $E_{Probe}$  is the electric field strength of the linear polarized probe beam,  $n_0$  is the unaffected refractive index and  $\Delta n$  is the refractive index change in the EOC caused by the presence of the THz electric field. The difference of the horizontal and vertical part of the electric field leads to the amplitude of the sensed THz electric field which is

$$\Delta E_{x,y} = 2 \cdot E_{Probe} \cdot \sin \Delta n. \quad (3.3)$$

Since the change of the field intensity is of the order  $\frac{\Delta I}{I} \approx 10^{-4}$  the final signal can be simplified and calculated by [91]

$$S(E_{THz}) \propto I_{Probe} \cdot \frac{\omega \cdot n_0^3 \cdot r_{41} \cdot L}{c}, \quad (3.4)$$

where  $\omega$  is the angular frequency of the optical NIR probe beam,  $L$  is the thickness of the crystal,  $I_{Probe}$  is the probe beam power and  $c$  is the speed of light.

---

<sup>2</sup>quarterwave plate

<sup>3</sup>Wollaston prism



### 3.2. Performance parameters of time resolved experiments

The result of every THz-TDS scan is a signal trace of the THz electric field transient from which already some basic specifications can be read. Since in reality no continuous scan can be performed and the scanning time window is not infinite certain limitations arise. According to the Fourier and sampling theorem the time delay between two neighboring points  $t_{p-p}$  determines directly the achieved bandwidth of the spectrum

$$B = \frac{1}{2 \cdot t_{p-p}}. \quad (3.5)$$

For instance a typical scanning distance between two points of  $50 \text{ fs}$  results in a bandwidth of  $10 \text{ THz}$ . Much more important is the achieved spectral resolution which is directly related to the width of the scanning time window  $T_{window}$  and so the scanning distance and the amount of data points. The spectral resolution  $\Delta\nu$  can be calculated by

$$\Delta\nu = \frac{1}{T_{window}}. \quad (3.6)$$

For a time window of  $50 \text{ ps}$  this would yield a resolution of  $20 \text{ GHz}$ . In general the resolution is only limited by the accessible time window but by elongating it usually more and more reflections from the optical system are sensed in this way. This results in a reduced data quality due to signal modulation (see chapter 4).

### 3.3. Data processing

As already mentioned, the result of every THz-TDS scan is the variation of the THz electric field in time. But a single signal trace with installed sample does not include any needful data to determine the optical properties due to a missing reference it can be compared to. Only if two scans are compared reasonable data processing is possible. In the simplest case this is a free space reference and the sample scan. From this data sets the frequency depending optical parameters like absorption coefficient and index of refraction can be extracted.

However, since the electric field is directly measured, the starting equation for the data processing is

$$\mathbf{E}_{Sample}(f) = \mathbf{E}_{Ref}(f) \cdot \mathbf{T}(f) \cdot e^{i \cdot k_0 \cdot \mathbf{n}(f) \cdot d}, \quad (3.7)$$

where  $k_0$  is the wave vector,  $\mathbf{n}$  is the complex refractive index,  $d$  is the sample thickness and  $\mathbf{T}$  is the Fresnel function to include the reflection losses at the sample/air interfaces given by

$$\mathbf{T}(f) = \frac{4 \cdot \mathbf{n}(f)}{(\mathbf{n}(f) + 1)^2}. \quad (3.8)$$

In these formulas the absorption is included in the complex refractive index given by the

### 3. Advanced terahertz time-domain spectroscopy setup

expression

$$\mathbf{n}(f) = n(f) + i \cdot \kappa(f), \quad (3.9)$$

where  $n$  is the real refractive index and  $\kappa$  is the imaginary part corresponding to the absorption in the material from which the absorption coefficient

$$\alpha(f) = \kappa(f) \cdot k_0, \quad (3.10)$$

can be determined. In terms of power absorption or intensity the absorption coefficient from Eq. 3.10 has to be doubled ( $I \propto E^2$ ). For the calculation of the optical properties of a given material the Eq. 3.7 has to be rewritten in

$$|\mathbf{E}_{Sample}(f)| \cdot e^{i \cdot \varphi_{Sample}} = |\mathbf{E}_{Ref}(f)| \cdot e^{i \cdot \varphi_{Ref}} \cdot |\mathbf{T}| \cdot e^{i \cdot \varphi_T} \cdot e^{i \cdot k_0 \cdot n \cdot d} \cdot e^{-i \cdot \alpha(f) \cdot d} \quad (3.11)$$

and split in amplitude

$$\frac{|\mathbf{E}_{Sample}(f)|}{|\mathbf{E}_{Ref}(f)|} = |\mathbf{T}| \cdot e^{-i \cdot \alpha(f) \cdot d}, \quad (3.12)$$

and phase information

$$e^{i \cdot (\varphi_{Sample} - \varphi_{Ref})} = e^{i \cdot \varphi_T} \cdot e^{i \cdot k_0 \cdot n(f) \cdot d}. \quad (3.13)$$

From these two equations the absorption coefficient

$$\alpha(f) = -\frac{\log\left(\frac{|\mathbf{E}_{Sample}(f)|}{|\mathbf{E}_{Ref}(f)| \cdot |\mathbf{T}|}\right)}{d} \quad (3.14)$$

and the refractive index

$$n(f) = \frac{(\varphi_{Sample} - \varphi_{Ref} - \varphi_T)}{k_0 \cdot d} \quad (3.15)$$

can be calculated. Due to the fact that in the implicit formula Eq. 3.7 two unknowns with complex values are included no direct calculation of them is possible.

One of the main problems thereby is finding proper initial values. Further, in many experiments the sample thickness is one of the additional unknowns so that three unknowns exist. This causes significant problems during the iterative process to approximate these parameters. One possibility to obtain the value of the sample thickness and the average refractive index value is to measure a large time window which includes the transmission and one or more internal reflections. In Fig. 3.3 such scan is shown for a GaP sample. From the delays of the pulses in respect to the reference point at  $0ps$  three time values  $t_1$ ,  $t_2$  and  $t_3$  can be extracted whereby  $t_2 = t_3$ . In this particular case  $t_1 = 2.5ps$  and  $t_2 = 7.01ps$ . With the help of the standard formulas (*distance = velocity · time*)

$$t_1 = \frac{d \cdot (n - 1)}{c}, \quad t_2 = \frac{2 \cdot d \cdot n}{c} \quad (3.16)$$

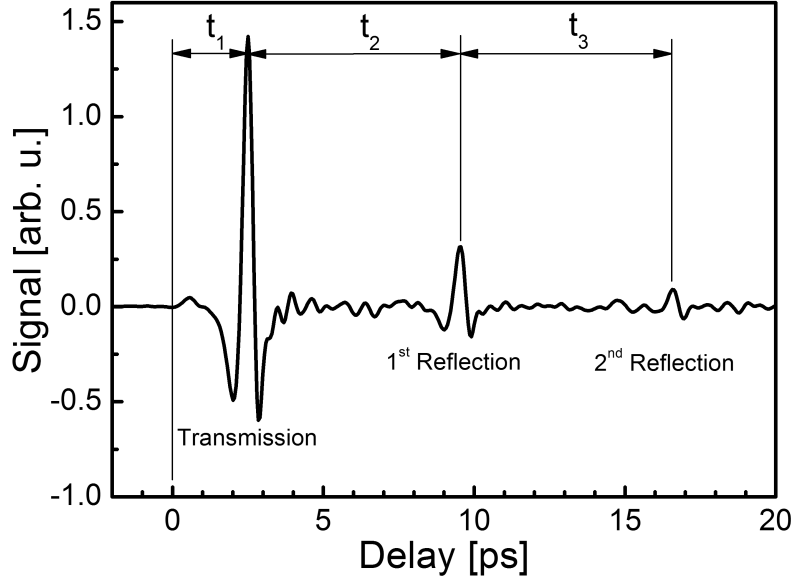


Figure 3.3.: THz-TDS signal trace of a 300  $\mu\text{m}$  thick GaP crystal including internal reflections.

the average refractive index  $n$  and sample thickness  $d$  can be calculated by

$$n = \frac{t_2}{t_2 - t_1}, \quad d = c \cdot \frac{t_2 - 2 \cdot t_1}{2} \quad (3.17)$$

In the case of the illustrated example this gives  $n = 3.49$  and  $d = 302 \mu\text{m}$  which are the correct values and sufficient enough for starting the iterative process.

### 3.4. Development of a high performance THz-TDS setup

One of the key objectives during this work was the subsequent improvement of the setup. At the beginning in the year 2003 the performance was limited and not suited for the tasks in the near future. The implemented improvements were manifold and located mainly in optics and electronics. The difficulty was to find the optimal trade-off so that the combination of all changes positively contribute to the overall performance parameters. The following sections show the starting point of the setup development in the year 2003. Followed by the improvements with all the pros and cons leading to the state-of-the-art THz-TDS setup used in the version of the year 2006 at the end.

#### 3.4.1. Initial THz-TDS setup (year 2003)

In Fig. 3.5 the THz-TDS setup in the year 2003 is shown. It represents the starting point of this PhD thesis. As all setup versions used during this work it was equipped with an dipole emitter antenna and an electro-optic sampling technique. Apart from the expenses

### 3. Advanced terahertz time-domain spectroscopy setup

making or obtaining such emitters and sensors this combination is very popular. It offers high output power  $1\text{ nW} - 1\text{ }\mu\text{W}$  with large bandwidth. In addition the detection scheme of electro-optic sampling is strongly polarization sensitive which offers the possibility to measure the orientation depending absorption (see chapter 5).

Since the improvements, described in the next sections include the main components with their pros and cons only the basic overview will be given here:

- Laser source: M1 from Femtolasers ( $<10\text{ fs}$ ,  $800\text{ mW}$ , see appendix A for details)
- Dipole antenna emitter: Gold stripes in  $300\text{ }\mu\text{m}$  distance on LT-GaAs with attached silicon lens
- THz signal modulation: Electrical modulation of the dipole emitter ( $0\text{--}100\text{ V}$ ,  $15\text{ kHz}$ , rectangular)
- Zig-Zag THz beam guiding
- NIR probe beam focusing: Spherical mirrors
- Beam combiner: ITO<sup>4</sup> coated glass plate
- Electro-optic detection:  $1\text{ mm}$  ZnTe
- Balanced photodetector circuit
- System performance:
  - Signal-to-noise ratio:  $\approx 1000$
  - Bandwidth:  $\approx 3\text{ THz}$
  - Spectral resolution:  $> 40\text{ GHz}$

For completeness in Fig. 3.5 the time-domain signal and spectrum of the setup is shown. Especially the limited resolution anticipated the measurement of narrow absorption lines like illustrated in chapter 5. In the extreme case two narrow lines are erroneously identified as single line. Further, many interesting absorption features of a lot of materials are located beyond  $3\text{ THz}$ . As in Fig. 3.5b is shown, already for frequencies above  $2\text{ THz}$  the achieved SNR is close to drop below  $20\text{ dB}$ . This limits the evaluated values of the calculated absorption coefficient because the position of the noise floor sets the limit. This means that the relation  $\alpha_{\text{real}} \geq \alpha_{\text{measured}}$  has to be taken into account (see Eq. 3.10).

These limitations show that there was an urgent need for improvements to fulfill the tasks in the future.

---

<sup>4</sup>indium tin oxide

### 3.4. Development of a high performance THz-TDS setup

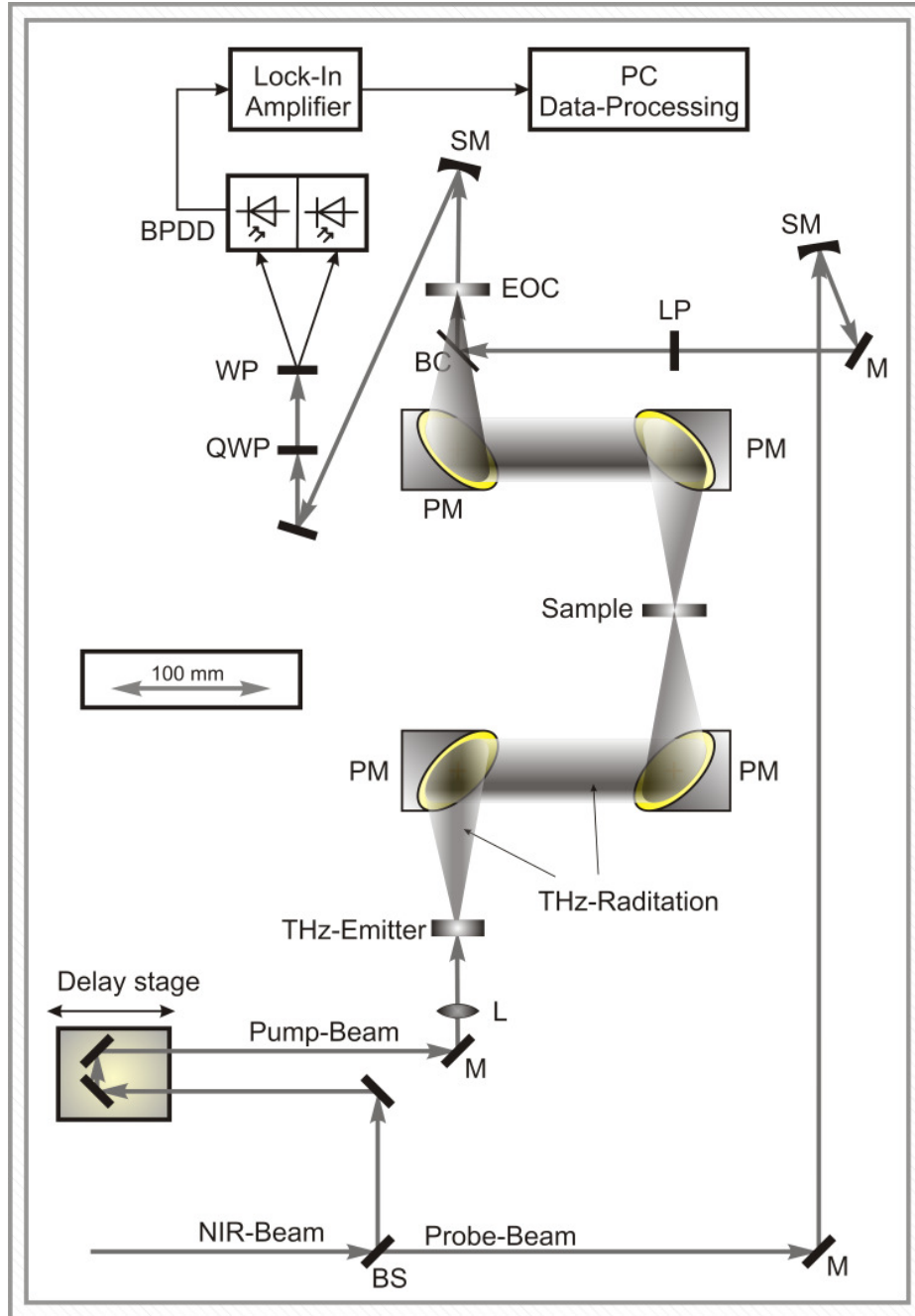


Figure 3.4.: Development level of the THz-TDS setup in the year 2003 (BS=beam splitter, BC=beam combiner, M=mirror, PM=parabolic mirror, SM=spherical mirror, L=lens, LP=linear polarizer, QWP=quarter wave plate, WP=Wollaston prism, BPDD=balanced photodiode detector).

### 3. Advanced terahertz time-domain spectroscopy setup

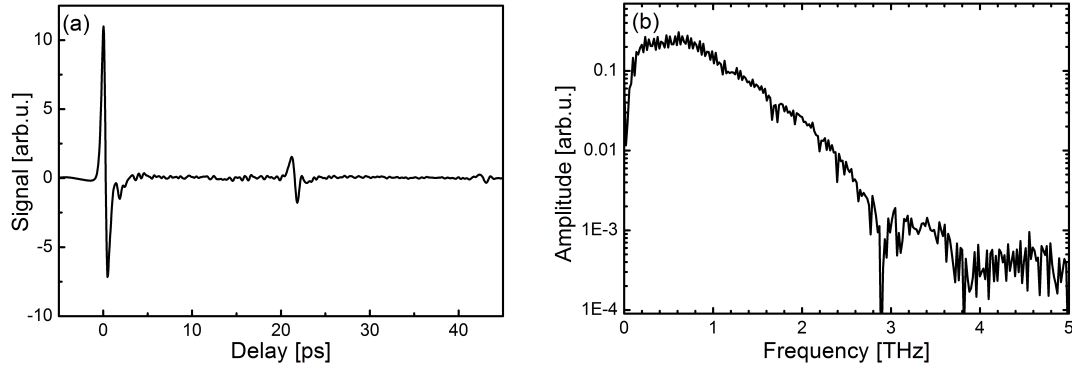


Figure 3.5.: (a) Time-domain signal and (b) spectrum of the THz-TDS setup in the year 2003.

#### 3.4.2. Improvements

The setup used in the year 2003 experienced several improvements. Many of them cannot be expressed in numbers because they contribute to more than one parameter of the optical system at once. Further, their combined performance can only be described by a sophisticated convolution which is in detail unknown. So mainly their working principle are described including their major gain.

##### Pulse laser source

At the beginning a M1 Ti:sapphire pulse laser with 800 mW power from Femtolasers was used. Instead of it a Tsunami pulse laser from Spectra-physics with 2000 mW was used. This resulted in a more than doubled laser power without any disadvantages. Since the the beam power of the pump and probe beam were doubled a more than quadrupled signal could be measured. A summary of the pulse laser specification is given in appendix A.

##### Emitter unit

The emitter unit was one of bottle necks in terms of lifetime. The first version consisted of gold stripes evaporated on LT-GaAs in a distance of 300  $\mu\text{m}$ . With an applied bias of 100 V this yielded an electric field of 3.3 kV/cm which was far below the typical electrical breakdown field in GaAs of about 10 kV/cm [75]. But even at this conditions the combined electrical and optical dissipation power was high enough to melt partly the gold layer on to top of the substrate. By driving the antenna more and more gold droplets moved within the applied electric field leading to a shortcut and the destruction of it. Another problem was the substrate material. LT-GaAs provides a very good electrical threshold limit and a short carrier life time resulting in short THz transients but due to the internal structure with the arsenic traps the emission is weak.

The first change was to increase the applied electric field. This was achieved by reducing the stripe line distance to 200  $\mu\text{m}$  and an increase of the applied voltage to >200 V. The

### 3.4. Development of a high performance THz-TDS setup

final electric field reached  $>10\text{ kV/cm}$ . This resulted in a linear increase of the emitted field. The previous short cut problems caused by the high dissipation power and the properties of gold were solved by the usage of chromium. Its advantages are its very good adhesion properties, the high melting temperature and its hardness.

Further, the experiments showed that any change of the capacitance of the structure had no influence on the emission. This means wider stripe lines, additional capacitive structures as energy storages or even another used metal did not change the emission or the maximum modulation frequency. This indicated that only the locally stored energy in the semiconductor material is or can be used for the emission process. So only broad metal stripes were deposited on the semiconductor material. This resulted in a simple design of very robust THz emitters with long operation lifetime.

The previous THz emitter unit was in addition equipped with a hemispherical silicon lens. Its task was to collect the emitted THz radiation from the emission point and to guide it to the next mirror without suffering from losses caused by total internal reflection. The big problem was the shape of this focusing component. Due to spherical aberration the emitted THz beam showed variances in the divergence depending on the hit position of the lens. As a consequence such beam cannot be guided in free space collinearly or optimally focused. As a solution the lens was simply removed. Without having such problematic focusing element an optimal Gaussian beam shape could be kept which led to an improved spectral quality of the signal. The drawback was a signal decrease of 50 % caused by total internal reflection in the substrate material which was compensated by other improvements explained later.

#### Beam guiding

Usually the optical design of commercially available measurement systems like FT-IR spectrometers is optimized in terms of beam size and its profile conservation. In this case the system's operator does not need to take care about those performance parameters. The situation changes if the system is home made and allows many degrees of freedom in the design of the optical system. This includes the very important topic of Gaussian beam shape conservation.

In THz optics mostly parabolic mirrors (PM) are used for focusing and guiding THz beams. If a PM is illuminated by a point like light source the radiation is collected and reflected as a collinear beam. Due to the special form of a PM the intensity distribution of the reflected beam is not homogeneous (Fig. 3.6). A mathematical description of this effect can be found in [98]. The beam parts reflected first, where the beam diameter is small, have a higher beam intensity than the last reflected parts. In the case that the next focusing PM is arranged in a zig-zag path (Fig. 3.6a) this distortion is impaired. This was the case in the original setup from 2003. In the focal point of the sample and EOC the Gaussian beam shape is deformed. Especially this causes problems if the beam has to be coupled to e.g. into a waveguide or into a structure with dimensions comparable to the

### 3. Advanced terahertz time-domain spectroscopy setup

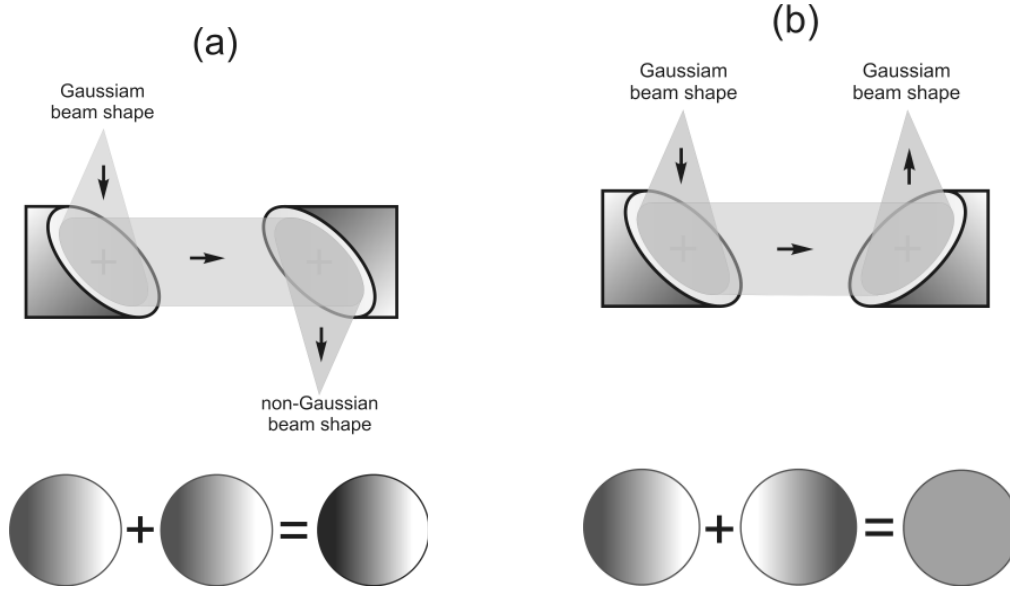


Figure 3.6.: (a) Wrong and (b) optimal beam guiding (top: scheme with parabolic mirrors, bottom= resulting beam intensity distribution - from [98]).

beam size. Then the spatial beam part with the highest intensity is not located in the middle of the object it was aimed on. Apart from spectral shaping effects this leads to a reduced signal.

A solution to this problem is either the usage of elliptical mirrors as explained in [98] or the beam guiding method illustrated in Fig. 3.6b. With Elliptical mirrors a beam is collected from a source of focal point and then focused immediately to the next point. This is the method of choice if a beam does not need to be guided collinearly over a long distance to prevent divergence effects. But if this is the case the other method has to be used. By reflecting the collinear beam with a PM with an inversed beam shape distribution function the original beam intensity distribution is recovered. This can be achieved by keeping a constant reflection angle. In general this means either a clockwise or counter clockwise beam guiding.

Beam guiding in THz-TDS setups includes the THz and probe beam combination as well. In the previous setup this was done by a ITO coated glass plate [99]. Such method offers a combination efficiency of the NIR and THz beam  $\sim 90\%$ . Compared to other beam splitters this value is already improved by a factor of more than 2. But ITO has some serious problems. Exposed to air the ITO layer degenerates very fast leading to a gradually decrease in the efficiency. The solution for this optical component was drilling a hole in the last focusing PM. The THz beam is still reflected as usual from the metal surface of it while the NIR probe is guided through a small hole in it and overlaps with the THz beam. By doing this a efficiency of more than 98% was achieved. An overview of the various beam splitters and their optical properties can be taken from Tab. 3.1.

Since the the overlap factor of the THz beam with the NIR beam at the electro-optic



### 3.4. Development of a high performance THz-TDS setup

Method / Material	THz ( $\lambda = 300 \mu\text{m}$ ) [%]	NIR ( $\lambda = 800 \text{ nm}$ ) [%]	Efficiency [%]
Silicon	65 (T)	20 (R)	13
Pellicle-BC	70 (T)	30 (R)	21
Glass	50 (R)	95 (T)	42.5
ITO coated glass	95 (R)	95 (T)	90.3
Mirror with hole	$\sim 99$ (R)	100 (T)	$\sim 99$

Table 3.1.: Efficiency of beam combiners (T = transparency, R = reflectivity).

detector plays a major role they have to be focused as good as possible. Especially this applies for the THz beam which can not be focused as good as the NIR beam due to the long wavelength. At the beginning the focal lengths in the optical system of the THz beam were equal. In the ideal case the  $300 \mu\text{m}$  diameter emission spot was directly imaged at the electro-optic crystal. For improving the optical information transfer from the THz beam to the NIR probe beam the THz beam focus has to be reduced. As already mentioned the antenna stripe line distance was reduced to  $200 \mu\text{m}$  and so the focus as well. Further by removing the lens of the emitter the outgoing beam was enlarged so that the full area of the first PM was illuminated with a FWHM of  $\sim 2 \text{ cm}$ . In Gaussian beam optics the best achievable beam waist  $\omega_0$  in a focus can be determined by

$$\omega_0 \geq \frac{2 \cdot \lambda \cdot f}{\pi \cdot D}, \quad (3.18)$$

where  $\lambda$  is the wavelength of the beam component,  $f$  is the focal distance and  $D$  is the diameter of the illuminated area of the PM. To improve the overlap of the beams the focal length of the last PM was halved. This resulted in a smaller beam waist and a doubled signal.

Another important topic in THz-TDS setups is the focusing method of the probe beam. Since for a long time was believed that standard lenses would introduce a dispersion to the probe pulse leading to an increased pulse width only spherical mirrors were used like in the setup of 2003. This method is the ideal way but has a major disadvantage. Since such mirrors are hit under an angle close to  $0^\circ$  any movement shifts the beam. This makes it impossible to adjust the focus at the EOC. Normally this is no problem but if a sample is placed in the THz beam the optical length is changed and so is the focus at the EOC. In the setup of 2006 this was solved by using lenses with negligible dispersion. By using NIR laser pulses with a length of  $\sim 100 \text{ fs}$  no dispersion is observed which elongated significantly the pulse. The big advantage of this method is that the NIR probe beam focus at the EOC can be fine adjusted and optimized.

## Detectors

The standard electro-optic sensor used in THz photonics for low frequencies is ZnTe. With  $1 \text{ mm}$  thickness as used in the setup from 2003 it offers a bandwidth up to  $2.5 \text{ THz}$ . This crystal was replaced by a  $300 \mu\text{m}$  thick GaP crystal with a bandwidth of  $7 \text{ THz}$ . Due

### 3. Advanced terahertz time-domain spectroscopy setup

to its lower electro-optic coefficient the sensitivity is reduced by a factor of 4 (see subsection 2.5.2) which is mostly compensated by the improvements described above.

A higher bandwidth means a thinner crystal too and this results in earlier appearing reflections which distort the spectrum and limit the spectral resolution. In 2003 the problem was not solved yet. Instead of a physical solution an computer assisted method was applied. Thereby the signal trace including all reflections was scaled shifted and subtracted from the original data. This was performed for all reflections. Two problems occurred:

First, the time scale resolution had to be increased either in reality or artificially by mathematical methods. Second, by propagating through a medium with frequency depending properties a transfer function had to be fitted which corresponded to the changes caused by the round-trip. However, this was a temporary solution. The final solution for this problem was the in-house development of a broadband metallic anti-reflection coating based on chromium. Without suffering from the reflections the scanning window can be extended and adjusted to the needed resolution. Since the chapter 4 is dedicated to the properties of ultra-thin metallic films the working principle is explained in detail there.

For many experiments it is convenient to have an incoherent detector available. So the EOC can be replaced by a bolometer or a Golay cell detector without changing the position of the sample or any other optical component. Especially this is of great help if the sample position influences the optical distance which the THz wave has to propagate. In this case the system can be optimized without suffering from time shifts of the THz signal transient. Further, if an active or nonlinear device is under investigation the power detection scheme can be used for measuring the output power as function of the driving current without removing the object.

### Electronics

As in every setup the used electronic plays a major role. In THz-TDS the signals are such weak that they have to be modulated to extract them at the end from the background. This can be done optically by chopping the beam or by modulation of the emission process. Latter was the choice for both setups. In this case the voltage drop at the dipole emitter is modulated with a given frequency. Formally this was done by a circuit shown in Fig. 3.7a. With this simple scheme a voltage of 100 V was switched on and off. This led to a rectangular voltage modulation at the emitter. This caused large current transients which limited the emitter's lifetime. Higher voltages were not possible due to electrical breakdowns.

The improved electric driving circuit for the emitter is shown in Fig. 3.7b. As OPAs<sup>5</sup> two PA83 from Apex were used (-120 to +120 V). The first OPA amplifies the input voltage. The output is fed to the first contact of the emitter while the other OPA is connected to the second emitter contact but with inverted phase. With a single OPA stage output voltages of only -120 to +120 V are possible but by taking the voltage drop between this

---

<sup>5</sup>operational amplifier

### 3.4. Development of a high performance THz-TDS setup

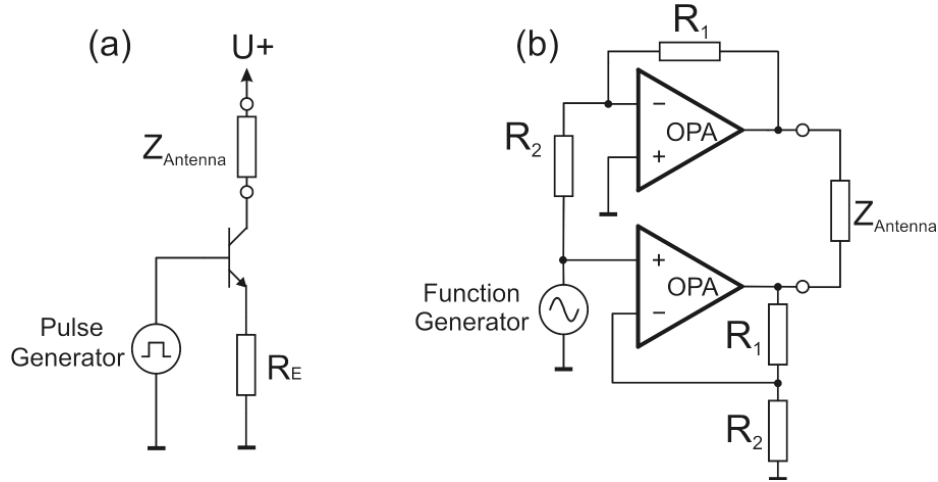


Figure 3.7.: Circuit for electrical modulation of the dipole emitter antenna in (a) 2003 and (b) 2006 (OPA=operational amplifier).

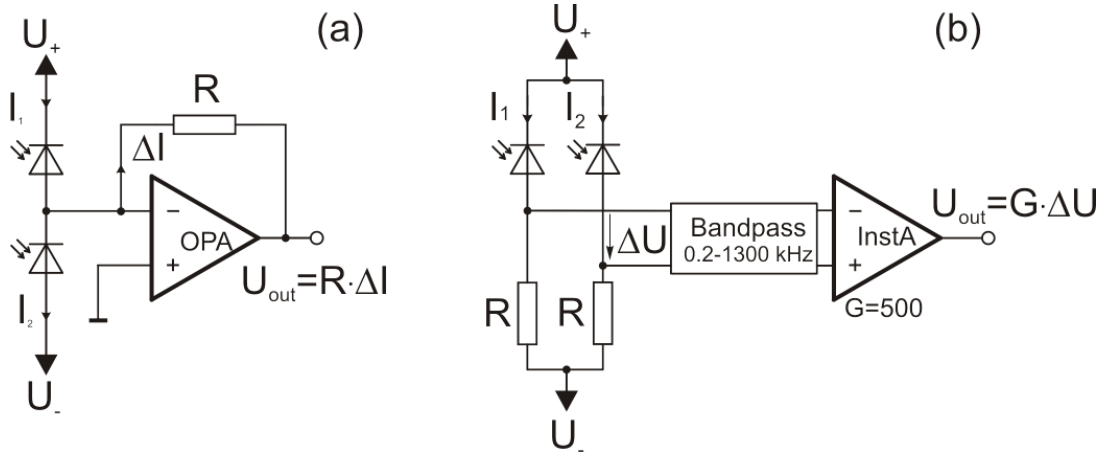


Figure 3.8.: Detector circuit from (a) 2003 and (b) 2006 (OPA=operational amplifier, InstA=instrument amplifier).

potential and the phase inverted potential the maximum voltage drop at the emitter is doubled (-240 to +240 V). The big advantage of this method is that the signal can be doubled without exceeding the electrical breakdown limit of the emitter. As with the old driving circuit modulation frequencies up to 30 kHz are obtained.

The information about the amplitude of the THz electric field is transferred to the NIR probe beam in the EOC by changing its polarization. This change is sensed by two photodiodes measuring the x- and y-component of the beam intensities. The difference of the diode signals is directly proportional to the THz electric field. Since the relative signal difference is about  $10^{-3} - 10^{-8}$ , a high precision detector circuit with integrated amplifier is needed (Fig. 3.8) to detect the difference currents of  $10 \text{ nA} - 1 \mu\text{A}$ . In the original form the signal was measured by a transimpedance converter. The difference current from the photodiodes was fed to an inverting OPA circuit. The measured THz electric field

### 3. Advanced terahertz time-domain spectroscopy setup

amplitude can be calculated with the measured signal level  $U_{out}$  by

$$E_{THz} = \frac{U_{out}}{R \cdot S \cdot P} \cdot \frac{\lambda_{NIR}}{2 \cdot \pi \cdot n^3 \cdot r_{41} \cdot l}, \quad (3.19)$$

where  $R$  is the resistor value,  $S$  is the sensitivity of the photodiodes,  $P$  is the photodiodes incident NIR probe laser power,  $\lambda_{NIR}$  is the probe laser light center wavelength and,  $n$ ,  $r_{41}$  and  $l$  are the EOC's refractive index, electro-optic coefficient and length, respectively. Especially, with this detector very low currents were distorted by electrical noise in the system. If very low currents, corresponding to the THz signal, are measured their value comes close to the input noise currents of the OPA.

Another major problem was the balancing of the detector. Apart from the real signal a much larger DC component emerged caused by laser fluctuations which saturated the amplifier. This limited the amplification factor and so the SNR. In the year 2003 a standard scan with 60 dB SNR took more than 30 minutes time. Further, the dynamic reserve was about 20 dB. This means if the signal amplitude dropped by more than 20 dB by absorption, e.g. in a sample, the SNR did it too.

In Fig. 3.8b the new detector design is shown. Main difference is the direct conversion of the incident laser power to a voltage drop. The voltage drop is then fed to a bandpass filter. Here most of the laser pulse fluctuations are filtered out so that mainly the real THz signal is fed to the instrument amplifier. The formula for the calculation of the THz electric field is similar to Eq. 3.19. Just the internal amplification  $G$  of the instrumental amplifier has to be added (Eq. 3.20) which is the major gain of this new circuitry.

$$E_{THz} = \frac{U_{out}}{R \cdot G \cdot S \cdot P} \cdot \frac{\lambda_{NIR}}{2 \cdot \pi \cdot n^3 \cdot r_{41} \cdot l} \quad (3.20)$$

A standard scan with this detector takes only 5 min any more with a SNR of 60 dB. Further, the dynamic reserve increased to >40 dB. This makes it possible to measure even highly absorbing objects.

#### Summary of improvements

In Tab. 3.2 the sum of all improvements is summarized including their pros and cons. One can immediately see that most of the changes have only pros so that the overall performance of the final THz-TDS setup significantly increased.

Not all setup improvements can be directly determined in hard numbers. Alone they contribute mostly linear to the overall performance but this relation does not apply if several effects are combined. If only the basic parameters are taken into account and summarized as follows

- Signal level: comparable
- Signal-to-noise-ratio: comparable

### 3.4. Development of a high performance THz-TDS setup

Topic	Year 2003	Year 2006	Pros	Cons
Laser source	M1	Tsunami	signal +	/
Emitter structure	300 $\mu\text{m}$ Au	200 $\mu\text{m}$ Cr	signal +	/
Emitter material	LT-GaAs	SI-GaAs	signal +	/
Emitter coupling	Silicon lens	plane GaAs	no distortion	signal -
THz guiding	zig/zag	round-trip	uniform beam	/
Beam combiner	ITO coated glass	mirror with hole	signal +	/
EOC	ZnTe, 1 mm	GaP, 300 $\mu\text{m}$	bandwidth +	signal -
Reflections	computer method	coating	resolution +	/
THz imaging	1:1	2:1	signal +	/
NIR focusing	spherical mirrors	lens	signal +	/
Emitter mod.	unipolar rect.	double sinus	signal +	/
Detector	noisy, no filter	low noise, filter	dynamic, reserve +	/

Table 3.2.: Summary of the THz-TDS setup improvements implemented.

- Decreased sensitivity of EOC by a factor of 12 (thinner crystal with lower eo-coefficient)
- Bandwidth increase of EOC:  $2.5 \rightarrow 7$  THz
- Scanning time:  $>6$  times faster

this results in a fundamental performance increase factor of 144 which is outstanding. Especially since the spectral resolution is not any more limited by the optical system the data quality increased significantly. Only the sample's properties limit this parameter.

#### 3.4.3. Final high performance THz-TDS system (year 2006)

In Fig. 3.9 the state-of-the-art THz-TDS setup in 2006 is shown. It integrates all improvements listed above. To our knowledge, it is the only system worldwide with such performance parameters. The bandwidth and the achievable spectral resolution make it a perfect tool for material science in THz optics. An electric field of more than  $200 \frac{\text{V}}{\text{cm}}$  can be achieved. Such electric field is high enough for standard experiments without being interested in nonlinearities which start above  $10 \frac{\text{kV}}{\text{cm}}$ .

In Fig. 3.10 the up-to-date time-domain signal and spectrum is shown. No reflection hamper the signal quality and in the spectrum even the detector cut-off for a 300  $\mu\text{m}$  thick GaP crystal is visible. The approximated SNR is in the standard case  $>60$  dB.

Further, the new setup can be easily adapted with a waveguide THz emitter [100] which replaces the standard emitter and is installed, if used, next to the sample. This emitter is a combination of the standard THz photo conductive emitter and a metallic waveguide (Fig. 3.11). As usual, the THz pulse is generated in a NIR pulse laser illuminated GaAs substrate between two biased metal contacts. Like shown in the illustration the wave is confined in one dimension between the metal contact surfaces. In the standard configuration the generated wave would divergence in one dimension forming a more or

### 3. Advanced terahertz time-domain spectroscopy setup

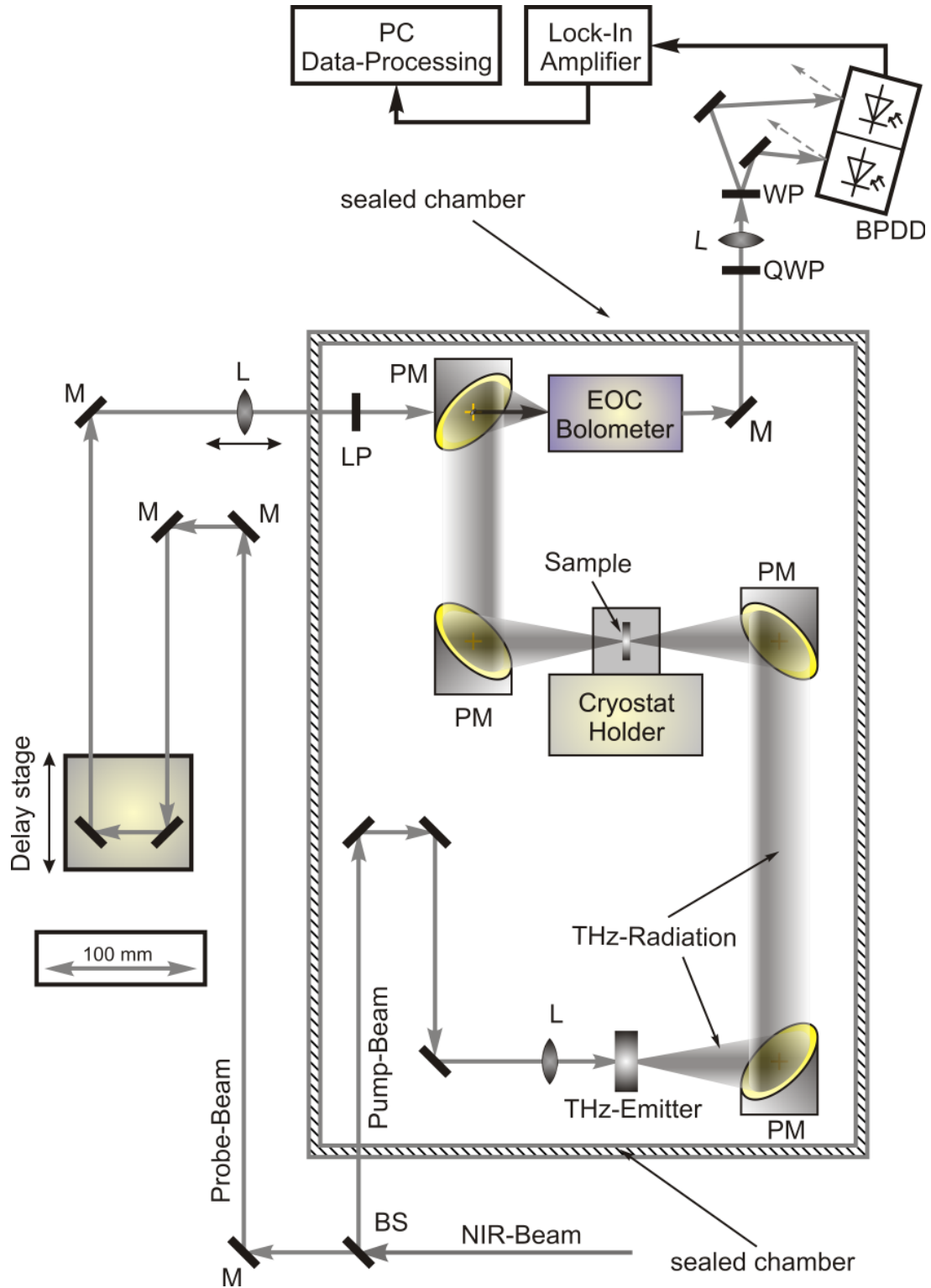


Figure 3.9.: Development level of the THz-TDS setup in 2006 (BS=beam splitter, BC=beam combiner, M=mirror, PM=parabolic mirror, L=lens, LP=linear polarizer, QWP=quarter wave plate, WP=Wollaston prism, BPDD=balanced photodiode detector).

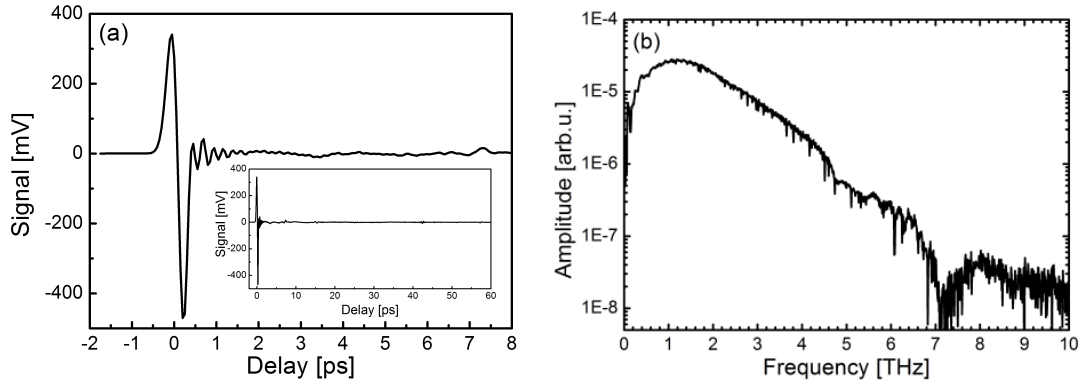


Figure 3.10.: THz-TDS signal in the year 2006. (a) Time-domain (inset:full time window) and (b) spectrum.

less cylindrical emission profile. But this can be avoided by a smart patterning of the top metal contact. If this is formed by just a broad gold stripe the generated THz wave is bound to it and travels along it.

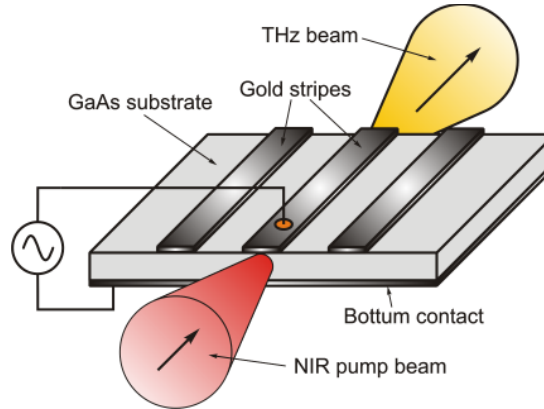


Figure 3.11.: Photoconductive THz waveguide emitter.

Apart from the similar performance the changed design shows significant advantages compared to the standard photo conductive emitters. First, there is no need anymore to separate the THz generation point from the sample object it should penetrate. As is shown in chapter 6 it can be directly attached to a similar shaped object like a semiconductor laser. Further, due to the patterned top metallization the generated THz wave is bound to the center of the metal stripes. In this way the wave can be guided directly to the place it should enter the sample object. Since at the optical emitter/sample interface less reflection losses occur compared to the standard emitter radiating into free space the coupling efficiency can be more than tripled. Which emitter design is used depends strongly on the purpose.





## 4. Metallic phase shift layers for broadband THz optical systems

### 4.1. Motivation

One of the key topics in optics is the control of electro-magnetic radiation in any aspect. This includes mainly the guiding of waves through various objects and optical interfaces. Especially latter is a big topic in optics. In general a big problem appears in an optical system with two or more interfaces between two materials with different optical properties. At such interface the material parameters change which has an impact on the wave penetrating it. According to the Fresnel formula for reflection and the boundary conditions [4] an additional wave propagating in the vice versa direction than the transmitted wave is generated. This has two major impacts. First, due to the split waves and the energy conservation axiom the power of the transmitted wave is reduced. The second impact is much worse. A back propagating wave can hit another optical interface. In this way it changes once more the direction. In the worst case it has then the same wave vector as the initial wave and propagates the same path along. At the starting interface the sequence is repeated. Since a general optical system contains several of such interfaces, multiple reflections of the original signal are produced.

Let us assume an optical system with a silicon sample and an electro-optic detector as illustrated in Fig. 4.1 to demonstrate this effect. A THz wave propagating through this system is reflected multiple times at every optical interface. The resulting THz-TDS signal is shown in Fig. 4.2. The signal trace demonstrates very well the problem in this case. A signal  $p(t)$  is followed by several replica. All of them contribute to the spectrum according to the formula

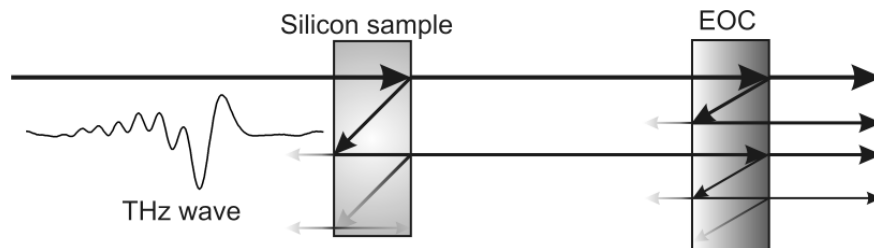


Figure 4.1.: Simplified THz optical system with silicon sample and electro-optic crystal (arrows indicate transmitted and reflected THz beams).

#### 4. Metallic phase shift layers for broadband THz optical systems

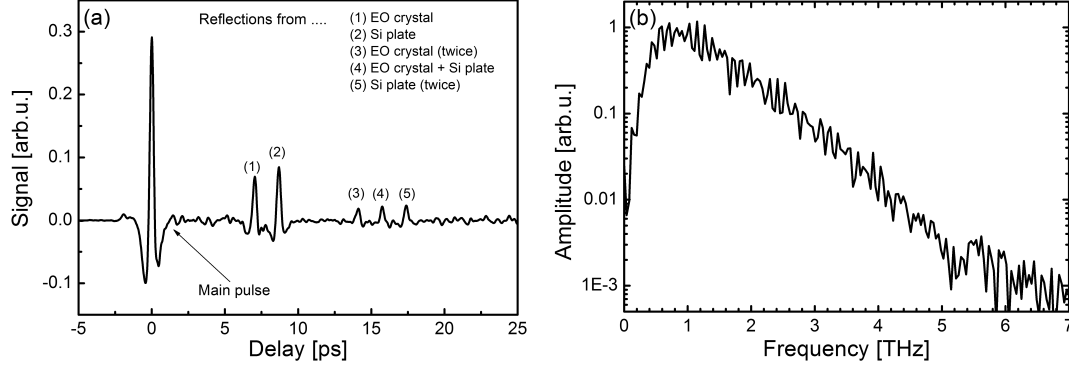


Figure 4.2.: THz-TDS signal of 400  $\mu\text{m}$  thick silicon substrate measured with a 300  $\mu\text{m}$  GaP electro-optic sensor. (a) Time-domain and (b) spectrum.

$$p(t) + \sum_i k_i \cdot p(t - T_i) \xrightarrow{FFT} P(\omega) + \sum_i k_i \cdot P(\omega) \cdot e^{j\omega \cdot T_i}, \quad (4.1)$$

where  $k_i$  is the scaling factor of the replica and  $T_i$  is the time shift of them in respect to the main signal. They manifest themselves as modulation of the original spectrum. A problem also found in FT-IR spectroscopy.

However, there do exist several solutions for this problem but they all they have their pros and cons. Some of them solve the problem while others just deal with them. A summary of the mainly used methods is given here.

##### 4.1.1. Narrow time window

The easiest way, at least for time-domain measurements, is to shorten the time window until no reflections are visible or included. For the signal shown in Fig. 4.2 this would be from -2 to +5 ps. The main drawback of this method is the loss of spectral resolution.

##### 4.1.2. Thick substrates

Another method to deal with the problem of reflections it to artificially postpone them. In general this means to increase the substrate's thickness. Essential for this method is that the substrate shows only low losses and has exactly the same optical properties as the material which produces the reflections. Especially this causes problems if the reflection producing interface comes from the sample itself. Either the material is expensive or the connection process is complicated and time consuming. For instance this technique is used to postpone the reflections in electro-optic sensors. For not suffering from the phase velocity mismatch (see section 2.5.2) the sensor is simply glued onto an electro-optical inactive substrate.

### 4.1.3. Tilted interfaces and surfaces

As mentioned above reflections are mainly sensed if they hit an optical interface under direct incidence. The situation changes when the beam hits the interface under some angle. Depending on the refractive index difference at the interface the beam angle in respect to the interface varies on both sides. This results in a changed position of the reflected beam. In the easiest case the reflection can be simply filtered by an aperture. However, to tilt every interface in the whole optical system is not possible in many case.

### 4.1.4. Computer assisted methods

A very complicated and imprecise technique to deal with reflections are computer assisted methods [19]. Hereby a long time window is scanned including the reflections and taken as wavelet [101]. Since reflections are replica of the undistorted transmitted signal the following procedure is performed. The complete signal is scaled, shifted to the position of the reflections and subtracted. In this way reflections are completely canceled. The problem is that the reflections cannot be canceled out. The reason for this is the needed knowledge of the transfer function  $H(\omega)$  corresponding to the reflections which shall be removed. Normally this function itself is the object of interest which includes the absorption spectrum [97]. Apart from these limitations this method is good suited for qualitatively snapshots with high spectral resolution. In this case  $H(\omega)$  is simply approximated by 1 for the anti-reflection algorithm.

## 4.2. Theory of anti-reflection layers

### 4.2.1. $\lambda/4$ -layers

All methods described so far just deal with the problems of reflections and do not really solve the origin of them. The standard solution at the moment is a  $\lambda/4$ -layer. The method bases on a thin dielectric optical layer which is deposited on the reflection causing interface [53]. Their working principle is as follows. In Fig. 4.3 the general scheme of a thin layer between two different optical ambiances is shown. In the general case this a dielectric substrate material on one and air on the other side. If a beam penetrates this interface multiple reflections are produced. According to the Fresnel formulas the complex reflection and transmission coefficient is given by

$$\mathbf{r}_{ij} = \frac{\mathbf{n}_i - \mathbf{n}_j}{\mathbf{n}_i + \mathbf{n}_j}, \quad (4.2)$$

and

$$\mathbf{t}_{ij} = \frac{2 \cdot \mathbf{n}_i}{\mathbf{n}_i + \mathbf{n}_j}, \quad (4.3)$$

where  $\mathbf{n}_i$  is corresponding complex refractive index of the materials at the interface. Further, in general a wave propagating through a layer sustains losses and the phase of the

#### 4. Metallic phase shift layers for broadband THz optical systems

electric field vector is changed. This is given by the complex transfer function

$$\mathbf{T}_i = e^{-j \cdot \mathbf{k}_i \cdot d_i}, \quad (4.4)$$

where  $\mathbf{k}_i$  is the complex wavevector and  $d_i$  is the layer's thickness. With these formulas the resulting reflection coefficient

$$\begin{aligned} \mathbf{R} &= \mathbf{r}_{12} + \mathbf{t}_{12} \cdot \mathbf{t}_{21} \cdot \mathbf{T}_2^2 \cdot \mathbf{r}_{23} + \mathbf{t}_{12} \cdot \mathbf{t}_{21} \cdot \mathbf{T}_2^4 \cdot \mathbf{r}_{23}^2 \cdot \mathbf{r}_{21} + \mathbf{t}_{12} \cdot \mathbf{t}_{21} \cdot \mathbf{T}_2^6 \cdot \mathbf{r}_{23}^3 \cdot \mathbf{r}_{21}^2 + \dots \\ &= \mathbf{r}_{12} + \mathbf{t}_{12} \cdot \mathbf{t}_{21} \cdot \mathbf{T}_2^2 \cdot \mathbf{r}_{23} \cdot \sum_{i=0}^{\infty} \mathbf{T}_2^{2i} \cdot \mathbf{r}_{23}^i \cdot \mathbf{r}_{21}^i \\ &= \mathbf{r}_{12} + \frac{\mathbf{t}_{12} \cdot \mathbf{t}_{21} \cdot \mathbf{T}_2^2 \cdot \mathbf{r}_{23}}{1 - \mathbf{T}_2^2 \cdot \mathbf{r}_{23} \cdot \mathbf{r}_{21}} = \frac{\mathbf{r}_{12} + \mathbf{r}_{23} \cdot \mathbf{T}_2^2}{1 + \mathbf{T}_2^2 \cdot \mathbf{r}_{23} \cdot \mathbf{r}_{12}} \end{aligned} \quad (4.5)$$

and transmission coefficient

$$\begin{aligned} \mathbf{T} &= \mathbf{t}_{12} \cdot \mathbf{T}_2 \cdot \mathbf{t}_{23} + \mathbf{t}_{12} \cdot \mathbf{T}_2^3 \cdot \mathbf{r}_{23} \cdot \mathbf{r}_{21} \cdot \mathbf{t}_{23} + \mathbf{t}_{12} \cdot \mathbf{T}_2^5 \cdot \mathbf{r}_{23}^2 \cdot \mathbf{r}_{21}^2 \cdot \mathbf{t}_{23} + \dots \\ &= \mathbf{t}_{12} \cdot \mathbf{T}_2 \cdot \mathbf{t}_{23} \cdot \sum_{i=0}^{\infty} \mathbf{T}_2^{2i} \cdot \mathbf{r}_{23}^i \cdot \mathbf{r}_{21}^i = \frac{\mathbf{t}_{12} \cdot \mathbf{T}_2 \cdot \mathbf{t}_{23}}{1 + \mathbf{T}_2^2 \cdot \mathbf{r}_{23} \cdot \mathbf{r}_{12}} \end{aligned} \quad (4.6)$$

of such interface can be calculated by a infinite series and the approximation  $\sum_i x^i \cong \left(\frac{1}{1-x}\right)$ . From Eq. 4.5 gets clear that the reflection vanishes if the relation

$$\mathbf{r}_{12} = -\mathbf{r}_{23} \cdot \mathbf{T}_2^2 \quad (4.7)$$

is fulfilled. In case of a dielectric substrate material and layer, means no complex refractive index ( $\kappa = 0$ ), this relation can be simplified and separated in phase and amplitude (Eq. 4.8).

$$r_{12} = -r_{23}, \quad \frac{4\pi}{\lambda_0} \cdot d_2 \cdot n_2 = (2 \cdot m - 1) \cdot \pi, \quad m \in \mathbb{N} \quad (4.8)$$

From this relation it gets clear that in the simplest case a layer which fulfills the conditions

$$n_2 = \sqrt{n_1 \cdot n_3}, \quad d_2 = \frac{\lambda_0}{4 \cdot n_2} \cdot (2 \cdot m - 1), \quad m \in \mathbb{N} \quad (4.9)$$

cancels effectively reflections. The factor  $\lambda_0/4$  in the last condition is giving the name of this method. Such layers are widely used in optics. For instance, this is the standard coating method for eyeglasses but in this particular case more than one anti-reflection layer has to be used to cover the complete visible spectrum. This demonstrates one of the weak points of this method. As can be seen from the second condition the layer thickness has a strong wavelength dependence. Beside their designed wavelength the effect vanishes and reappears according to Eq. 4.8. This is the reason why they are not suited for broadband applications like THz-TDS. Furthermore, for THz frequencies a layer thickness of a few 10  $\mu\text{m}$  would be needed which is technically difficult to achieve with high uniformity.

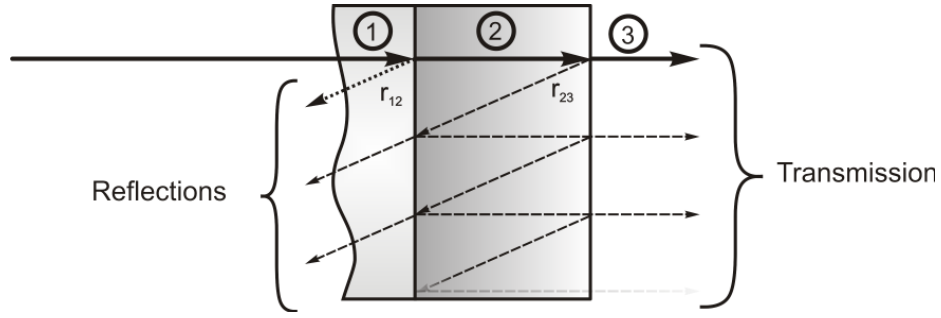


Figure 4.3.: General optical scheme of a thin layer (2) sandwiched between a substrate material (1) and air (3).

#### 4.2.2. Metallic anti-reflection coating

As mentioned above a  $\lambda/4$ -layer coating has only one degree of freedom to suppress reflections which is the thickness. The appropriate  $180^\circ$  phase change to fulfill the matching condition from Eq. 4.7 is achieved by propagating a certain distance forth and back through the layer to achieve it. Since only dielectric materials are involved a traveling wave sustains no adjustable phase change at the optical interfaces. The situation changes if one of the involved materials is highly absorbing resulting in a complex refractive index. In this case the reflection coefficient calculated by the Fresnel formula (Eq. 4.2) becomes complex too. This additional phase change can be exploited to suppress effectively reflections. Starting with Eq. 4.7 and a complex refractive index  $\mathbf{n} = n + i \cdot \kappa$  ( $\kappa \neq 0$ ) and this leads to the general matching conditions

$$|r_{12}| = |r_{23}| \cdot e^{-\frac{4 \cdot \pi}{\lambda_0} \cdot d \cdot \kappa}, \quad \phi_{r_{12}} = -\phi_{r_{23}} - \frac{4 \cdot \pi}{\lambda_0} \cdot d \cdot n. \quad (4.10)$$

As one can see, the existence of the additional phases extend the degrees of freedom. This opens theoretically the possibility of a broadband anti-reflection coating (ARC). But with these degrees of freedom the requirements for the coating material raises as well. For instance, as a major pre-condition Eq. 4.10 shall show no wavelength dependence. This can only be achieved by fulfilling the expression in terms of amplitude as well as in the phase matching condition separately. This would lead to the simplified matching conditions

$$|r_{12}| \approx |r_{23}|, \quad \phi_{r_{12}} \approx -\phi_{r_{23}}. \quad (4.11)$$

Therefore, an ideal coating material should have the following properties:

- Low absorption
- Complex refractive index for large phase shifts
- Deposition of ultra-thin layers for low absorption
- Control parameter to adjust the material's properties

#### 4. Metallic phase shift layers for broadband THz optical systems

Especially the last point is the most difficult to achieve. Many materials show a huge range of possibilities to adjust their properties. For instance, this can be temperature and pressure or in the case of liquid crystals even an applied electric field. But the changes induced in such a way are not big enough and far away from being applicable for the required needs. The solution for this problem is not a special material. It is rather the complete group of metals. Metals fulfill most of the properties stated above. Even the refractive index can be directly influenced by the layer thickness. According to the Drude model [102] the conductivity  $\sigma$  of a metal is given by

$$\sigma = \frac{e^2 \cdot \tau \cdot n}{m_e}, \quad (4.12)$$

where  $e$  is the elementary charge,  $n$  is the electron density,  $\tau$  is the collision time of the carriers and  $m_e$  is the mass of them. For a bulk metal the parameters of Eq. 4.12 are constant so is the conductivity. The only parameter which can be influenced is the collision time which can be dramatically decreased in a thin metal layer. In this way the lateral movement, in respect to the layer, can be brought down which has a direct impact on the resistivity of the layer. All values from the material's bulk resistivity up to infinite are possible [103]. Since metals show a huge complex refractive index [104] the phase jump of a reflected electromagnetic wave at a metal/dielectric optical interface can be adjusted. From Eq. 4.2 and the optical scheme from Fig 4.3 the phase jump at an optical interface is given by

$$\phi_{ij} = \arctan \left[ -\frac{2 \cdot n_j}{n_j^2 - n_i^2 - \kappa_i^2} \right], \quad (4.13)$$

where  $i$  and  $j$  are the indexes for the material the wave is coming from and entering. This phase change introduced at a thin metallic layer can be exploited as an anti-reflection coating. In addition, metals show a constant real refractive index up to their plasma frequency

$$\omega_p = \sqrt{\frac{n \cdot e^2}{\varepsilon_0 \cdot m_e}}, \quad (4.14)$$

while the complex value scales more or less linearly up to this frequency. Most metals have this critical value located in the NIR or even higher [4]. Above this frequency metals become transparent and find mainly application in x-ray optics [53]. However, in general the optical properties stay constant or scale linearly within a wide frequency range from microwaves up to near infrared light. For the proper determination of the right ARC thickness for a given material system the thickness dependent optical properties have to be measured at first. Since the determination of the thickness depending complex refractive index is a very sophisticated procedure another method for the direct approximation is used.

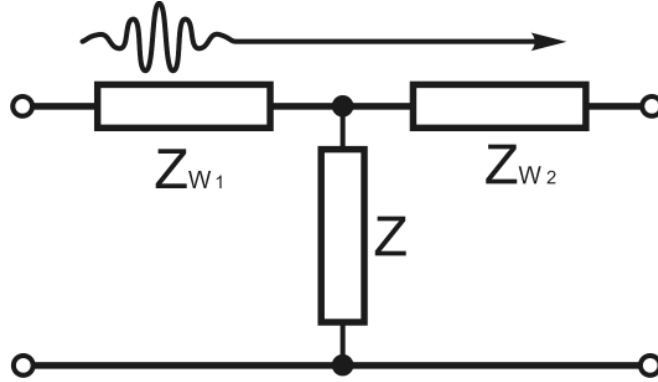


Figure 4.4.: Scheme of two waveguides connected via a parallel shunt impedance.

#### 4.2.3. Wave impedance matching approach

The above mentioned theory claims that all internal reflections within the ARC layer sums up in a way so that the primary reflection is canceled. An alternative method is to adopt a standard method applied in communication engineering. This electro-dynamic approach deals with reflections in terms of wave impedance matching conditions. The electro-dynamic pendant for the optical interface shown in Fig. 4.3 is illustrated in Fig. 4.4. Thereby two cubicles of given wave impedance are connected via a parallel shunt impedance. Compared to the other scheme and for the case of dielectrics the real part of the refractive index  $n_i$  is replaced by the wave impedance  $Z_i$  with the relation

$$Z_{W_i} = \frac{Z_0}{n_i}, \quad (4.15)$$

where  $Z_0 = \sqrt{\frac{\mu_0}{\epsilon_0}} \approx 377 \Omega$  is the wave impedance of vacuum. Like in optics with the refractive indexes, the wave impedances can be used to determine the reflection and transmission coefficients at an electrical interface [3]. However, as well known from electro-dynamics at such connection point no reflections are produced if at this point the wave impedances on both sides have the same value. In general the wave impedance of the right side material cannot be modified because in most cases this is a given material to use. But as mentioned above, the parallel shunt resistor opens the needed degree of freedom to connect two different waveguides.

As illustrated in Fig 4.4 a wave approaches from the left waveguide the electrical interface. It senses the effective wave impedance of the right waveguide with the parallel shunt impedance. The wave boundary condition for a reflectionless passover demands the same wave impedance value at both sides. The optimal value for the parallel resistor can be determined by the wave impedance matching condition

$$\frac{1}{Z_{W_1}} = \frac{1}{Z_{W_2}} + \frac{1}{Z} \longrightarrow Z = \frac{Z_{W_1} \cdot Z_{W_2}}{Z_{W_2} - Z_{W_1}}. \quad (4.16)$$

Already from this relation the limitations of this method become clearly visible. Since

#### 4. Metallic phase shift layers for broadband THz optical systems

the resistor value has to be positive the denominator of the formula has to be positive as well. This condition limits the effectiveness of this method for interfaces where the wave propagates from a medium with low wave impedance into a medium with high wave impedance. In terms of optics this means an interface where a wave enters a relatively less dense material (e.g. a semiconductor/air interface). However, the electro-dynamic scheme cannot be directly allocated to optics due to the discrete impedance. This has to be replaced by a thin metallic layer with thickness  $d$  dependent sheet resistance  $R_S$  which can be determined by

$$R_S(d) = \frac{\rho(d)}{d}, \quad (4.17)$$

where  $\rho$  is the layer's effective resistivity. With this relation and Eq. 4.16 the optimal metal layer thickness can be determined by

$$d = \rho(d) \cdot \frac{n_1 - n_3}{Z_0} \longrightarrow d = f(\text{metal}, \Delta n) \quad (4.18)$$

which is a implicit function of the used metal and the refractive index mismatch at the interface. The implicit character of the formula prevent an exact solution. Thus the exact knowledge about the function  $\rho(d)$  is essential solving Eq. 4.18. Depending on this function the right thickness can be calculated directly or in an analytic manner.

As shown above the electro-dynamic approach for rating a convenient metallic anti reflection coating (MARC) is a straightforward task. The more complicated optical approach with complex refractive index is only needed in special cases. This applies either if the used material shows frequency dependent properties or the layer has such a thickness that a wave propagating in it sustains an additional phase change according to 3.11. As long as the involved material parameters do not show such dependency the electro-dynamic approach is faster, easier to apply and so the method of choice.

### 4.3. Electrical characterization of ultra-thin chromium layers on glass

As explained in the previous section metals with their unique optical material parameters are well suited for the application as broadband phase shift layers for anti-reflection coatings. Especially in the THz frequency range they are unrivaled due to their much higher located plasma frequency. However, apart from their basic parameters due to their affiliation to the group of metals other properties are needed and preferred for application. These are mainly:

- Very good adhesion properties
- High melting point if laser illumination is considered
- Fast build up of continuous films



### 4.3. Electrical characterization of ultra-thin chromium layers on glass

- Low conductivity resulting in thin layers if applied as MARC

The adhesion property is very important since this method shall be applicable for various materials without restrictions. Especially this includes semiconductors, plastics and glasses of any kind. Another important parameter is the optical threshold damage limit. Since some of the optical power is absorbed by the metal layer it should exhibit a high melting point.

The last two needed parameters are the most important. Since the conductivity of metal films is determined by their thickness it is essential to control it as good as possible. This can be achieved by a precise direct control of the film thickness. Further, the low pressure deposition process of metallic layers shows a characteristic behavior building a continuous film. At first islands are built which are then interconnected by increasing the film thickness. Especially gold shows such tendency [105] which finds broad application range in optics and semiconductor physics. But the application of gold as MARC has some serious obstacles. With its high bulk conductivity the proper sheet impedance cannot be set exactly. By depositing gold, it starts to arrange in the form of islands. Without interconnections of these islands no macroscopic conductivity is achieved. These islands grow but do not start to interconnect until a threshold thickness is reached. Then these relatively large islands start to interconnect resulting in a jump in the conductivity close to the bulk value. Since a typical sheet impedance (see. Eq. 4.16) for MARC is in the range of  $128 - 377 \Omega$  ( $\Delta n = 1..3$ ) the thickness range to set is too narrow in combination with a proper thickness control.

Material	Gold	Chromium
Electrical conductivity $[\frac{S}{m}]$	$45.2 \cdot 10^6$	$7.74 \cdot 10^6$
Melting point $[K]$	1337	2130
Vickers hardness $[\frac{MN}{m^2}]$	216	1060
Heat conductivity $[\frac{W}{m \cdot K}]$	317	92.7
Lattice type	Fm-3m	Im-3m
Atomic layer distance $[pm]$	408	291
Adhesion property	bad	very good
Needed thickness for continuous film $[nm]$	>10	2-3
Plasma frequency $[nm]$	$\sim 530$	< 400
Oxidation affinity	no	just surface layer

Table 4.1.: Parameters of gold and chromium (from [75, 106]).

The metal which fulfills most of the requirements is chromium. Compared to gold it shows superior properties for the application as MARC. The basic properties of gold and chromium are summarized in Tab. 4.1. Especially the high resistivity, its adhesion capability and the fast built up of a continuous film are a big advantage for the precise sheet impedance control. The AFM<sup>1</sup>-images shown in Fig. 4.5 proof this very important property where thin chromium layers were deposited by e-beam onto glass plates. Already

<sup>1</sup>atomic force microscope

#### 4. Metallic phase shift layers for broadband THz optical systems

a 3 nm thick metal film shows no separated island formations. This gets clear by comparing it with the image of the 8.3 nm thick chromium film.

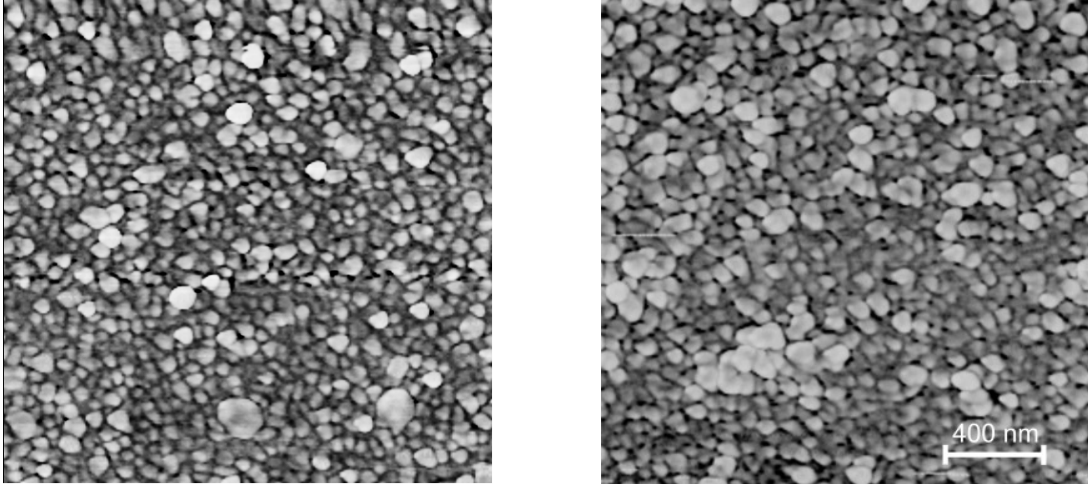


Figure 4.5.: AFM image ( $2 \times 2 \mu\text{m}$ ) of a 3 nm (left) and 8.3 nm (right) thick chromium film deposited by e-beam vaporization onto a glass plate at a pressure of  $\sim 10^{-6} \text{ mbar}$ .

For the characterization of ultra-thin chromium layers a series of glass plates was coated with film thicknesses 2-9 nm. Then the resistance was measured with a standard four point measurement technique [107, 65]. From the measured thickness dependent voltage drop and current ( $U(d)$ ,  $I(d)$ ) the real sheet impedance

$$R_{\square}(d) = \frac{U(d)}{I(d)} \cdot \frac{\pi}{\ln 2} \cdot 0.2204 \quad (4.19)$$

can be determined by using the correction factor from [108] which considers the geometry of the measurement arrangement. In Fig. 4.6 the effective film resistivity is shown. It illustrates clearly that even a 9 nm thick film shows a resistivity one order larger than the resistivity of the bulk material. From these data the thickness dependent resistivity can be approximated by

$$\rho(d) = a_1 \cdot e^{-b_1 \cdot d} + a_2 \cdot e^{-b_2 \cdot d} + \rho_0 \quad (4.20)$$

with the fitting parameters in Tab. 4.2. The run of the curve and the fact that it can be fitted by two exponential functions suggests the following assumption. The first exponential function describes the island formation and their interconnection process. This happens up to a layer thickness of 3 nm. From this thickness on the resistivity is dominated by the second exponential term. In this range the resistivity is controlled by the gradually decreasing collision rate caused by the confinement of electrons in one dimension. This is the direct evidence that in this way the mean free path of the electrons perpendicular to the film orientation is affected.

#### 4.4. Optical characterization of ultra-thin chromium layers on silicon

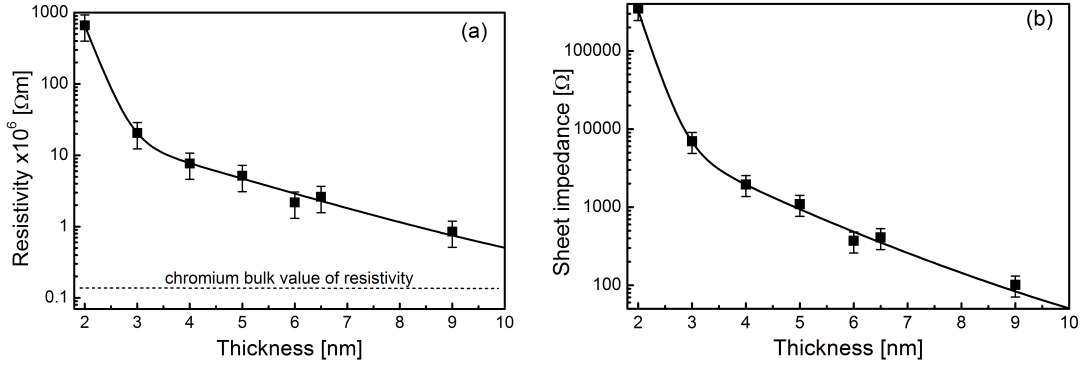


Figure 4.6.: (a) Resistivity and (b) sheet impedance of ultra-thin chromium films deposited on glass plates as a function of thickness measured by a 4-point probe. Data fit made by two exponential functions.

Parameter	Value
$a_1 [\Omega m]$	4.131
$b_1 [m^{-1}]$	$-4.385 \cdot 10^9$
$a_2 [\Omega m]$	$55.32 \cdot 10^{-6}$
$b_2 [m^{-1}]$	$-498.5 \cdot 10^6$
$\rho_0 [\Omega m]$	$127 \cdot 10^{-9}$

Table 4.2.: Fitting parameters for chromium film resistivity.

#### 4.4. Optical characterization of ultra-thin chromium layers on silicon

The electrical characterization of ultra-thin chromium layers on glass presented in the last section is the first necessary step to determine the proper film properties as a function of the layer thickness. Further, with the chromium coated glass plates the properties in the NIR (800-820 nm) can be tested. This data on reflection, transmission and absorption is shown in Fig. 4.7. As expected the transmission drops fast with increased film thickness while the reflectivity and the absorption of the chromium film rises. The reduced NIR transmission has an impact on the application of these films shown later in this chapter.

For the characterization of chromium films in the THz frequency range glass substrates are useless for measurements in transmission mode due to their high absorption. For the characterization in this long wavelength range semiconductor substrate materials are well suited. For this purposes a series of 400  $\mu m$  thick high resistive silicon plates ( $\rho > 3000 \Omega cm$ ) were coated with a chromium layer. High resistive silicon is transparent and it has negligible dispersion at THz frequencies [109]. The chromium layers of a thickness from 2 to 9 nm were deposited by e-beam evaporation in a high vacuum chamber ( $p < 5 \cdot 10^{-6} mbar$ ). For the optical characterization THz-TDS was applied. In Fig. 4.8 the transmission signal through the uncoated silicon plate is shown. Multiple reflections from the eo-sensor and the sample itself are visible which hamper the data processing of

#### 4. Metallic phase shift layers for broadband THz optical systems

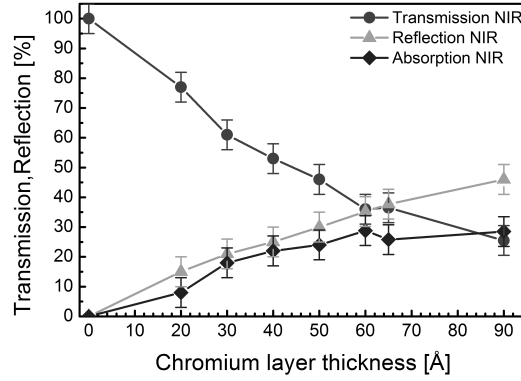


Figure 4.7.: NIR transmission, reflection and absorption of ultra-thin chromium films on glass plates.

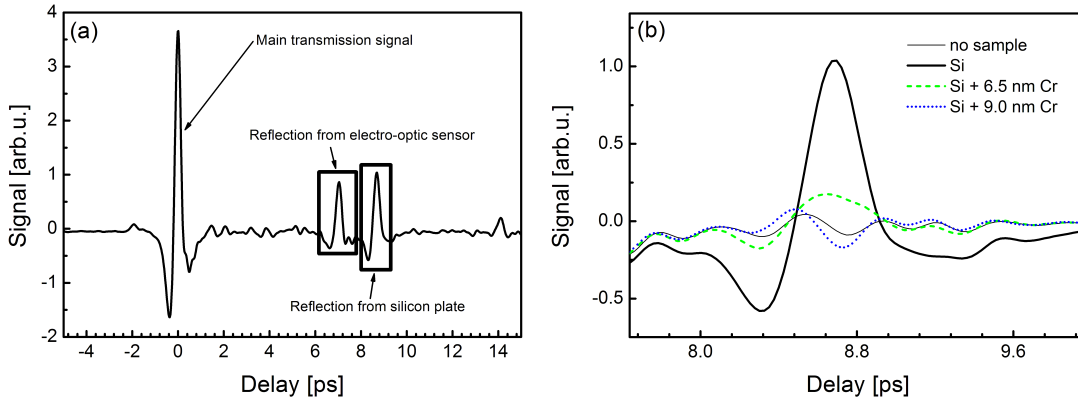


Figure 4.8.: (a) Transmitted THz-TDS signal through a 400  $\mu\text{m}$  thick silicon plate and (b) zoomed time window of reflection caused by the silicon/air interfaces for two chromium film thicknesses.

the measured signal.

The situation changes completely when the sample is coated with a conductive layer. First, the transmitted signal amplitude drops according to the data shown in Fig. 4.9. Much more interesting is the impact on the reflections within the coated silicon substrate. Relatively the amplitude of the reflection drops much faster with increasing thickness than the transmission. Even more, by exceeding a certain value, corresponding to the optimized sheet impedance, the phase of the reflection flips indicating an overcompensation of the wave impedance mismatch. This is very well illustrated in Fig. 4.8 for a chromium below and above the optimal value. This phase flip can also be explained by the Eq. 4.2.

From the measured data a refractive index of  $n_{\text{Si}} = 3.25$  was approximated which corresponds to an wave impedance of  $116\Omega$ . With Eq. 4.16 the optimal sheet impedance for the MARC can be determined. For this case of silicon this is  $167.6\Omega_{\square}$ . In Fig. 4.9 the measured and simulated results for the transmission and reflection amplitude is shown. The data indicate that the results from the resistivity measurements which are used for

#### 4.4. Optical characterization of ultra-thin chromium layers on silicon

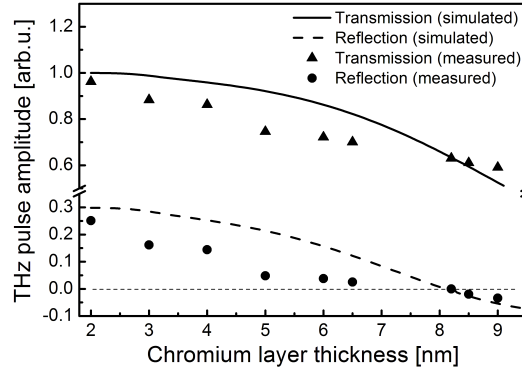


Figure 4.9.: Reflection and transmission amplitude as a function of chromium film thickness. Point data shows the optical results and the data plotted as lines is calculated from the sheet impedance fit from the electrical results.

the fitting function slightly differ from the optical results. In general the optical results show a higher effective sheet impedance than the electrical measurements but only for thin layers. For thicker layers the results match better. The reasons for this discrepancy are manifold.

First the sheet impedance geometry was not optimal due to the limited availability of larger glass substrates. Further, it is possible to track the sheet impedance directly during the deposition process by placing two stripes in a certain distance onto the glass plates. But also in this case imprecise values are measured due to the high deposition temperature of the material compared to the room temperature under use. Second, the formation of islands and the build up of a continuous film is strongly influenced by the surface structure, quality and the material itself. In the case of the presented measurements a characterization on silicon would be much more precise.

From Fig. 4.9 the optimal chromium layer thickness could be derived. The thickness to achieve a MARC on silicon was calculated to be 8.1 nm which was finally deposited on one silicon plate. The results are shown in Fig. 4.10. With MARC the reflection, before appearing at  $\sim 12$  ps, vanishes and does not hamper any more further data processing.

The drawback of MARC is the attenuation of the transmitted pulse. In general the same amount of power is consumed to suppress the reflection as would have been reflected without coating. This rule of thumb of doubled losses is valid for all dielectric material systems which can be easily be proven by the Fig. 4.4 and using Eq. 4.2. The outstanding advantage of this technology is illustrated by looking at the spectral ratio of the main pulse with and without MARC (Fig. 4.10). Over a broad spectral range the amplitude stays constant and is only limited by the dropped SNR at high frequencies.

As described above the anti-reflection effect should work as long as the metal's corresponding plasma frequency is well undershot. Since THz-TDS with the used emitter and sensor described in chapter 3 is limited to the frequency band 0.1-7 THz another method was used to proof the working principle at higher frequencies. For this purpose FT-IR

#### 4. Metallic phase shift layers for broadband THz optical systems

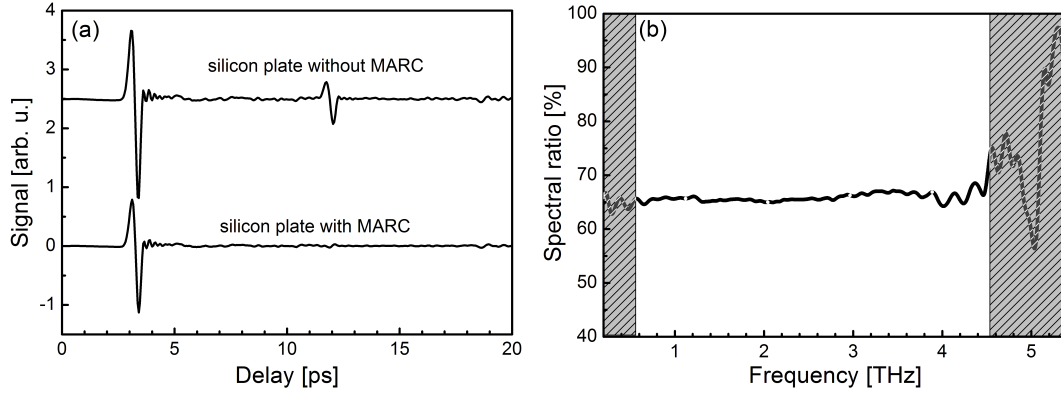


Figure 4.10.: THz signal comparison of a 300 μm thick silicon plate with and without MARC. (a) Time-domain signals (data are offset for clarity) and (b) spectral ratio of the transmitted THz pulses [marked areas indicate low SNR regions].

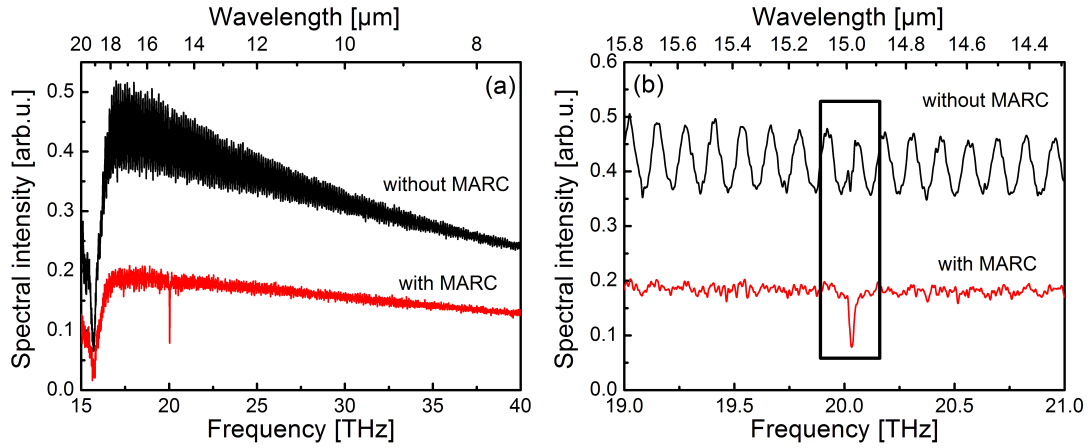


Figure 4.11.: Transmission spectrum of 350 μm thick GaAs substrate with and without MARC. (a) Full spectrum and (b) zoomed windows with marked  $CO_2$  absorption line at 20.04 THz.

was applied. Without obtained phase information (see chapter 2) only the spectral power density spectrum (PDS) can be used to visualize the MARC effect. In this case the modulation amplitude of the spectrum is the quality factor which should be as small as possible. In Fig. 4.11 the transmission results of MARC in the frequency range of 15-40 THz are shown. The data illustrates very well that with proper coating the spectrum's modulation disappears. Even in this frequency range the anti-reflection technique is still fully working. This indicates an application for shorter wavelengths depending on the plasma frequency of the used metal.

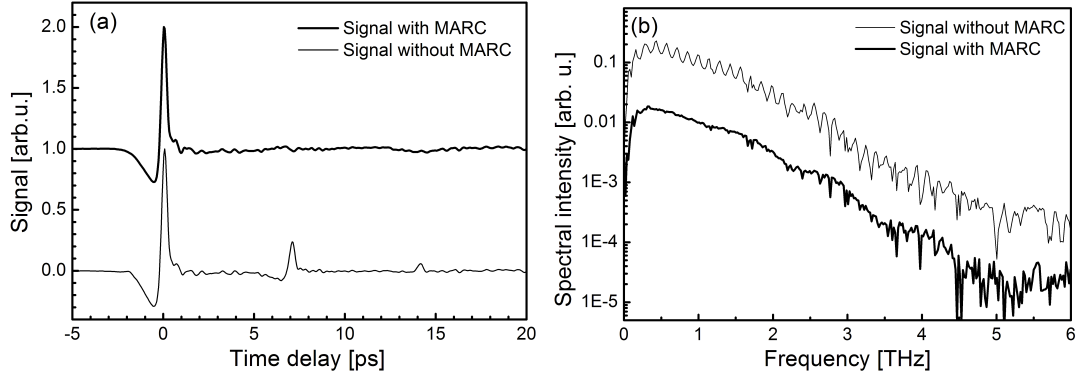


Figure 4.12.: THz signal from a  $300\,\mu\text{m}$  thick GaP electro-optic sensor with and without MARC. Time-domain (left), spectrum (right).

## 4.5. High performance electro-optic detector

The initial motivation to analyze the optical properties of ultra-thin metallic layers in the THz frequency range was to suppress reflections within the electro-optic sensor. Without suffering from reflections the sensed time window can be elongated which results in an enhanced spectral resolution of the used THz-TDS system. For this task the knowledge about the electrical properties of ultra-thin chromium layers and their characterization on silicon made before was necessary. With this know-how the proper chromium film thickness for MARC on a gallium phosphide (GaP) eo-sensor was determined. From the time-domain measurement the effective refractive index of GaP was approximated with  $n_{\text{GaP}} = 3.45$ . To establish a MARC at such eo-sensor/air interface a chromium layer with a sheet impedance of  $R_{\square} = 147.8\,\Omega$  is required. This value is reached for a layer thickness of 8.3 nm. The results on a chromium coated GaP eo-sensor are shown in Fig 4.12. The time-domain signal shows only a very weak reflection visible at 7 ps. The opposite phase of it indicates that in this case a slight overcompensation occurred. This overcompensation vanished after one month of usage. This indicates an increased sheet impedance due to oxidation.

## 4.6. Conclusions

In this chapter the theory, principle and realization of a new type of broadband anti-reflection coating was presented. The shown data demonstrate that such ultra-thin metallic layers effectively suppress any kind of reflections at an optical interface of two dielectric materials. The exploited optical phase shift effect at an dielectric/metal interface shows very well that this new type of technology is even suited for much higher frequencies up to visible light maybe. Especially chromium showed outstanding properties for the application as MARC. This is mainly the very good controllable sheet impedance and its adhesion property. Due to latter property nearly any material can be coated including

#### 4. *Metallic phase shift layers for broadband THz optical systems*

ceramics and plastics.

As shown in Fig. 4.7 even NIR radiation is absorbed which indicates that the plasma frequency of chromium is located even at higher frequencies. In the case of eo-detection, where the NIR probe is guided through the eo-crystal, this leads to an attenuation of the probe beam. For crystals with an refractive index  $n > 3$  more than 50 % of the incident power is absorbed. This shows the need for new material for this task. A material not presented here but best suited as MARC is indium-tin-oxide (ITO). It has similar properties but it is transparent for NIR radiation due to its plasma frequency located below the visible electro-magnetic spectrum. Compared to chromium the application of ITO is limited to THz frequencies. Further, due to the fact that ITO is already partly oxidized no additional aging effect could be observed.

In summary metallic phase shift layers present the state-of-the-art anti-reflection technology for infrared systems. Compared to many other methods on this field they really suppress reflections at an optical interface. The final choice for the best suited conductive material depends on the actual application of MARC, the frequency region of interest and the material to coat.



## 5. THz optical properties of sucrose single crystals

### 5.1. Introduction

In general spectroscopic results show the optical properties of materials. In the simplest case, the sample object consists of individual molecules which are randomly arranged. This means the system shows no asymmetry regarding the orientation of absorption features and so all possible vibrational modes are more or less sensed at once. In this case the polarization of the analyzing light field does not contribute to the measured material properties. The situation changes if crystalline materials with a periodic structure are involved. In this case orientation sensitive absorption spectra are expected. The optical properties of crystals depend strongly on the bond type which stabilizes and forms their structure [75].

In nature, many atoms and molecules have a strong tendency building a periodic structure which reduces the free enthalpy and so the internal energy. This process is called crystallization. If the environmental conditions (temperature, pressure, etc.) benefit this process the constituents start to arrange in a certain way building a compact structure caused by interconnection links. Crystals can be divided in two main groups which are atomic and molecular crystals which exhibit either strong or weak bonding forces. In both cases the optical properties are mainly determined by the bond type and their orientation. Depending on the forces between the constituents these bonds can be divided in [75]:

- Covalent bonds,
- Ionic bonds,
- Metallic bonds,
- Inter-molecular bonds.

In the easiest case of covalent bonds only atoms with similar affinity and four valence electrons are involved (e.g. this is the case for Si, Ge, C). By building a periodic structure the neighboring atoms share these electrons to complete their valence electron configuration. This bond type is not limited to crystals built by a single element. But if a covalent bond is built between two different elements the shared electrons are concentrated around the atom with the higher electronegativity. This causes that the molecule shows in close proximity a sensible electric field. This inhomogeneous charge density distribution is responsible for the inter-molecular forces explained later.

## 5. THz optical properties of sucrose single crystals

Similar happens in ionic crystals but thereby a metallic and non-metallic atom is involved. The non-metallic atom with the higher electronegativity completes its electron configuration while the metal atom remains positively charged. In both cases the electrons stay localized and are only shared with the surrounding atoms. The bonding forces and the periodicity of the crystal structure determines directly the orientation dependence of the optical properties. Since covalent and ionic bonds result in stiff forces between the individual atoms the strongest modes are located in the NIR and visible spectrum.

Most of the elements in nature are metals. Like other materials they build a crystalline structure but in this case the electrons are not bound to a certain atom (see chapter 4). In metals the valence electrons are only weakly bound to the atom they belong to. Already at low thermal energies the electrons start freely to move within the lattice structure. They form a so-called electron gas which surrounds the remaining positively charged atomic nucleus.

The above described covalent, ionic and metallic bonds have in common that the involved atoms share in one or another way their valence electrons with their neighborhood. This results in very stiff and strong coupling forces. Contrary to them, the last group of crystals base on another type of forces. In this case the crystalline structure is not built by atoms but by molecules. They form a periodic structure by exhibiting weak bonding forces between the involved individual molecules. For instance, such forces are responsible for the crystalline structure of water ice [110]. The strongest representative of these weak bonding forces are hydrogen bonds which are responsible for the arrangement of large macro-molecules in a crystalline structure.

### 5.2. Molecular crystals

As described above crystals cannot be built only by strong coupling forces between the atomic constituents. Depending on the electronegativity of the atoms within a molecule the charge density and so the average electron distribution is not homogeneous. This causes Coulomb forces between locally charged parts of a molecule. In the case of molecular crystals these forces are formed between positively charged hydrogen atoms and negatively charged oxygen atoms. Due to this such inter-molecular connection is called hydrogen bond.

For instance benzoic acid builds a molecular crystals by hydrogen bonds (Fig. 5.1). But as can be seen in this illustration more than one hydrogen bond can be built between the molecules. In comparison to the crystallization process in atomic crystals, the molecular crystal formation process has much more degrees of freedom. This means, the crystal can consist of more than one kind of molecules and the crystallization process can even result in a formation of hydrogen bonds within a single molecule [111]. This factor complicates the pre-estimation which molecule combination is able to build a molecular crystal and what are its properties. However, this complexity shows the potential of such structures as well. Proper materials can be joined showing new properties.

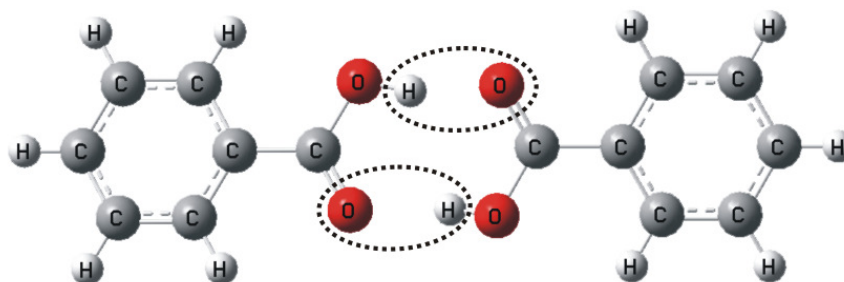


Figure 5.1.: Hydrogen bonds between benzoic acid molecules.

Compared to atomic crystals the group of molecular crystals exhibit remarkably different performance. The importance of those materials has been demonstrated by the increased number of applications in the last years. For instance DAST<sup>1</sup> [112] found application in optics and pentacene [113] in electronics. Especially the knowledge of vibrational modes is essential for the understanding of the optical and electrical properties of molecular crystals. In addition, the observed vibrational modes of such crystals, unlike atomic crystals, are rarely mapped to the microscopic movement of the involved crystal constituents and molecules. Contrary to atomic crystals, the molecular crystals have lattice vibrational modes at relatively low frequencies. Due to the weak bonding forces between relatively heavy molecules. The knowledge about these modes can be used to determine the phonon dispersion/scattering properties of such crystals. This information together with the data of vibrational modes of single molecules refines the knowledge of the bond potentials of these molecules. In the following such properties of molecular crystals are demonstrated by sucrose single crystals.

### 5.3. Sucrose single crystals

The saccharides represent a very important subgroup of molecular crystals, not only in chemistry and biology but also in physics. For instance saccharides play a major role in the human metabolism as an energy source for muscles and brain activities. In spite of the huge effort, the chemical interactions of saccharides, like fructose, glucose, dextrose and sucrose, with the surrounding environment are not fully understood yet. Free bonds, polarity, and shape of equipotential surfaces of molecules determine their reactivity and are therefore objects of great interest.

One of the most important saccharides is sucrose ( $C_{12}H_{22}O_{11}$ ) [111]. Sucrose is a molecule built of fructofuranose and glucopyranose connected via an oxygen atom (Fig. 5.2). In the crystalline structure the sucrose molecule is folded and two additional hydrogen bonds to oxygen atoms are formed within a single molecule. The binding between the molecules in the crystal structure is also done by several hydrogen bonds. In this way every sucrose molecule is connected with the neighboring molecules by several weak bonds

<sup>1</sup>4-N,N-dimethylamino-4'-N'-methyl-4-stilbazolium tosylate

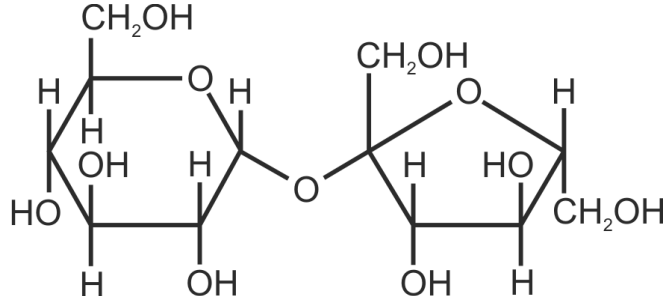


Figure 5.2.: Molecular structure of sucrose.

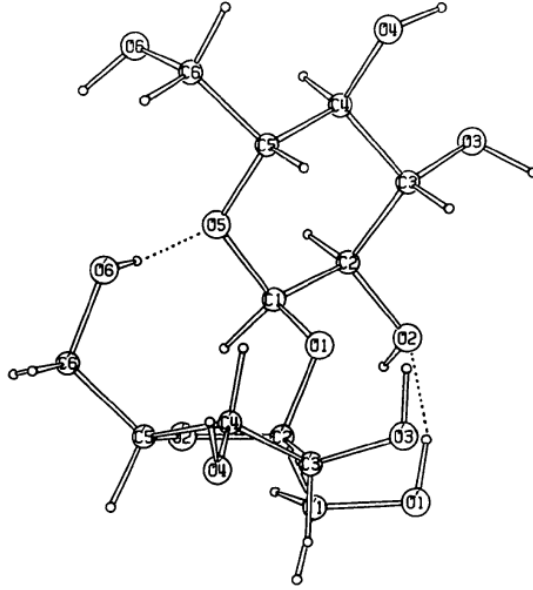


Figure 5.3.: Folded sucrose molecule with intra-molecular hydrogen bonds (marked by dotted lines).

forming a three dimensional structure which is illustrated in Fig. 5.3. Detailed information about the crystallographic structure of sucrose measured by neutron diffraction can be found in [114].

Since the sucrose molecules themselves are heavy and the bonds between them are not stiff, absorption features due to vibrational modes in the THz frequency range is observed. Such absorption was recently demonstrated on polycrystalline samples by Walter *et al.* [115]. They showed absorption spectra of sucrose, D-(+)-glucose, and D-(-)-fructose at 10 and 300 K obtained by THz-TDS. They have demonstrated a temperature shift of the absorption peaks and the effect of protonation/deuteration on the vibrational mode frequencies. Earlier data on the sucrose absorption features in the THz frequency region were published by Upadhyaya *et al.* [10] and Nishizawa *et al.* [116]. The former group pointed out the intermolecular origin of the observed vibrational modes from the comparison of the absorption spectra of glucose and sucrose.

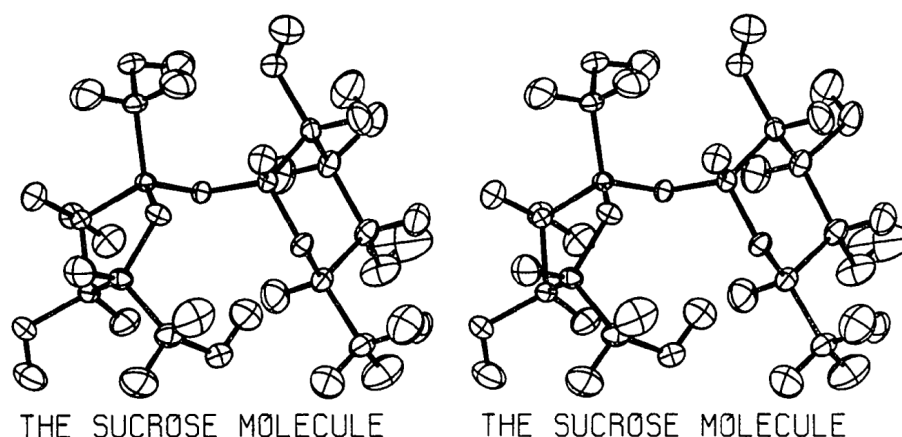


Figure 5.4.: Stereoscopic view of the sucrose molecule (from [114])

### 5.3.1. Sucrose crystal structure and growth

Although the crystallographic structure of sucrose is well known (Fig. 5.4) and the properties in the visible and NIR region were studied [117, 114] only little attention was paid to the identification of the individual vibrational modes in a sucrose single crystal.

The direct identification of the vibrational modes is only possible if single crystals are available. Since pure sucrose is only commercially available as powder the crystals had to be home made. The single crystals of sucrose were obtained by a controlled crystallization from a saturated solution in a water/glycol mixture (see e.g. [118, 119]). Sucrose crystallizes in a monoclinic structure. The crystal contains two molecules per unit cell and belongs to the  $P2_1$  space group [117]. The only element of symmetry is the binary rotation around the  $b$ -axis. The other crystal axis  $a$  and  $c$  are perpendicular to the  $b$ -axis and the angle between them is about  $103.3^\circ$ . The typical shape of sucrose single-crystals and the orientation of axes are schematically shown in Fig. 5.5.

To access the dipoles associated with the vibrational modes of the crystal, three about 1.5 mm thick samples were prepared (labeled A-, B-, and C-cut) by cutting and polishing from the same grown bulk crystal. This avoids discrepancies between the sample slabs due to small variations during the crystal growth. The sample planes for A-, B-, and C-cut were the  $bc'$ -,  $ac'$ -, and  $ab$ -plane, respectively. For simplicity instead of the  $c$ -axis, that is about  $103^\circ$  of the  $a$ -axis, rather an axis labeled  $c'$  perpendicular to both  $a$ - and  $b$ -axis was chosen. The sucrose crystal samples were mounted in a liquid helium continuous-flow cryostat for preventing line broadening due to thermal lattice vibrations and placed in the THz beam path. The absorption measurements were performed in transmission mode. The measured THz time-domain signal was later processed using a fast Fourier transformation algorithm to get the spectral information of the transmitted THz electric field. This spectrum is compared to the reference THz spectrum measured in the same set-up after removal of the sample. The real and imaginary part of the refractive index of the sample are determined as described in chapter 3 which is a straight forward task.

## 5. THz optical properties of sucrose single crystals

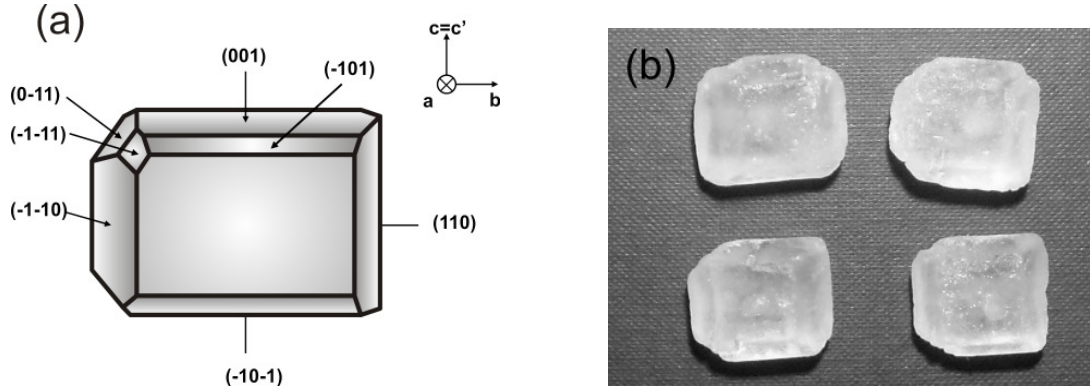


Figure 5.5.: (a) Schematic of the typical shape of a sucrose single crystal with assigned main planes and (b) photo of typical sucrose single crystals.

For the THz-TDS scans a time window of 54 ps was used that provides a spectral resolution of about 18.5 GHz. Further the setup volume, where the THz beam was present, was purged by dry nitrogen. This removed the disturbing effect of water vapor absorption which could, in the worst case, overlap and mask the vibrational modes of the single sucrose crystal.

### 5.3.2. Experimental results on single sucrose crystals

In Fig. 5.6 the absorption spectra for three different orientations of the THz polarization with respect to the sucrose crystal measured at a temperature of 5 K are shown. Namely, the results for the polarization parallel to  $a$ -,  $b$ -, and  $c$ -axis are shown. Different absorption lines and their strength for various orientations of the THz polarization are clearly visible. These spectra were fitted with a set of 13 modes with Lorentzian line shape according to

$$\alpha_{mode}(f) = \alpha_{max} \cdot \frac{1}{\pi} \cdot \frac{\frac{\Delta f_{FWHM}}{2}}{(f-f_0)^2 + \left(\frac{\Delta f_{FWHM}}{2}\right)^2}, \quad (5.1)$$

where  $\alpha_{max}$  is the maximum absorption coefficient,  $f_0$  is the center frequency, and  $\Delta f_{FWHM}$  is the line width of the vibrational mode. The resulting parameters of the line position and the linewidth are listed in Table 5.1. The error margins of the position and the linewidth of the vibrational modes are 18 and 9 GHz respectively. The positions of the absorption lines correlate well to those obtained by Walter et al. [115], as well as by Upadhyaya et al. [10] for the polycrystalline sucrose employing THz-TDS.

Vibrational modes of sucrose in the frequency range 0.2–5 THz were also measured by Nishizawa et al. [116] using a tunable cw terahertz source with a spectral resolution of 3.3 GHz. For polycrystalline sucrose embedded in a polyethylene pellet and held at room temperature (295 K) they observed absorption peaks at 1.5, 1.9, 2.05, 2.15 THz and broad features (several overlapping peaks) at 2.4–3.0, 3.2–3.7 THz and above 4.0 THz. With regard to the given spectral resolution, the temperature broadening of absorption peaks, and

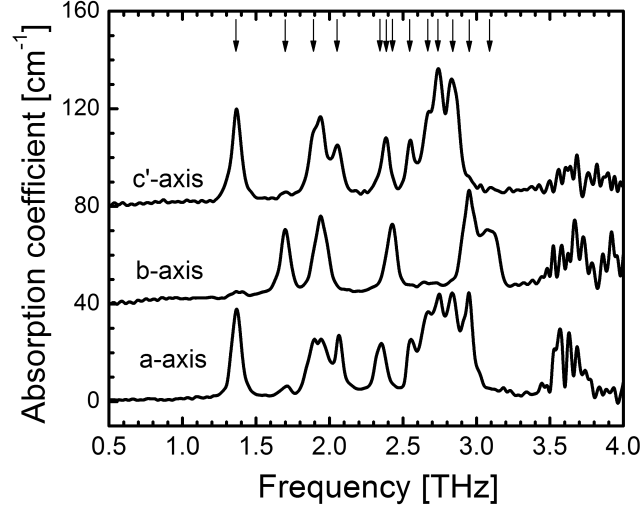


Figure 5.6.: Absorption spectra for three different orientations of polarization measured at 5 K. Polarization of THz radiation was parallel to a-, b-, and c'-axis of the sucrose crystal (5.5b). The curves are vertically offset for clarity and arrows indicate the identified vibrational modes.

Label	Frequency [THz]	FWHM [GHz]
1	1.37	77
2	1.70	75
3	1.88	69
4	2.06	71
5	2.38	75
6	2.43	81
7	2.54	77
8	2.66	80
9	2.74	62
10	2.83	68
11	2.95	90
12	3.05	78
13	3.12	81

Table 5.1.: THz optically active vibrational modes of sucrose crystals in the frequency range 0.5-3.5 THz observed at 5 K (error margins for the position and the linewidth are about 18 and 9 GHz, respectively).

## 5. THz optical properties of sucrose single crystals

the position shift of absorption features originating from phonons [10], the results also well correlate with those of Nishizawa's. Compared to these previously published data the experimental setup with its high bandwidth is capable to complete and extend the knowledge about the vibrational modes of sucrose. At first the experiments are performed at 5 K. This allows to identify all individual modes separately without suffering from overlapping of thermally broadened absorption lines. The second enhancement is that by using single crystals instead of polycrystalline samples, like the other groups, the absolute orientation of the identified vibrational modes can be directly mapped to the crystal structure of sucrose.

The THz-TDS measurement setup provides a dynamic range of about 60 dB at 1.5 THz and then the dynamic range decreases to 20 dB at 3.5 THz. The data obtained for frequencies  $> 3$  THz are already strongly obscured by a low signal-to-noise ratio of the detected THz electric field and are omitted from the analysis. The given measurement dynamic range and the thickness of the samples allow to access absorption coefficients up to  $30 \text{ cm}^{-1}$  [120].

The measurement on the sucrose single crystal gives lower absorption losses compared to those obtained on polycrystalline sucrose [115] by a factor more than 4. An explanation for this discrepancy can be beam scattering at individual sucrose micro crystals with different crystal planes. The control measurement on the same sucrose material, but in powder form (finely ground sucrose crystals embedded in polyethylene powder and pressed into a pellet form) showed very strong attenuation of the transmitted THz signal. This scattering effect has not been analyzed further, although it is worth to be targeted in future experiments. On the other hand, alternative THz results on sucrose provided the absorption coefficients closer to our observations [116].

The sucrose crystal exhibits a small natural optical activity in the visible range (400-800 nm) due to the spiral alignment of the sucrose molecules (Fig. 5.4) in the crystal structure. This results in a rotation of the plane of polarization by  $22^\circ \text{ cm}^{-1}$  for light traveling along the axis normal to the (100)-plane and  $-64^\circ \text{ cm}^{-1}$  for light traveling along the other axis [121]. This potential problem of polarization rotation is minimized by the choice of thin sample thicknesses of 1-1.5 mm. For example, for a 1 mm thick A-cut sample, a rotation less than  $7^\circ$  is expected. This value is comparable to the angular resolution in the experiment.

Since the detection scheme of a THz-TDS system is very sensitive to the polarization of the measured THz pulse, it is exploited to map the dipole orientations of the sample. The interaction strength between the electromagnetic field and the dipoles within the crystal structure should vary as cosine of the angle between them. Therefore, to get the information about the orientation of dipoles in the sucrose single crystal the absorption spectra for various angles between the dipoles and the THz electric field are measured. Moreover, the measurements have to be performed at least in two different projection planes to get an unambiguous set of three-dimensional data for each dipole. That means, by combining the data from two projection planes or crystal cuts, respectively, the dipole's orientation can be identified. A third dataset would comprise redundant information but



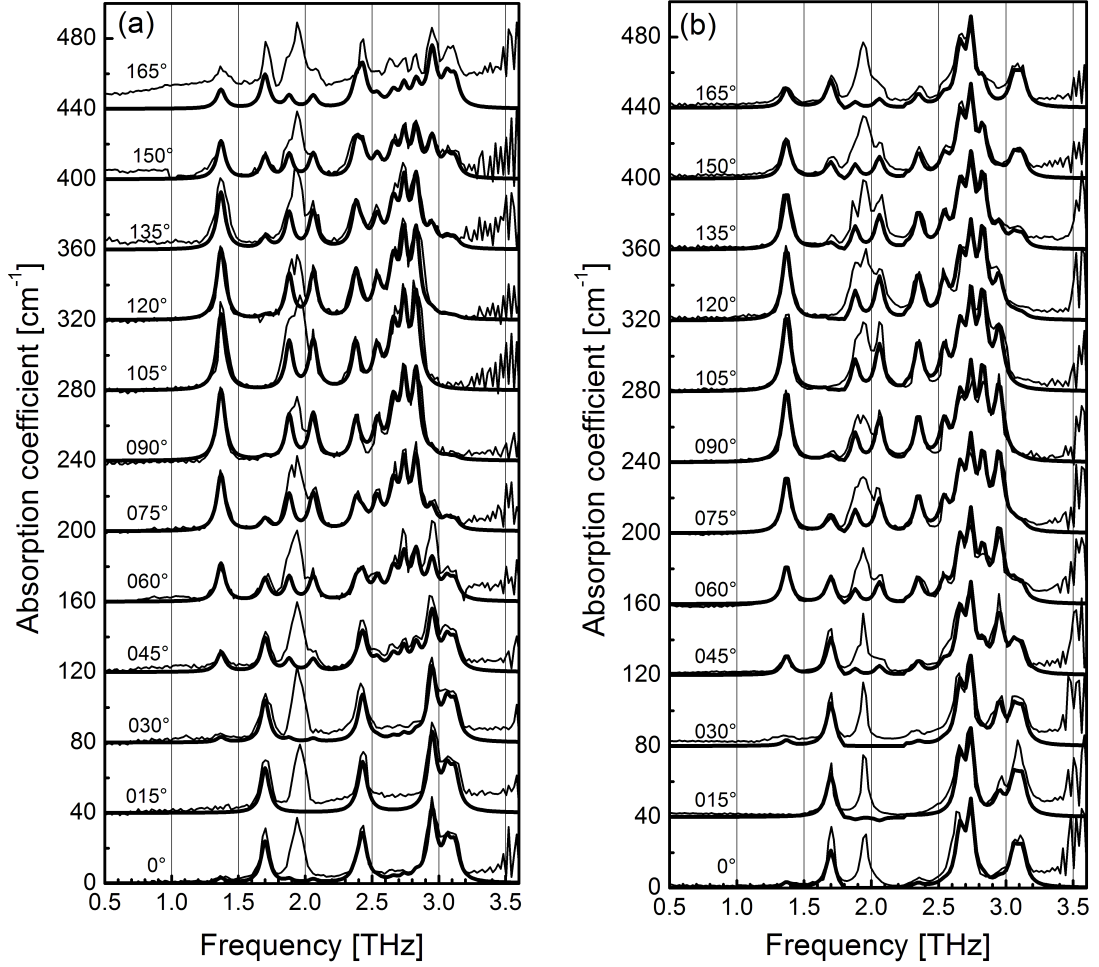


Figure 5.7.: Absorption spectra for different polarization orientations for A-cut (a) and C-cut (b) at 5 K (thin lines). Spectra were fitted with a sum of Lorentzian peaks (thick lines) whose parameters are listed in Tab. 5.1 and are off-set for clarity.

can be used as control measurement. A full set of consistent data could be obtained for a A- and C-cut sample. The B-cut sample, made from the same bulk crystal, did not survive the number of cooling cycles. So only a incomplete dataset could be obtained.

In theory, the angular dependent spectroscopic information is obtained by making scans over a complete  $360^\circ$  turn. Since it is technically difficult to perform scans by rotating continuously the sample inside of the cryostat, an angular step size of  $15^\circ$  was chosen and performed over a range of only  $180^\circ$ . The final analysis to find the actual position of the absorption peaks is done by Fourier fitting of the experimental data. This data processing is valid since it assures that the sampling theorem (feature size  $>$  twice of sampling interval) is not broken. In addition, since only dipole like activity of the vibrational modes is expected data measured in the angular range of  $0$ - $180^\circ$  contains information for the complete  $360^\circ$  turn.

In Fig. 5.7 absorption characteristics for A- and C-cut of the sucrose single crystal are

## 5. THz optical properties of sucrose single crystals

shown. The graphs show the angular pattern of the absorption that repeats every  $180^\circ$ , which is the common behavior of infrared active dipole modes. Spectra obtained for the individual projection planes (i.e. A- and C-cut) were again fit with a set of Lorentzian shaped peaks with parameters summarized in Tab. 5.1. The obtained projections of the dipoles provide an unambiguous determination of their orientation in the sucrose crystal. The angular data obtained from A- and C-cut are reasonably consistent with those measured for a small set of scans done with a B-cut sample. Small variances between the main sample planes are caused by the limited accuracy of the polishing process during sample preparation which is  $\approx 5^\circ$ . In addition, the datasets for the A- and the C-cut show an angular independent absorption feature at about 1.95 THz which fits well also with the measurements of the B-cut dataset. This isotropic absorption feature is not fully understood yet but is a common behavior of such large molecules embedded in a crystal structure. However, since this is a constant feature it does not hamper the data processing and the Lorentzian line shape fitting.

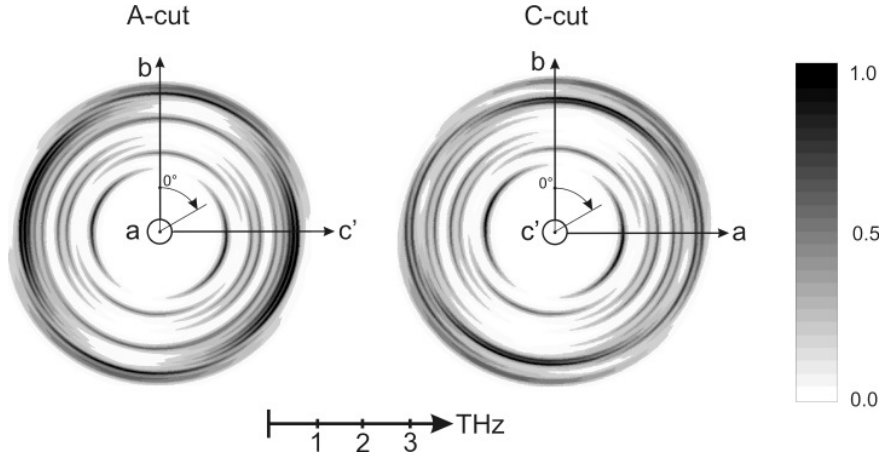


Figure 5.8.: Angular dependence of the absorption peaks for A-cut (left) and C-cut (right).

The orientation of the dipoles is well illustrated in the polar plots of absorption (Fig. 5.8). The observed angular modulation of the peak amplitudes allows to determine the dipole's orientation projections into a given observation plane. Because of the step size in the angular dependence measurement of  $15^\circ$ , the error margin for the dipole's orientation is about half of the step size, i.e.  $\approx 7^\circ$ . The Tab. 5.2 summarizes the experimental results and deduces the final dipole orientations of the observed vibrational modes in sucrose single crystals as shown in Fig. 5.9. This data and the graphical illustration in Fig. 5.8 shows clearly that many modes share the same orientation. This is in good agreement with the resonant absorption behavior of long chained structures, in this case, a molecular crystal formed by soft hydrogen bonds.

In addition, the dipoles show a remarkable tendency. By comparing their orientation with the crystal's unit cell which consists of two sucrose molecules as shown in Fig. 5.10, most of the dipoles share similar orientation as the major hydrogen/oxygen bonds between

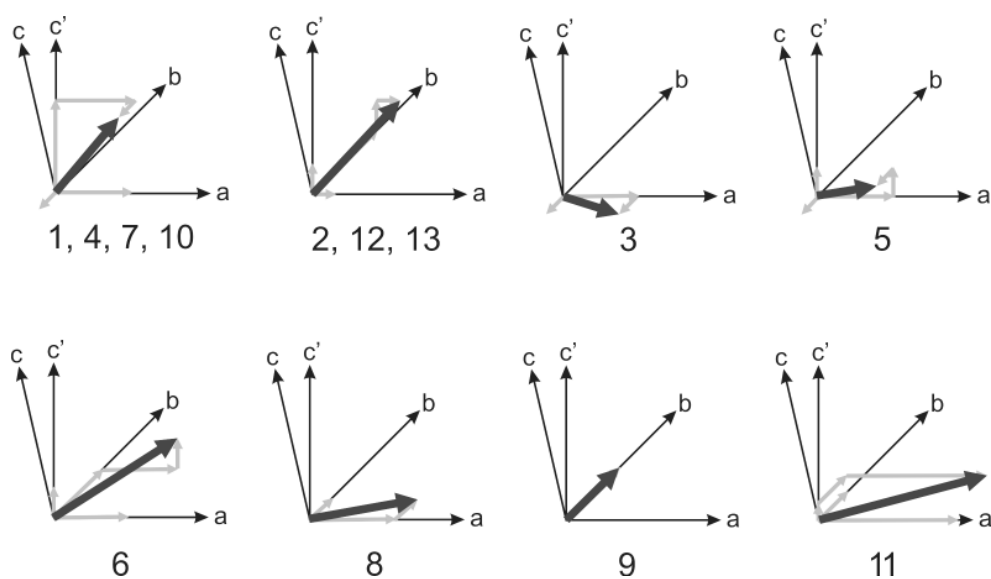


Figure 5.9.: Orientation of dipoles corresponding to the observed vibrational modes in the sucrose single crystal.

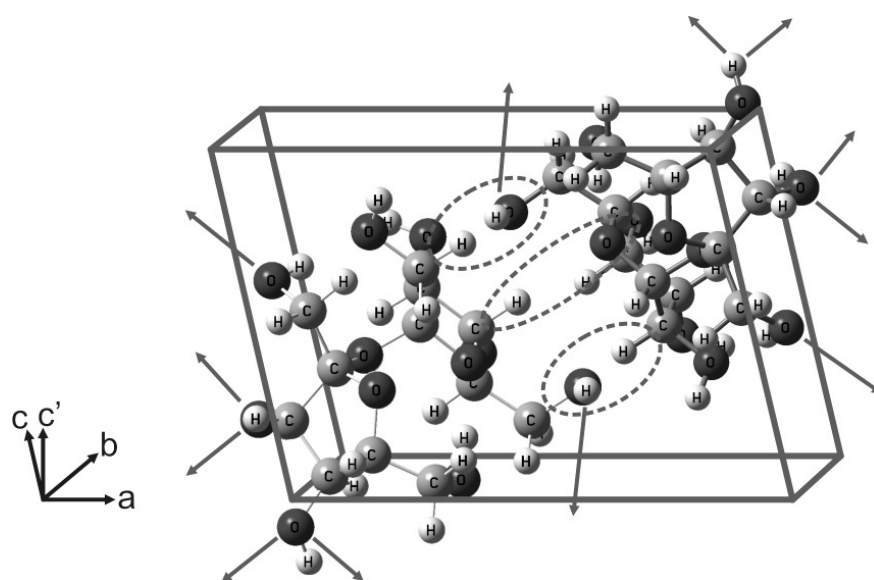


Figure 5.10.: Single unit cell of sucrose with two molecules (dashed lines and arrows indicate hydrogen-oxygen bonds).

## 5. THz optical properties of sucrose single crystals

Label	$\alpha$	$\beta$	$\gamma$	$e_a$	$e_b$	$e_{c'}$
1	15	105	45	0.6947	-0.1861	0.6947
2	-75	15	45	0.2505	0.9351	0.2505
3	15	105	90	0.9659	-0.2588	0.0000
4	15	105	45	0.6947	-0.1861	0.6947
5	15	135	75	0.9351	-0.2505	0.2505
6	45	15	75	0.6947	0.6947	0.1861
7	15	105	45	0.6947	-0.1861	0.6947
8	15	0	90	0.9659	0.2588	0.0000
9	-90	0	0	0.0000	1.0000	0.0000
10	15	105	45	0.6947	-0.1861	0.6947
11	-15	15	5	0.9462	0.2496	0.0668
12	-75	15	45	0.2505	0.9351	0.2505
13	-75	15	45	0.2505	0.9351	0.2505

Table 5.2.: Orientation of the unit dipoles ( $e_a, e_b, e_{c'}$ ) of THz optically active vibrational modes of a sucrose single crystal in the frequency range 0.5-3.5 THz given in the coordinate system of the sample (orthogonal a, b, and c') as well as in the crystal coordinates (a, b, and c) from Ref. [111, 122].  $\alpha$  means the angle from  $a$ -axis in the  $ab$ -plane,  $\beta$  is the angle from  $b$ -axis in the  $bc'$ -plane, and  $\gamma$  is the angle from the  $c'$ -axis in the  $ac'$ -plane.

the molecules. This gives a first indication regarding the molecule's particular movement for the observed THz active vibrational modes.

## 5.4. Conclusions

In this chapter was presented the THz-TDS study of anisotropic optical activity of molecular crystals made of sucrose ( $C_{12}H_{22}O_{11}$ ). The terahertz active vibrational modes of the crystal in the frequency range of 0.1-3.5 THz were identified in several projection planes. By combining the datasets from these different planes the orientation of the corresponding dipoles of the vibrational modes could be correlated to the single crystal structure of sucrose. The gained results extend the knowledge of molecular crystals and their optical parameters measured so far [123].

In addition, the identified orientation of the dipoles associated with the modes provide a first indication for the determination of the molecular movement in crystals. For instance, the results can be used for the prediction of optical parameters of new molecular crystals or computer simulation programs. Especially this would improve the accuracy and the speed of the analyzing algorithms. Further, since with the new method presented here a full insight in the optical activity of a structure is gained, it can be used to evaluate the application potential of various molecular crystals in a direct way.

## 6. Phase resolved transmission spectroscopy of terahertz quantum cascade lasers

### 6.1. Motivation

In the previous chapters THz-TDS was applied to study the optical properties of ultra-thin metal layers and the angular absorption characteristics of sucrose single crystals. In both cases the results show clearly the potential of this new measurement technique for upcoming tasks in the future. However, with some limitations both experiments could have been done also by FT-IR. Both sample types were optically active but showed not light amplification capability. This means, as far as nonlinearities can be neglected, that these samples can be treated as LTI<sup>1</sup> system. Only in the case of reflections the time-domain measurement technique gives a direct handle to the origin of them which is normally hidden by FT-IR or similar measurements. The real big purpose of THz-TDS are experiments where directly the phase resolved electric field is of interest. Especially this is the case if an active nonlinear media like an optical amplifier is under investigation. Then the material or device can be fully investigated. This includes its dynamics as well as the common other properties like the spectrally resolved absorption. This opens the possibility of investigating gain materials for lasers. The knowledge about such kind of measurements would help to improve any kind of laser operating in the THz frequency range.

As explained in chapter 2 a laser consists of much more than just a gain medium. The gain medium itself is embedded in a complete optical system designed for a special purpose. Hence, the output is determined by both of them. This makes is rather complicated to access all properties of the gain medium with the resonator around it. Perfect condition would be achieved if the gain medium itself is the resonator. Then the laser could be investigated without changing its properties or lasing conditions by additional optics within the cavity. Especially this is the case for semiconductor lasers. In the simplest case such devices consist of a laser diode with cut facets which act as end mirrors of the resonator. Through these facets light is emitted but can also be coupled in for measurement purposes.

Usually lasers are measured by emission spectroscopy (Fig. 6.1). In the simplest case the light emission of the laser is measured by FT-IR. In this way only the following properties can be directly measured:

---

<sup>1</sup>linear time invariant

## 6. Phase resolved transmission spectroscopy of terahertz quantum cascade lasers

- Output power
- Emission wavelengths
- Linewidth
- Light/current characteristics

By just measuring the emission of a light source any kind of losses stay usually hidden. Only in special configurations it is possible to determine the laser's waveguide losses [124]. Thereby two lasers are arranged directly as tandem or as multisection laser is used. One laser acts as single line reference while the other is examined. But with this technique only at the laser's emission wavelength this measurement can be done. All other parts of the spectrum stay masked. Further, the accuracy is very low ( $\pm 50\%$ ) and are far away from the real needs.

The situation changes completely by applying time resolved transmission spectroscopy like THz-TDS. By utilizing such measurement scheme much more than the usual emission properties can be accessed as are described above. First, by measuring the transmission through the active medium all optical properties are measured. This includes its amplification capabilities as well as all losses. Further, there is no essential need that the object of interest is lasing. Even if the lasing condition ( $\text{gain} > \text{losses}$ ) is not fulfilled the net gain in the structure can be measured because all changes relative to the reference signal are sensed. This opens new fields in laser research. For instance, temperature activated losses which hamper lasing operation can be easily measured.

Second, by measuring in time-domain the dynamics of the active medium is accessible. Since the different effects or reactions in the medium have different dynamics this technique can even distinguish them and get access to their real origin. By FT-IR the measured spectrum would be just a superposition of all observed effects and signals without any time information. But in time-domain it is possible to perform local FFTs (e.g. with data from 2ps long time slices) which would provide the dynamics and the spectrum of the observed effects as well. This means, the so-called THz seed pulse pumps, or so to say kicks, the active material which answers this disturbance by a oscillatory response. Further, as described in the previous chapters reflections are usually generated at any

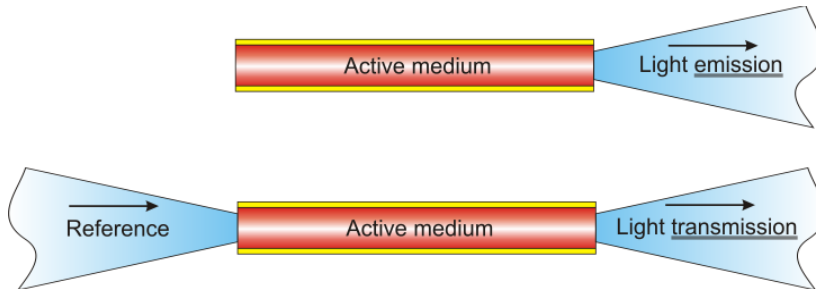


Figure 6.1.: Emission (top) and transmission spectroscopy (bottom) scheme of a laser.

optical interface (e.g. the boundary of the active medium). This makes it possible to observe something else. Namely, how lasing operation starts and develops in time. So far, this process could not be observed directly. In summary the advantages and options of time resolved transmission spectroscopy can be summarized as follows:

- Reference signal makes quantitative and qualitative comparisons possible
- Time-domain measurement scheme make dynamics of processes accessible
- Gain spectrally resolved
- Losses spectrally resolved
- Separation of effects by time resolved spectrum analysis

The examination with time-resolved transmission spectroscopy is not the only option which can be done with an active medium. If a medium with inversion of population is penetrated by an broadband optical pulse in the right way it should start to amplify all spectral components overlapping with its gain spectrum. If the amplification bandwidth would be as large as the optical pulse propagating through it this would lead to a perfect pulse amplifier. Since the direct generation of strong optical pulses is usually much more expensive than the proper amplification of weak pulses this would lead to a series of new applications. Especially in the MIR and THz frequency range such strong broadband sources would be of great importance in physics, chemistry and a lot of other fields.

For the demonstration of the measurement techniques and the described effects the quantum cascade laser is best suited. It consists of a semiconductor gain medium with cleaved facets acting as end mirrors and semi-transparent output couplers. Apart from the fact that it offers good measurement conditions, this relatively new laser type is still under development. Many effects in the active medium, temperature related losses and others are not fully understood yet. THz-TDS of QCLs could provide urgently needed information for the subsequent improvement and redesign of these lasers operating at THz frequencies.

## 6.2. Introduction to Quantum cascade lasers

### 6.2.1. Interband vs. intraband lasers

One of the main laser type for various applications is the bandgap semiconductor laser. Compared to other laser types (see e.g. chapter 2) they offer a series of superior properties. These are mainly high output power compared to the laser's size and the possibility of electrical pumping instead of optical pumping like it is necessary in gas and other solid-state lasers. At the moment their emission wavelengths cover a huge part of the electromagnetic spectrum starting from UV<sup>2</sup> down to infrared light [52]. However, in such lasers the bandgap energy determines the emission wavelength which is related to the material they

---

<sup>2</sup>ultra-violet

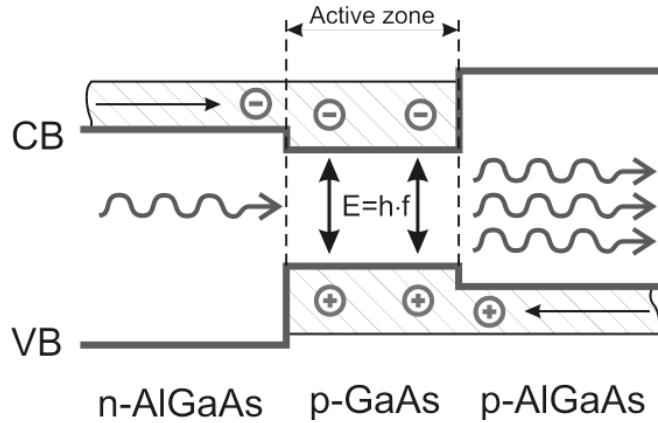


Figure 6.2.: Bandstructure scheme of a typical bandgap heterostructure semiconductor laser.

are made of. In Fig. 6.2 the typical scheme of a standard bandgap semiconductor laser is shown. Due to an applied electric field electrons and holes are injected into the laser's active zone. They radiative recombine there emitting one photon per electron/hole pair. As it is shown in the illustration the emission frequency is determined by the energy difference between the conduction band (CB) and the valence band (VB). Both are directly given by the material properties. This has a dramatic impact on the possible emission wavelengths of lasers based on this physical scheme. This means, not every emission wavelength is covered by a proper semiconductor material and most material combinations do not necessarily lead to a bandgap with a direct optical transition essential for light amplification.

There is a big lack of proper solid materials for long wavelength operation  $\lambda > 10 \mu\text{m}$  and especially for materials below the reststrahlenband ( $\lambda > 50 \mu\text{m}$ ) of GaAs. The solution for this problem are material systems with optical intraband transitions between their conduction subbands (Fig. 6.3). Thereby the light emission process does not take place between the conduction and valence band by radiative recombination of an electron with a hole. Rather the optical transition is performed within the conduction band. This has two major advantages. First, as shown and indicated in Fig. 6.3 such transitions have a narrower line width because in contrast to interband systems the optical transition takes place between similar shaped bands with equal energy gaps even for different momentums. Further, intraband transitions can be adjusted by bandgap engineering. Theoretically this means, all energy transitions smaller than the conduction band offset between the involved materials are possible.

By proper arrangement of ultra-thin layers of different materials a so called heterostructure is formed. This is typically done by solid source MBE<sup>3</sup> [125] or MOCVD<sup>4</sup> which offers high film thickness precision and quality. Depending on the materials and the layer thicknesses the energy sublevels can be designed and calculated by solving the Schrödinger equation and the dipole density matrix formalism [126] for a given heterostructure. A

<sup>3</sup>Molecular beam epitaxy

<sup>4</sup>Metalorganic vapour phase epitaxy



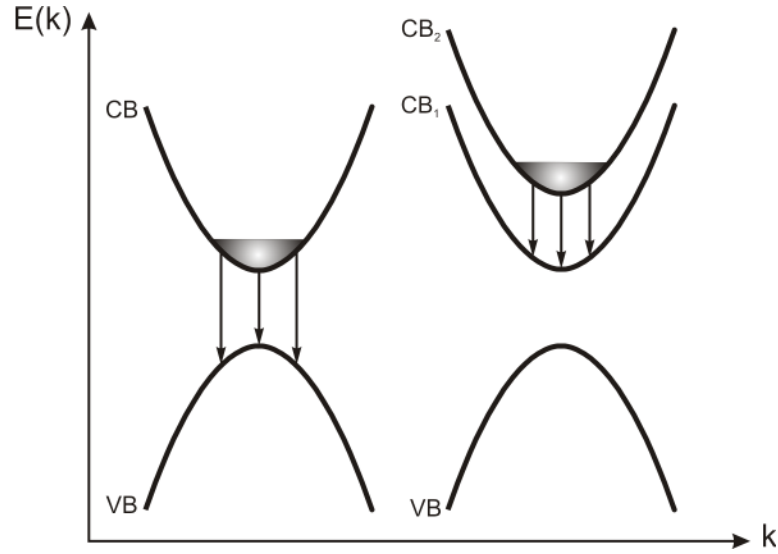


Figure 6.3.:  $E(k)$ -diagram of an interband (left) and an intraband (arrows indicate optical transition).

detailed description of QCL engineering and design can be found in [126, 127].

One of the most commonly used material system for designing heterostructures is *GaAs/AlGaAs* which have almost the same lattice constant and hence do not suffer from lattice mismatch problems [128]. By sandwiching a thin layer of *GaAs* between two barrier regions of  $Al_xGa_{1-x}As$  a quantum well structure is formed. The resulting energy levels within the quantum well are located between the conduction band edge of the involved materials (Fig. 6.4). But a single quantum well cannot be an effective intraband laser material. For this electrons have to be injected into the active zone and after the light emission process again extracted so that the light amplification process can be repeated. This is achieved by arranging such structures right after each other and biasing them. In this way the energy levels of the individual section get resonantly coupled [126]. In Fig. 6.4 the simplified scheme of such structure is illustrated. In every section an electron emits one photon and tunnels through a barrier to the next light emission section. Due to this repetition of equal sections the complete structure is called cascade.

The idea about such cascaded superlattice heterostructure structure is very old. The first theoretical concept was claimed by Kazarinov and Suris in 1971 [129]. Already their concept included the idea of an optical transition designed by bandgap engineering and electrons emitting one photon per cascade. Especially latter was a completely new idea in contrast to bandgap lasers where an electron is lost after emitting one photon.

However, it took more than 20 years more until this idea was realized as quantum cascade laser (QCL) by Faist et al. [14]. This first laser operated in the MIR at  $4.2\ \mu\text{m}$ . In addition, at this time the laser was operated in pulsed mode at liquid helium (lHe) temperature. Till today MIR laser made big progress and reached room temperature operation, continuous-wave mode and high output power up to several 100 mW [130, 131]. Although at this

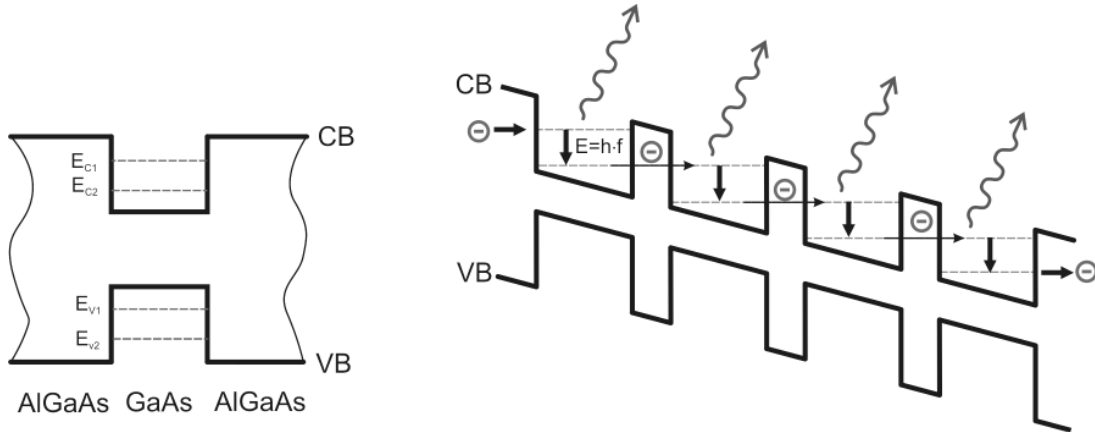


Figure 6.4.: Quantized energy levels in a heterostructure quantum well (left) and simplified bandstructure diagram of a biased quantum cascade structure (right).

time the physics and design of MIR-QCLs was well understood lasing operation could not be obtained at THz frequencies below the Reststrahlenband of GaAs. It was fast found out that at such low energies other mechanisms like electron/electron scattering have to be taken into account to effectively fill the upper lasing level and to remove carriers from the lower level of the lasing transition. First electroluminescence experiments proofed the possibility of light emission at THz frequencies [132]. The first concept of a THz-QCL was stated by Köhler et al. [133] who also demonstrated the first realization of a QCL operating in the THz frequency range [20]. Especially here QCLs are urgently needed due to a huge lack of convenient coherent light sources.

### 6.2.2. Terahertz quantum cascade laser design parameters

Since the first realization and proof of principle this laser type made large steps towards real applications. For this purpose the performance parameters of such lasers have had to be improved. This included mainly:

- Long wavelength emission
- High output power
- Low threshold current
- Low dissipation power
- High operation temperature
- Continuous-wave operation

Some of these parameter are fully or partly achieved already. Mainly the work of Williams et al. [21, 134, 24] demonstrates well the potential of THz-QCLs. But still this device is

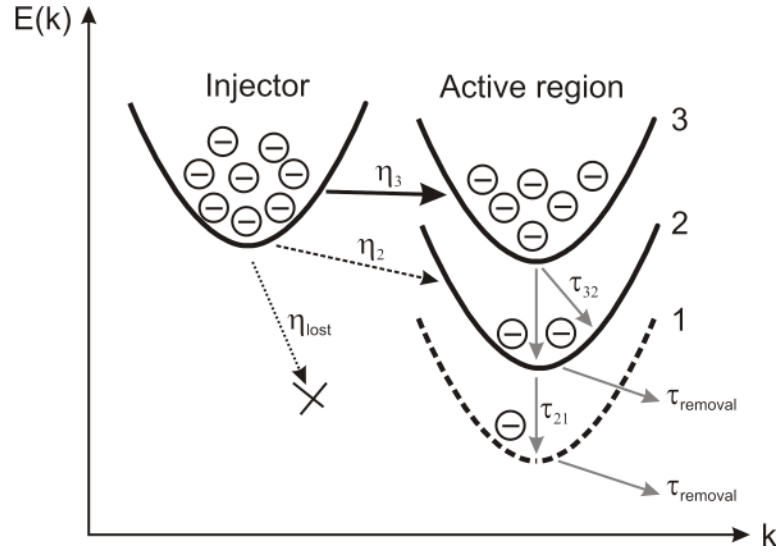


Figure 6.5.: Simplified bandstructure  $E(k)$ -diagram of a QCL with injector and active region states.

not fully understood yet. Various designs have been developed to cover different needs and applications. But so far, every design had its own performance parameters.

The gain achieved by a particular design can be described by a model illustrated in Fig. 6.5. Further the gain

$$G = \sigma \cdot \Delta n \quad (6.1)$$

is proportional to the transition cross section  $\sigma$  and to the population inversion  $\Delta n$ . In this general model the population inversion for a given structure can be modelled by [135]

$$\Delta n = \frac{J}{q_0} \cdot \frac{1}{n} \sum_{i=1}^n (1 - \eta_{lost})^i \cdot \left[ \tau_3 \eta_3 \cdot \left( 1 - \frac{\tau_2}{\tau_{32}} \right) - \eta_2 \tau_2 \right], \quad (6.2)$$

where  $\tau_x$  is the total electron lifetime at an certain energy level,  $\tau_{xy}$  is the intersubband electron lifetime between two states,  $\eta_x$  are the fractions of the total current  $J$  injected into the individual states,  $n$  are the number of cascades and  $q_0$  is the elementary charge. A very important parameter is the current fraction  $\eta_{lost}$  which indicates how many electrons are not effectively injected into the laser's active region but rather lost in the conduction band of the of the barrier material. Since this happens in each cascade its impact on the overall inversion is modelled by  $\frac{1}{n} \sum_{i=1}^n (1 - \eta_{lost})^i$ . However, as in all lasers the design has the function to optimize the gain and so the population of inversion. Mainly this includes to prevent phonon assisted scattering of electrons into the continuum which is strongly temperature dependent as well as proper filling of the upper lasing level and the removal of carrier from the lower lasing level.

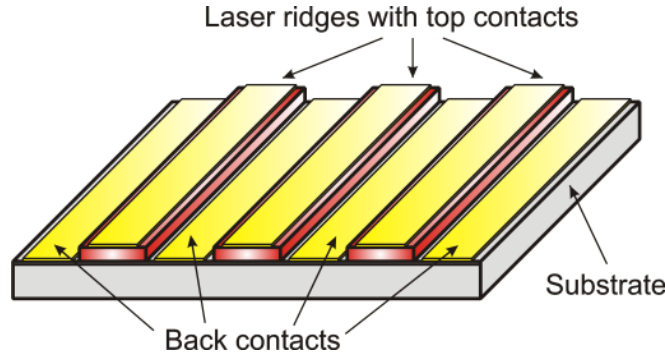


Figure 6.6.: Typical realization a QCL fabricated on a semiconductor substrate.

### 6.2.3. Waveguiding and mode confinement

Typically the waveguide and optical cavity of a QCL has the shape of a long slab (Fig. 6.6), also called laser ridge, which has a length up to a few millimeter and a width comparable to its emission wavelength. In this configuration the electrical contacts are formed on the top and bottom of the slab. Apart from the optimization of the active zone which determines directly the gain of the laser material the waveguiding properties of the slab determine if and under what conditions lasing operation is possible. The lasing condition (gain > losses) in a QCL can be approximated by

$$G \cdot \Gamma \geq \alpha, \quad (6.3)$$

where  $G$  is the gain of the active region,  $\Gamma$  is the confinement factor of the laser mode with its active zone and  $\alpha$  are the summarized losses. Latter can be split into waveguide losses  $\alpha_w$  and the mirror losses

$$\alpha_m = -\frac{\ln(R)}{L}, \quad (6.4)$$

where  $R$  is the reflectivity of the facets and  $L$  is the length of the laser. Since the mirror losses are given by the reflectivity of the end facets of the waveguide material the corresponding losses can only be minimized by implementing a high reflective coating (HRC) onto one facet. For the typically used material systems like GaAs this has a value of about 33 %. So by optimizing the reflectivity by a HRC the mirror losses can only be reduced by a factor of 2.7. Much more potential is included in the optimization of the waveguide structure which has direct impact on the waveguide losses as well as on the confinement factor. Further, if a sub wavelength vertical confinement is used for waveguiding this has a direct impact onto the mirror losses as is explained later.

### Cladding

The standard method in optics for guiding waves is to implement a so called optical cladding [50]. An example scheme for this method is shown in Fig. 6.7. Thereby the

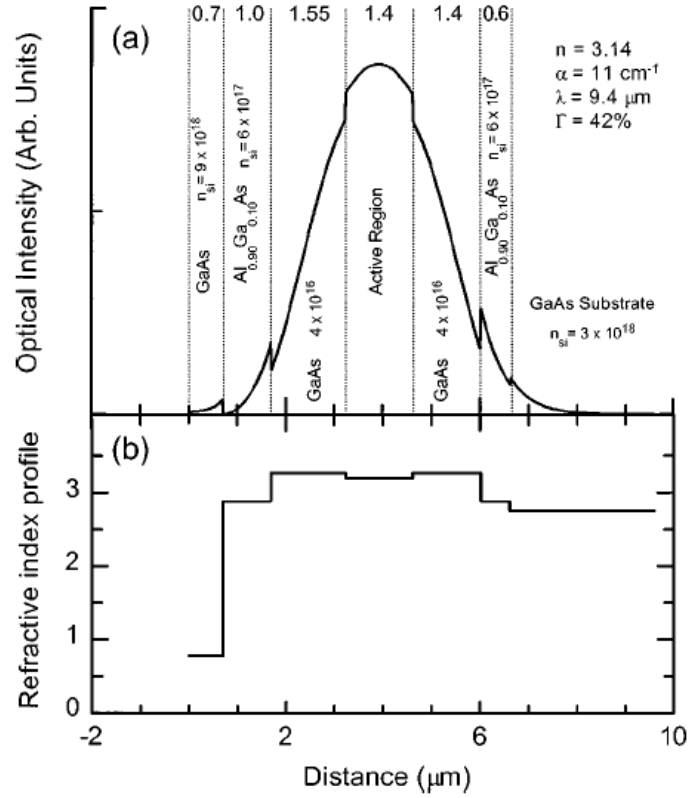


Figure 6.7.: (a) Mode intensity profile in the dielectric waveguide in the direction perpendicular to the layers. The numbers on top of the figure are their thicknesses in  $\mu\text{m}$ . Material composition and the doping concentration in  $\text{cm}^{-3}$  are also indicated. (b) Refractive index profile in the direction perpendicular to the layers (from [128]).

wave propagates in a material surrounded by one or more layers made of dielectric materials with lower refractive index. Due to the resulting total internal reflections at this optical interface the waves stay in the optically high dense material if their angle of incidence is larger than

$$\Theta_c = \arcsin\left(\frac{n_2}{n_1}\right), \quad (6.5)$$

where  $n_1$  is the refractive index of the core material and  $n_2$  of the cladding. Since dielectrics or at least moderately doped materials are used for the cladding such confinement method is low loss and easy to implement. For instance such method is used in semiconductor bandgap lasers and most MIR-QCLs. In all QCLs the lateral waveguiding is made by the air/semiconductor interface of the ridges where the surrounding air acts as cladding. The vertical confinement in QCLs by cladding is only possible in MIR-QCLs. The reasons for this is explained later. However, in such a way a confinement factor  $\Gamma > 0.9$  [128] can be achieved. This factor can be even improved by growing MIR-QCLs on highly doped semiconductor substrates ( $n_{\text{Si}} > 10^{18} \text{ cm}^{-3}$ ). Since the plasma resonance frequency of

## 6. Phase resolved transmission spectroscopy of terahertz quantum cascade lasers

heavily doped semiconductors like GaAs or Si is below the MIR frequency range, the real part of the refractive index drops significantly at MIR frequencies (see Fig. 6.7). This leads to a increased refractive index contrast and a higher confinement factor. The typical realization of a QCL made with cladding or a surface plasmon (explained below) is illustrated in Fig. 6.6

### Surface plasmon waveguide

In THz-QCLs ( $\lambda \approx 100 \mu m$ ) a mode confinement method described above is not possible. The reason for this is a conjunction of many reasons. First, a high quality MBE growth is only possible for structures with a thickness of a few  $10 \mu m$ . This is mainly related with the long time needed for the growth ( $\sim 10 \frac{\mu m}{day}$ ) of a standard sample and the drift of the deposition rates and layer quality during such a long span of time. Due to this limitation the active zone is usually much thinner than the wavelength. This causes a deep penetration of the wave into the cladding. As mentioned above the plasmon frequency of a typical heavily doped semiconductor material is not located below THz frequencies. This results in high Drude losses caused by free carrier absorption [134]. A solution for this problem are so called surface plasmon waveguides as they were used for the first realized THz-QCLs [20]. Thereby the mode is confined between heavily doped semiconductor or metal layers within the active zone (Fig. 6.8). Due to the vertical subwavelength confinement the mode is mostly guided in an undoped low loss substrate like GaAs resulting in a low confinement factor (typically  $\Gamma = 0.13$ ) resulting in high threshold currents but high output powers.

### Double metal confinement

The todays standard waveguide design in THz-QCL basic research is to sandwich the active zone between two metal/semiconductor interfaces which is a special case of surface plasmon waveguides (Fig. 6.8). A detailed description about the technological processes can be found in [134]. Here the mode is squeezed directly between two metal layers resulting in a confinement factor close to unity. Since the active zone is smaller than the emission wavelength of THz-QCLs this type of mode confinement suffers from much larger losses than in surface plasmon waveguides which are typically 6 times larger.

But the sub wavelength confinement has an additional impact on the facet's reflectivities in the resonator. They rise close to unity too. This results in much lower mirror losses which nearly vanish and compensate more than fully the increased waveguide losses (Eq. 6.3). This leads in comparison to surface plasmon waveguides to decreased threshold current densities. Although such low threshold current is one of the major objectives in QCL design they show only low output powers due to the high facet reflectivity. Such waveguides are mainly used if low driving currents are needed or a new laser design has to be tested.

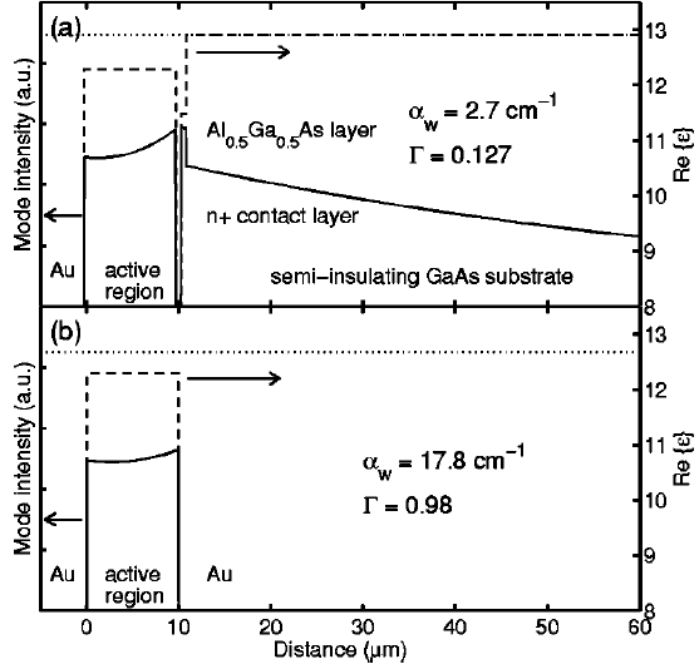


Figure 6.8.: Mode intensities (solid lines) and the real part of the dielectric constant  $\epsilon(\omega)$  (dashed lines) for the (a) SI-surface-plasmon waveguide and (b) double-sided metal waveguide. The dotted line represents the square of the modal effective index (from [134]).

### 6.3. THz quantum cascade laser samples and wave coupling

One of the main objectives during this work was the comparison of different THz-QCLs from various viewpoints. Mainly these interests were focused on the:

- Gain below and above threshold current
- Real gain bandwidth
- Amplification of few cycle THz pulses
- Dynamic of initiated pulse amplification
- Changed losses by operating or heating the device

All of them are of great interest and urgently needed for the next stage of development. Final objective is to use the results and the gained experiences for the direct suggestion of improvements to THz-QCL designers. This would lead to an active quality control of the redesign of such lasers in the viewpoints mentioned above. Especially the losses in these structures are of great interest.

In addition, to obtain the above mentioned performance parameters of THz-QCLs proper methods for the coupling of pulsed THz radiation have to be developed, tested and optimized.

### 6.3.1. Specification of THz quantum cascade laser samples

For the following experiments two different THz-QCLs were used. In this work they are referred as T1 and T2. Their properties are summarized in Tab. 6.1. Apart from their slightly different physical dimensions they have different design wavelengths. Although they are based on the same bound-to-continuum design and material system [136] significantly different optical properties should be measurable by THz-TDS.

Laser	T1	T2
Center emission line [THz, $\mu\text{m}$ , meV]	2.87 / 105 / 11.87	2.05 / 146 / 8.48
THz beam coupling method	silicon lens + aperture	waveguide coupler
Design of active zone	bound-to-continuum	bound-to-continuum
Material system	$\text{GaAs}/\text{Al}_{0.15}\text{Ga}_{0.85}\text{As}$	$\text{GaAs}/\text{Al}_{0.15}\text{Ga}_{0.85}\text{As}$
Ridge length [mm]	2	1.6
Ridge width (active, full) [ $\mu\text{m}$ ]	110 / 200	250 / 250
Theoretical mode spacing [GHz]	22	28
Active zone thickness [ $\mu\text{m}$ ]	12	14
Waveguide type	surface-plasmon	surface-plasmon
Substrate thickness [ $\mu\text{m}$ ]	200	200
Number of periods	90	110
Peak output power [mW]	15	50
Applied electric field [kV/cm]	2.1	1.5
Threshold current density [ $\text{A}/\text{cm}^2$ ]	105	115

Table 6.1.: Quantum cascade laser specification and dimensions.

The bandstructure diagram for both QCL operated at optimal bias conditions is shown in Fig. 6.9. In the diagrams the typical bandstructure characteristic of the bound-to-continuum active zone design is visible. Here the effective injection of electrons into the upper lasing level is achieved by a staircase like structure and the well separated next energy level above it. This corresponds to a high filling rate of the upper lasing level and a low loss of electrons into the continuum (see Eq. 6.2). The different lasing transition and the fact that both QCLs have the same injector structure should result in a corresponding behavior or spectral features observable in transmission experiments. A detailed description of the QCLs used in this work can be found in [137, 23].

The main difference between T1 and T2 are their emission spectra. Regardless of the applied driving current T1 shows only one main lasing line apart from two very weak side modes separated by the mode spacing (Fig. 6.10). This behavior stays in contrast to the emission spectrum of T2 where the emission lines as a function of the current do not stay fixed and more than one is observed. The single and multimode emission properties measured by THz-TDS is discussed in the next sections.



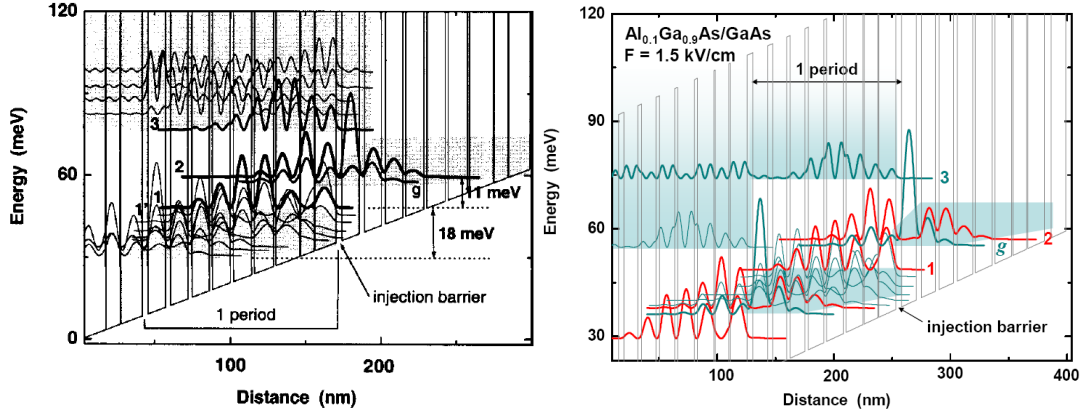


Figure 6.9.: Bandstructure diagram of the QCLs (from [136, 23]). (left) T1 and (right) T2.

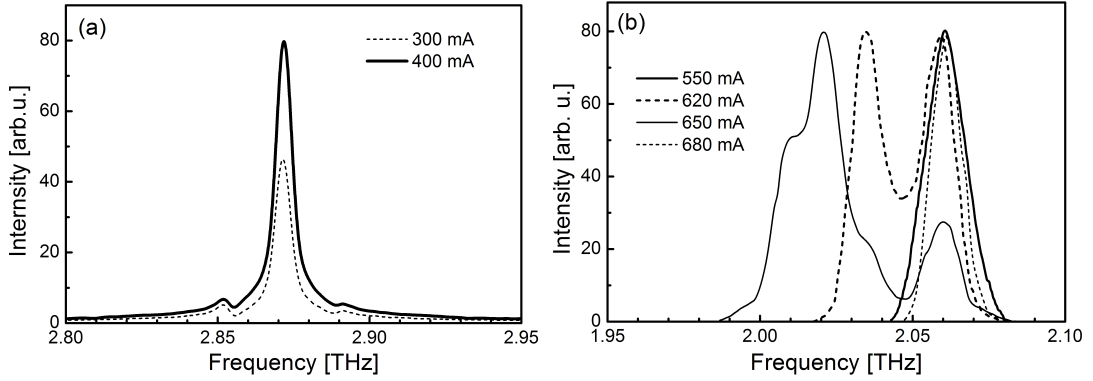


Figure 6.10.: Optical output spectrum of (a) T1 and (b) T2. The current values for T2 correspond to the laser measured in referred publication at 5 K and are scaled to lasers dimensions (from [137]).

### 6.3.2. Wave coupling and light vs. current characteristics

As explained at the beginning of this chapter, one of the main objectives was to develop an efficient method for coupling broadband free space THz pulses into a QCL's waveguide. The coupling method should provide:

1. High efficiency referred to free space signal
2. Direct guiding and focusing of THz pulses into one particular QCL waveguide
3. Suppression of bypassing signal components

First point is the typical demand for every coupling method. As much as possible radiation should be coupled. The second and third point is directly related to the special requirements for this experiment. Usually more than one laser ridge is processed on a single chip. This makes it essential to guide the wave directly to a chosen laser ridge. Otherwise parts of the THz pulse would propagate through the unused chip parts and other parts

## 6. Phase resolved transmission spectroscopy of terahertz quantum cascade lasers

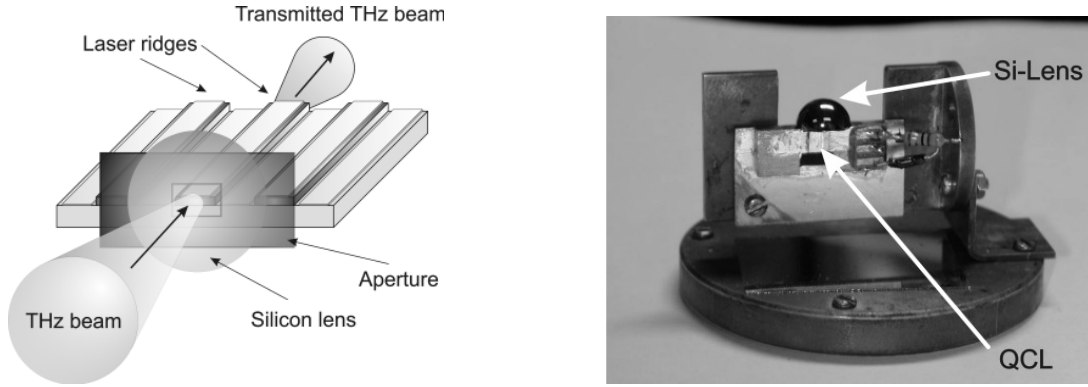


Figure 6.11.: Scheme of incouple optics into a QCL's waveguide (left). Photograph of a THz-QCL mounted on a cryostat finger (right). Arrows indicate the laser and the incouple optics with silicon lens.

will simply travel beyond it. This problem has two impacts on the measured transmission signal. First, the signal consists of more than one THz pulse. In general the pulse through the sample or laser and replica which took other paths through the optical system. This results in difficulties to distinguish between them and their reflections caused by the optical interfaces in the system. Second, only the signal through the active zone is of interest. Other components like the substrate mode through the other parts of the chip does not carry information regarding the active zone. In this case only the waveguide losses of this mode can be observed. To fulfill the above claimed needs for proper wave coupling two different methods were developed and successfully applied respectively to the QCLs T1 and T2.

The initial method used for T1 implements an additional optical system in front of the QCL under investigation. The principle and realization of this lens coupling method is illustrated in Fig. 6.11. The optics consists of two components. First part is a  $200 \times 200 \mu\text{m}$  metal aperture fabricated onto a silicon plate of  $300 \mu\text{m}$  thickness. This plate was then put in direct optical contact onto one of the laser ridges. In this way the bypassing signal parts were masked and only the signal through one laser is measured. Further, on this aperture a silicon lens is placed. In this way the THz beam is further focuses directly into the QCL's waveguide and the coupling into the waveguide takes place at an interface of materials with similar optical properties (Si and AlGaAs/GaAs). Since the wavelength at the optical interface is reduced by a factor of more than three due to the material's refractive index the coupling efficiency into the  $\sim 10 \mu\text{m}$  thick active zone rises by the same factor. Apart from the advantage that this improves the overlap between the coupled wave and active zone this minimizes reflection losses at this interface due to the similar optical properties. The reduced reflectivity at this facet of the QCL has an impact on the threshold current which is shown later.

The second and latter applied coupling method used for T2 is an integrated waveguide emitter/coupler (see chapter 2). Instead of coupling externally generated THz waves the

### 6.3. THz quantum cascade laser samples and wave coupling

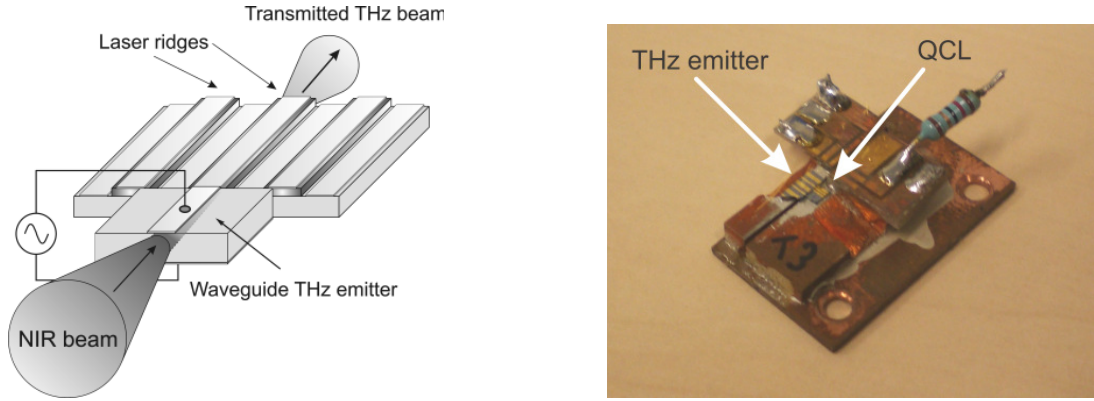


Figure 6.12.: Scheme of a THz waveguide emitter directly coupled with a QCL (left). Photograph of a THz-QCL mounted on a copper holder (right).

emission process and waveguiding is made at once. In front of the QCL a THz waveguide emitter is placed. In this particular case the top contact has the same size as the QCL's laser ridge (Fig. 6.12). At the position between the biased metal stripes the NIR laser beam generates a THz wave which is bound to the top metalization. In this way the wave is guided directly into the QCL. Compared to the lens coupler this method has significant advantages which are:

- Setup dimensions are smaller due to integrated emitter/waveguide unit
- Better mechanical stability
- Easier and faster alignment due to visible pump instead of invisible THz beam

In this work the waveguide coupler turned out to be the best choice. Especially since it shows equal transmission signals compared to the lens coupler with externally THz generation. In Fig. 6.13 a typical transmission signal through the laser structure of T1 and T2 are shown. At the emission frequencies of the T1 and T2 a signal dynamic of  $\sim 39\text{ dB}$  and  $\sim 14\text{ dB}$  respectively is achieved. More than convenient for THz-TDS experiments of reasonable expenditure of time.

As already mentioned above both coupling methods have an additional consequence on the QCLs threshold currents. By installing additional optical components at one QCL facet its reflectivity becomes smaller. Resulting in larger mirror losses which have to be compensated by additional gain achieved by larger driving currents. Indeed, for both QCLs with their individual coupling optics the threshold, compared to the corresponding publications increased by about  $20\text{ A/cm}^2$ . The resulting output power vs. driving current characteristic (LI-curve) is shown in Fig. 6.14. In the following sections these figures are referred as lasing region.

## 6. Phase resolved transmission spectroscopy of terahertz quantum cascade lasers

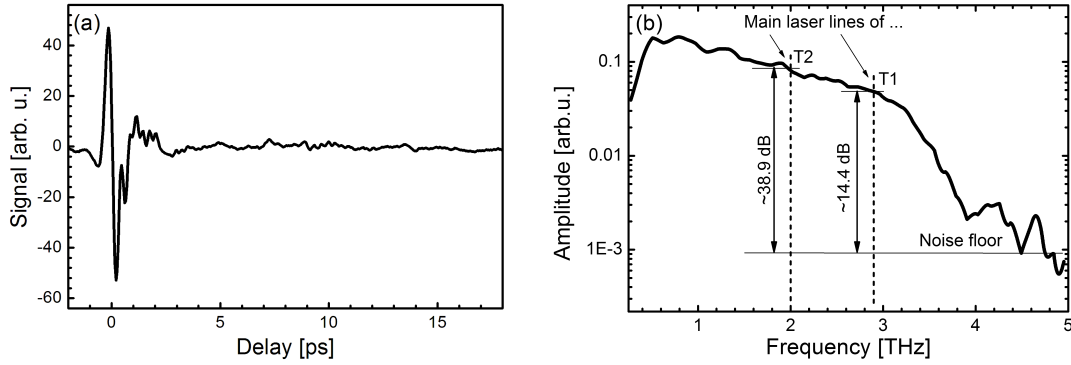


Figure 6.13.: Typical transmission signal through T1 and T2 measured by THz-TDS. (a) Time-domain and (b) spectrum.

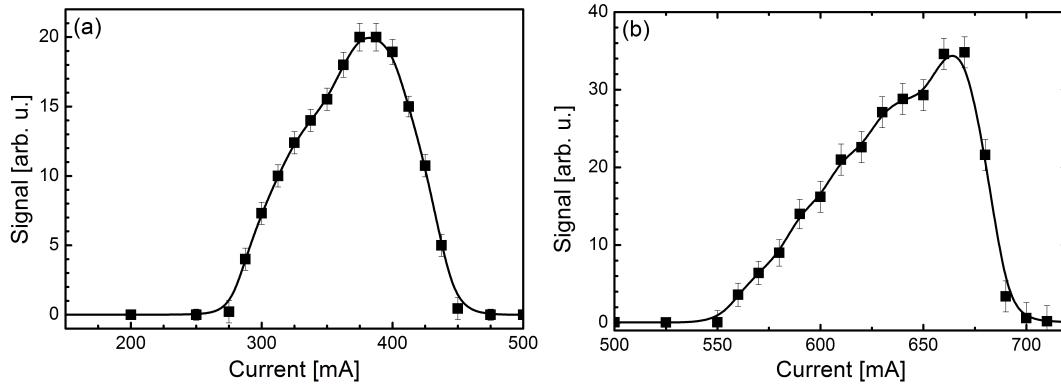


Figure 6.14.: QCLs output power as a function of the driving current for the laser (a) T1 and (b) T2.

## 6.4. Modulation spectroscopy technique

For obtaining the results and parameters of THz-QCLs explained at the beginning of this chapter usually simple on/off spectroscopy techniques are applied. This means THz-TDS signal traces are recorded for two different conditions. In this particular case of an electrically driven device this includes the state on and off. In this way the impact on the reference signal, measured before for the condition 'off', as a result of the operated device is measured. Since for such experiments these two signal traces are measured sequentially that can result in system drift problems.

By activating the device not only loss and gain mechanisms as might be desired become visible. A lot of other physical effects change the environmental conditions and so, disturb significantly the measured results. One of the main problem is the energy consumption of the device resulting in a temperature increase compared to the measured reference signal. Since the real thermal conditions in an actively operated device like a QCLs are more or less unknown this results in a random temperature distribution. As is shown later this temperature increased is strongly dependent on the current level during operation.

### 6.5. Coherent probing of terahertz quantum cascade lasers

However, due to the locally increased temperature the optical properties are changed. Further, the mechanical properties and dimensions of the surrounding installations like the heatsink of the laser changes too. Serious problems are caused by the following parameters:

- Position of laser on the heatsink
- Heat conductivity of the heatsink
- Optical properties of the waveguide

Especially the last two points are the most disruptive for the measurements. By performing time-resolved experiments any change of the refractive index results in a changed delay of the measured signal. In other terms, by applying on/off spectroscopy techniques interesting optical parameters and data can be distorted.

The solution for this problem is modulation spectroscopy. Thereby the THz signal and the QCL emission are modulated at different frequencies  $\omega_1$  and  $\omega_2$  with constant phase relation between them. According to the well known trigonometric theorem [138]

$$k_1 \cdot \cos(\omega_1) \cdot k_2 \cdot \cos(\omega_2) = \frac{k_1 \cdot k_2}{2} \cdot [\cos(\omega_1 + \omega_2) + \cos(\omega_1 - \omega_2)] \quad (6.6)$$

two new signals at the sum and difference frequency are generated. Since the strengths  $k_i$  of the original signals are split apart and mixed the final signal strength at the new generated frequencies is  $\frac{k_1 k_2}{2}$ . This shows the capability of this measurement scheme making even small signals visible by strongly modulating it by another source. Further, compared to on/off spectroscopy the modulation techniques shows a much higher dynamic reserve and a low 1/f noise if the sum frequency is used [65]. Latter is clear due to the up shifted frequency while the other is not trivial. Let us assume a measurement system with a SNR of 60 dB and relative signal changes of 1 % which are caused by operating the device. This results in a SNR of 20 dB for the real signal of interest. While the dynamics of 40 dB is simply lost due to the full scale needed to measure the carrier signal. Due to applied modulation spectroscopy the carrier signal is at another frequency than the on it modulated signal. In this case the full SNR of 60 dB can be exploited for measuring the real signal which corresponds to an increase of dynamic reserve of 40 dB. The quality increase can be either used to maximize the signal quality or to reduce the needed measurement time.

A graphical illustration of this modulation scheme is shown in Fig. 6.15 for two signals modulated at 4 and 5 Hz and equal signal amplitude. The corresponding difference and sum frequency is 1 and 9 Hz respectively with 50 % signal amplitude compared to the initial signals.

## 6.5. Coherent probing of terahertz quantum cascade lasers

Main objective of this work was to bring forward the proof of principle of coherent probing of active devices operating in the THz frequency range. In addition, it should be shown

## 6. Phase resolved transmission spectroscopy of terahertz quantum cascade lasers

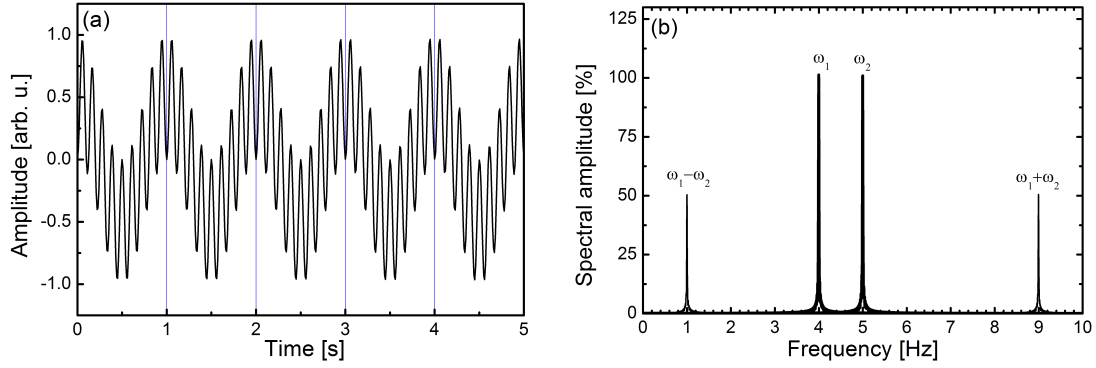


Figure 6.15.: Modulation signal of two beating frequencies at 4 and 5 Hz in (a) Time-domain and (b) frequency.

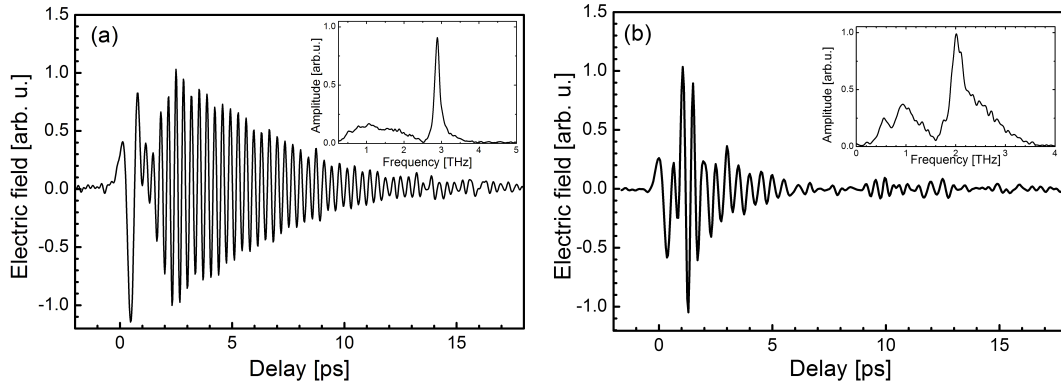


Figure 6.16.: Modulation signal of T1 (a) and T2 (b). Signal measured at QCLs maximum output power (insets show corresponding spectrum).

what parameters are accessible with THz-TDS and to compare the results with standard measurement techniques like FT-IR. For this task the above introduced THz-QCL samples were used as representative medium. Further, new coupling methods and measurement techniques were applied. All ideas and progress during the time span of this work lead finally to the results and successes presented in the next chapters.

### 6.5.1. Applied modulation spectroscopy

For the QCL characterization the above described modulation spectroscopy technique was applied. In this way just the signal differences due to the laser operation were sensed without any background signal. By coupling THz pulses into the laser's active medium they become seeded and the initiated response of it can be sensed in time. The experiments were done under certain conditions to get access to various device parameters as are shown later. However, the result of every measurement is a time-resolved signal trace corresponding directly to the transmitted electric field.

In Fig. 6.16 the modulation spectroscopy signals (further on just called 'signals') are

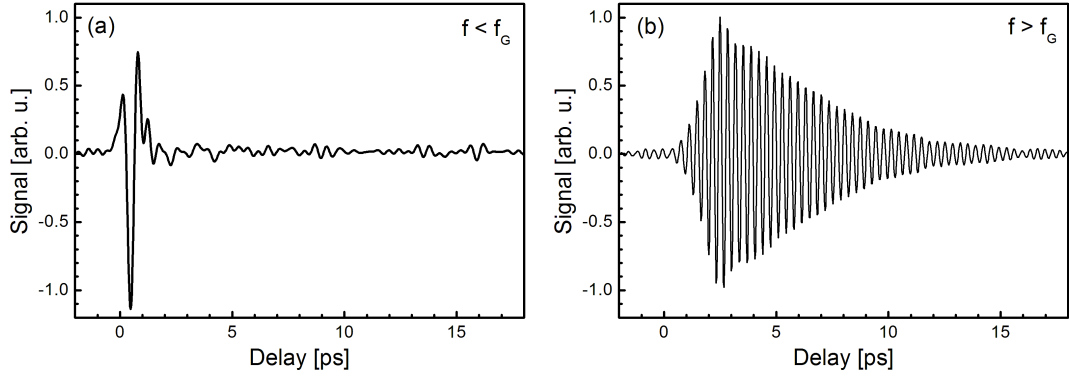


Figure 6.17.: (a) Low-pass and (b) high-pass (right) filtered ( $f_G = 2.5 THz$ ) modulation signal of T1 (Fig. 6.16) at full output power.

shown for the lasers T1 and T2 operated at full output power level. Although the lasers have different emission lines (see Tab. 6.1) their signal shape in time-domain looks similar. The spectral information and meaning of these similarities gets clear by comparing the signals with the full transmission signal (Fig. 6.13). Each signal consist of at least two components. The leading part is a replica of the probe pulse located within the first few picoseconds after the THz pulse excitation. This part is the same in both cases but more pronounced for T1 since it is spectrally more separated from the other part. This initial signal part is followed by long oscillation decaying with a time constant of  $5.2 ps$  for T1 and  $2 ps$  for T2 which corresponds to the linewidth of the corresponding spectral feature and is explained later.

The mentioned spectral components can be separated by proper low- and highpass filtering. This separation is illustrated for T1 in Fig. 6.17. Compared to T2 here the spectral regions of reduced losses and gain are clearly defined and correspond to an instant and oscillatory response of the excited system. First, is caused by losses and reduced absorption occurring concurrently with the incidence THz pulse (Fig. 6.17a). More information can be obtained by looking at the highpass filtered signal (Fig. 6.17b). Here it is well seen that the THz probe pulse acts as so called seed pulse too. After the active medium is seeded it starts to amplify coherently spectral components matching with its gain bandwidth. The gain bandwidth relative to the emission frequency corresponds to a fast or slow decay of this oscillation like it is shown in Fig. 6.16 for the used QCLs.

This spectral separation of spectral components can be illustrated more detailed by time windowed FFT analysis. In contrast to wavelet analysis [139] where the local identity of the chosen pulse shape is tested here a  $2 ps$  time window was simply shifted over the whole signal trace and a FFT was calculated. The individual spectra were arranged to the plot shown in Fig. 6.18. The plot proofs well that in the signal trace of T1 two distinct activities separated in time and frequency take place.

## 6. Phase resolved transmission spectroscopy of terahertz quantum cascade lasers

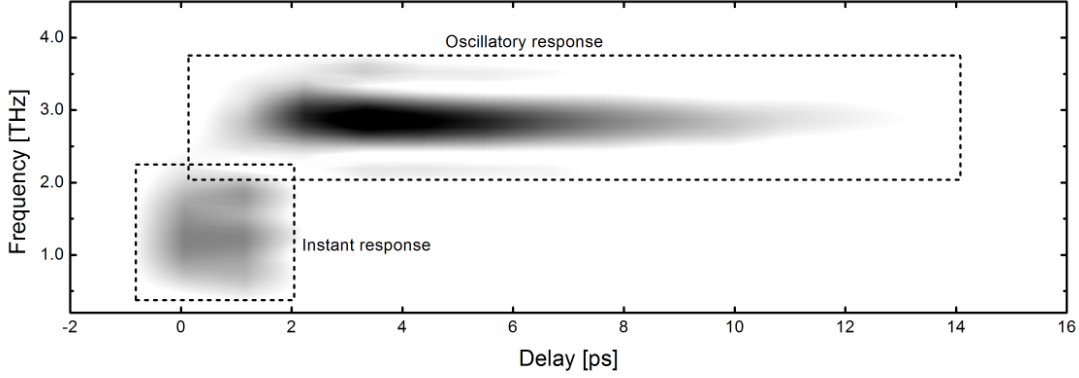


Figure 6.18.: Time-resolved FFT analysis of the modulation signal of T1 operated at full power (Fig. 6.16). 2 ps time windows were shifted over the whole modulation signal.

### 6.5.2. Gain characterization and laser emission lines

In laser physics the characterization of the gain medium is one of the most important tasks before building a laser. This includes mainly the current or pumping light field dependency of the gain and its absolute value. Latter is of great importance since in combination with the losses it determines the stable lasing operation. By performing the gain measurements in transmission mode gain can be observed already before lasing operation starts. Very important in laser physics is to evaluate the light amplification capability of a material. For determining the gain of the QCL materials a series of signal traces like shown in Fig. 6.16 was recorded at different driving currents. The frequency dependent gain  $g(I, \omega)$  in terms of power provided by a material can be calculated as

$$E_{QCL,on}(I, \omega) = E_{Reference}(\omega) \cdot e^{\frac{g(I, \omega)}{2} \cdot L}, \quad (6.7)$$

where  $E(\omega)$  is the spectrally resolved electric field,  $I$  is the driving current, and  $L$  is the length of the device. But as mentioned above no on/off measurement scheme was used. As a consequence Eq. 6.7 cannot be used to evaluate the lasers gain. In the case of applied modulation spectroscopy where the temporal change of the electric field  $\Delta E_{QCL,on}(I, t)$  is measured the standard formula has to be modified. The resulting gain spectrum can be obtained by the adopted formula

$$\Delta E_{QCL,on}(I, \omega) = K \cdot E_{Reference}(\omega) \cdot \left( e^{\frac{g(I, \omega)}{2} \cdot L} - 1 \right), \quad (6.8)$$

where the linear factor  $K$  summarizes all effects having an impact on the modulation amplitude like the QCL's driving duty cycle.

The results of the gain measurements of T1 and T2 using Eq. 6.8 are shown in Fig. 6.19. One can clearly see that gain is observed below lasing operation takes place. Up to the maximum value of  $14 - 15 \text{ cm}^{-1}$  the gain rises more or less linear with the driving current.



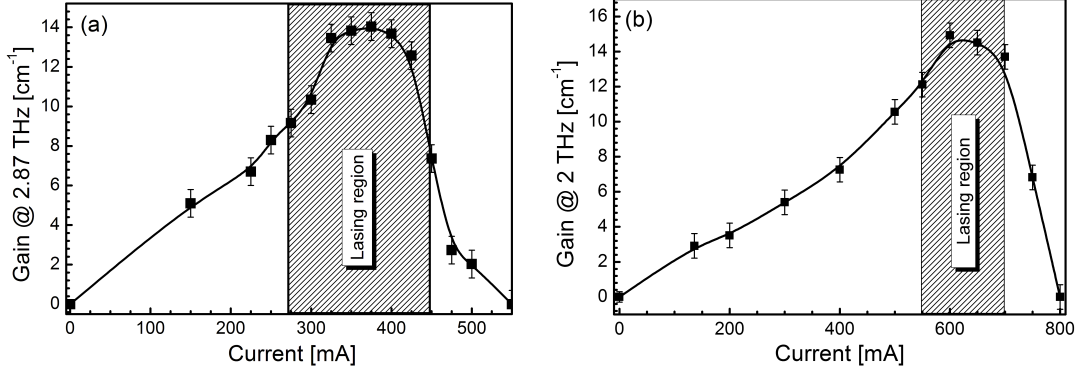


Figure 6.19.: Current dependency of single pass maximum gain of the QCLs T1 (a) and T2 (b) (shaded parts indicate the lasing region of the lasers) .

Such characteristic was expected and corresponds to the gradual alignment of the individual cascades. By applying an electric field the bandstructure gets tilted as illustrated in Fig. 6.4. The process of cascade alignment does not happen instantly. This would be only the case in a perfectly grown structure without interface roughnesses and precise layer thicknesses which exists only in theory. However, in reality the alignment of the individual cascades happens gradually. By increasing the bias field more and more cascades align properly (see Fig. 6.4). This gives the measured gradually increasing gain until lasing starts by exceeding the threshold current. Above this current value this tendency changes. The linear gain increase stops. This behavior stands in good agreement with the laser theory. When lasing operation starts the gain at the lasing wavelength is mostly consumed by the now emitted light field. This leads to a reduced optical gain sensed by the THz probe beam. In the figures this is conspicuous by the flattened top of the curves. At the end of the lasing region the cascades start to break up due to the high applied bias. But like below the threshold current value, some gain is still observable. This manner is pursued by exceeding the upper lasing threshold current. Here still gain can be measured and has linear falling off tendency but drops much faster.

The gain values presented here are proven and represent the minimal values. The transmitted THz pulse propagates not only through the active zone of the QCLs due to the mode profile. It spreads into the substrate the laser was grown on. By including typical confinement factors  $\Gamma \approx 0.25$  [23, 20] the real gain value is expected to be in the range of  $40 \text{ cm}^{-1}$ . Similar calculated values have been reported by Williams et al. [140]. Our first demonstration of spectrally resolved gain measurements show the potential of such experiments to get access of proven values unknown so far. Further, the measured values for the gain are not falsified by a changed refractive by driving the device's active zone [141]. This was verified by the THz pulse position which was the same for all conditions.

Apart from the absolute numbers concerning the gain, spectrally resolved transmission measurements like THz-TDS provide much more information. Since the probe pulses sensed by THz-TDS carry a broad spectrum the position, shape and bandwidth of the

## 6. Phase resolved transmission spectroscopy of terahertz quantum cascade lasers

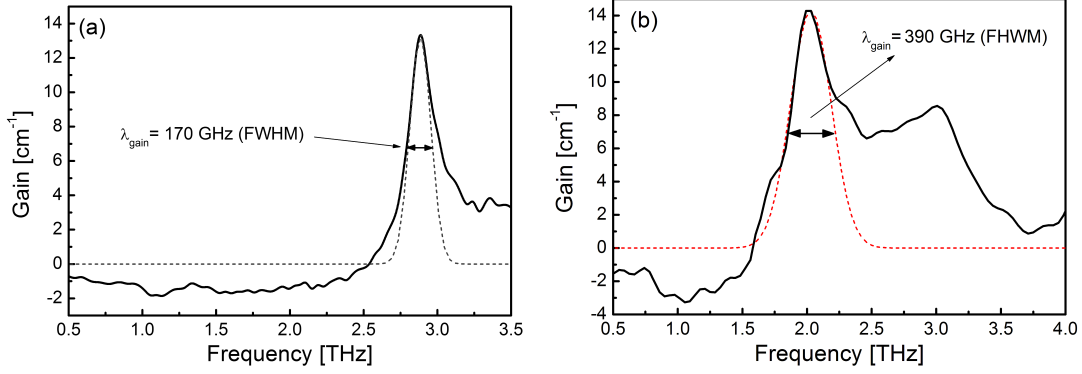


Figure 6.20.: Spectrally resolved gain/reduced losses for T1 (a) and T2 (b) operated at full output power (dotted line indicate gain bandwidth fitted by a Gaussian line shape).

gain spectra are obtained. This information is very important. For instance the resonator could be redesigned so that the waveguide losses are low at frequencies where the gain is high. Further, as mentioned above the cascades start to align gradually. One of the main reasons for this behavior are quality inaccuracies during the growth. As a consequence they align at different bias levels and show different emission wavelengths. This inhomogeneous broadening is directly responsible for the oscillation length shown in Fig. 6.17. The broader the gain bandwidth the shorter the oscillations are and vice versa. For the used QCLs the gain bandwidth was fitted by a Gaussian line shape (Fig. 6.20). T1 exhibits 170 GHz bandwidth while T2 has one of 390 GHz. For future broadband pulse amplification this parameter is of great importance. This fact and the efforts to achieve mode-locking in QCLs (see chapter 2.3.1) strongly dependent on the gain bandwidth. Therefore, to achieve broadband amplification with high gain will be an important task in the future.

From the data shown in Fig. 6.20 even the different lasing transitions can be evaluated by calculating the spectrally resolved refractive index where resonances become visible. Theoretically the discrete FFT algorithm provides a phase which corresponds to the refractive index but the information content of it is almost zero. Since the FFT provides only phase information in the range  $]-\pi, \pi]$  no phase devolution can be correctly traced due to the discrete values. Without having a continuous phase the course between two points is unknown. Many mathematical programs offer a numerical procedure called “unwrap” function which tries to estimate the real phase course but the quality of the final results is more or less unknown. The correct spectrally resolved phase can be instead calculated by the Kramers-Kronig relation [142]. With this relation and the spectral information from Fig. 6.20 corresponding to an absorption  $\alpha(\omega)$  the phase can be determined by

$$\Delta n(\omega) = \frac{c}{\pi} \cdot PV \int_0^\infty \frac{\alpha(\Omega)}{\Omega^2 - \omega^2} d\Omega, \quad (6.9)$$

where  $c$  is the vacuum speed of light and  $PV$  means the principal value of the integral.

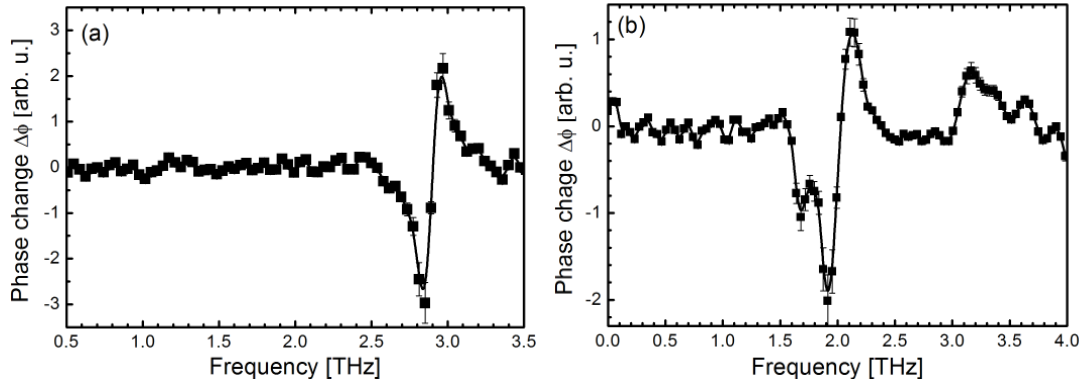


Figure 6.21.: Phase diagram of the gain spectra of (a) T1 and (b) T2.

The calculated phase is shown in Fig. 6.21. The shape correlates well with the gain and the position of the emission lines of the QCLs (Fig. 6.10). Fig. 6.21a shows that T1 has only one gain region exhibiting the typical phase of a resonance. For laser T2 the situation is different. At least two resonances are observable. One at  $\sim 1.9$  and the other at  $\sim 2.1$  THz indicating the existence of two gain regions aligned at the same bias level. This property explains its more than doubled bandwidth compared to T1. The limited resolution and the lack of other available sources does not allow to specify this more in detail. But the results show how powerful THz-TDS is for the study of this very interesting parameter.

### 6.5.3. Spectral hole burning

The results presented above showed the spectral position, bandwidth and the absolute number of the gain in two QCLs as a function of the driving current. By seeding the QCL's active region it amplifies certain parts of the THz probe pulse. As already mentioned above and shown in Fig. 6.19 the slope of the current dependence of the gain changes when exceeding the laser's threshold current. Since the data shown in Fig. 6.20 is just part of a huge THz-TDS measurement series the resolution was limited by the scanning time and the system drift. At this conditions no spectral feature due to lasing operation can be observed in detail. As a rule of thumb the relation

$$\text{measurement time} \propto \text{spectral resolution} \times \text{signal quality} \quad (6.10)$$

can be approximated. For the observation of spectral hole burning as a consequence of lasing activities the resolution was increased up to 20 GHz by a long term scan. This made it possible to observe spectral hole burning effects shown in Fig. 6.22. When the QCLs start lasing the inversion in the active zone at the emission line is consumed by this activity. The photons emitted by this action have of course equal phase but no set phase relation compared to the reference THz probe pulse. Out of the reference phase this radiation cannot be sensed and its radiation spectrum is lost. In the figure the lasing lines

## 6. Phase resolved transmission spectroscopy of terahertz quantum cascade lasers

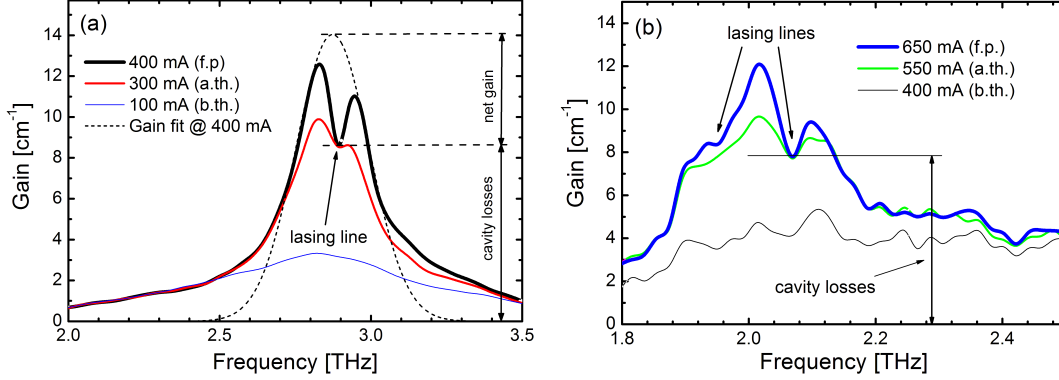


Figure 6.22.: Gain spectra with observable spectral hole burning due to lasing operation in T1 (a) and T2 (a). (f.p.=full power, b.th=below threshold, a.th.=above threshold).

are identified by kinks. As shown in the optical output spectrum (Fig. 6.10) T1 showed only one emission line while T2, due to its wide gain spectrum, is capable to emit on several lines. This corresponds very well with the results gained by THz-TDS. The gain spectra rise with the same shape as shown in Fig. 6.20. But by exceeding the threshold current value the gain at the lasing lines, 2.87 THz for T1 and 1.94 & 2.07 THz for T2, stays constant. From this data important parameters can be read out.

First, the observed gain at the kinks corresponds to the optical cavity losses at this emission line for the coupled THz pulse. The waveguide of T1 at 2.87 THz shows waveguide losses of  $8.5 \text{ cm}^{-1}$ . In addition, by drawing a Gaussian fit corresponding to the inhomogeneous broadened lasing transition into the gain curve diagram a net gain of  $5 \text{ cm}^{-1}$  could be observed without considering the confinement factor. Both values are consistent with the above presented gain estimation including the confinement factor. The waveguide losses in T2 are 8.3 and  $7.7 \text{ cm}^{-1}$  for the measured emission lines at 1.94 and 2.07 THz, respectively. Latter mode spacing is consistent with the values presented in Tab. 6.1. In the case of T2 a correct value for the net gain was hindered by the deformed gain spectra shape. This hampered a Gaussian fit like done for T1 which is essential for the determination of this value.

### 6.5.4. Longitudinal spatial hole burning and gain shift

All results presented above were measured and calculated using single pass signal data. In this way the combined gain/loss characteristics in the structure could be determined. But gain and reduced losses cannot be separated. Further, in this way the dynamics of initiated lasing cannot be observed. To obtain this information multipass data is needed.

Every THz seed pulse coupled to the laser's waveguide is partly reflected at the end facets. This leads to multiple round-trip signals which manifest themselves as delayed pulses. Since these pulses sustain cavity gain and losses more than once they show differ-

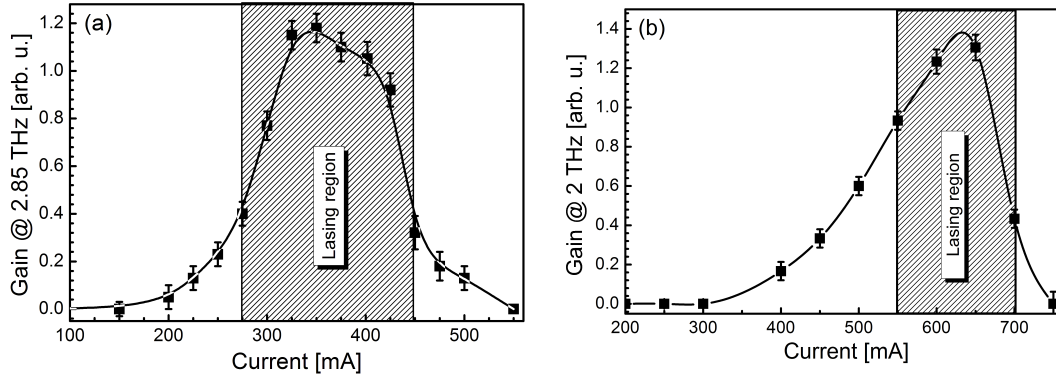


Figure 6.23.: Gain/current dependency of the first round-trip signal within (a) T1 and (b) T2.

ent spectra and current dependency in respect to each other. As mentioned in section 6.3.2 the attached incoupling optics (lens and waveguide coupler) open slightly the cavity. This has several impacts on the transmission and modulation signals. First, it reduces the reflectivity at the facet where the additional optical components are attached and results in a weaker round-trip signal of the coupled THz wave and a slightly increased threshold current ( $\sim 20 \text{ A/cm}^{-2}$ ) is observed for both lasers. As a consequence the multipass gain/current characteristics looks different from than shown in Fig. 6.19. The corresponding gain/current curves for the first round trip signals are shown in Fig. 6.23. Compared to the single pass signals gain appears at much higher currents ( $I_{T1,threshold,3passes} = 150 \text{ mA}$ ,  $I_{T2,threshold,3passes} = 300 \text{ mA}$ ). This behavior gets clear if the lasing condition ( $\text{gain} > \text{losses}$ ), directly probed by this experiment, is taken into consideration. Below the threshold level the coupled THz wave experiences gain but losses as well. Without fulfilled lasing condition latter effect dominates and the signals decrease after each pass and spectrally shapes. This shows the increased threshold current for the observed modulation signal. This mechanism and tendency carries on until after a series of round-trips the current/gain characteristic of the modulation signals shapes equally compared to the light-current (L-I) curves (Fig. 6.14) of the corresponding QCL. Under this condition finally the lasing condition is fulfilled. Since the facet reflectivity and mode profile is mostly unknown the values in Fig. 6.23 can only be given in arbitrary units.

Apart from this lasing condition the above described effect can only be explained by another effect present in laser too. When lasing operation starts a standing electric field wave pattern is formed. This results in a second order grating (Fig. 6.24). In the nodes where the electric field of the standing wave is zero the full gain is available for the amplification of the transmitted THz seed pulse. In the antinodes the situation is vice versa. Here the strong local electric field vector couples to the optical transition and is amplified leading to a gain clamping. This effect, also called longitudinal spatial hole burning (LSHB) [143], has a direct impact on the local refractive index distribution. LSHB can be measured by transmitting a beam perpendicular to the laser's waveguide and comparing it with a

## 6. Phase resolved transmission spectroscopy of terahertz quantum cascade lasers

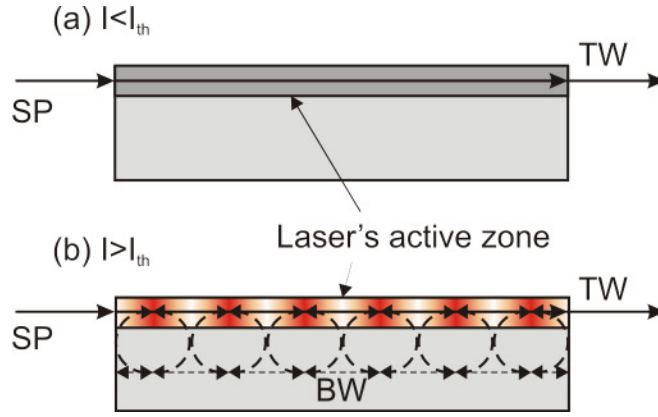


Figure 6.24.: Scheme of the local power intensity distribution of a QCL waveguide below (a) and above threshold (b) current (SP=seed pulse, BW=backward wave, TW=transmitted wave).

reference which reflects the refractive index pattern. Since the metallic top contacts of the QCLs prevent such measurement a indirect proof of LSHB is considered.

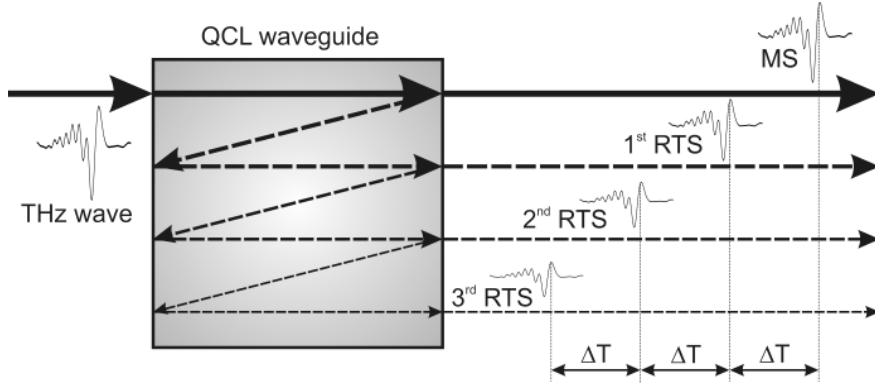


Figure 6.25.: Optical scheme of the THz signals transmitted through a QCL waveguide (MS: main signal, RTS: round trip signal,  $\Delta T$  round trip time).

For this proof, the round-trip signals in T1 (Fig. 6.26) and T2 (Fig. 6.27) are measured. An illustration of these delayed round-trip signals in the THz-QCL waveguide is shown in Fig. 6.25. Subsequent to the main signal the internal reflections are sensed which are delayed by multiples of the round-trip periods. For the used lasers these signals are delayed by  $\sim 47.5 ps$  and  $\sim 38.9 ps$  for T1 and T2, respectively. Without refractive index grating these round-trip signals should be just a time delayed replica of the single pass signals. In this case changes can mainly occur due to spectral changes by the waveguide losses and gain saturation effects. Since the peak electric field in the experiments presented here is far below the non-linear regime ( $E_{THz} < 100 V/cm$ ) latter effect is not expected. Further, if linear changes like waveguide losses occur the signal should not change its delay given by the round-trip time.

This is not the case for the measured signal traces (see Fig. 6.26 and Fig. 6.27) . Taking

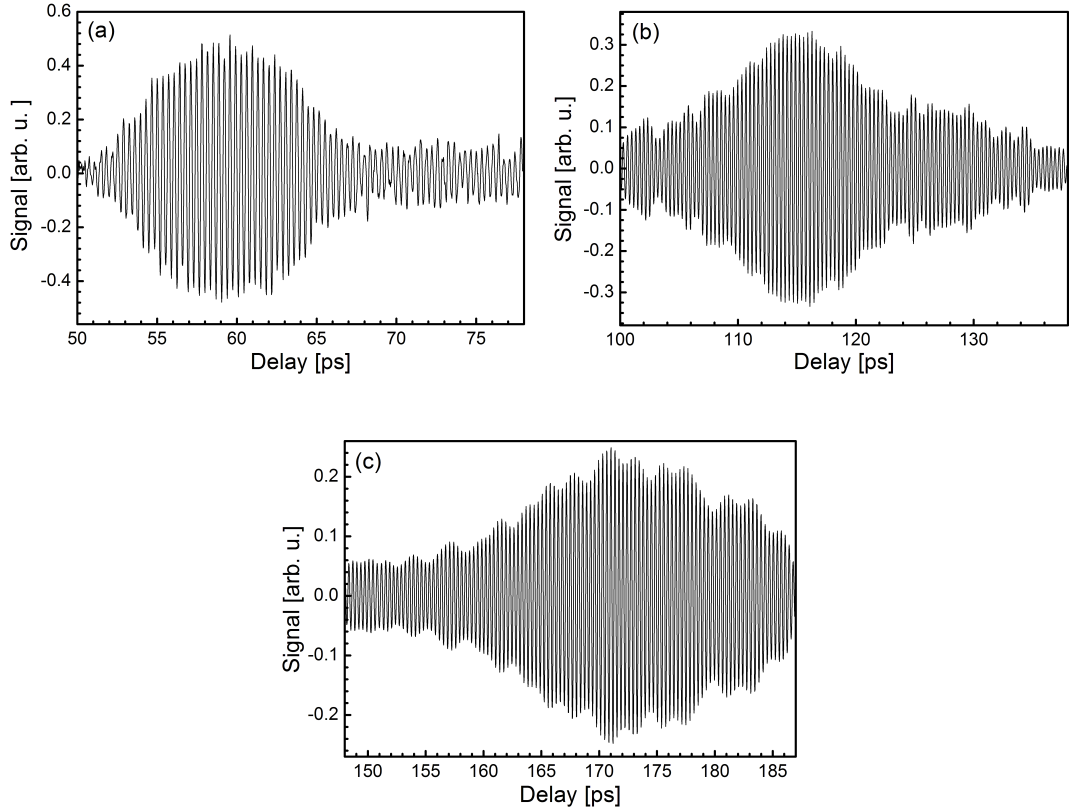


Figure 6.26.: Round trip signals through T1. (a) 3 passes, (b) 5 passes and (c) 7 passes (signals are lowpass filtered  $f_G = 3.5 THz$ ).

the position of the maximum electric field amplitude of the main oscillation frequency an additional delay per round-trip of  $\sim 9 ps$  and  $\sim 3.5 ps$  occurs for T1 and T2, respectively. Apart from the changed gain/current characteristics of the first internal reflected signal (Fig. 6.23) this additional delay is an evidence of the existence of LSHB in the QCLs. On the formed grating the THz pulse is partly back scattered at every node/antinode optical interface. Apart from this delay these multisection reflections in the QCL have another impact on the signal shape. Due to the optical grating the structure's optical properties get extremely frequency selective. The consequence of this is illustrated in the round-trip figure sequence of T1 (Fig. 6.26). Starting from the single pass signal (Fig. 6.16) the shape of the modulation signal changes. First, spectral components die off by frequency selective amplification and losses. Second, frequency selective scattering in the laser resonator happens. These two effects are responsible for the signal shaping. After 3 passes the THz signal's (Fig. 6.26a) low frequency components related to reduced losses and absorption vanished mostly. The originally long decaying oscillation forms a symmetric bubble shaped signal which is longer than the original. Further, due to the LSHB this leading part is followed by a cw THz wave with constant amplitude. This process is repeated and the oscillation length gets longer and longer. Already after 7

## 6. Phase resolved transmission spectroscopy of terahertz quantum cascade lasers

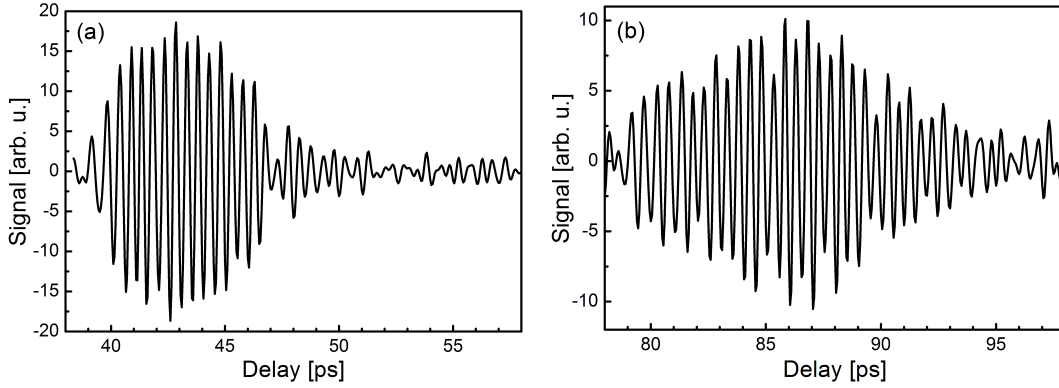


Figure 6.27.: Round trip signals through T2 after (a) 3 passes and (b) 5 passes.

passes the original transmitted THz pulse formed a more than 30 *ps* long oscillation which is headed and followed by a lasting cw THz wave.

Apart from the indication of LSHB in the QCLs, the evolution of this cw wave can be interpreted as starting lasing activities. For the single pass THz pulse the active zone provides the largest available gain in the structure. Resulting in a very fast rising signal amplitude followed by a long decay. After passing the end facet the wave propagates back through a partly depleted region which has still not finished its local gain recovery process. For the back propagating THz pulse this means that for the leading parts no full gain is available but the on-going gain recovery process amplifies other components of the THz pulse. So, the THz pulse starts to form a bubble lead and followed by a cw wave. After each cavity pass the THz pulse's core part gets longer and weaker until it cannot be anymore distinguished from the cw wave.

In spite to normal lasers, where most likely vacuum fluctuations are responsible for the initiation of stimulated emission [52], here this process is initiated by the coupled THz seed pulse acting as system disturbance. Since this seed pulse has known phase this lasing process can be directly observed which stands in contrast to the other effects which are launched with random phase.

The round-trip signals show another interesting detail. From the single pass signal the gain curve can be determined which is important for the development of a THz semiconductor pulse amplifier. But for redesign issues of THz-QCLs it is of great interest to know the real gain shape for the multi round-trip signals. Especially, this information cannot be obtained by emission spectroscopy or FT-IR. Latter measures the cumulative signal and cannot pick out a certain time window to make the signal dynamics visible. As in all lasers the cavity length determines the mode spacing and the lasing condition defines which modes are allowed. Especially, if the mode spacing is large it can happen that the gain spectrum does not overlap with only one mode or they are not located in the maximum. Usually such circumstance is exploited to obtain a single mode laser.

Examining the spectra from the individual time windows it gets clear that both QCLs



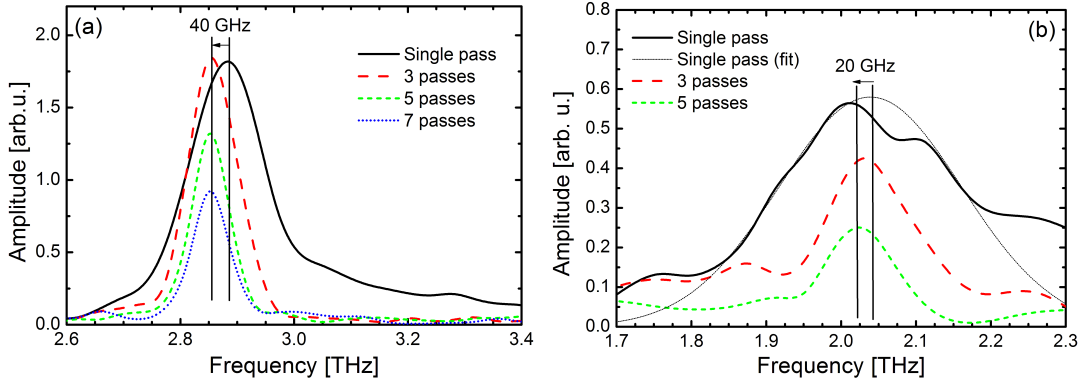


Figure 6.28.: Spectral comparison of internal round-trip signal of (a) T1 and (b) T2 .

are not optimally designed (Fig. 6.28) or the available gain spectra for the coupled THz probe pulse and the lasing mode are different. However, for the coupled mode the gain spectra get narrower, smaller and shift to lower frequencies (2.85 THz for T1 and 2.02 THz for T2). They get narrower due to frequency selective scattering (LSHB) and already after 5 passes the final gain spectra for the coupled mode is established.

As is shown in Fig. 6.28 the spectral amplitude after each roundtrip decreases. As one would complain now, this stands in conflict with the expected continuously amplified signal whose amplitude should rise or stay constant. The explanation for this artifact is trivial and has two reasons. First, the oscillation gets longer but weaker due to energy conservation in the active zone. So parts of the signal components become hidden in the noise floor. Second, due to the pulse lengthening signal components become located outside of the measured time window which is limited due to system drift during the measurement. Further, after a few passes the signals cannot be any more separated by time windows because they overlap. These circumstances prevent a proper determination of the gain spectra characteristic as a function of the signal passes.

### 6.5.5. Spectral limitations caused by thermally activated absorption

The modulation spectroscopy technique introduced and successfully applied in this work enabled the measurement of the real gain in THz-QCLs. It provides for the first time an insight view in this difficult devices and their physics. As explained above simple on/off transmission experiments would not have been able to provide the presented data. Apart from the problems with the limited dynamic reserve the temperature conditions would prevent proper data processing due to thermally induced changes in the involved materials.

But transmission measurements made in on/off mode can provide helpful data and information about the optical properties of the QCL's active zone and its waveguide. For instance in this way thermally activated absorption mechanisms can be observed and quantified. This information would be of great interest since THz-QCLs are limited to cryogenic

## 6. Phase resolved transmission spectroscopy of terahertz quantum cascade lasers

operation conditions. As explained above these devices have to be cooled (at least to liquid nitrogen  $T \approx 77K$ ) to prevent thermally assisted depopulation of inversion. By comparing the absorption data obtained at various temperatures for the activated and switched off device the real device temperature can be determined.

Typically in emission spectroscopy experiments of QCLs the heat sink temperature is stated as device temperature. But due to the distance between the temperature sensor of the cryostat cold finger and the mounted laser, the temperature conditions on both places are different. Only in pulsed operation mode and at small duty cycles the heat sink temperature corresponds more or less with the device temperature. But such operation condition is far away from the cw operation needed for commercial applications.

To analyze the thermally induced changes the laser T1 was selected and installed in a temperature controlled liquid helium cooled cryostat. The THz pulse coupling was made by an aperture and a lens as explained above. The spectral changes in the laser's waveguide were obtained by pulse transmission in the temperature range 5-300 K. Since mainly the changes correlated with temperature increase were of interest, the absorption was evaluated relatively using the formula

$$\alpha(\omega, T) = -2 \cdot \frac{\ln \left( \frac{E_{QCL}(\omega, T)}{E_{QCL,off}(\omega, 5K)} \right)}{L_{WG}}, \quad (6.11)$$

where  $E(\omega, T)$  is the electric field spectral amplitudes of the measured transmitted THz probe pulse measured at 5 K and  $L_{WG}$  is the length of the THz-QCL waveguide. The THz pulse spectrum  $E_{QCL,off}(\omega, 5K)$  for the inactive device at 5 K was taken as reference. In such representation the increase or decrease of the losses in the laser waveguide are represented directly - the reduced or increased gain with respect to the conditions at 5 K is presented as increased or decreased absorption in the spectrum respectively.

The temperature dependence of the absorption in the THz-QCL without applied bias is shown in Fig. 6.30a. For the unbiased laser the losses of the waveguide at 5 K are almost frequency independent and were estimated to be  $8 \pm 1 \text{ cm}^{-1}$ . This value is in reasonable agreement with that calculated for the given THz-QCL design [136, 144] and is assigned to Drude absorption in the QCL active region, doped contact layers and the top waveguide metallization. The absorption increases with rising heatsink temperature. In the unbiased case the heatsink and device temperatures are considered to be equal. The onset of the absorption is observed at a temperature of about 50 K. Above this temperature an absorption feature centered at about 3 THz appears. By increasing the laser's temperature this absorption band gets stronger and broadens mainly towards lower energies. At 150 K the calculated absorption coefficient at 3.1 THz is  $\sim 32 \text{ cm}^{-1}$  which is the maximum observable value due to the dynamic range of the measurement (at given frequency). The origin of this absorption band is discussed later in detail.

Quantitatively, the temperature dependence of the absorption  $\alpha(\omega, T)$  at the 3.1 THz absorption peak is shown in an Arrhenius plot (Fig. 6.29). Using the relation

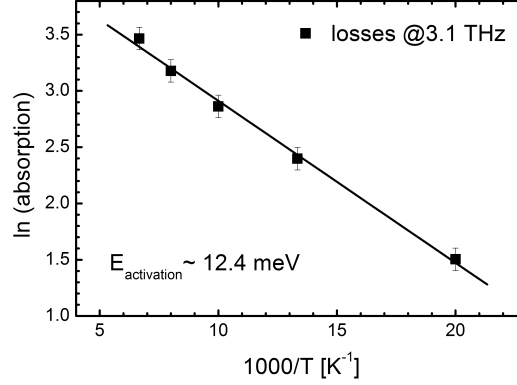


Figure 6.29.: Arrhenius plot of the absorption feature at 3.1 THz.

$$\alpha(\omega, T) \propto \exp\left(-\frac{\Delta E_a}{k_B \cdot T}\right), \quad (6.12)$$

where  $\Delta E_a$  is the activation energy,  $k_B$  is the Boltzman constant and  $T$  is the device temperature, an activation energy of this absorption feature of 12.4 meV is obtained.

The increase of the operational temperature above 100 K is associated also with an increase of the absorption over the whole observed frequency range, as a result of the absorption by thermally activated free carriers. An activation energy of the order of 0.18 eV is estimated for this process.

Measurements for the THz-QCL biased at the condition of the maximum THz output power ( $I=380$  mA) were also performed. The QCL was driven by  $7 \mu\text{s}$  long current pulses with a duty cycle of  $\sim 15\%$ . In Fig. 6.30b the temperature dependence of the waveguide losses in the active device are shown. As before the spectrum of the inactive device measured at 5 K was taken as reference. Already here differences due to the gain centered at 2.87 THz can be observed. Those changes get much more pronounced by building the difference between the obtained spectra.

Since all absorption spectra were derived by the same reference they can be subtracted without restrictions. This is shown in Fig. 6.30c. The gain is observed at the frequency of  $\sim 2.87 \text{ THz}$  as indicated by the negative peak in the spectra obtained at 5 and 25 K. At heat sink temperatures above 50 K the gain disappears and the difference spectra show additional losses (positive peaks at 2.87 and 3.1 THz). Since the absorption increases with the temperature, the observed additional losses at 3.1 THz indicate that the actual operation temperature in the laser's active region is higher than the heat sink temperature.

We have estimated these temperature difference using Eq. 6.12 and an activation energy of 12.4 meV. Between 25 and 50 K, the temperature of the QCL's active region is about 15-20 K higher than that of the heatsink. This difference is illustrated in Fig. 6.31a. Similar findings were presented for a comparable THz-QCL with a surface plasmon waveguide by Vitiello et al. using micro photoluminescence measurements [145]. At higher temperatures the difference between the active region and the heat sink increases up to 35-40 K at 80 K.

## 6. Phase resolved transmission spectroscopy of terahertz quantum cascade lasers

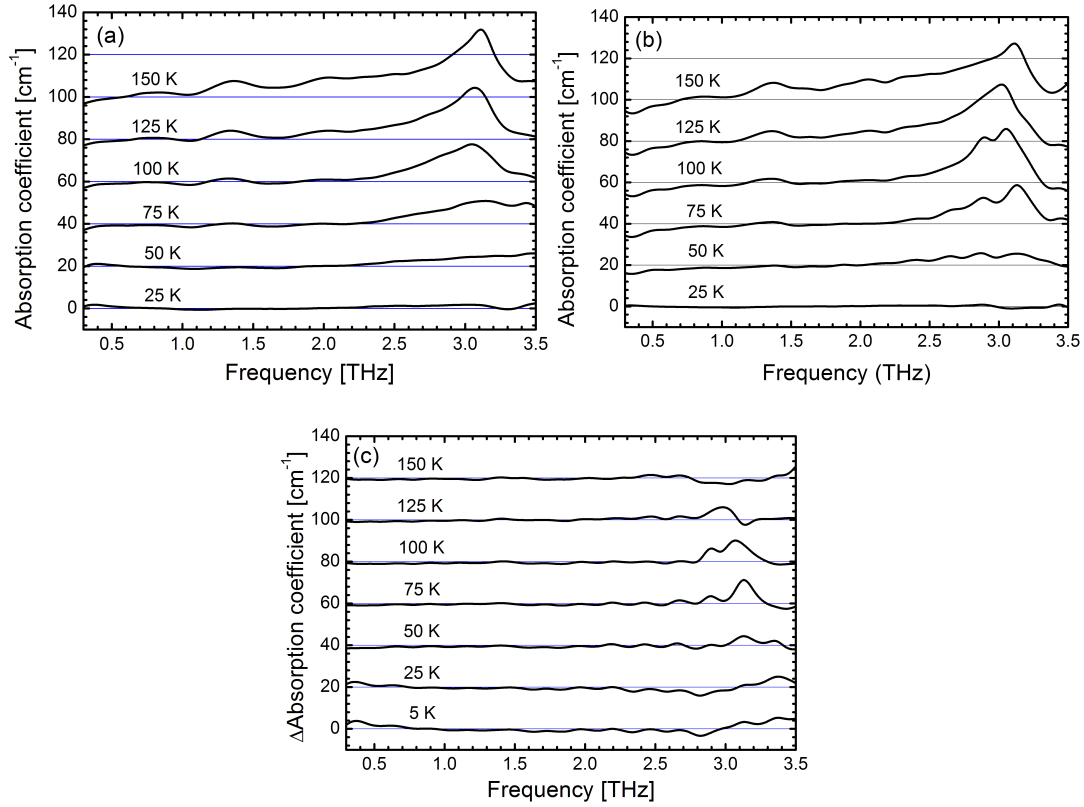


Figure 6.30.: Temperature dependent transmission absorption spectra for (a) QCL off, (b) QCL on and (c) change in the absorption transmission spectra (the figures are offset for clarity).

This gives a real device temperature of 115-120 K. Beyond this temperature the difference apparently drops and vanishes at 150 K (Fig. 6.31b). Reason for this observed drop is the above mentioned limitation by the signal dynamic range and photon assisted scattering of electrons into the continuum. Latter are in contrast with the observed broadband effect. However, in principle we correlate it with the roll-off of the THz-QCL output power [136].

The observed thermally activated optical absorption can be explained by a three energy level model (Fig. 6.32a). In this model electrons are located at the lowest level 1 and the optical transition 2-3 has an energy of 12.4 meV. With increasing temperature, the middle energy level 2 is populated by electrons from level 1 and thus the optical transition 2-3 becomes active, too. As the position of the individual energy levels depends on the applied electric field, the biased and unbiased QCL should exhibit different optical transitions. The intraband transitions origin can be ruled out also due to the active region design in which the energy width of the injector structure subband  $< 12$  meV, while the first and second subbands are separated by 18 meV. But since the observed absorption feature appears at the same wavelength in both, biased and unbiased, cases it proves that the origin of the absorption is not solely related to the energy levels in the structure.

This thermally activated absorption process can be explained by the presence of silicon

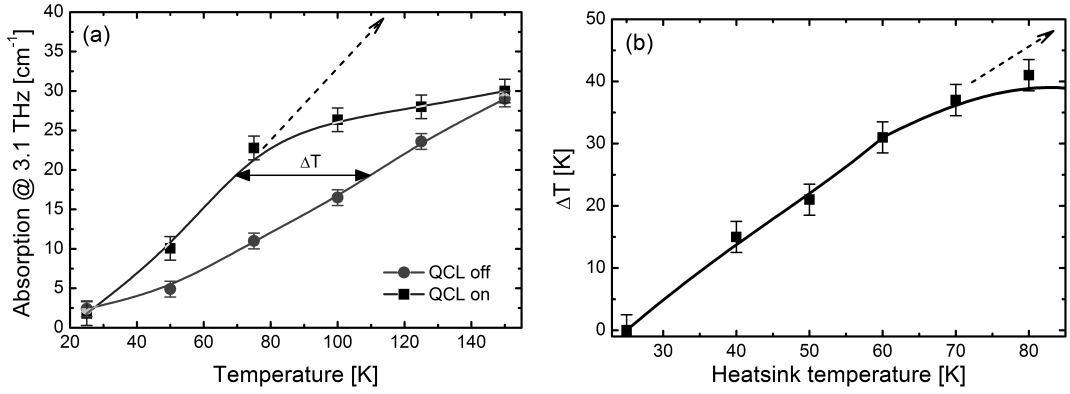


Figure 6.31.: (a) Comparison of temperature depending absorption in QCL T1 switched on and off. (b) Internal temperature difference of operated QCL compared to heatsink temperature.

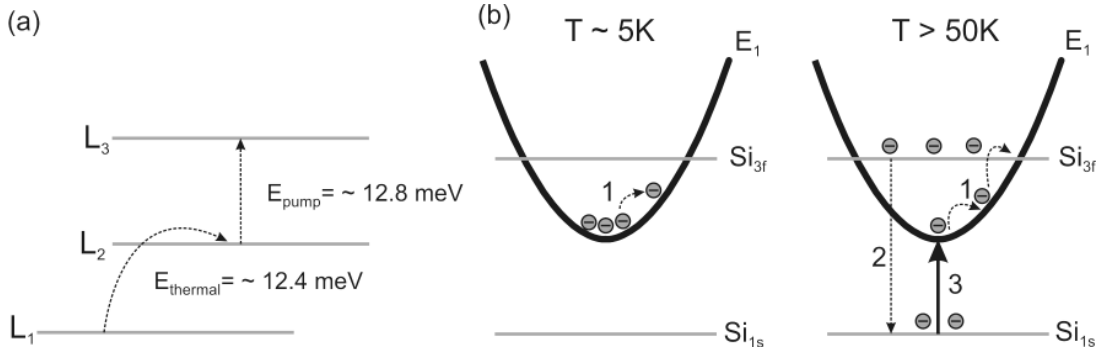


Figure 6.32.: (a) Three stage model for thermally activated losses and (b) configuration coordinate diagram of silicon donors in a GaAs quantum well. (1 - phonon scattering of electrons on the energy level; 2 - capture of electron on the donor defect site; 3 - optical transition from the donor to the heterostructure energy level). The optical transition 1 widens towards the low energies with increasing temperature due to the phonon scattering.

donors in the quantum cascade structure. In the THz-QCL heterostructure of laser T1 the silicon doping is placed in the 12 nm thick quantum well in the  $Al_{0.15}Ga_{0.85}As/GaAs$  heterostructure [146]. The activation energy, corresponding to the optical transition  $Si^{1s} \rightarrow GaAs_{QW}^{E1}$ , is about 12.5 meV. To explain the observed absorption in the THz-QCL and its thermal activation the following claim is formulated. The energy level structure of the silicon donors in the GaAs contains the excited state that is resonant with the energy level  $E1$  in the GaAs quantum well (Fig. 6.32b). In the normal state, the electrons are thermally activated from the donor ground state and redistributed between different energy levels in the conduction band. Let us consider the energy levels of the excited neutral donor laying about 12 meV above the quantum well ground state.

By increasing the device's temperature electrons are occupying the lowest energy level. From here they are intensively phonon scattered and can achieve energies high enough to

## 6. Phase resolved transmission spectroscopy of terahertz quantum cascade lasers

reach the excited state of the donors  $Si_{3f}$  and then relax fast to their ground state. The capture of the electrons on the donor sites leads to two effects. First, the density of the occupied absorbing sites increases due to the increased electron density. That means the absorption at the optical transition from the donor ground state to the heterostructure subband increases with temperature. Second, electrons captured on the donor sites are effectively removed from the laser's active region. This results in a decreased gain. Indeed, temperature dependence of the decrease of the gain at 2.87 THz exhibits almost the same activation energy  $\sim 12.5 meV$  as the absorption at 3.1 THz.

The observed thermally induced absorption seems to be one of the major reasons why THz-QCLs based on the bound-to-continuum or similar designs stop lasing at high temperature. Especially this applies for the THz-QCL used for characterization and similar devices based on the same design.

### 6.6. Conclusions

This chapter was dedicated to time-resolved THz transmission spectroscopy of quantum cascade lasers. It was shown that these devices cannot be examined and investigated only by emission spectroscopy like FT-IR because many crucial parameters cannot be accessed. But with THz-TDS in transmission mode the dynamics and internal properties of THz-QCLs can be measured. Latter include optical as well as thermal parameters. Further, by the direct measurement of the electric field from a QCL this was the first demonstration of phase resolved measurements of stimulated emission. Especially the comparison of these parameters for two QCLs operating at different emission frequencies (2 and 2.87 THz) resulted in a new understanding of these devices [147, 148].

Most results shown in this chapter rely mainly on the applied modulation spectroscopy measurement technique. Without this technique the signal dynamic range would be too low. Especially all results related with gain, reduced losses and absorption depend strongly on this new applied measurement scheme. This dramatically increases signal quality and enabled high resolution scans already at low duty cycles of the electrically driven device [149].

As was shown, with applied transmission signal modulation the real gain potential in QC heterostructures can be directly determined. The impact and potential of the performed measurements get clear by assuming the following fact. Sometimes a laser does not start lasing operation due to unexpected losses although the gain material was properly designed. In this case only photo luminescence measurements can give a hint about the emission capabilities. But in contrast to such measurements THz-TDS can directly proof the gain capability of a material below the threshold current of lasing operation. But furthermore, by coupling broadband THz pulses into the laser's waveguide its full gain bandwidth including the current dependence could be sensed. Thereby the laser with the larger gain bandwidth showed features in the phase diagram corresponding to a gain region consisting of two optically active transitions. This design feature was unmeant but shows

on the other side the potential of THz-TDS measurements for the QCL's active region redesign.

Further, it was shown that THz-TDS is capable measuring many physical effects present in a laser's active medium like spectral and spatial hole burning. Completely new is the time-domain measurement of the round-trip signals in the lasers whose spectra could be obtained by measuring the signals within proper time windows. The shape and the spectra of these signals allowed to identify and distinguish between net gain and reduced absorption. Both effects mixed up in the single pass signal. But furthermore, the multi-pass signals show the first moments of initiated lasing activities. After a THz seed pulse excites the laser's active region a wave is launched which shapes after each pass. Already after 3 passes the main signal is followed by a continuous wave which corresponds to a lasing like emission. Since the phase of the THz probe pulse is known its effect can be directly accessed compared to the self initiated lasing operation of the QCL which stays hidden due to the unknown phase of the photons.

In addition thermally activated loss mechanisms were investigated. As explained in this chapter the device temperature is crucial for QCLs operating in the THz frequency range. Any increase of the device temperature has a direct impact on the absorption spectrum and the net gain conditions. By comparing the temperature dependence of absorption characteristics of the activated and inactive device important conclusion could be obtained regarding the real device temperature and loss mechanisms. In the laser T1 an absorption band located close to its gain region appeared. In this particular laser and similar devices based on the bound-to-continuum design the observed mechanism seems to be one of the major reasons hampering high temperature operation of the laser. Further, the results presented here show clearly that the measured heatsink temperature gives no information regarding the laser's internal temperature. Depending on the duty cycle and the heat transfer the device temperature is much higher than expected so far. Temperature differences up to 40 K were observed. To our knowledge this was the first direct analysis of the real temperature conditions in THz-QCLs.





## 7. Summary and outlook

### 7.1. Summary

In this thesis the state-of-the-art potential of terahertz time-domain transmission spectroscopy was demonstrated in many fields of physics. Starting with a detailed description of the main techniques for generating and sensing of incoherent THz radiation, most of this work was dedicated to pulsed THz radiation and its direct application. This special kind of coherent radiation is capable measuring a series of optical as well as many other physical parameters of materials. Compared to other electromagnetic waves THz radiation is capable penetrating many materials with an inherent broadband spectrum. This was well demonstrated by many different examples. Further, the importance of a high quality THz-TDS setup and proper high performance measurement techniques was demonstrated. Especially without latter most of the effects presented in this work would not have been measurable.

#### 7.1.1. Setup and measurement technique

As explained above, apart from the gained results on various fields this work was dedicated to the setup and measurement techniques. Starting point was a low performance setup resulting in limited quality of the results. One after the other weak point of it was identified, revised or at least improved. THz emitters and sensors were exchanged. Optics and electronics optimized. Apart from sophisticated changes this included simple actions like a modified beam guiding for a homogeneous beam profile as well. All changes together resulted in an outstanding system performance and much faster data acquisition. Further, proper local signal amplification or accurate signal potential separation helped obtaining larger signal dynamics with large reserve. Latter was extensively used to measure weak signals with high dynamics in the experiments performed at the end of this work where also a new modulation spectroscopy technique was applied.

#### 7.1.2. Metallic phase shift layers for THz frequencies

In this chapter the properties of ultra-thin metal layers were successfully analyzed. The results were mainly a spin-off product. Main motivation was their application as anti-reflection coating. For this purpose a series of thin chromium as well as ITO layers were deposited on Si and GaAs substrates and characterized. By controlling the layer thickness and so the mean free path of the electrons the conductivity of the metal film can be set.

## 7. Summary and outlook

Compared to  $\lambda/4$  layers, used usually in optics, these metal layers show outstanding performance. Since the phase shift effect takes place at the metal/dielectric interface and is not related with the propagation distance within it, the effect is more or less wavelength independent. As long as the used metal keeps its conductivity constant the phase shift and anti-reflection effect remains active. Only at high frequencies approaching the metal's plasma frequency the effect becomes weaker and vanishes. Further, due to the high refractive index of such metal layers the phase shift effect stays constant even at incident angles  $\neq 0^\circ$ . Equipped with such properties these layers are perfectly suited for free space optics and commercial applications discussed later. As all inventions this technology has a drawback. Since the effect relies on electromagnetic induction eddy current losses are generated. Depending on the optical properties of the material to coat losses occur. As rule of thumb the higher the refractive index mismatch at an optical interface the higher the absorption losses due to the properly designed metallic anti-reflection layer.

### 7.1.3. Terahertz optical activity of sucrose single crystals

Another topic were the optical properties of molecular crystals. Such crystals are built by so called hydrogen bonds. In contrast to chemical or atomic bonds, where electrons are shared between atoms, here only charged atoms or constituents are involved. Due to the different electronegativity of the involved atoms building a molecule some of them get positively and some negatively charged. This results in bonding forces, caused by this charge distribution, between molecules but as well as within them. Latter causes a torsion of the molecule. However, due to these soft forces between the molecules forming the crystal absorption characteristic located in the THz frequency band were observed. For this demonstration sucrose single crystals were grown, cut into well orientated slabs and measured. Finally the results from the individual planes were merged to obtain a full three dimensional data set as was shown. By comparing the obtained data with the real molecular structure, measured by neutron diffraction, the data can be used to map the observed vibrational modes with the crystal structure and its main axis.

### 7.1.4. Coherent probing of stimulated emission

The largest part of this work was dedicated to the coherent probing of stimulated emission of THz quantum cascade lasers. For this task the above mentioned modulation spectroscopy measurement technique was applied. By coupling broadband THz pulses into the laser's waveguide the gain and losses can be directly measured. This included their spectral shape, current dependency and dynamics. Especially latter could only be obtained by time-resolved measurements of the main and round-trip signals within the laser's waveguide. FT-IR emission spectroscopy would not be able to obtain such information. Since the coupled photons have known phase, compared to the random phase of the laser's own emission, the evolution of stimulated emission, in this case initiated by the coupled THz seed pulse, could be measured for the first time in time-domain. The round-trip signals

for several passes show how the THz seed pulse establishes a continuous wave. Further, by comparing the results from two lasers with different emission frequencies (2 and 2.87 THz) important conclusion could be obtained. They show similar absorption and reduced loss characteristics but different gain spectra. Even indications were obtained for two active optical transitions in one laser. Apart from the gain measurements the temperature dependence of waveguide losses for one laser were measured. Thereby a narrow band absorption feature could be obtained located close to the gain spectrum of the laser. The observed absorption is one of the main reasons why the laser under investigation and most probably similar devices stop lasing at higher temperatures. Further, this narrow band absorption can be used to determine the real device temperature. This was done by comparing the data of the biased and unbiased device. In this way, a temperature difference up to 40 K and more compared to the heat sink could be determined. This shows the discrepancy between the real temperature conditions in a QCL's active zone and the published values.

## 7.2. Outlook

During this thesis a lot of question for various effects in physics and chemistry were answered. But in addition by exploring these fields a lot of new questions and ideas for future tasks originated. Every topic presented in this work left open work for upcoming activities on the field of THz photonics and physics. In general it was shown what THz-TDS can be used for and what it is capable. This was presented in terms of application, control and amplification of few cycle THz radiation.

### 7.2.1. Measurement technique and applied optics

There is still a lot of potential in the measurement technique of THz-TDS itself. This includes mainly the involved electronics and optics. Although the emitter antenna unit was improved in terms of lifetime and emitted light field amplitude a closer look at it could result in new improvements. The antenna shape and the waveform of the driving electric field have for sure an impact on the performance of the emitted THz pulse amplitude and bandwidth. Further, material science has to be included as well as cooling issues. Materials with higher electron mobility and heat conductivity can improve the THz power output. Another interesting field is the emission process of dipole emitters itself. Many effects are not studied and understood in detail.

Another important device in every THz-TDS setup is the detector. In the particular case a balanced photodiode detector. Here the sensor unit itself can be improved but the amplifier circuit as well. The interplay between them is crucial for proper device performance. As was inspected at the end of this work, but not shown, the spatial beam stability plays a major role in short term noise effects. The solution to this problem will lead to a big step towards mobile systems in the future.

Apart from electronics the optical system of such setup comprises huge potential for

## 7. Summary and outlook

improvements. As shown in this work special attention has been taken at the beam guiding which determines the beam shape and so the incouple performance into other structures. Depending on the application the beam guiding can be optimized or certain combination of optical components have to be prevented. For instance if parabolic mirrors are used for free space beam guiding no mirror objective shall be used because no Gaussian beam shape is provided. This is only one example what shall and what shall not be done.

### 7.2.2. Application and commercial products

The chapter about the absorption characteristics of sucrose single crystals showed one of the possible applications. THz transparent materials with spectral features in this frequency range can be fully characterized in terms of orientation dependent absorption. The full three dimensional data can give an insight in new materials. Already the data presented here can help to provide needful information for many software products dealing with the estimation of vibrational modes and other material relevant physical parameters. Molecular crystals represented in this work by sucrose are interesting agents of a large group of materials. Due to their inhomogeneous charge distribution these crystals should exhibit a large electro-optic coefficient. Maybe this will lead to new class of low cost sensors for the THz frequency range in the future.

### 7.2.3. Control of pulsed THz radiation

Compared to continuous waves the control of pulsed radiation with its inherent large bandwidth is very important for high performance optical systems. Here in this work the control topic was represented by a broadband anti-reflection coating and an integrated THz emitter/waveguide unit. Latter was used for high performance coupling into THz-QCLs without suffering from problems caused by free space optics. Both examples presented here imply a series of other possibilities. The optical mechanism used for the anti-reflection effect can be most probably adapted for other applications. For instance dichroic mirrors for broadband applications. Thereby proper conductive materials can be used to set exactly the transition frequency between reflectance and transmittance. Further by placing such coating in a resonator structure the transition area between these two properties can maybe be optimized. Even other optical structures exhibiting the phase shift effect of the metallic anti-reflection coating are conceivable.

Further, the here presented integrated waveguide emitter structure can be adapted for other issues as well. This means the size can be still reduced improving the incouple efficiency to other structures and similar designs can be exploited making so called micro optics. Latter could maybe find application in a new generation of optical THz micro chips or highly integrated optoelectronic devices.

#### 7.2.4. Amplification of THz pulses

Last topic of this work was dedicated to gain and absorption measurements in THz quantum cascade lasers. The measurements proofed that THz pulses coupled into such devices exhibit a strong amplification. This amplification corresponds well with the gain bandwidth of the laser under investigation. For instance, with a  $5\text{ mm}$  long device having a modal gain of  $\sim 14\text{ cm}^{-1}$  an amplification factor of more than 250 would be achievable. However, since only 2-10 % of the initial THz field amplitude could be coupled to the laser's waveguide structure and the effective amplification factor (for the  $2\text{ mm}$  long devices presented here) was only 2 the overall gain was negative. Although the physics of those devices got clearer and a lot of new experiences were gained, relies the main goal of real pulse amplification still in the future. Maybe the combination of integrated THz optics and proper anti-reflection coatings could help building such device. This would also represent then the first step towards a mode-locked quantum cascade laser. So to say, the last open main topic in QCL science remaining. For this and real applications depending on room temperature operation any thermal effects present in these lasers has to be investigated in detail. A starting point in this direction represents this thesis.



## A. Pulse laser specifications

During the work for this thesis two different femtosecond pulse laser systems were used. Since the details of these lasers are not of imminent importance and anyway, the working principle of such lasers is explained in chapter 2 here in this appendix part the exact working parameters are summarized. Both laser systems are Ti:sapphire pulse lasers using the Kerr-lensing effect (chapter 2.3.1) for passive mode-locking.

For all experiments presented in this work the Tsunami pulse laser system from Spectra-Physics [150] was used (Fig. A.1). The laser is equipped with a prism compressor within a slit is installed for wavelength tuning. For standard experiments where the generation of THz radiation is made by photoconductive switches infrared pulses of about 120 fs (FWHM) are more than sufficient to generate sub-picosecond THz pulses. Further, another advantage of the Tsunami laser system is its wavelength tunability. Experience values showed an optimum system performance of the THz-TDS setup for wavelengths about 815-820 nm. This is related with the bandgap energies of Si and GaAs used as detector and emitter material respectively.

The second laser system is a M1 Femtosource from Femtolasers [151]. It was only used at the beginning of this work and then replaced by the above described laser. The schematic of the M1 laser is shown in Fig. A.3. Compared to the other system it provides less output power but much shorter optical pulses. This results in a very high peak power of the emitted laser pulses which is essentially needed for some experiments which are not shown here. For obtaining ultrashort laser pulses of  $\sim 12$  fs the pulse compression is done by a set of chirped mirrors (see chapter 2.3.1 for details).

A comparison of the emission spectrum and a complete list of the performance parameters of both lasers is shown in Fig. A.2 and Tab. A.1.

Pulse laser	<b>Tsunami</b>	<b>M1</b>
Center emission wavelength [nm]	820	800
Emission wavelength tunability [nm]	720-850	NO
Emission bandwidth FWHM [nm]	10-12	100-120
Pulse width FWHM [fs]	120	12
Pump power [W]	10	7
Output power [W]	1.8-2.0	0.8
Repetition rate [MHz]	82	82
Pulse compression type	Prisms	Chirped mirrors

Table A.1.: Pulse laser specifications of Tsunami and M1 system.

### A. Pulse laser specifications

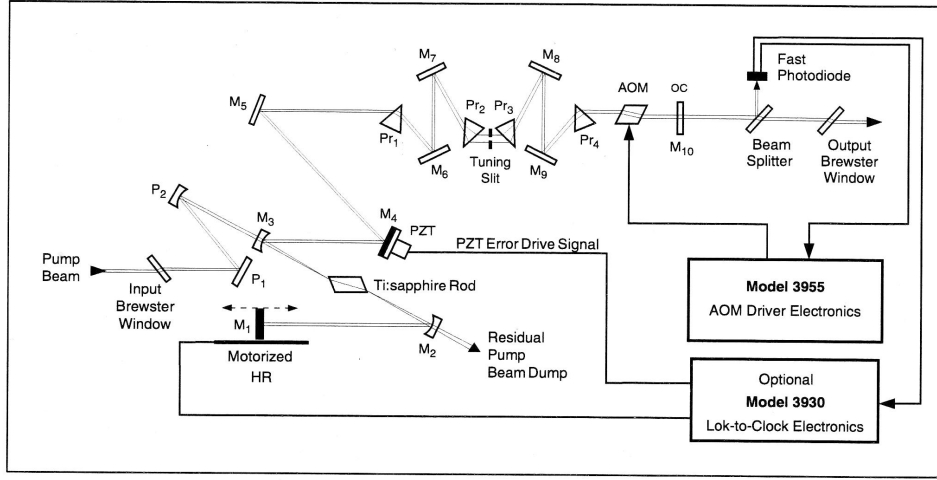


Figure A.1.: Scheme of the Tsunami pulse laser (from [150]).

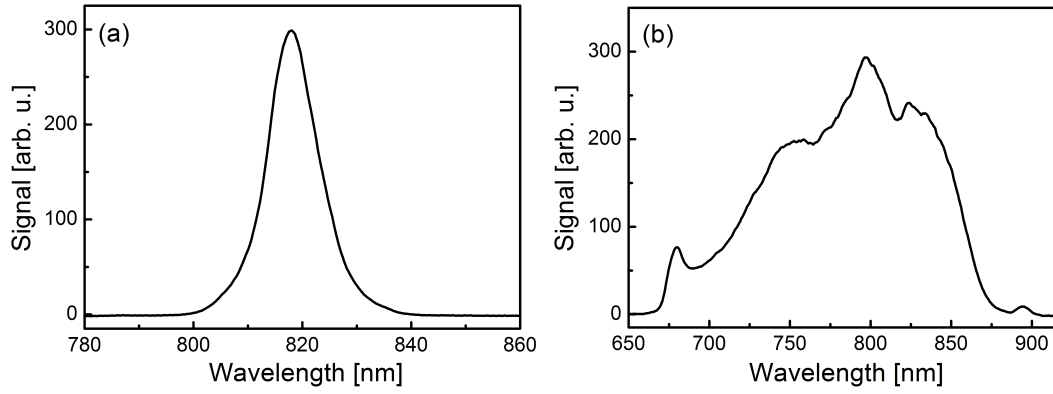


Figure A.2.: Emission spectrum of (a) Tsunami and (b) M1 pulse laser.

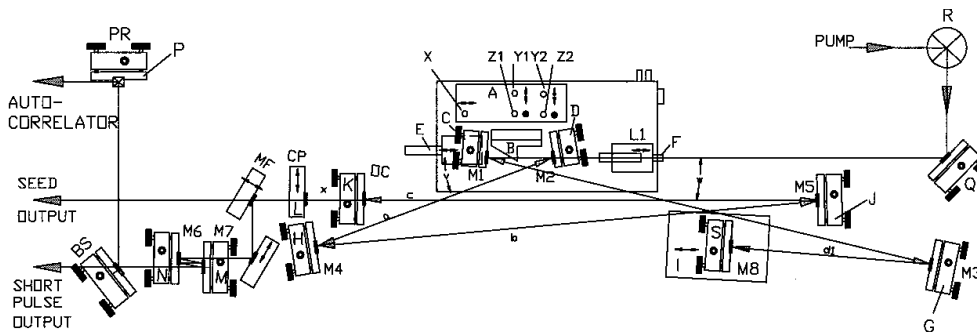


Figure A.3.: Scheme of the M1 pulse laser (from [151]).



# Bibliography

- [1] M.-L. H. van Nispen, *400000 Jahre Technikgeschichte. Von der Steinzeit bis zum Informationszeitalter*, Nikol Verlagsgesellschaft, 2005.
- [2] F. Sezgin, *Wissenschaft und Technik im Islam*, Johann Wolfgang-Göthe-Universität Frankfurt a.M, 1 ed., 2003.
- [3] J. D. Jackson, *Klassische Elektrodynamik*, Walter de Gruyter (Berlin, New York), 2002.
- [4] M. Born and E. Wolf, *Principle of Optics*, Cambridge University Press, 7th (expanded) ed., 1999.
- [5] W. C. Röntgen, “On a new kind of rays,” *Nature* **53**, p. 274, 1896.
- [6] D. S. Venables and C. A. Schmuttenmaer, “Spectroscopy and dynamics of mixtures of water with acetone, acetonitrile, and methanol,” *J. Appl. Phys.* **113**, p. 11222, 2000.
- [7] R. L. Poynter and H. M. Pickett, “Submillimeter, millimeter, and microwave spectral line catalog,” *Appl. Opt.* **24**, p. 2235, 1985.
- [8] M. A. Janssen, *Atmospheric remote sensing by microwave radiometry*, Wiley-Interscience, 1993.
- [9] B. M. Fischer, M. Walther, and P. Jepsen, “Far-infrared vibrational modes of dna components studied by terahertz time-domain spectroscopy,” *Phys. Med. Biol.* **74**, p. 3807, 2002.
- [10] P. C. Upadhyay, Y. C. Shen, A. G. Davies, and E. H. Linfield, “Far-infrared vibrational modes of polycrystalline saccharides,” *Vib. Spectrosc.* **35**, p. 139, 2004.
- [11] D. M. Mittleman, S. Hunsche, L. Boivin, and M. C. Nuss, “T-ray tomography,” *Opt. Lett.* **22**, p. 904, 1997.
- [12] R. N. Hall, G. E. Fenner, J. D. Kingsley, T. J. Soltys, and R. O. Carlson, “Coherent light emission from gaas junctions,” *Phys. Rev. Lett.* **9**(9), p. 366, 1962.
- [13] J. B. Gunn, “Instabilities of current in III-V semiconductors,” *IBM J. Res. Devel.* **8**, 1964.

## Bibliography

- [14] J. Faist, F. Capasso, D. Sivco, C. Sirtori, A. L. Hutchinson, and A. Y. Cho, “Quantum cascade laser,” *Nature* **264**, p. 553, 1994.
- [15] D. H. Auston and A. M. Glass, “Optical generation of intense picosecond electrical pulses,” *Appl. Phys. Lett.* **20**(10), p. 398, 1972.
- [16] R. Mcglaughlin, A. Corchia, M. B. Johnston, Q. Chen, C. M. Ciesla, D. D. Arnone, G. A. C. Jones, E. H. Linfield, A. G. Davies, and M. Pepper, “Enhanced coherent terahertz emission from indium arsenide in the presence of a magnetic field,” *Appl. Phys. Lett.* **76**, p. 2038, 2000.
- [17] M. Walther, P. Plochocka, B. Fischer, H. Helm, and P. Jepsen, “Collective vibrational modes in biological molecules investigated by terahertz time-domain spectroscopy,” *Biopolymers (Biospectroscopy)* **67**, p. 310, 2002.
- [18] M. Walther, B. Fischer, M. Schall, H. Helm, and P. Jepsen, “Far-infrared vibrational spectra of all trans, 9-cis and 13-cis retinal measured by thz time-domain spectroscopy,” *Chem. Phys. Lett.* **332**, p. 389, 2000.
- [19] J. Kröll, “Few cycle thz spectroscopy and imaging,” Master’s thesis, TU-Vienna, Department of electrical engineering, 2003.
- [20] R. Köhler, A. Tredicucci, F. Beltram, H. E. Beere, E. H. Linfield, A. G. Davies, D. A. Ritchie, R. C. Iotti, and F. Rossi, “Terahertz semiconductor-heterostructure laser,” *Nature* **417**, p. 156, 2002.
- [21] B. Williams, S. Kumar, Q. Hu, and J. Reno, “High-power terahertz quantum-cascade lasers,” *Electron. Lett.* **42**(2), 2006.
- [22] A. J. L. Adam, I. Kasalynas, J. N. Hovenier, T. O. Klaassen, J. R. Gao, E. E. Orlova, B. S. Williams, S. Kumar, Q. Hu, and J. L. Reno, “Beam patterns of terahertz quantum cascade lasers with subwavelength cavity dimensions,” *Appl. Phys. Lett.* **88**(151105), 2006.
- [23] J. Alton, S. S. Dhillon, C. Sirtori, A. de Rossi, M. Calligaro, S. Barbieri, H. E. Beere, E. H. Linfield, and D. A. Ritchie, “Buried waveguides in terahertz quantum cascade lasers based on two-dimensional surface plasmon modes,” *Appl. Phys. Lett.* **86**(71109), 2005.
- [24] B. Williams, S. Kumar, Q. Hu, and J. Reno, “Operation of terahertz quantum-cascade lasers at 164 k in pulsed mode and at 117 k in continuous-wave mode,” *Opt. Express* **13**, p. 3331, 2005.
- [25] D. Leisawitz, W. Danchi, M. DiPirro, L. D. Feinberg, D. Gezari, M. Hagopian, J. C. Mather, S. H. Moseley, R. F. Silverberg, W. D. Langer, M. Shao, M. . R. Swain, H. W. Yorke, J. Staguhn, and Z. Xiaolei, “Far-ir/submillimeter space interferometry:

- scientific motivation and technology requirements,” *2001 IEEE Aerospace Conference Proceedings* **1**, pp. 1995–2004, 2001.
- [26] H. Baehr and K. Stephan, *Heat and Mass-Transfer*, Springer (Berlin), 1 ed., 2006.
  - [27] K. F. Brennan and A. S. Brown, *Theory of modern electronic semiconductor devices*, John Wiley & Sons, Inc., 2002.
  - [28] W. H. Haydl, “A wide-range variable frequency gunn oscillator,” *Appl. Phys. Lett.* **12**, p. 357, 1968.
  - [29] W. H. Haydl, S. Smith, and R. Bosch, “100-ghz gunn diodes fabricated by molecular beam epitaxy,” *Appl. Phys. Lett.* **37**, p. 556, 1980.
  - [30] H. Eisele, “Inp gunn devices for 400-425 ghz,” *Electron. Lett.* **42**(6), 2006.
  - [31] J. T. Lü and J. C. Cao, “Terahertz generation and chaotic dynamics in gan ndr diode,” *Semicond. Sci. Technol.* **19**, pp. 451–456, 2004.
  - [32] S. Chung and N. Balkan, “Fabry-perot gunn laser,” *Appl. Phys. Lett.* **86**(211111), 2006.
  - [33] A. Dargys and J. Kundrotas, *Handbook on Physical Properties of Ge, Si, GaAs and InP*, Science and Encyclopedia Publishers (Vilnius), 1994.
  - [34] A. Staprans, “High-power microwave tubes,” *IEEE Int. Electron. Dev. Meet. Tech. Digest* **1**, p. 245, 1976.
  - [35] A. Starprans, E. W. McCune, and J. A. Ruetz, “High-power linear-beam tubes,” *Proc. IEEE* **3**, 1973.
  - [36] P. H. Siegel, “Terahertz technology,” *IEEE Trans. Micro. Tech.* **50**(3), p. 910, 2002.
  - [37] G. G. Grüner, *Millimeter and Submillimeter Wave Spectroscopy of Solids*, Springer (Berlin, Heidelberg, New York), 1998.
  - [38] A. V. Raisanen, “Frequency multipliers for millimeter and submillimeter wavelengths,” *Proc. IEEE* **80**(11), 1992.
  - [39] R. W. Boyd, *Nonlinear optics*, Academic Press (San Diego), 1992.
  - [40] T. Chang and T. Bridges, “Laser action at 452, 496, and 541  $\mu\text{m}$  in optically pumped  $\text{CH}_3\text{F}$ ,” *Opt. Comm.* **1**, p. 423, 1970.
  - [41] T. Chang, T. Bridges, and E. Burkhardt, “cw submillitmeter laser action in optically pumped methyl fluoride, methyl alcohol, and vinyl chloride gases,” *Appl. Phys. Lett.* **17**, p. 249, 1970.

## Bibliography

- [42] T. Chang, T. Bridges, and E. Burkhardt, "cw laser action at 81.5 and 263.4  $\mu\text{m}$  in optically pumped ammonia gas," *Appl. Phys. Lett.* **17**, p. 357, 1970.
- [43] M. S. Tobin and T. W. Daley, "Optically pumped  $\text{CHClF}_2$  and  $\text{C}_2\text{H}_5\text{I}$  submillimeter wave lasers," *IEEE J. Quant. Electron.* **16**(6), p. 592, 1980.
- [44] R. I. McCormick, H. O. Everitt, F. C. de Lucia, and D. D. Skatrud, "Collisional energy transfer in optically pumped far-infrared lasers," *IEEE J. Quant. Electron.* **23**(12), p. 2069, 1987.
- [45] M. Inguscio, G. Moruzzi, K. M. Evenson, and D. A. Jennings, "A review of frequency measurements of optically pumped lasers from 0.1 to 8 thz," *J. Appl. Phys.* **60**(12), p. 161, 1986.
- [46] R. Köhler, A. Tredicucci, F. Beltram, H. Beere, E. Linfield, A. Davis, D. Ritchie, R. Lotti, and F. Rossi, "Terahertz semiconductor-heterostructure laser," *Nature* **417**, p. 156, 2002.
- [47] D. A. G. Deacon, L. R. Elias, J. M. J. Madey, G. J. Ramian, H. A. Schwettman, and T. I. Smith, "First operation of a free-electron laser," *Phys. Rev. Lett.* **38**(16), p. 892, 1977.
- [48] I. B. Bernstein and J. L. Hirshfield, "Theory of a free-electron laser," *Phys. Rev. Lett.* **40**(12), p. 761, 1978.
- [49] L. R. Elias, "High-power, cw, efficient, tunable (uv through ir) free-electron laser using low-energy electron beams," *Phys. Rev. Lett.* **42**(15), pp. 977–981, 1979.
- [50] W. S. C. Chang, *Principles of lasers and optics*, Cambridge University Press, 2005.
- [51] C. Rulliere, *Femtosecond Laser Pulses*, Springer (Berlin), 1998.
- [52] A. E. Siegman, *Lasers*, University Science Books, 1986.
- [53] G. Reider, *Photonik*, Springer (Wien), 1997.
- [54] A. Stingl, M. Lenzer, W. Bachtold, and F. Krausz, "sub-10-fs mirror dispersion controlled ti:sapphire laser," *Opt. Lett.* **20**, p. 602, 1995.
- [55] R. Kersting, J. N. Heyman, G. Strasser, and K. Unterrainer, "Coherent plasmons in n-doped gaas," *Phys. Rev. B* **58**, p. 4553, 1998.
- [56] J. Darmo, G. Strasser, T. Müller, R. Bratschitsch, and K. Unterrainer, "Surface-modified gaas terahertz plasmon emitter," *Appl. Phys. Lett.* **81**, p. 873, 2002.
- [57] W. Lukosz and R. E. Kunz, "Light emission by magnetic and electric dipoles close to a plane surface. i. total radiated power.," *J. Opt. Soc. Am.* **67**, p. 1607, 1977.

- [58] D. H. Auston, K. P. Cheung, and P. R. Smith, "Picosecond photoconducting hertzian dipoles," *Appl. Phys. Lett.* **45**(3), p. 284, 1984.
- [59] K. Sakai, *Terahertz Optoelectronics*, Springer (Berlin, Heidelberg), 2005.
- [60] L. Duvillaret, F. Garet, J. F. Roux, and J. L. Coutaz, "Analytic modeling and optimization of terahertz time-domain spectroscopy experiments using photoswitches as antennae," *IEEE J. Sel. Top. Quantum-Electron.* **7**(4), p. 615, 2001.
- [61] R. Menzel, *Photonics*, Springer (Berlin), 2 ed., 2006.
- [62] S. Graf, H. Sigg, and W. Bachtold, "High-frequency electrical pulse generation using optical rectification in bulk GaAs," *Appl. Phys. Lett.* **76**, p. 2647, 2000.
- [63] A. Nahata, A. S. Weling, and T. F. Heinz, "A wideband coherent terahertz spectroscopy system using optical rectification and electro-optic sampling," *Appl. Phys. Lett.* **69**(16), p. 2321, 1996.
- [64] T. Bartel, P. Gaal, K. Reimann, M. Woerner, and T. Elsaesser, "Generation of single-cycle THz transients with high electric-field amplitudes," *Opt. Lett.* **30**, p. 2805, 2005.
- [65] R. Patzelt, *Elektrische Meßtechnik*, Springer (Wien, New York), 1996.
- [66] G. F. Knoll, *Radiation Detection and Measurement*, John Wiley & Sons, 2000.
- [67] P. L. Richards, "Bolometer for infrared and millimeter waves," *J. Appl. Phys.* **76**(1), p. 1, 1994.
- [68] D. P. Neikirk and D. B. Rutledge, "Air-bridge microbolometer for far-infrared detection," *Appl. Phys. Lett.* **44**(2), p. 153, 1983.
- [69] A. Rahman, G. de Lange, and Q. Hu, "Micromachined room-temperature microbolometer for millimeter-wave detection," *Appl. Phys. Lett.* **68**(14), p. 2020, 1996.
- [70] W. B. Song and J. J. Talghader, "Design and characterization of adaptive microbolometers," *J. Micromech. Microeng.* **16**, pp. 1073–1079, 2006.
- [71] *Microtech Instruments Inc. Datasheet: Golay Cell detector* ([www.mtinstruments.com/downloads/GolayCellDatasheet.pdf](http://www.mtinstruments.com/downloads/GolayCellDatasheet.pdf)), 2006.
- [72] D. E. Collins, "Vibration insulating mounting for a golay cell," *Review of Scientific Instruments* **36**(6), p. 850, 1965.
- [73] K. Yamashita, A. Murata, and M. Okuyama, "Miniaturized infrared sensor using silicon diaphragm based on golay cell," *Sensors and Actuators A* **66**, pp. 29–32, 1998.
- [74] H. P. Beerman, "The pyroelectric detector of infrared radiation," *IEEE Transactions on Electron Devices* **16**(6), pp. 554–557, 1969.

- [75] G. Fasching, *Werkstoffe für die Elektrotechnik*, Springer (Wien), 2005.
- [76] S. Bauer, S. Bauer-Gogonea, and B. Ploss, “The physics of pyroelectric infrared devices,” *Applied Physics B* **54**, pp. 544–551, 1992.
- [77] *Microtech Instruments Inc. Datasheet: Pyroelectric sensors* ([www.mtinstruments.com/downloads/PyroelectricDetectorDatasheet.pdf](http://www.mtinstruments.com/downloads/PyroelectricDetectorDatasheet.pdf)), 2006.
- [78] C. B. Roundy and R. L. Byer, “Sensitive LiTaO<sub>3</sub> pyroelectric detector,” *J. Appl. Phys.* **44**(2), p. 929, 1973.
- [79] Z. Jiang, F. G. Sun, and X. C. Zhang, “Terahertz pulse measurement with an optical streak camera,” *Opt. Lett.* **24**, p. 1245, 1999.
- [80] P. R. Smith, D. H. Auston, and M. C. Nuss, “Subpicosecond photoconducting dipole antennas,” *IEEE J. Quantum Electron.* **24**(2), p. 255, 1988.
- [81] S. G. Park, M. R. Melloch, and A. M. Weiner, “Comparison of terahertz waveforms measured by electro-optic and photoconducting sampling,” *Appl. Phys. Lett.* **73**(22), p. 3184, 1998.
- [82] S. Kono, M. Tani, P. Gu, and K. Sakai, “Detection of up to 20 thz with a low-temperature-grown gaas photoconductive antenna gated with 15 fs pulses,” *Appl. Phys. Lett.* **77**(25), p. 4104, 2000.
- [83] Q. Wu and X.-C. Zhang, “Free-space electro-optic sampling of terahertz beams,” *Appl. Phys. Lett.* **67**(24), p. 3523, 1995.
- [84] Q. Wu and X.-C. Zhang, “Ultrafast electro-optic field sensors,” *Appl. Phys. Lett.* **68**(12), p. 1604, 1996.
- [85] Y. Cai, I. Brener, J. Lopata, J. Pfeiffer, J. B. Stark, Q. Wu, X. C. Zhang, and J. F. Federici, “Coherent terahertz radiation detection: Direct comparison between free-space electro-optic sampling and antenna detection,” *Appl. Phys. Lett.* **73**(4), p. 444, 1998.
- [86] S. G. Park, M. R. Melloch, and A. M. Weiner, “Comparison of terahertz waveforms measured by electro-optic and photoconducting sampling,” *Appl. Phys. Lett.* **73**(22), p. 3184, 1998.
- [87] Q. Wu and X. C. Zhang, “Free-space electro-optic sampling of mid-infrared pulses,” *Appl. Phys. Lett.* **71**(10), p. 1285, 1997.
- [88] Q. Wu and X.-C. Zhang, “7 terahertz broadband gap electro-optic sensor,” *Appl. Phys. Lett.* **70**, p. 1784, 1997.
- [89] Q. Wu, M. Litz, and X. C. Zhang, “Broadband detection capability of znTe electro-optic field detectors,” *Appl. Phys. Lett.* **68**(21), p. 2924, 1996.

- [90] C. Winnerwisser, P. U. Jepsen, M. Schall, V. Schyja, and H. Helm, "Electro-optic detection of thz radiation in  $\text{LiTaO}_3$ ,  $\text{LiNbO}_3$  and  $\text{ZnTe}$ ," *Appl. Phys. Lett.* **70**(23), p. 3069, 1997.
- [91] C. Winnerwisser, *Elektrooptische Detektion von ultrakurzen elektro-magnetischen Pulsen*. PhD thesis, Albert-Ludwigs Universität Freiburg, 1999.
- [92] P. Han, M. Tani, and X. C. Zhang, "Use of the organic crystal dast for terahertz beam applications," *Opt. Lett.* **25**(9), p. 675, 2000.
- [93] M. Schall and P. U. Jepsen, "Freeze-out of difference-phonon modes in znte and its application of thz pulses," *Appl. Phys. Lett.* **77**(18), p. 2801, 2000.
- [94] P. C. M. Planken, H. K. Nienhuys, H. J. Bakker, and T. Wenckebach, "Measurement and calculation of the orientation dependence of terahertz pulse detection in znte," *J. Opt. Soc. Am. B* **18**(3), pp. 313–317, 2001.
- [95] N. H. Schiller and R. R. Alfano, "The streak camera," *Laser Focus* **18**(8), p. 43, 1982.
- [96] P. Y. Han, M. Tani, M. Usami, S. Kono, R. Kersting, and X.-C. Zhang, "A direct comparison between terahertz time-domain spectroscopy and far-infrared fourier transform spectroscopy," *J. Appl. Phys.* **89**, p. 2357, 2001.
- [97] L. Duvillaret, F. Garet, and J. Coutaz, "Highly precise determination of optical constants and sample thickness in terahertz time-domain spectroscopy," *Appl. Opt.* **38**, p. 409, 1999.
- [98] J. A. Murphy, "Distortion of a simple gaussian beam on reflection from off-axis ellipsoidal mirrors," *Int. J. Infrared and Millimeter Waves* **8**(9), p. 1165, 1987.
- [99] T. Bauer, J. S. Kolb, T. Löffler, E. Mohler, H. G. Roskos, and U. Pernisz, "Indium-tin-oxide-coated glass as dichroic mirror for far-infrared electromagnetic radiation," *J. Appl. Phys.* **92**(4), p. 2210, 2002.
- [100] S. Coleman and D. Grischkowsky, "Parallel plate thz transmitter," *Appl. Phys. Lett.* **84**(5), p. 654, 2004.
- [101] J. S. Walker, "Fourier analysis and wavelet analysis," *Notices of the AMS* **44**, p. 658, 1997.
- [102] P. Drude, "Zur elektronentheorie der metalle," *Ostwalds Klassiker der exakten Wissenschaften* **298**, 2006.
- [103] B. Carli, "Reflectivity of metallic films in the infrared," *J. Opt. Soc. Am.* **67**, p. 908, 1977.

## Bibliography

- [104] M. A. Ordal, R. J. Bell, R. W. Alexander, and M. R. Q. L. L. Long, "Optical properties of fourteen metals in the infrared and far infrared: Al, co, cu, au, fe, pb, mo, ni, pd, pt, ag, ti, v, and w," *Appl. Opt.* **24**, p. 4493, 1985.
- [105] S. Norrman, T. Andersson, and C. G. Granqvist, "Optical properties of discontinuous gold films," *Phys. Rev. B* **18**(2), p. 674, 1978.
- [106] R. G. Ross and W. Hume-Rothery, "High temperature x-ray metallography : I. a new debye-scherrer camera for use at very high temperatures ii. a new para-focusing camera iii. applications to the study of chromium, hafnium, molybdenum, rhodium, ruthenium and tungsten," *J. Less-Common Metals* **5**(3), p. 258, 1963.
- [107] L. J. Swartzendruber, *Correction factor tables for four-point probe resistivity measurements on thin, circular semiconductor samples*, National Bureau of Standards, 1964. Technical Note 199.
- [108] H. T. S. Division, "Geometric factors in four point resistivity measurement." Internal Note, May 1968. Bulletin No. 472-13.
- [109] M. Exter and D. Grischkowsky, "Carrier dynamics of electrons and holes in moderately doped silicon," *Phys. Rev. B* **41**, p. 12140, 1990.
- [110] C. Zhang, K. S. Lee, X. C. Zhang, X. Wei, and R. Shen, "Optical constants of ice Ih crystal at terahertz frequencies," *Appl. Phys. Lett.* **79**(4), p. 491, 2001.
- [111] C. A. Beevers, T. R. R. McDonald, H. J. Robertson, and F. Stern, "The crystal structure of sucrose," *Acta Cryst.* **5**, p. 689, 1952.
- [112] X. Zheng, S. Wu, R. Sobolewski, R. Adam, M. Mikulics, P. Kordos, and M. Siegel, "Electro-optic sampling system with a single-crystal 4-n,n-dimethylamino-4'-n'-methyl-4-stilbazolium tosylate sensor," *Appl. Phys. Lett.* **82**(15), p. 2383, 2003.
- [113] J. H. Schön, C. Kloc, and B. Batlogg, "Efficient photovoltaic energy conversion in pentacene-based heterojunctions," *Appl. Phys. Lett.* **77**(16), p. 2473, 2000.
- [114] G. M. Brown and H. A. Levy, "Further refinement of the structure of sucrose based on neutron-diffraction data," *Acta Cryst. B* **29**, p. 790, 1972.
- [115] M. Walther, B. M. Fischer, and P. U. Jepsen, "Noncovalent intermolecular forces in polycrystalline and amorphous saccharides in the far infrared," *Chem. Phys.* **288**, p. 261, 2003.
- [116] J. Nishizawa, K. Suto, T. Sasaki, T. Tanabe, and T. Kimura, "Spectral measurement of terahertz vibrations of biomolecules using gap terahertz-wave generator with automatic scanning control," *J. Phys. D: Appl. Phys.* **36**, p. 2958, 2003.
- [117] R. C. Hynes and Y. L. Page, "Sucrose, a convenient test crystal for absolute structures," *J. Appl. Cryst.* **24**, p. 352, 1991.



- [118] R. Kumaresan and S. M. Babu, “Crystal growth and characterization of sucrose single crystals,” *Mat. Chem. Phys.* **49**, p. 83, 1997.
- [119] G. Sgualdino, E. Scandale, D. Aquilano, G. Vaccari, and G. Mantovani, “The growth of large sucrose crystals from solution,” *Material Science Forum* **203**, p. 43, 1996.
- [120] P. U. Jepsen and B. M. Fischer, “Dynamic range in terahertz time-domain transmission and reflection spectroscopy,” *Opt. Lett.* **30**, p. 29, 2005.
- [121] J. M. Halbout and C. L. Tang, “Phase-matched second-harmonic generation in sucrose,” *IEEE J. Quant. Electron.* **18**, p. 410, 1982.
- [122] R. Kumaresan and S. M. Babu, “Crystal growth and characterization of sucrose single crystals,” *Mater. Chem. Phys.* **49**, p. 84, 1997.
- [123] J. Kröll, J. Darmo, and K. Unterrainer, “Terahertz optical activity of sucrose single-crystals,” *Vib. Spectrosc.* **43**, pp. 324–329, 2007. accepted, article in press.
- [124] M. Rochat, M. Beck, J. Faist, and U. Oesterle, “Measurement of far-infrared waveguide loss using a multisection single-pass technique,” *Appl. Phys. Lett.* **78**, p. 1967, 2001.
- [125] A. Cho, “Film deposition by molecular beam techniques,” *J. Vac. Sci. Tech.* **8**, p. 531, 1971.
- [126] G. Bastard, *Wave mechanics applied to semiconductor heterostructures*, John Wiley & Sons Inc., 1990.
- [127] W. R. Frensley and N. G. Einspruch, *Heterostructure and quantum well devices*, Academic Press (San Diego), 1994.
- [128] C. Sirtori, P. Kruck, S. Barbieri, P. Collot, J. Nagle, M. Beck, J. Faist, and U. Oesterle, “GaAs/A<sub>x</sub>Ga<sub>1-x</sub>As quantum cascade lasers,” *Appl. Phys. Lett.* **73**, p. 3486, 1998.
- [129] R. F. Kazarinov and R. A. Suris, “Possibility of the amplification of electromagnetic waves in a semiconductor with a superlattice,” *Soviet Phys. Semiconductors* **5**, p. 707, 1971.
- [130] J. Faist, F. Capasso, C. Sirtori, D. Sivco, J. N. Bailargeon, A. L. Hutchinson, S. G. Chu, and A. Y. Cho, “High power mid-infrared ( $\lambda=5\mu\text{m}$ ) quantum cascade lasers operating above room temperature,” *Appl. Phys. Lett.* **68**, p. 3680, 1996.
- [131] Y. S. Yu, S. Silvken, A. Evans, S. R. Darvish, J. Niguyen, and M. Razeghi, “High power  $\lambda=9.5\mu$  quantum-cascade lasers operating above room temperature in continuous-wave mode,” *Appl. Phys. Lett.* **88**(91113), 2006.

## Bibliography

- [132] R. Colombelli, A. Straub, F. Capasso, C. Gmachl, M. I. Blakey, A. M. Sergent, S. N. G. Shu, K. W. West, and L. N. Pfeiffer, "Terahertz electroluminescence from superlattice quantum cascade structures," *J. Appl. Phys.* **91**, p. 3526, 2002.
- [133] R. Köhler, R. C. Iotti, A. Tredicucci, and F. Rossi, "Design and simulation of terahertz quantum cascade lasers," *Appl. Phys. Lett.* **79**, p. 3920, 2001.
- [134] B. S. Williams, S. Kumar, H. C. Callebaut, and Q. Hu, "Terahertz quantum-cascade laser at 100  $\mu\text{m}$  using metal waveguide for mode confinement," *Appl. Phys. Lett.* **83**, p. 2124, 2003.
- [135] J. Faist, M. Beck, T. Aellen, and E. Gini, "Quantum-cascade lasers based on a bound-to-continuum transition," *Appl. Phys. Lett.* **78**, p. 147, 2001.
- [136] S. Barbieri, J. Alton, H. E. Beere, J. Fowler, E. H. Linfield, and D. A. Ritchie, "2.9 thz quantum cascade lasers operating up to 70 k in continuous wave," *Appl. Phys. Lett.* **85**(10), p. 1674, 2004.
- [137] C. Worrall, J. Alton, M. Houghton, S. Barberieri, H. E. Beere, D. Ritchie, and C. Sirtori, "Continuous wave operation of a superlattice quantum cascade laser emitting at 2 thz," *Optics Express* **14**(1), p. 171, 2006.
- [138] H. J. Dirschmid, *Mathematische Grundlagen der Elektrotechnik*, Vieweg Verlagsgesellschaft, 4 ed., 1992.
- [139] C. Blatter, *Wavelets. Eine Einführung*, Vieweg, 2 ed., 2003.
- [140] B. Williams, S. Kumar, H. Callebaut, Q. Hu, and J. L. Reno, "3.4 thz quantum cascade laser operating above liquid nitrogen temperature," *Electron. Lett.* **39**, p. 915, 2003.
- [141] M. Schall and P. Jepsen, "Photoexcited gaas surfaces studied by transient terahertz time-domain spectroscopy," *Opt. Lett.* **25**(1), p. 13, 2000.
- [142] V. Lucarini, J. J. Saarinen, K. E. Peiponen, and E. M. Vartiainen, *Kramers-Kronig relations in optical materials research*, Springer-Verlag, 1 ed., 2005.
- [143] J. N. Fehr, M. A. Dupertuis, T. P. Hessler, L. Kappei, P. E. Selbmann, B. Deveaud, J. L. Pleumeekers, J. Y. Emery, and B. Dagens, "Direct observation of longitudinal spatial hole burning in semiconductor optical amplifiers with injection," *Appl. Phys. Lett.* **78**, p. 4079, 2001.
- [144] M. Martl, J. Darmo, J. Kröll, and K. Unterrainer, "Waveguide analyzes of surface plasmons." to be published in Appl. Phys. Lett.

- [145] M. S. Vitiello, G. Scamarico, V. Spagnolo, J. Alton, S. Barbieri, C. Worrall, H. E. Beere, D. A. Ritchie, and C. Sirtori, "Thermal properties of thz quantum cascade lasers based on different optical waveguide configurations," *Appl. Phys. Lett.* **89**(021111), 2006.
- [146] P. Bhattacharya, *Properties of III-V Quantum Wells and Superlattices*, INSPEC London, 1996. Ch. 4.
- [147] J. Kröll, J. Darmo, K. Unterrainer, S. Dhillon, C. Sirtori, X. Marcadet, and M. Calligaro, "Spectral limitation in terahertz quantum cascade laser design caused by thermally activated absorption." to be published in *Appl. Phys. Lett.*, 2007.
- [148] J. Kröll, J. Darmo, K. Unterrainer, S. Dhillon, C. Sirtori, X. Marcadet, and M. Calligaro, "Spatial hole burning in thz quantum cascade lasers measured by time-domain spectroscopy." submitted to *Appl. Phys. Lett.*, 2007.
- [149] J. Kröll, J. Darmo, K. Unterrainer, S. Dhillon, C. Sirtori, X. Marcadet, and M. Calligaro, "Phase resolved measurement of stimulated emission." submitted to *Nature*, 2007.
- [150] *User Manual, "Tsunami: Mode-locked Ti:sapphire Laser," Spectra-Physics, 1995.*
- [151] *User Manual, "FEMTOSOURCE 20/20 HP/PRO/PRO HP/M1," Femtolasers, 2000.*



# Publications

## Journal papers

- [J1] J. Kröll, J. Darmo, and K. Unterrainer, “High performance electro-optic detector,” *Electron. Lett.* **40**, pp. 763-764, 2004.
- [J2] J. Darmo, T. Müller, W. Parz, J. Kröll, G. Strasser, and K. Unterrainer, “Few-cycle terahertz generation and spectroscopy of nanostructure,” *Philosophical Transactions of the Royal Society of London A* **362**, pp. 251-262, 2004.
- [J3] J. Darmo, V. Tamosiunas, G. Fasching, J. Kröll, K. Unterrainer, M. Beck, M. Giovannini, J. Faist, C. Kremser, and P. Debbage, “Imaging with a Terahertz quantum cascade laser,” *Optics Express* **12**, pp. 1879-1884, 2004.
- [J4] J. Kröll, J. Darmo, and K. Unterrainer, “Time and frequency resolved THz spectroscopy of micro- and nano-systems,” *Acta Physica Polonica A* **107**, pp. 92-98, 2005.
- [J5] J. Kröll, J. Darmo, K. Unterrainer, “Terahertz optical activity of sucrose single-crystals,” *Vibrational Spectroscopy* **43**, p.324 , 2007.
- [J6] J. Kröll, J. Darmo, K. Unterrainer, S. S. Dhillon, C. Sirtori, X. Marcadet, and M. Calligaro, “Phase resolved measurement of stimulated emission,” submitted to *Nature*, 2007.
- [J7] J. Darmo, J. Kröll, K. Unterrainer, S. S. Dhillon, C. Sirtori, X. Marcadet, and M. Calligaro, “Longitudinal spatial hole burning in terahertz quantum cascade lasers,” submitted to *Appl. Phys. Lett.*, 2007.
- [J8] J. Kröll, J. Darmo, K. Unterrainer, S. S. Dhillon, C. Sirtori, X. Marcadet, and M. Calligaro, “Spectral limitation in terahertz quantum cascade laser design: Thermally activated absorption” to be submitted to *Appl. Phys. Lett.*, 2007.

## Conference proceedings

- [P1] J. Kröll, J. Darmo, K. Unterrainer, S. Dhillon, C. Sirtori, X. Marcadet, and M. Calligaro, “Terahertz quantum-cascade laser dynamics in time-domain,” - 28th International Conference on the Physics of Semiconductors, Vienna, Austria, 24.07.2006 - 28.07.2006.

## Conference contributions

- [C1] J. Darmo, G. Strasser, J. Kröll, and K. Unterrainer, "Heterostructure-Based Photoconductive Terahertz Emitters," - GMe Annual Report 2003, Gesellschaft für Mikro- und Nanoelektronik, 2004, 3-901578-12-9, S. 53.
- [C2] J. Darmo, J. Kröll, and K. Unterrainer, "THz evanescent field spectroscopy," - The Joint 30th International Conference on Infrared and Millimeter Waves & 13th International Conference on Terahertz Electronics, Willimsburg, Virginia, USA; 19.09.2005 - 23.09.2005; in: "IRMMW-Thz 2005", (2005), ISBN 0-7803-9349-X; Paper-Nr. MA2-4, 2 S.
- [C3] J. Darmo, J. Kröll, M. Hulman, K. Unterrainer, and H. Kuzmany, "Terahertz time-domain linear spectroscopy of single-walled carbon nanotube film," - International Conference on Advanced Semiconductor Devices and Microsystems (ASDAM), Smolenice, Slovakia; 17.10.2004 - 21.10.2004; in: "IEEE Conference Proceedings of the 5th International Conference on Advanced Semiconductor Devices and Microsystems 2004 04 EX876", (2004), ISBN 0-7803-8535-7; S. 239 - 242.
- [C4] J. Darmo, J. Kröll, V. Tamosiunas, G. Fasching, K. Unterrainer, G. Strasser, M. Beck, M. Giovannini, and J. Faist, "Optical control processes in terahertz quantum-cascade laser waveguides," - Conference on Lasers and Electro-Optics, Baltimore, USA; 22.05.2005 - 27.05.2005; in: "Technical Digest", (2005), ISBN 1-55752-770-9; Paper-Nr. QTh16.
- [C5] J. Darmo, J. Kröll, and K. Unterrainer, "Time and frequency resolved THz spectroscopy of micro- and nano-systems," - 12th International Symposium on Ultrafast Phenomena in Semiconductors, Vilnius, Lithuania (eingeladen); 22.08.2004 - 25.08.2004; in: "Book of Abstracts", (2004), ISBN 9986-9284-4-3; S. 13.
- [C6] J. Darmo, J. Kröll, and K. Unterrainer, "Time-domain spectroscopy of THz quantum cascade lasers: Theoretical and experimental aspects," - IRMMW-THz 2006, Shanghai, China; 18.09.2006 - 22.09.2006; in: "Conference Digest", (2006), 1-4244-0400-2; S. 154.
- [C7] J. Darmo, J. Kröll, K. Unterrainer, M. Hulman, and H. Kuzmany, "Absorption of single-wall carbon nanotubes at Terahertz frequencies," - 12th International Conference on Terahertz Electronics, Karlsruhe, Deutschland; 27.09.2004 - 01.10.2004; in: "IEEE Conference Digest of the 2004 IRMMW 2004/THz 2004 04EX857", (2004), ISBN 0-7803-8490-3; S. 409 - 410.
- [C8] J. Darmo, J. Kröll, K. Unterrainer, M. Hulman, and H. Kuzmany, "Terahertz time-resolved linear spectroscopy of single-wall carbon nanotube films," - CLEO/IQEC 2004, San Francisco, USA; 16.05.2004 - 21.05.2004; in: "Technical Digest", (2004), Paper-Nr. JMB7, 2 S.

- [C9] J. Darmo, J. Kröll, K. Unterrainer, M. Hulman, and H. Kuzmany, "Terahertz time-resolved linear spectroscopy of single-wall carbon nanotube films," - CLEO/IQEC 2004, San Francisco, USA; 16.05.2004 - 21.05.2004; in: "Technical Digest", (2004), Paper-Nr. JMB7, 2 S.
- [C10] J. Kröll, J. Darmo, K. Unterrainer, W. Schrenk, and G. Strasser, "Enhanced emission and detection techniques for Terahertz time-domain spectroscopy," - OSA Topical Meetings: Optical Terahertz Science and Technology, Orlando, Florida, USA; 14.03.2005 - 16.03.2005; in: "Conference Program", (2005).
- [C11] J. Kröll, J. Darmo, S. Dhillon, K. Unterrainer, and C. Sirtori, "TuA1d: THz & quantum Cascade Structures," - 28th International Conference on the Physics of Semiconductors, Vienna, Austria; 24.07.2006 - 28.07.2006; in: "Programme and Abstracts", (2006), S. 51.
- [C12] J. Kröll, J. Darmo, G. Fasching, A. Benz, T. Roch, A.M. Andrews, W. Schrenk, V. Tamosiunas, G. Strasser, and K. Unterrainer, "Optical control in active terahertz waveguides," - The Joint 30th International Conference on Infrared and Millimeter Waves & 13th International Conference on Terahertz Electronics, Williamsburg, Virginia, USA; 19.09.2005 - 23.09.2005; in: "IRMMW-THz 2005", (2005), ISBN 0-7803-9349-X; Paper-Nr. RA1-5, 2 S.
- [C13] J. Kröll, J. Darmo, G. Fasching, G. Strasser, and K. Unterrainer, "Optical processes in terahertz quantum-cascade laser waveguides," - International School of Solid State Physics, Erice, Italy (eingeladen); 20.07.2005 - 26.07.2005; in: "International School of Solid State Physics 35th Workshop: Physics and Technology of THz Photonics", (2005), S. 3.
- [C14] J. Kröll, J. Darmo, and K. Unterrainer, "High resolution Terahertz time-domain spectroscopy," - CLEO/IQEC 2004, San Francisco, USA; 16.05.2004 - 21.05.2004; in: "Technical Digest", (2004), Paper-Nr. JMB5, 2 S.
- [C15] J. Kröll, J. Darmo, and K. Unterrainer, "Optical control of terahertz lasers," - 12th International Conference on Applied Physics of Condensed Matter, Mala Lucivna, Slovak Republic; 21.06.2006 - 23.06.2006; in: "Proceedings", (2006), S. 296 - 300.
- [C16] J. Kröll, J. Darmo, and K. Unterrainer, "Properties of ultra thin metal layers in the THz region," - Terahertz Workshop 2004 Technology and Application, Freiburg, Germany; 17.02.2004; in: "Book of Abstracts", (2004), S. 16.
- [C17] J. Kröll, J. Darmo, and K. Unterrainer, "Terahertz electrodynamics of ultra thin Cr layer," - The 28th Workshop on Compound Semiconductor Devices and Integrated Circuits held in Europe, Smolenice, Slovakia; 17.05.2004 - 19.05.2004; in: "WOCSDICE 2004", (2004), ISBN 80-227-2050-X; S. 125 - 126.

- [C18] J. Kröll, J. Darmo, and K. Unterrainer, "Terahertz spectroscopy of vibrational modes of molecular crystal of sucrose," - 11th International Conference of Terahertz Electronics, Karlsruhe, Deutschland; 27.09.2004 - 01.10.2004; in: "IEEE Conference Digest of the 2004 IRMMW 2004/THz 2004 04EX857", (2004), ISBN 0-7803-8490-3; S. 89 - 90.
- [C19] J. Kröll, J. Darmo, and K. Unterrainer, "Ultra-thin metallic layers studied by broadband Terahertz time-domain spectroscopy," - 12th International Conference on Terahertz Electronics, Karlsruhe, Deutschland; 27.09.2004 - 01.10.2004; in: "Conference Digest of the 2004 Joint 29th International Conference on Terahertz Electronics", (2004), ISBN 0-7803-8490-3; S. 465 - 466.
- [C20] J. Kröll, J. Darmo, and K. Unterrainer, "Ultra-thin metallic layers studied by broadband Terahertz time-domain spectroscopy," - International Symposium OPTRO 2005, Paris, France; 09.05.2005 - 12.05.2005; in: "Abstracts", European Space Agency, (2005), 3 S.
- [C21] J. Kröll, J. Darmo, and K. Unterrainer, "Ultra-thin metallic layers studied by broadband Terahertz time-domain spectroscopy," - International Symposium OPTRO 2005, Paris, France; 09.05.2005 - 12.05.2005; in: "Abstracts", European Space Agency, (2005), 3 S.
- [C22] J. Kröll, J. Darmo, K. Unterrainer, S. Dhillon, C. Sirtori, X. Marcadet, and M. Calligaro, "Coherent probing of quantum cascade laser emission by terahertz time-domain spectroscopy," - IRMMW-THz 2006, Shanghai, China; 18.09.2006 - 22.09.2006; in: "Conference Digest", (2006), 1-4244-0400-2; S. 154.
- [C23] J. Kröll, J. Darmo, K. Unterrainer, S. Dhillon, C. Sirtori, X. Marcadet, and M. Calligaro, "Terahertz time-domain spectroscopy of a quantum cascade laser," - CLEO/QELS, Long Beach California, USA; 21.05.2006 - 26.05.2006; in: "Post-deadline papers", (2006), ISBN 1-55752-815-2; 2 S.
- [C24] J. Kröll, J. Darmo, and K. Unterrainer, "Quantum cascade laser dynamics probed by broad-band Terahertz pulses," - Junior Scientist Conference 2006, Vienna, University of Technology; 19.04.2006 - 21.04.2006; in: "Proceedings", (2006), ISBN 3-902463-05-8; S. 311 - 312.
- [C25] M. Martl, J. Darmo, J. Kröll, and K. Unterrainer, "Terahertz surface plasmons: Time-domain analysis," - Physics of Intersubband Semiconductor Emitters, Summer School, Palazzone di Cortona, Italy; 25.06.2006 - 30.06.2006; in: "Programme and Abstracts", (2006), S. 1 - 2.
- [C26] T. Müller, F. Schrey, G. Fasching, J. Darmo, J. Kröll, W. Parz, A.M. Andrews, T. Roch, W. Schrenk, G. Strasser, and K. Unterrainer, "'THz Spectroscopy of Semiconductor Nanostructures and Applications,'" - International School of Solid State Physics, Erice, Italy (eingeladen); 20.07.2005 - 26.07.2005; in: "International School of Solid State Physics 35th Workshop: Physics and Technology of THz Photonics", (2005), S. 2.



- [C27] T. Müller, F. Schrey, G. Fasching, J. Darmo, J. Kröll W. Parz, A.M. Andrews, T. Roch, W. Schrenk, G. Strasser, and K. Unterrainer, "Ultrawide band THz spectroscopy applied to semiconductor nanostructures," - Mid-Infrared Coherent Sources (MICS) 2005, Barcelona, Spain (eingeladen); 06.11.2005 - 11.11.2005; in: "Book of Abstract", (2005), S. 5 - 6.
- [C28] V. Tamosiunas, G. Fasching, J. Darmo, J. Kröll G. Strasser, K. Unterrainer, R. Colombelli, C. Gmachl, K. West, L. Pfeiffer, and F. Capasso, "Magnetic quantization in terahertz Quantum cascade lasers," - 13th International Winterschool on New Developments in Solid State Physics, Mauterndorf, Austria; 15.02.2004 - 20.02.2004; in: "Book of Abstracts", (2004), S. 120.
- [C29] K. Unterrainer, J. Darmo, J. Kröll, T. Müller, G. Strasser, and T. Le, A. Stingl, "Cavity enhanced THz generation," - Photonics West, San Jose, CAL, USA (eingeladen); 24.01.2004 - 29.01.2004; in: "Technical Summary Digest", (2004), S. 401.
- [C30] J. Darmo, J. Kröll, G. Fasching, A. Benz, K. Unterrainer, A.M. Andrews, T. Roch, W. Schrenk, and G. Strasser, "Active photonics structures for terahertz frequencies," - 11th International Workshop on Applied Physics of Condensed Matter, Mala Lucivna, Slovakia; 15.06.2005 - 17.06.2005.
- [C31] J. Darmo, J. Kröll, T. Müller, G. Strasser, and K. Unterrainer, "Cavity enhanced THz generation," - Terahertz and Gigahertz Electronics and Photonics III, part of the Photonics West Symposium Optoelectronics 2004: Integrated Optoelectronics Devices, San Jose, USA (eingeladen); 24.01.2004 - 29.01.2004.
- [C32] J. Darmo, J. Kröll, G. Strasser, C. Kremser, and K. Unterrainer, "Few-cycle THz properties of bio-molecules," - 11th International Conference of Terahertz Electronics, Sendai, Japan; 24.09.2003 - 26.09.2003.
- [C33] J. Darmo, J. Kröll, G. Strasser, and K. Unterrainer, "Linear spectroscopy and imaging with compact Terahertz sources," - Terahertz Workshop 2004 Technology and Application, Freiburg, Germany (eingeladen); 17.02.2004.
- [C34] J. Darmo, J. Kröll, G. Strasser, K. Unterrainer, and C. Kremser, "Spectroscopy and imaging with few-cycle Terahertz radiation," - International Workshop on Applied Physics of Condensed Matter (APCOM) 2003, Mala Lucivna, Slovakia; 11.06.2003 - 13.06.2003.
- [C35] G. Fasching, A. Benz, J. Kröll, J. Darmo, V Tamosiunas, R. Zobl, A.M. Andrews, T. Roch, W. Schrenk, G. Strasser, and K. Unterrainer, "Design and applications of THz quantum-cascade lasers," - Montanuniversität Leoben, Leoben, Austria (eingeladen); 10.11.2005.
- [C36] T. Müller, F. Schrey, G. Fasching, J. Darmo, J. Kröll, W. Parz, K. Unterrainer, A.M. Andrews, T. Roch, and W. Schrenk, "Generation and application of THz radiation in semiconductor nanostructures," - European Materials Research Society Spring Meeting, Nice, France (eingeladen); 29.05.2006 - 02.06.2006.

- [C37] V. Tamosiunas, R. Zobl, G. Fasching, T. Müller, J. Darmo, J. Kröll, G. Strasser, K. Unterrainer, R. Colombelli, C. Gmachl, K. West, L. Pfeiffer, and F. Capasso, "Field Control of THz Quantum Cascade Lasers," - International Conference on Physics of Semiconductor (ICPS), Flagstaff, USA; 26.07.2004 - 30.07.2004.
- [C38] J. Kröll, J. Darmo, G. Fasching, A. Benz, T. Roch, M. Andrews, W. Schrenk, V. Tamosiunas, G. Strasser, and K. Unterrainer, "Optical control in active terahertz waveguides," - The- Joint 30th International Conference on Infrared and Millimeter Waves (IRMMW), Williamsburg, USA; 19.09.2005 - 23.09.2005.
- [C39] J. Darmo, J. Kröll, and K. Unterrainer, "THz evanescent field spectroscopy," - The- Joint 30th International Conference on Infrared and Millimeter Waves (IRMMW), Williamsburg, USA; 19.09.2005 - 23.09.2005.
- [C40] J. Kröll, J. Darmo, V. Tamosiunas, G. Fasching, G. Strasser, K. Unterrainer, M. Beck, M. Giovannini, and J. Faist, "Optical control processes in terahertz quantum-cascade laser waveguides," - Conference on lasers and electro-optics 2005 (CLEO), Baltimore, USA, 23.05.2005 - 27.05.2005.

## Award



### Prix de la meilleure communication poster:

J. Kröll, J. Darmo, and K. Unterrainer, "Ultra-thin metallic layers studied by broadband Terahertz time-domain spectroscopy," - International Symposium OPTRO 2005, Paris, France; 09.05.2005 - 12.05.2005

# Acknowledgements

I would like to use this opportunity to thank persons for the help and support during the last years. Without the help from a lot of people this work would not have been such successful. First, I would like to thank my supervisor Prof. Dr. Karl Unterrainer who gave me the chance working in this research team on the field of terahertz time-domain spectroscopy. Further, I would like to thank my good friend and chief advisor Dr. Juraj Darmo. The education and training I got from him on various fields in physics and chemistry was the main motor for this thesis. Especially, the topic of pulse amplification with quantum cascade lasers was an idea he had already many years ago. Also I want to thank Prof. Dr. Jürgen Smoliner and Dr. Frederik Felix Schrey for many interesting discussions on the field of semiconductors and measurement techniques. Their comments were all the time very helpful in times of unsolved physical problems or open questions. Latter were often successfully discussed with a good beer or cocktail after work.

Many thanks also to Dr. Sukhdeep Dhillon from University Paris 7 and Prof. Dr. Carlo Sirtori from Thales Research & Development. In a time of frustration due to failed experiments caused by a lack of proper laser material they provided high performance terahertz quantum cascade lasers which were perfectly suited for the experiments presented in this work.

There are too many people who helped me to namecheck, but instead I would like to thank all members of the photonics and solid state electronics institute. The support given by these people was a confident component of this work.

Further I would like to thank my parents Erika and Josef. They supported me for many years and during time periods of unsolved problems or deep frustrations their encouragement helped me proceeding my work. Also they were and still are a harbor of peace and good meals.

Last, but for sure not least, I want to thank my wife and my son. Nancy gave me all the time very important support and at the very end of my thesis she made the largest present to me she was able to give. My son Josef Leonard was born at 10. January 2007 and is my pride and joy. During the long time writing this thesis a look in his deep blue eyes helped to proceed faster finding more time to play with him.



# Curriculum Vitae

## Personal data

Name: Dipl.-Ing. Josef KRÖLL  
Family status: Married, 1 child  
Date of birth: 17.November.1975  
Place of birth: Vienna, Austria  
Nationality: Austria  
Address: Seitenberggasse 67/7/7, A-1160 Vienna, Austria  
EMail: josef.kroell@gmail.com



## Education and army service

- 07/03 - now PhD study at the Vienna University of Technology  
Thesis title: "High performance THz time-domain spectroscopy:  
Application, control and amplification of few cycle THz radiation"  
Estimated date of viva-voce: Spring 2007
- 10/97 - 06/03 Study of electrical engineering at the Vienna University of Technology  
Branch of study: Computer engineering  
Diploma thesis title: "Few cycle Terahertz spectroscopy and imaging"  
Final degree with distinction
- 07/95 - 02/96 Army service: Armored forces - Zwölfaxing barracks
- 09/90 - 06/95 School of electrical engineering - Schellinggasse in Vienna  
Branch of education: Energy technology and high power electronics  
University entrance diploma with distinction
- 09/86 - 06/90 Grammar school - Schuhmeierplatz in Vienna  
Graduation with distinction
- 09/82 - 06/86 Elementary school - Julius Meinl in Vienna  
Graduation with distinction

## Career history

- 07/03 - now    Project-Assistant at the Vienna University of Technology  
Integrated Project - TeraNova (EU)  
“Novel Terahertz Sensing & Imaging Systems for Biotechnology, Healthcare,  
Security & Process Monitoring”
- 07/06            Organization of the symposium: ICPS 2006 in Vienna  
Responsibility: Presentation technique, catering and poster presentations
- 07/96 - 10/01   T-Systems: 2nd level support service and server administration
- 04/96 - 06/96   Student trainee at SIEMENS PSE (project Spectrum EDF)
- 90/90 - 06/95   Several internships at SIEMENS, AEG, Kone and Donaukraft

## Abilities

- Skills:            Semiconductor-, femtosecond- and quantum cascade lasers  
Optical systems  
Semiconductor processing  
Time resolved infrared spectroscopy  
III-V semiconductors  
Optical and electrical measurement techniques
- Languages:       German (native speaker), English (business fluent)
- Computer literacy: Windows, Linux, Office, C++, LabView, MatLab, OriginLab, CorelDraw

## Hobbies

- Sport:     Skiing, Inline-skating
- Others:    Traveling, Computer science



